SISSA - International School for Advanced Studies

Dusty Star-Forming Galaxies and Supermassive Black Holes at High Redshifts: *In Situ* Coevolution

Thesis Submitted for the Degree of
"Doctor Philosophiæ"

Supervisors
Prof. Andrea Lapi
Prof. Gianfranco De Zotti
Prof. Luigi Danese

Candidate
Claudia Mancuso

October 2016

To my fiancè Federico, my sister Ilaria,
my mother Ennia, Gaia and Luna,
my Big family.

"Quando canterai la tua canzone, la canterai con tutto il tuo volume,
che sia per tre minuti o per la vita, avrá su il tuo nome."
Luciano Ligabue

Contents

List of Figures

List of Tables

Declaration of Authorship

I, Claudia Mancuso, declare that this thesis titled "Dusty Star-Forming Galaxies and Supermassive Black Holes at High Redshifts: *In Situ* Coevolution" and the work presented in it are my own.
I confirm that:

- This work was done while in candidature for the degree of Doctor of Philosophy at SISSA.
- Where I have consulted the published work of others, this is always clearly attributed.
- Where I have quoted from the work of others, the source is always given. With the exception of such quotations, this thesis is entirely my own work.
- I have acknowledged all main sources of help.
- This thesis is mainly based on the Mancuso et al. (2015), Mancuso et al. (2016a) and Mancuso et al. (2016b, submitted) papers.

Abstract

We have exploited the continuity equation approach and the star-formation timescales derived from the observed 'main sequence' relation (Star Formation Rate vs Stellar Mass), to show that the observed high abundance of galaxies with stellar masses $\gtrsim$ a few $10^{10}\,M_{\odot}$ at redshift $z \gtrsim 4$ implies the existence of a galaxy population featuring large star formation rates (SFRs) $\psi \gtrsim 10^{2}\,M_{\odot}\,\mathrm{yr}^{-1}$ in heavily dust-obscured conditions. These galaxies constitute the high-redshift counterparts of the dusty star-forming population already surveyed for $z \lesssim 3$ in the Far-InfraRed (FIR) band by the *Herschel* space observatory. We work out specific predictions for the evolution of the corresponding stellar mass and SFR functions out to $z \sim 10$, elucidating that the number density at $z \lesssim 8$ for SFRs $\psi \gtrsim 30\,M_{\odot}\,\mathrm{yr}^{-1}$ cannot be estimated relying on the UltraViolet (UV) luminosity function alone, even when standard corrections for dust extinction based on the UV slope are applied. We compute the number counts and redshift distributions (including galaxy-scale gravitational lensing) of this galaxy population, and show that current data from *AzTEC-LABOCA*, *SCUBA-2* and *ALMA-SPT* surveys are already digging into it. We substantiate how an observational strategy based on a color preselection in the far-IR or (sub-)mm band with *Herschel* and *SCUBA-2*, supplemented by photometric data via on-source observations with *ALMA*, can allow to reconstruct the bright end of the SFR functions out to $z \lesssim 8$. In parallel, such a challenging task can be managed by exploiting current UV surveys in combination with (sub-)mm observations by *ALMA* and *NIKA2*. The same could be done with radio observations by *SKA* and its precursors.

In particular we have worked out predictions for the radio counts of star-forming galaxies down to nJy levels, along with redshift distributions down to the detection limits of the phase 1 Square Kilometer Array MID telescope (SKA1-MID) and of its precursors. To do that we exploited our SFR functions with relations between SFR and radio (synchrotron and free-free) emission. Our results show that the deepest SKA1-MID surveys will detect high-z galaxies with SFRs two orders of magnitude lower compared to *Herschel* surveys. The highest redshift tails of the distributions at the detection limits of planned SKA1-MID surveys comprise a substantial fraction of strongly lensed galaxies. The SKA1-MID will thus provide a comprehensive view of the star formation

history throughout the re-ionization epoch, unaffected by dust extinction. We have also provided specific predictions for the EMU/ASKAP and MIGHTEE/MeerKAT surveys.

We finally provide a novel, unifying physical interpretation on the origin, the average shape, the scatter, and the cosmic evolution for the main sequences (MS) of star-forming galaxies and active galactic nuclei at high redshift $z \gtrsim 1$. We achieve this goal in a model-independent way by exploiting the redshift-dependent SFR functions, and the deterministic evolutionary tracks for the history of star formation and black hole accretion, gauged on a wealth of multiwavelength observations including the observed Eddington ratio distribution. We further validate these ingredients by showing their consistency with the observed galaxy stellar mass functions and active galactic nucleus (AGN) bolometric luminosity functions at different redshifts via, again, the continuity equation approach. Our analysis of the main sequence for high-redshift galaxies and AGNs highlights that the present data strongly support a scenario of *in situ coevolution* for star formation and black hole accretion, envisaging these as local, time coordinated processes.

Chapter 1

Introduction

The main ingredients to build up galaxies are dark matter (DM) in halos, stars and supermassive black holes (BHs), which are known to populate the central regions of the biggest galaxies. The basic idea of standard cosmological scenarios is that primordial density fluctuations grow, thanks to gravitational instability driven by cold collisionless DM, painting a "bottom up" ΛCDM (cold dark matter) scenario of structure formation. From a theoretical perspective, N-body simulations (e.g. Diemand et al., 2007; Springel et al., 2008; Tinker et al., 2008; Stadel et al., 2009) have been able to account for the large scale matter distribution in the Universe as determined by the primordial dark matter perturbations evolving into bound, virialized structures ('halos') under the action of gravity. Using numerical hydrodynamic techniques in which gravity, hydrodynamics and thermodynamics are implemented, and their equations concurrently solved for grid cells, such codes are able to model galaxy formation down to halo scales. However, on smaller, (sub-)galactic scales, the complexity of baryonic physics takes over, and it is necessary to implement ad hoc recipes in order to model phenomena as star-formation, BH accretion, feedbacks, etc, making it extremely difficult to provide an ab initio description of all these relevant processes, that moreover occur on vastly different spatial and time scales. This limitation is also connected to the extremely demanding computational requirements. These issues cause the poor predictive capability of current approaches (see Frenk and White, 2012; Scannapieco et al., 2012; Somerville and Davé, 2015) based on such hydrodynamic codes (e.g. Vogelsberger et al., 2014; Dubois et al., 2014; Khandai et al., 2015; Kaviraj et al., 2016). The (semi-)analytic (SAMs) models (e.g. Bower et al., 2006; Croton et al., 2006, 2016; Fanidakis et al., 2011; Guo et al., 2011; Menci et al., 2012; Somerville et al., 2012; Somerville and Davé, 2015) instead does not explicitly solve fundamental equations for particles or grid cells, while they adopt simplified flow equations for bulk components: they are able, for example, to trace how much hot gas cools and turns into stars, or how feedback processes remove

the same gas, stopping the star formation (SF) process. On the other side they have problems in reproducing observations of scaling relations, as for example the slope of the star-forming Main Sequence (see Somerville and Davé, 2015, for a review). Hybrid models are also used to study galaxy formation and evolution: they consist in evolving forward the hydrodynamic properties of baryons in galaxies that have been initialized with idealized conditions (Casey et al., 2014). Their advantage is that they can reach high resolution (a few-100 pc), at the cost of having no knowledge of the cosmological context of the galaxies, making impossible to evolve them forward to infer properties of the descendants of high-z objects. Such difficulties of theoretical models have originated a longstanding debate concerning the main actors in regulating galaxy and BH formation and evolution. Three popular scenarios are currently (still) on the market. The first one relies on a prominent role of merging among dark matter halos as the main driver of the evolution processes (e.g. Bower et al., 2006; Croton et al., 2006; Hopkins et al., 2006; Fanidakis et al., 2012; Somerville and Davé, 2015). An alternative view assumes that star formation and black hole accretion are supported by steady cold gas streams along filaments of the cosmic web (e.g. Dekel et al., 2009; Bournaud et al., 2011). Finally, an alternative view envisages star formation and BH accretion in galaxies to be essentially *in situ* processes (e.g. Lapi et al., 2006, 2011, 2014; Lilly et al., 2013; Aversa et al., 2015; Mancuso et al., 2016), triggered by the early collapse of the host dark matter halos, but subsequently controlled by self-regulated baryonic physics and in particular by energy feedback from supernovae and AGNs. DM halos assembly is attributed to processes occurring in two phases: the first one is an early fast collapse, during which the central regions reach a dynamical quasi equilibrium, while the second one is a slow accretion phase, during which only the halo outskirts are affected (Zhao et al., 2003; Wang et al., 2011; Lapi and Cavaliere, 2011). The rapid star formation occurring in the central regions of the halo during the first phase is considered the leading process in galaxy formation (see Lapi et al., 2011, 2014; Cai et al., 2013).
This latter scenario has recently received robust support from observations of high redshift ($z \gtrsim 1$) dusty star-forming galaxies, an abundant population discovered via wide areas far-IR/(sub-)mm surveys with *Herschel*, *SPT*, *LABOCA*, and *SCUBA2*, in many instances thanks to strong gravitational lensing by foreground objects. Specifically, high-resolution follow-up observations of these galaxies in the far-IR/(sub-)mm/radio band via ground-based interferometers, such as *SMA*, *VLA*, *PdBI* and recently *ALMA* has revealed star formation to occur in a few collapsing clumps distributed over spatial scales smaller than a few kpc, and at an overall efficiency lower than 20% (e.g. Finkelstein et al., 2013; Negrello et al., 2014; Neri et al., 2014; Rawle et al., 2014; Riechers et al., 2014; Ikarashi et al., 2015; Dye et al., 2015; Ma et al., 2015a; Simpson et al., 2015; Harrison et al., 2016; Scoville et al., 2016).

Given that the different phases of galaxy formation present many different physical conditions, both depending on the type and size of the galaxies and on the evolutionary

phase itself, to properly address the problem is necessary to use multiwavelength data from many different surveys, that can help in understanding the processes involved, starting from the formation of first stars to the present-day galaxy properties, such as forms, sizes, masses, colors, luminosities, metallicities and clustering. One possibility to comprehend the global picture is to focus on the emission properties of the different galaxy populations as a whole, tracing for example the evolution of the galaxy luminosity density from the far-UV (FUV) to the far-Infrared (FIR), empirically determining a global star formation history of the Universe.

The star formation in galaxies can be inferred from lines like Lyα and Hα, and from continuum emission in the ultraviolet (UV), infrared (IR), radio and X-ray bands (see Sect.2.4 and Kennicutt and Evans (2012a) for a review). In the local Universe a significant fraction of the star formation in galaxies occurs in dust-enshrouded environments (e.g. Carilli et al., 2013; Madau and Dickinson, 2014a), with a clear tendency for dust extinction to become more severe as the star formation rate (SFR) increases. Dust causes the UV emission from young massive stars, which traces the SFR, to be absorbed and reradiated in the far-IR band; thus a combined measurement of UV and far-IR luminosities would constitute a sound probe of the SFR.

Even at high redshift dusty star-forming galaxies are quite common, as shown by the large surveys obtained by ground- and space-based instruments in the recent years (for a review, see Casey et al., 2014). The tendency for dust obscuration to increase with SFR is also confirmed by the increase of the UV-continuum slope $\beta_{\rm UV}$ with raising luminosity in UV-selected galaxies up to $z \sim 8$ (see Bouwens et al. (2014), and references in their Fig. 1; also Reddy et al. (2012); Coppin et al. (2015)).

The correlation of the UV slope $\beta_{\rm UV}$ with the ratio of the IR to UV luminosity (dubbed IRX ratio) in star-forming galaxies has been commonly exploited in order to estimate their dust absorption (e.g. Meurer et al., 1999). The former is in fact related to the absorption coefficient $A_{\rm UV}$, which is strictly related to the IRX ratio, that can read IRX=$(10^{0.4S_{\rm UV}} - 1)\times$B, where B is a bolometric correction. As a matter of fact, far-IR observations of UV-selected galaxies confirmed that the estimates of dust attenuation based on the $\beta_{\rm UV}$-IRX correlation are reliable for objects with SFR $\psi \lesssim 30\,M_\odot$ yr^{-1} (e.g. Lee et al., 2012; Reddy et al., 2012, 2015; Coppin et al., 2015). On the other hand, the scatter of the $\beta_{\rm UV}$-IRX relation largely widens with increasing $\beta_{\rm UV}$ and IRX (i.e., with increasing SFR on the average), making the dust correction quite uncertain for SFR $\psi \geq 30\,M_\odot$ yr^{-1} (e.g. Chapman et al., 2000; Goldader et al., 2002; Conroy, 2013, for a recent review).

The relevance of dust absorption is evident from the shape and redshift evolution of the luminosity function at the bright end (e.g. Mao et al., 2007; Bouwens et al., 2009; Cai et al., 2014; Bowler et al., 2015), which shows how the uncertainty in the extinction strongly affects SFR determinations inferred from UV surveys. At redshift up to $z \sim$

3 the effect has been statistically quantified by Aversa et al. (2015), by comparing the SFR function as derived from the UV luminosity function (corrected for the dust absorption basing on the UV slope) with that inferred by the far-IR surveys obtained with the SPIRE instrument on board of *Herschel* (see Lapi et al., 2011; Gruppioni et al., 2013, 2015; Magnelli et al., 2013). These authors have shown that UV surveys start to undersample galaxies endowed with SFR $\psi \geq 30\,M_{\odot}$ yr^{-1}, even when corrected by dust attenuation on the basis of the UV slope β-IRX correlation. They have also highlighted that the galaxy stellar mass function at $z \lesssim 3$ can be recovered from the intrinsic SFR function. At higher redshifts $z \geq 3$ the direct comparison is hampered by the fact that, while the UV luminosity function is soundly determined up to redshift $z \sim 8$ (e.g. Bouwens et al., 2015; Finkelstein et al., 2015a; Bowler et al., 2015), the far-IR luminosity function is not yet available due to the sensitivity limits of current instruments.

To circumvent the problem, Aversa et al. (2015) have argued that the continuity equation applied to SFR and stellar mass can provide an important clue to the distribution of the intrinsic SFR even at $z \geq 4$. In this vein, it is worth noticing that the spectral energy distribution (SED) for large samples of high redshift galaxies has been recently determined from the UV to near-/mid-IR, allowing for sound estimate of the photometric redshift, stellar mass, dust extinction, SFR and age of stellar populations (e.g. Duncan et al., 2014; Speagle et al., 2014; Salmon et al., 2015; Grazian et al., 2015; Caputi et al., 2015; Stefanon et al., 2015), with due caveats related to the degeneracy among these parameters (e.g. Conroy, 2013).

As presented in many works, estimate of the galaxy stellar mass function at substantial redshift has been obtained by combining the observed mass-to-UV light ratio and the UV luminosity function (e.g. Stark et al., 2009; González et al., 2011; Lee et al., 2012; Song et al., 2015). However, both these key ingredients are expected to be affected by dust extinction at high UV luminosity. Moreover, the correlation $M_{\star} - M_{\rm UV}$ is largely scattered. Note that such a relation is also relevant for the definition of the so called 'main sequence', once the UV luminosity is translated into SFR, provided that the dust effects are properly taken into account.

Bypassing the UV selection, deep optical/near-IR/mid-IR imaging provided by the *HST*, *Spitzer*, and the *VLT* on CANDELS-UDS, GOODS-South, and HUDF fields have recently been exploited in order to determine the galaxy stellar mass function at redshift $z \geq 3$, with the stellar mass derived from the SED fitting technique including nebular emission (Duncan et al., 2014; Grazian et al., 2015; Caputi et al., 2015). The stellar mass function has been computed by weighting the galaxies with the $1/V_{\rm max}$ Schmidt's estimator (Schmidt, 1968). The outcome agrees with that derived only for UV-selected galaxies when large intrinsic scatter ≥ 0.5 dex in the $M_{\star} - M_{\rm UV}$ relation is assumed (see Fig. 9 in Duncan et al., 2014). Such a wide scatter suggests that a fraction of the low

luminosity UV-selected galaxies are already massive, and that either they are already quiescent or they form most of their stars within a dusty interstellar medium (ISM; see also Grazian et al., 2015). As a matter of fact, Song et al. (2015) notice the increase of massive but faint UV galaxies at lower redshift, suggesting that the role of the dust is increasingly relevant with cosmic time. Also Bowler et al. (2015) point out that the bright end of the UV luminosity function appears to steepen from $z \sim 7$ to 5, possibly suggesting the onset of dust obscuration. Additional evidence for the presence of dust at quite high redshift is confirmed by observations of quasars (e.g. Bolton et al., 2011), direct detection from *ALMA* (e.g. Weiß et al., 2013; Swinbank et al., 2014; da Cunha et al., 2015) and indirectly from the nature of high-z gamma ray bursts (e.g. Schady et al., 2014).

In this work we have derived a determination of the intrinsic SFR and stellar mass functions, unbiased with respect to dust obscuration; these are indeed crucial ingredients for our physical understanding of galaxy formation and evolution. For example, these functions can be used to obtain *intrinsic* relationships of the SFR/stellar mass vs. the dark matter halo mass via the abundance matching technique (e.g. Vale and Ostriker, 2004; Shankar et al., 2006; Moster et al., 2013; Behroozi et al., 2013). We shall see that the exploitation of such intrinsic relationships, as opposed to those derived after dust corrections based on the UV slope, leads to naturally solve a couple of critical issues in galaxy formation and evolution, pointed out by Steinhardt et al. (2016) and by Finkelstein et al. (2015a). The former authors claim massive high-redshift galaxies to have formed impossibly early according to standard models of galaxy assembly; the latter authors point out an unexpected increase of the stellar to baryon fraction in bright galaxies at high redshift.

Given the importance of understanding the behavior of the star formation rate functions (SFRFs) at the bright end up to high redshifts, in order to shed light on how galaxies built up at early ages, we also provide some selection techniques that will help to populate the bright end of the SFRFs at high z >4, including an analysis of the capabilities of the radio emission to pinpoint such objects. In particular we derived number counts and redshift distribution predictions for the SKA and its precursors, to study the capability of such instruments to help the understanding of the formation and evolution of galaxies.

Dusty star-forming galaxies feature stellar masses strongly correlated to the SFR, in the way of an almost linear relationship dubbed 'Main Sequence', with a normalization steadily increasing as a function of redshift, and with a limited scatter around 0.3 dex (Daddi et al., 2007; Elbaz et al., 2007; Pannella et al., 2009, 2015; Rodighiero et al., 2011, 2014; Speagle et al., 2014; Whitaker et al., 2014; Renzini and Peng, 2015; Salmon et al., 2015; Tasca et al., 2015; Erfanianfar et al., 2016; Kurczynski et al., 2016). Taking advantage of our SFR functions, we present an analysis of such a relation and

a new interpretation in line with the *in situ* scenario.

Turning on the last ingredient that play a role in galaxy formation, the central supermassive BH, we point out that some degree of coevolution between it and its host galaxy must be present. It is indicated by observed tight relationships between the central BH masses and the host galaxy properties, as stellar mass in old stars, luminosity, velocity dispersion, morphological indicators (e.g. Kormendy and Richstone, 1995; Magorrian et al., 1998; Ferrarese and Merritt, 2000; Gebhardt et al., 2000; Tremaine et al., 2002; Marconi and Hunt, 2003; Häring and Rix, 2004; McLure and Dunlop, 2004; Ferrarese and Ford, 2005; Graham, 2007; Greene and Ho, 2007; Lauer et al., 2007; Gültekin et al., 2009; Kormendy and Bender, 2009; Vika et al., 2009; Graham et al., 2011; Sani et al., 2012; Beifiori et al., 2012; McConnell and Ma, 2013; Kormendy and Ho, 2013; Ho and Kim, 2014; Shankar et al., 2016), and by recognizing a parallel evolution of the star formation rate density (SFRD) for galaxies and of the luminosity density for active galactic nuclei (AGNs; e.g. Boyle and Terlevich, 1998; Franceschini et al., 1999; Heckman et al., 2004; Marconi et al., 2004; Silverman et al., 2009; Madau and Dickinson, 2014b; Aird et al., 2015).

Recent, model-independent statistical analysis based on the continuity equation and the abundance matching techniques (see Peng et al., 2010; Moster et al., 2010, 2013; Behroozi et al., 2013; Aversa et al., 2015; Caplar et al., 2015; Mancuso et al., 2016) have demonstrated that dusty star-forming galaxies with SFRs $\gtrsim 10^2\, M_\odot\, \mathrm{yr}^{-1}$ constitute the progenitors of passively-evolving systems with large stellar masses $M_\star \gtrsim 10^{11}\, M_\odot$, that are indeed found to be abundant even at high redshift $z \gtrsim 1$ (see Bernardi et al., 2013; Santini et al., 2012a; Ilbert et al., 2013; Duncan et al., 2014; Tomczak et al., 2014; Caputi et al., 2015; Mawatari et al., 2016; Song et al., 2016). These results offer an exciting bridge between the astrophysics of galaxies and AGNs, since massive objects are thought to become passive when their star formation is quenched by the energetic feedback from the central supermassive BH (see Silk and Rees, 1998; Fabian, 1999; King, 2003; Granato et al., 2004; Di Matteo et al., 2005; Lapi et al., 2006, 2014; King, 2014).

A great impulse in the study of the role played by supermassive BHs in galaxy evolution has recently come from: (i) X-ray followup observations of AGNs growing at the center of star-forming galaxies selected in the far-IR/(sub-)mm or in the K-band (e.g. Borys et al., 2005; Alexander et al., 2005, 2008; Laird et al., 2010; Symeonidis et al., 2010; Xue et al., 2010; Georgantopoulos et al., 2011; Carrera et al., 2011; Melbourne et al., 2011; Rafferty et al., 2011; Mullaney et al., 2012a; Johnson et al., 2013; Wang et al., 2013b; Delvecchio et al., 2015; Rodighiero et al., 2015); (ii) far-IR/(sub-)mm followup observations of the star formation process in galaxies hosting X-ray selected AGNs (e.g. Page et al., 2004, 2012; Stevens et al., 2005; Lutz et al., 2010; Shao et al., 2010; Mainieri et al., 2011; Harrison et al., 2012; Mullaney et al., 2012b, 2015; Rosario

et al., 2012; Rovilos et al., 2012; Santini et al., 2012b; Azadi et al., 2015; Barger et al., 2015; Stanley et al., 2015; Harrison et al., 2016) or mid-IR/optically selected quasars (e.g. Omont et al., 1996, 2001, 2003; Carilli et al., 2001; Priddey et al., 2003; Wang et al., 2008; Walter et al., 2009; Serjeant et al., 2010; Bonfield et al., 2011; Mor et al., 2012; Xu et al., 2015; Netzer et al., 2016; Harris et al., 2016).

These observational studies have revealed a well defined behavior of the average SFR in the host galaxies with respect to the bolometric AGN luminosity (see review by Alexander and Hickox, 2012); specifically, the SFR is found to be roughly constant for moderate AGN luminosities, while for high luminosities it stays constant or decreases in X-ray selected AGNs, and increases steeply in mid-IR or optically selected quasars (QSOs). A correlation between the average AGN luminosity and the stellar mass emerges also when focusing on mass-selected galaxy samples. All these relationships are often interchangeably referred to as 'AGN main sequence'.

The theoretical interpretation, especially in the range of AGN luminosities investigated via X-ray stacking, is far from trivial; phenomenological models (Aird et al., 2013; Caplar et al., 2015; Hickox et al., 2014; Stanley et al., 2015) call into play AGN variability, as inspired from the merging scenario (see Di Matteo et al., 2005; Hopkins et al., 2005; Hopkins and Hernquist, 2009; Novak et al., 2011; Hopkins et al., 2013, 2016) and inferred from consistency with the locally observed Eddington ratio distribution. Variability can effectively weaken an underlying correlation between AGN luminosity and SFR, if the AGN luminosity substantially changes (i.e., by more than an order of magnitude) over much shorter timescales than the star formation across the galaxy. We shall show that such stochastic model faces instead some problems in reproducing the AGN luminosity functions observed at high $z \gtrsim 1$.

The plan of the thesis is the following: in Chapter 2 we give an overview of the process of star formation in galaxies, then in Chapter 3 we present our SFR functions and validate them. In Chapter 4 we start from the SFR functions and propose some methods to hunt dusty star forming galaxies in the IR. The same thing, but in the radio band, is done in Chapter 5. In Chapter 6 and 7 we present an analysis, based on our SFR functions, of the Main Sequence of star forming galaxies and AGNs, respectively. Finally, in Part 8 we summarize our results.

Throughout this work we adopt the standard flat concordance cosmology (Planck Collaboration XIII 2015) with round parameter values: matter density $\Omega_M = 0.32$, baryon density $\Omega_b = 0.05$, Hubble constant $H_0 = 100\,h$ km s^1 Mpc^1 with $h = 0.67$, and mass variance $\sigma_8 = 0.83$ on a scale of $8\,h^{-1}$ Mpc. Stellar masses and luminosities (or SFRs) of galaxies are evaluated assuming the Chabrier's (2003) initial mass function (IMF).

Chapter 2

Star Formation in galaxies

The processes of star formation in galaxies are one of the bulk ingredients that need to be understood and reproduced in order to shed light on the formation and evolution of galaxies. Important constraints on star formation theories are given by the mass and luminosity functions of the stellar component in galaxies: a mass-luminosity relation, in fact, provides information on how the stellar mass has grown. Note that the main contributors of the stellar mass component are old, low-mass stars ($M < 1\ M_{\odot}$), which emit essentially in the K-band, while the stellar luminosity is mainly contributed by younger higher-mass stars ($M > 1\ M_{\odot}$), which emit essentially in the UV band.

When trying to reconstruct the formation history of galaxies via the formation history of stars in the Universe, it is necessary to take into account some elements that are fundamental to do not occur in big mistakes.
The stars that we can observe in single galaxies span large ranges of masses, ages and metal abundances; their UV light can be strongly attenuated by dust in the galaxy, making UV measurements unreliable to reconstruct the SFR, that will be, in this case, better constrained by IR light, which is emitted by the heated dust. Usually a galaxy spectrum is made up of composite stellar population, and its true distribution is generally unknown: for most of the observed galaxies, in fact, it is possible to observe only the integrated light, i.e. the integrated spectrum of the object. It is then very difficult to separate the different contributions without being affected by some degeneracy of the observables. Given the composite nature of stellar populations, it is moreover necessary, when we interpret the observed light, to make some simplifying assumptions, such as the form of the Initial Mass Function (IMF), the wavelength dependance of dust attenuation, etc.

In this chapter we give an overview on the main ingredients that must be assumed or used in order to reconstruct the SFR function of the galaxies, for which we give an estimation in Chapter 3.

2.1 Initial Mass Function (IMF) and Stellar Population Synthesis (SPS)

The stellar Initial Mass Function (IMF) gives the relative probability for the formation of stars with different masses, that originally have been formed along the main sequence. It underlies the relation between mass, light and stellar population and controls the proportion of hot, bright stars (i.e. those dominating the emission of light in the UV) and cool faint stars (i.e. those dominating the mass function, that emit essentially in the K-band). Since stars with different masses evolve at different rates, it also regulates the evolution of the integrated stellar population in color and luminosity.

From and observational point of view, it is not that easy to constrain the stellar IMF: in fact neither photometric (colors) or spectroscopic (lines) measurements of a galaxy can uniquely characterize its underlying IMF. One of the few ways to have a reliable estimation consists in counting stars as a function of mass, but obviously this is possible only for an extremely limited sample of very nearby stellar populations (namely within our Galaxy or in its satellites). Another possibility would be to use kinematics as velocity dispersion or rotation curves, derived from measurements of mass-to-light ratios for galaxies, to obtain a mass that can be compared with the luminosity. Unfortunately such measurements are very difficult to obtain, especially for faint galaxies at high redshifts.

Because of all these issues, in general people assume the IMF to be universal, considering the same shape at all times in all galaxies. The most usual functional form is a power law, and was originally proposed by Salpeter (1955) for stellar masses 1 $M_\odot$<M_*<100 $M_\odot$. It writes

$$\xi(\log m) = \frac{dN}{d\log m} = Cm^{-x} \tag{2.1}$$

with N= stellar number density per logarithmic mass bin, C= normalization constant and x=power law exponent, that according to Salpeter (1955) is x$\sim$ 1.35.

Another possibility for the IMF shape, presented by Miller and Scalo (1979) is a Gaussian distribution, that extends the IMF below M_*=1$M_\odot$:

$$\xi(\log m) = \frac{A}{\sqrt{2\pi}\sigma} \exp\left[-\frac{(\log m - \log m_c)^2}{2\sigma^2}\right] \tag{2.2}$$

with A=normalization constant, log m_c= mean mass and σ^2=variance in log m.

Other possibilities have been proposed by Kroupa (2001), who models the IMF as a broken power law, and by Chabrier (2003), who uses instead a power law for high masses ($M_*\geq$ 1$M_\odot$) and a log-normal distribution at lower masses (M_*<1$M_\odot$).

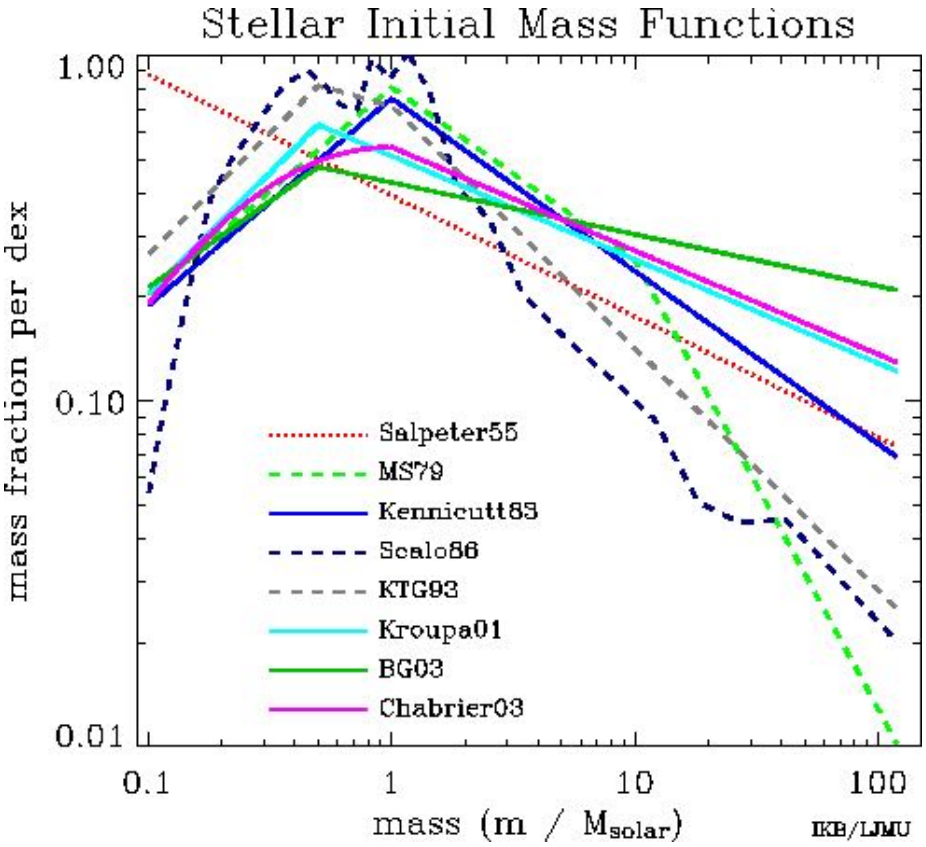

Figure 2.1 **Different IMFs:** mass fraction per dex as a function of stellar mass, the curves are normalized as that the area under each curve is unity, and are assumed to be valid in the interval 0.1 $M_{\odot}$<M_{*}<120 $M_{\odot}$. The different lines refer to Salpeter (1955) (red dotted), Miller and Scalo (1979) (green dashed), Kennicutt (1983) (blue solid), Scalo (1986) (black dashed), Kroupa et al. (1993) (grey dashed), Kroupa (2001) (cyan solid), Baldry and Glazebrook (2003) (green solid) and Chabrier (2003) (magenta solid). The figure is to be acknowledged to Ivan Baldry (his research page).

Different IMFs are given in figure 2.1 for comparison: to obtain reasonable Mass-to-Light (M/L) ratios and galaxy colors to be compared with observations, the best renditions are those given by Kennicutt (1983), Kroupa (2001), Baldry and Glazebrook (2003) and Chabrier (2003). In fact the extrapolation of the Salpeter (1955) IMF down to M_{*}<1$M_{\odot}$would give an excess of low-mass stars with respect to what is observed. On the other hand, the Scalo (1986) and Kroupa et al. (1993) IMFs, which are based on galactic disk measurements, would underestimate the number of high mass stars, since the Star Formation History (SFH) of the Galaxy is complicated. Let's now compare the Saltpeter and Chabrier IMFs: the former is too rich in low-mass stars and might overestimate the stellar masses, while the latter predicts masses which are a factor ~ 1.7 lower (Pozzetti et al., 2007). Because of this the IMF decreases of a factor ~$(1.7)^{1+\alpha}$,

and for a typical value $\alpha \sim$ -1.2, as pointed out by Perez-Gonzalez et al. (2008), it means a decrease of $\sim$ 0.5 dex (Li et al., 2011).

The choice of the IMF affects also the Spectral Energy Distribution (SED) of galaxies (see Sect. 2.3). Throughout this work we adopt a Chabrier (2003) IMF.

2.1.1 SPS

Given a certain IMF, the Spectral Energy Distribution (SED) of a stellar population at a time t can be computed as follow:

$$L_\lambda(t) = \int_0^t dt' \int_0^\infty dZ' \psi(t', Z') L_\lambda^{(\mathrm{SSP})}(t - t', Z'; \phi) \tag{2.3}$$

where $\psi(t', Z')dt'dZ'$ is the mass at the birth of stars which formed in the time interval t', t'+dt' and metallicity range Z', Z'+dZ', while $L_\lambda^{(\mathrm{SSP})}(t, Z; \phi)$ is the SED of a single stellar population (SSP) of unit mass with age t and metallicity Z, formed with a given IMF $\phi(m)$. $\psi(t, Z)$ is obtained by summing over the SF histories of all the progenitors. The SSP luminosity is then related to the one of a single star as follows

$$L_\lambda^{(\mathrm{SSP})}(t, Z; \phi) = \int_{m_L}^{m_U} L_\lambda^{(\mathrm{star})}(t, Z, m)\phi(m)\, d\mathrm{lnm}. \tag{2.4}$$

The $L_\lambda^{(\mathrm{SSP})}(t, Z; \phi)$ is provided by several libraries that take into account different ages, metallicities and IMFs (Bruzual A. and Charlot, 1993; Maraston, 2005; Bressan et al., 1998; Vazdekis et al., 2015), and are based on theoretical stellar evolution tracks and either theoretical or observed stellar spectra.

2.2 Dust in galaxies

Galaxies with ongoing star formation, especially if it is running at high rates, are full of dust. It produces two different effects on the incident radiation: it can scatter the light and/or absorb it. To recover the total amount of original radiation one needs to sum these two components (scattered and absorbed). The effect of the dust onto the radiation itself is called (total) extinction, and the scattered and absorbed light components are a measure of it.

To correctly understand the nature of dust extinction is necessary to reproduce its variation as a function of the wavelength of the incident radiation: regarding single stars, this is usually done by considering two of them having the same spectral type, one strongly obscured in contrast with the other one which is completely clear. The differences in their observed intensities give information about the physical properties of the intervening material, making it possible to recover the extinction curve (or law)

of the observed object. This process has been developed for local samples of galaxies (Calzetti et al., 1994; Calzetti, 1999; Calzetti et al., 2000), including the Milky Way (Seaton, 1979; Howarth, 1983) and the Large Magellanic Cloud (Howarth, 1983). For these objects the extinction law has been modeled also theoretically (Charlot and Fall, 2000). For galaxies which are not local, instead, it is very difficult to recover observationally the extinction curve; this is because, in general, the process described above can be applied to stars, that cannot be resolved in non-local galaxies, and furthermore, for such objects, there is an additional issue concerning the fact that photons can be scattered both into and out the line of sight, and the optical depth of the dust itself can vary a lot from star to star. Because of such reasons, in general, for non-local galaxies a mean dust attenuation curve is assumed. Unfortunately galaxies are different from one another, so there not exist a single extinction curve that is equally appropriate for all of them. For example, galaxies that are highly star-forming have a huge amount of dust, that makes their UV emitted light to be almost completely absorbed and re-radiated in the IR part of the spectrum (Buat et al., 2005; Burgarella et al., 2005). It is very important, in the case of these galaxies, to be able to correctly model the dust attenuation curve, since their SFRs, inferred using UV emission not properly corrected for dust extinction, can be underestimated up to one order of magnitude. This highlight even more that an accurate knowledge of the effects of the dust in galaxies is needed, especially if one wants to use observations at wavelengths affected by such attenuation to infer some general properties of the galaxies, and use them to put constraints on the evolutionary processes.

In literature there are, in the end, three main approaches to estimate the dust attenuation in the UV band:

- The slope β of the power law of the UV continuum in the range $1300\,angstrom \leq \lambda \leq 2600\,angstrom$: $f_\lambda \propto \lambda^\beta$ (Calzetti et al., 1994; Calzetti, 1999; Calzetti et al., 2000; Bouwens et al., 2012, 2014; Mashian et al., 2016). In general it is made the strong assumption that β is sensitive only to dust attenuation, and not, for example, to the mean age of the dust-heating population, the dust/star geometry, or the dust properties

- The IRX relation, which is the ratio between UV and IR emission: if the FIR emission is considered as being the optical/UV emission from the stars after being reprocessed by the dust (Wang and Heckman, 1996; Heckman et al., 1998; Meurer et al., 1999; Hao et al., 2011), this gives an estimation of how much extinction is occurring in the galaxy. Since it is independent on the dust distribution and properties (Buat and Xu, 1996; Gordon et al., 2000; Cortese et al., 2006, 2008), it is a better estimator of the dust attenuation, once assumed that at least a little amount of UV radiation can arrive to the observer.

- The attenuation in the Hα line as derived from the Balmer line Hα /Hβ (i.e., the Balmer decrement): if the SFR as derived from the Hα luminosity is in agreement with the one derived from the the dust-corrected UV emission, then the observed emission ratio Hα / UV can be used to infer the amount of dust attenuation. Another possibility is to assume an attenuation law for the dust (e.g. Buat, 1992; Treyer et al., 2007). Due to its strong model dependance, this indicator suffers of large systematic uncertainties.

In recent times the second indicator has been applied to derive the attenuation in local galaxies using both the IR/FUV (Far-UltraViolet) ratio and the FUV/NUV (Near-UltraViolet) ratio (Hao et al., 2011). Once derived the SFR functions for the galaxies, the authors understood that the correction based on the FUV/NUV color strongly underestimates the SFRs for galaxies that are highly star-forming. This strengthens even more the need for IR data in order to properly estimate the dust extinction in galaxies, especially when dealing with high SFRs $\geq$ 100 $M_{\odot}yr^{-1}$ (Lapi et al., 2011; Gruppioni et al., 2013). Also for IRX $\geq$ 10 the information carried by the FUV suffers of large uncertainties, making in any case the determination of the dust attenuation unreliable.

The correction β/IRX ratio is usually adopted when only UV data are available (Meurer et al., 1999). It has been initially proposed for low-z galaxies, and then tested and applied also to higher redshifts (Reddy et al., 2010; Overzier et al., 2011; Bouwens et al., 2013, 2014). Unfortunately the spread around the relation becomes huge when the values of β and of the attenuation increase, making the estimate of the attenuation less reliable. It is true that the latter is less dispersed for galaxies with low SFRs $\psi \leq 1$ $M_{\odot}yr^{-1}$; in this cases the correction for the attenuation is more reliable and, on average, small (Bouwens et al., 2013). This conclusion is supported also by Hopkins et al. (2001) when inferring the UV attenuation by relating the Hα attenuation and the Calzetti extinction curve.

In general the mean dust attenuation increases with redshift up to $z \sim$ 1-1.5, where it has its maximum, then it decreases rapidly. In fact, as the Universe becomes younger, the galaxies have less time to produce large amount of dust and metals, and this is shown by Madau and Dickinson (2014b) and Cai et al. (2014), who give a metallicity for the intergalactic medium (IGM) that is lower than the solar one at $z \geq$6. In this case, at very high redshifts, the UV dust corrected data starts to be a more reliable diagnostic for the SFR; as we will show in Chapter 3, this is valid only for galaxies at very high redshifts (i.e. $z >$8), since the dust absorption appears to be still present, even if in lower amount, up to $z \sim$7-8, as confirmed by the few galaxies with very high SFRs found by Riechers et al. (2013) and Watson et al. (2015).

2.3 Spectral Energy Distribution (SED)

The information on galaxy stellar, dust and gas content, and their physical properties are contained into the galaxy Spectral Energy Distribution (SED). Via the SED fitting technique, which consist in finding the best theoretical template able to reproduce the observed data, it is possible to infer many properties from the SED of a galaxy, like the redshift, the age of the stellar population, the mass in stars, the IMF, physical properties and amount of gas and dust. To model an SED usually it is utilized the stellar population synthesis technique, which consist in summing spectra of single stars, that are supposed to compose a galaxy, in order to reconstruct the overall spectrum of the whole galaxy (Charlot and Bruzual, 1991; Bruzual A. and Charlot, 1993; Bressan et al., 1994; Worthey, 1994; Fioc and Rocca-Volmerange, 1997; Maraston, 1998; Leitherer et al., 1999; Vazdekis, 1999; Walcher et al., 2011; Conroy, 2013, see also Sect.2.1.1).

In general a galaxy can emit at many wavelengths: each one can be connected to a different component of the galaxy itself. For example the UV to sub-mm wavelengths (from 0.1 μm to $\sim$ 1000 μm, e.g. Kennicutt and Evans (2012b)), which constitute the bulk of the galaxy emission, are dominated by the stellar light plus AGN component (if present). The intrinsic emission from the stellar population peaks at UV-NIR wavelengths. This light is often attenuated by the presence of dust in the galaxy, that absorbs the UV photons and re-emits them thermally in the Far-IR ($\lambda \sim 100$ μm), shifting the peak of the emission at higher wavelengths (see Fig. 2.3, solid line is a less attenuated SED with respect to the one represented by the dashed line, as can be seen by the shift of the emission peak towards the IR band, and the lower emission at UV wavelengths). This happens especially in galaxies where the star formation process is still ongoing, even though some obscuration due to the diffuse dust is present also in "dead" galaxies. Thus to study highly star-forming galaxies it is necessary to have FIR data, while for quiescent galaxies the best wavelength window is the UV-NIR.

Many models are nowadays able to consistently predict the SED of galaxies from the UV to FIR wavelengths (Silva et al., 1998; Devriendt et al., 1999; da Cunha et al., 2008; Groves et al., 2008; Noll et al., 2009): in Fig.2.3 we show an example of one of them, underlining the different components that are included to reproduce the observed SED. The necessary ingredients are the intrinsic starlight emission (UV-NIR, blue line), a dust attenuation model in order to suppress the emission and recover the observed data, an empirical spectrum for the Polycyclic Aromatic Hydrocarbons (PAHs) emission (the spikes in the region at $\sim$ 10 μm), and the dust emission, which is separated into the contribution derived from the diffuse ISM (cirrus, solid green line) and the one due to the dust contained in star-forming regions (Molecular Clouds (MC), dashed green line).

Actually in order to properly map the SED of a galaxy and infer its properties it is

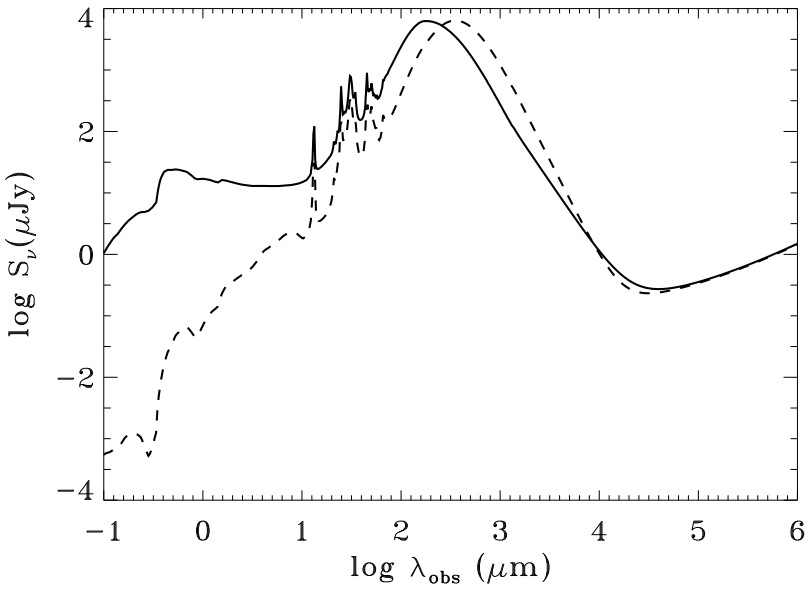

Figure 2.2 **SED of strongly obscured and less obscured galaxies:** in this figure we show an SED of a galaxy with SFR=20 $M_\odot$/yr in two different stages of evolution. The solid line represents the galaxy at the beginning of its life, when only a mild dust attenuation is present, while the dashed line shows the galaxy in a more evolved (and dusty) stage of evolution, when most of the UV light has been absorbed and re-emitted at higher wavelengths by the dust.

necessary to include also the radio emission: it is in fact typical of star-forming galaxies, and is directly proportional to the star formation processes (Bressan et al., 2002; Prouton et al., 2004; Vega et al., 2008; Mancuso et al., 2015). In Fig.2.4 we show an SED which is comprehensive of the radio emission: for comparison we put on it the observed fluxes of the galaxy NGC 7090 at different wavelengths λ. In this case we did not use the SED fitting technique, and this explains the non-perfect agreement with a couple of IR data-points (IRAS measurements, stars); we just wanted to underline the presence of radio emission correlated with star formation, and in particular the separated contribution of the two radio components, the synchrotron (long dashed cyan) and the free-free (long dashed magenta) (see Sect.2.4.6).

Since the SED is representative of all the components of a galaxy, if an AGN is present, its contribution to the SED should appear: generally the AGNs are luminous in the IR band, given the thermal emission from the dust in their tori around accretion disks. In principle, then, they can be a source of contamination for the IR emission correlated to star formation, that is commonly used as an intrinsic SFR tracer (see Sect.2.4). Actually, as a matter of fact, the AGN contribution to the IR emission peaks

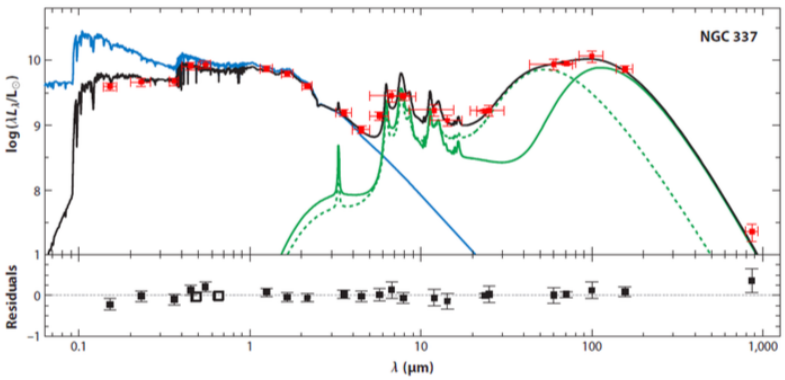

Figure 2.3 **SED of NGC337 modeled with different components:** the overall SED in shown by the black solid line, it is composed by the unattenuated starlight (blue solid line), the dust attenuation that lower the UV emission down to fit the observational data (red points), the dust contribution separated in cirrus (green solid) and molecular clouds (green dashed) emission. The figure is adapted from da Cunha et al. (2008).

at $20-40\,\mu$m with a rapid fall-off at longer wavelengths, because the emission is dominated by hot dust grains (cf. Fig. 5 of Delvecchio et al. 2014). Theoretical works have shown that this fall-off is weakly dependent on geometry, clumpiness of the torus, and orientation of the line of sight (e.g., Pier & Krolik 1992; Granato & Danese 1994; Efstathiou & Rowan-Robinson 1995; Nenkova et al. 2008), and their results well match the observed SEDs of local AGNs. In Fig. 2.5 we present the typical rest-frame SEDs of obscured AGNs (referring to both local and high$-z$ objects) as fitted by Siebenmorgen et al. (2015), together with different SEDs typical of star-forming, dust-obscured galaxies. The SEDs of the AGNs are computed using a 3D radiative transfer code, and take into account many different basic parameters that determine the AGN structure; the emission from the AGNs is considered to be anisotropic below its far-IR peak, and isotropic at longer wavelengths, while the dust grains are chosen to be fluffy, since their absorption cross sections seem to suggest an attenuation which is in a better agreement with observations of obscured AGNs. The SEDs of star-forming galaxies are the Cosmic Eyelash (our reference), the average from the ALESS sample (Swinbank et al., 2014; da Cunha et al., 2015) which is similar to the classic SED of Arp220, (see Rangwala et al., 2011), and the local ULIRG+Seyfert1 galaxy Mrk231 (e.g. Polletta et al., 2007). The plot actually illustrates the relative contribution of an obscured AGN and of its host dusty galaxy, under the assumption that their integrated luminosity over the range $3-1100\,\mu$m is the same (a conservative hypothesis for most of (sub-)mm selected galaxies). In order to test the SFR function at $z \gtrsim 3$, the statistics of counts and lensed objects at $\lambda \sim 1400\,\mu$m (Weiß et al., 2013) are extremely informative. This observational wavelength corresponds to rest-frame $\lambda \gtrsim 200\,\mu$m for galaxies at $z \lesssim 6$. From Fig. 2.5 it is apparent that the obscured AGN flux/luminosity is $\lesssim 10\%$ with respect to

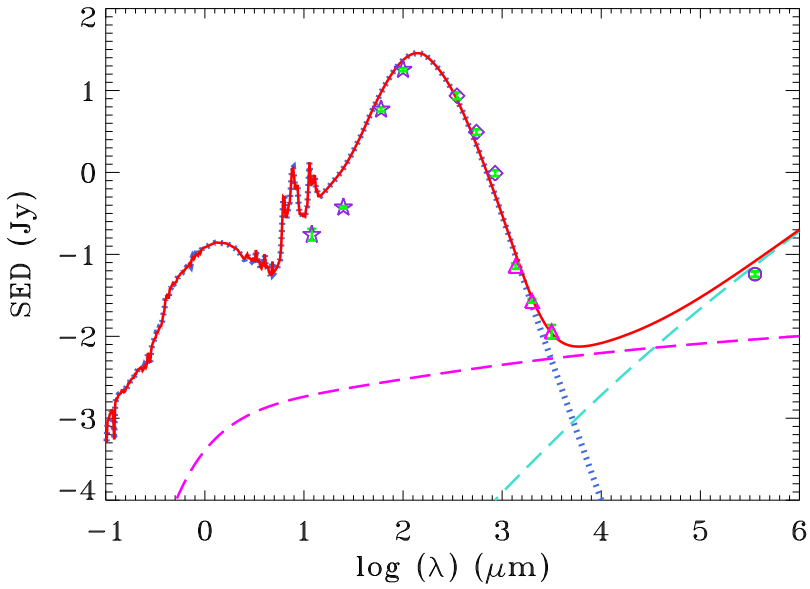

Figure 2.4 **SED with radio-components:** here we show a general SED comprehensive of the radio synchrotron (long dashed cyan) and free-free (long dashed magenta) components. The dotted blue line is the cold dust component of the SED. For comparison we report also the observed fluxes of NGC 7090. In this case we did not perform an SED fitting analysis, the data points are just presented to make a comparison with the shape of the modeled and observed SED.

that of the host galaxy.

This conclusion is also supported by Delvecchio et al. (2014), who have performed broad-band SED decomposition in about 4000 galaxies detected at 160 μm by *Herschel* in the redshift range $z \sim 0-3$.

Also Swinbank et al. (2014) and da Cunha et al. (2015) reported observations with *ALMA* of 99 high$-z$ sub-mm galaxies in the ECDFS with multi-wavelength observations, covering a very wide spectral range. These authors show that the composite spectrum of such galaxies in the wavelength range $\lambda \sim 10-1000\,\mu$m can be well represented by the superposition of three grey-bodies referring to different dust components, cold, warm and hot, with temperatures $T \approx 20-30$ K, $50-60$ K and $80-120$ K, respectively. The hot component peaking at around 30 μm suggests the presence, in a statistical sense, of an AGN contribution, which becomes irrelevant at $\lambda \gtrsim 70-80\,\mu$m.

All in all, the combination of the short lifetime for luminous AGNs and of their SED makes the AGN component irrelevant as for the purposes of this work (for example for recovering the far-IR/(sub-)mm counts). A general discussion on the luminosity function and counts of AGN type 1, 2 and 3 (the latter being those growing at the

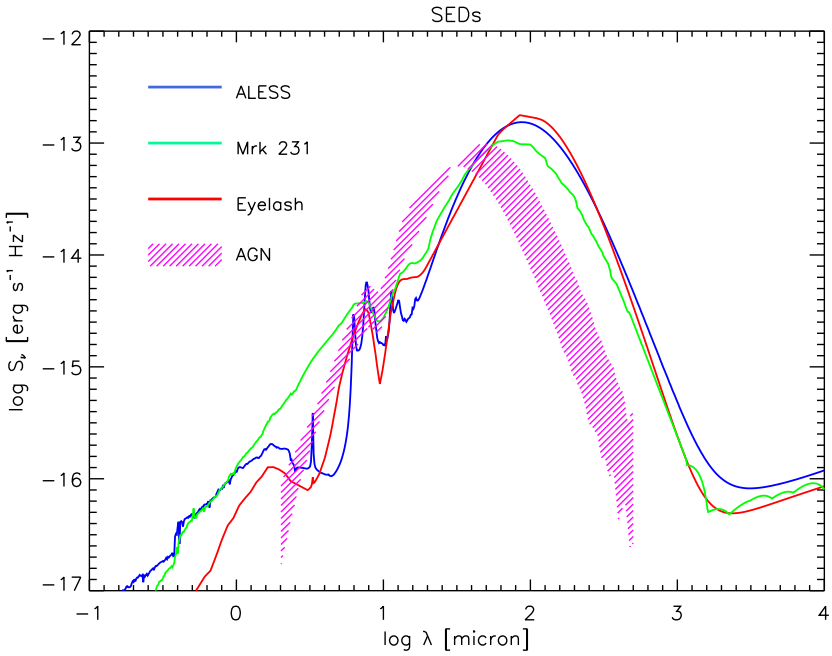

Figure 2.5 **SED comparison:** we present the comparison among the SEDs of three typical dust-obscured, star-forming galaxies (normalized in the range $3 - 1100\,\mu$m to 1 erg s^{-1}): red line refers to the Cosmic Eyelash (Ivison et al., 2010), blue line to the average from ALESS galaxies (Swinbank et al., 2014; da Cunha et al., 2015), and green line to Mrk231 (e.g. Polletta et al., 2007). The typical SEDs of obscured AGNs (including both low- and high-z objects) is plotted as a magenta region (Siebenmorgen et al., 2015).

center of star-forming galaxies at substantial redshift) at wavelengths ranging from UV to mm bands was presented by Cai et al. (2013). We stress that these findings do not exclude relationships between the star formation and the central black hole accretion history (e.g. Alexander and Hickox, 2012; Kormendy and Ho, 2013; Lapi et al., 2014; Aversa et al., 2015).

2.4 SFR tracers

The Star Formation Rate of a star-forming galaxy is the key ingredient to understand the galaxy formation and the evolutionary properties of the object: many different indicators can be used to recover it, and all of them have their own advantages and disadvantages (see Madau and Dickinson (2014b); Kennicutt (1998); Kennicutt and Evans (2012b) for a review). Here we give a brief overview of the most commonly used.

2.4.1 Emission lines

Star formation usually occurs in HII regions, and produces nebular line emission from ionized gas. The most common line tracers of star formation are then, for example, the Hydrogen recombination lines, such as Hα and Lyα [$\lambda_{\rm rest}$ =1216 angstrom]; they are in fact strongly related to the photoionization rates, which are on turn due to intense UV radiation from OB stars, and hence can trace star formation quite directly. However they can be affected by the presence of an AGN and also suffer from old stellar population contamination. The Lyα is also affected by dust extinction within the galaxy, given that it is a resonance line, scattered by neutral hydrogen atoms; after having escaped from the progenitor galaxy, it also can be absorbed by HI clumps present in the IGM. Other possibilities are the OII [$\lambda_{\rm rest}$ =3727 angstrom] and the OIII [$\lambda_{\rm rest}$ =5007 angstrom] lines, that in any case depend on the ISM conditions, such as metallicity or excitation. There exist also less extinguished lines in the NIR, for example the Paschen α, which unfortunately is weak, and consequently less easy to find. It can be used, in any case, to detect SFRs only at very low redshifts, at least until the advent of new facilities as JWST, that will make possible to measure Paschen α for a significant number of galaxies up to cosmological distances.

2.4.2 X-ray flux

Recent star formation is associated also to X-ray luminosity, in particular the one deriving from X-ray binaries, Supernovae (SNe), SN remnants and massive stars. In addition to this there is a correlation between the 2-10 keV fluxes and the IR and non-thermal radio continuum emission (Bauer et al., 2002; Ranalli et al., 2003; Symeonidis et al., 2011), even though those relations need to be calibrated (Ranalli et al., 2003; Persic et al., 2004). The integrated hard X-ray emission has been largely used as an SFR tracer in recent times (Colbert et al., 2004; Lehmer et al., 2010), applying the calibration by Ranalli et al. (2003). The deepest *Chandra* fields have been able to identify individual star-forming galaxies up to $z \sim 1$, while taking advantage of the stacking technique applied to UV-selected galaxy samples, it was possible to reach fainter fluxes up to z <4, and upper limits for the fluxes even at higher redshifts (see Reddy and Steidel, 2004; Lehmer et al., 2005; Laird et al., 2005, 2006; Basu-Zych et al., 2013). All this types of analysis are obviously possible only in absence of AGN contribution, that would, in case, completely overcome the contribution due to star formation.

2.4.3 UV luminosity

UV light is directly emitted by young, massive stars. In particular the FUV light (λ ∼1500 angstrom, rest frame) is considered to be one of the best tracers of star

formation in galaxies. In the past years many observations have been carried out in this band, in order to recover the SFR of galaxies: some of them have been performed with the *Galaxy Evolution Explorer (GALEX)* (Martin et al., 2005), which provided NUV and FUV fluxes for hundreds of thousands of galaxies even at high redshifts, or the *XMM Optical Monitor* (Mason et al., 2001), the *Swift UV/Optical Telescope* (Roming et al., 2005), the *Ultraviolet Imaging Telescope* on the ASTRO missions (Stecher et al., 1997; Marcum et al., 2001), and the *Hubble Space Telescope* (HST), especially for nearby objects. Also the MID-UV emission is sometimes used to trace star formation processes: it is less reliable than the FUV because it can be contaminated by the emission from long-lived low mass stars.

In general, when trying to recover the SFR from UV measurements, it is necessary to take into account some facts: first of all the UV luminosity output from a stellar population depends on its metallicity (usually less metal rich stars produce more UV light). We can express the relation between SFR and L_ν(FUV) as

$$\mathrm{SFR} = K_{\mathrm{FUV}} \times L_\nu(\mathrm{FUV}) \tag{2.5}$$

where the conversion factor K_{FUV} depends on the the star formation history of the galaxy (i.e. its metal enrichment) as well as from the IMF choice. It will also have an evolution with the redshift, in particular its value is expected to raise with increasing z (see Madau and Dickinson, 2014b). In general the effects due to metallicity and redshift counterbalance each other, making possible to assume an almost constant conversion factor at a given IMF.

The UV emission, however, presents also another important issue: it can be strongly absorbed by the dust and re-emitted in the FIR band (see Sect. 2.4.4 and 2.4.5). The attenuation can reduce the UV luminosity of a galaxy up to a few percent of its intrinsic value, thus a proper estimation of the dust absorption is needed to correct for such a contamination. In any case SFRs deduced from a combination of UV and IR measurements are in general thought to be more reliable. (see Sect. 2.4.5)

2.4.4 IR emission

Also the IR luminosity can be used as a tracer of SFR, if the latter occurs in dust enshrouded environments. In fact the bolometric luminosity of a completely obscured stellar population can be recovered starting from the integrated total (3-1100 μm) IR emission of the galaxies (Kennicutt, 1998).

In general the unobscured starlight is not traceable using IR emission. In order to properly account for the missing radiation related to star formation it is then necessary to calibrate the conversion between IR emission and SFR accurately (Hirashita et al., 2001). On the other hand there is some contamination in the IR due to evolved stars that

heat the dust and contribute, sometimes not marginally, to the total IR light, leading to an overestimation of the SFR (Sauvage and Thuan, 1992; Walterbos and Greenawalt, 1996; Cortese et al., 2008; Kennicutt et al., 2009; Hao et al., 2011).

The spectrum of dust emission is made up of different components, that are heated at different temperatures, making it fairly complex; the MIR continuum ($\lambda < 30\mu$m), is dominated by the emission from PAHs and absorption bands from silicates. Their strength is related to the ISM metallicity, though they are also affected by complex phenomena including photodissociation in the strongest starbursts. In addition these wavelengths can deeply suffer from AGN contamination.

As already introduced in Sect. 2.3, in the FIR the heated dust in galaxies can have two different natures: the dust in the cirrus is more diffuse and can also be heated by old stars, while the dust in molecular clouds is a more direct tracer of the star formation processes occurring inside the HII regions. In particular the cirrus component emission depends on several aspects, as the stellar content, the dust content and their spatial distribution. For the cirrus the temperature of the dust is usually low ($\sim$ 25 K), so the IR emission related to it has typically longer wavelengths with respect to those emitted in the molecular clouds (Silva et al., 1998; Rowlands et al., 2014). It has been observed in local galaxies: for example Hao et al. (2011) found that ~50% of the IR emission was contributed by cirrus emission in nearby star-forming galaxies with $\psi \lesssim 30$ $M_\odot$/yr . When the star formation increases, however, the fraction of cirrus emission decreases consequently (Clemens et al., 2013), thus for strongly star-forming galaxies with $\psi \gtrsim$ 100 $M_\odot$/yr and $L_{IR} \gtrsim 10^{12} L_\odot$, such as Arp220, it accounts only for a few percent of the total IR emission (Silva et al., 1998; Rowlands et al., 2014). A possible source of contamination can, again, be due to AGNs contribution; as already discussed in Sect. 2.3, however, the peak of their emission will be at wavelengths much shorter than those typical of the emission of molecular clouds, making them not that dangerous for the SFR estimations at such wavelengths.

2.4.5 UV vs IR

Which is the most complete SFR tracer? As already mentioned, the biggest constrain to be considered when trying to infer the SFR from UV emission is that, especially in highly star forming galaxies, the star formation processes occur in dust enshrouded environments, causing suppression of the UV emission in favor of the IR reprocessed light. Then the IR emission can be looked at the best tracer for star formation processes; actually also this type of emission suffers from contaminations, for example from old stellar population. Moreover it is true that, especially for those galaxies that are forming stars at low rates, not all the UV light is reprocessed by the dust. Since the amount of dust is strictly connected to the formation of stars, if the star formation process is slow,

so it is the production of dust, resulting in a not completely dust obscured galaxy. The solely IR emission, in this case, would underestimate the intrinsic SFR, since also UV light can actively trace it.

The best way to trace SFR in galaxies using such tracers is then to combine them in a relation that looks like the following:

$$\mathrm{SFR_{tot}} = K_{\mathrm{FUV}} \times L_{\nu}(\mathrm{FUV}) + K_{\mathrm{FIR}} \times L_{\nu}(\mathrm{FIR}) \tag{2.6}$$

where the conversion factors can be estimated empirically (Kennicutt and Evans, 2012b), and the $\mathrm{L_{FUV}}$ does not take into account the dust extinction.

In this way, the intrinsic SFR can be estimated without risking to neglect some contribution. Unfortunately up to now the FIR surveys, thanks to *Herschel*, can detect galaxies with SFR $\psi > 100$ $\mathrm{M_{\odot}/yr}$ only up to $z \sim 3$; to go to higher redshifts is impossible due to detection limits. The majority of estimations of SFR functions at high z is then made by using UV data with the addition of a correction for dust extinction; the one which is commonly used is the UV spectral slope β (see Sect.2.2), that have been exploited to determine an empirical average dust attenuation curve for a sample of local UV bright star-forming galaxies (Calzetti et al., 1994, 2000). Meurer et al. (1999) and Overzier et al. (2011) then used both UV and FIR data at low redshifts to empirically calibrate the β-IRX relation: it turned out to be tight and broadly consistent with the Calzetti attenuation law at low redshifts. Given that, the relation has been extrapolated to higher redshifts to try to account for dust attenuation even where FIR data are not yet on disposal. The problem in this case is that the corrections must take into account all dust components, namely the one related to the presence of the diffuse cirrus, as well as the one related to molecular clouds. Goldader et al. (2002), for example, found that nearby ULIRGs strongly deviates from the Meurer β-IRX relation, having very large IRX values and relatively blue β. At high redshifts, moreover, Reddy and Steidel (2004) and Reddy et al. (2006, 2010, 2012), even finding that the β-IRX extinction law was appropriate for the majority of LBGs at $z \sim 2$, also pointed out that galaxies with SFRs $\psi < 100$ $\mathrm{M_{\odot}/yr}$ showed systematic deviations from such relation. In general galaxies that have been selected on the basis of their IR emission are found to deviate from the Meurer/Calzetti attenuation law: in these cases the UV slope β correction lead to strongly underestimate the global, intrinsic SFRs. In Chapter 3 we will present a different method to go beyond the redshift limit given by *Herschel* surveys, and estimate the SFR functions on a redshift range $0 \leq z \leq 10$.

2.4.6 Radio emission

Another tracer of star formation is the radio emission. It is separated into two contributions, the synchrotron and the free-free emission, and is unbiased with respect to dust

extinction, being then a good tracer up to high redshifts. The synchrotron emission is produced by SNe, and its legitimation as a reliable SFR tracer comes from its relation with the FIR emission (see Helou et al., 1985; Condon, 1992; Yun et al., 2001; Ivison et al., 2010; Jarvis et al., 2010; Bourne et al., 2011; Mao et al., 2011). Actually there are many physical processes, such as propagation of relativistic electrons, strength and structure of the magnetic field, size and composition of dust grains, that must cooperate to produce this relation (Bell, 2003; Lacki et al., 2010). In addition the synchrotron emission could be contaminated, even by a large factor, by faint nuclear radio activity, and this would bias the estimation of the SFR.

Another radio SFR tracer is the free-free emission from the gas ionized by massive young stars (Murphy, 2009; Murphy et al., 2015). Being directly proportional to the production rate of ionizing photons it provides a direct measure of the SFR without the complication of dust attenuation encountered in the optical/UV. It has a flat spectrum and is expected to show up at frequencies of tens of GHz. The interpretation of data at these frequencies may be complicated by the presence of "anomalous" dust emission (Planck Collaboration XX et al., 2011, and references therein) attributed to spinning dust grains (e.g., Draine and Lazarian, 1998). However a significant contribution of this component to the global emission of galaxies has not been proved yet (Murphy et al., 2012; Planck Collaboration XXV et al., 2015).

The radio emission in general suffers of contamination from AGN Radio Loud population up to fluxes $S_{\rm lim} \sim$ mJy, and the present radio facilities are not yet able to go much beyond this limit at ν=1.4 GHz, providing an unbiased estimation of SFRs in star-forming galaxies. The current deepest radio surveys (see de Zotti et al., 2010, for a review) have not been carried out at frequencies high enough, or are not deep enough to see the transition from the synchrotron to the free-free dominance, but with the advent of the Square Kilometer Array (SKA), and partially with its precursors, it will be possible to efficiently select high-z star-forming galaxies via their free-free emission at high frequencies, and via the synchrotron emission at low z.

Chapter 3

Star Formation Rate Functions

One of the principal ingredients that helps in understanding properly how galaxies has formed and evolved is their history of star formation. In this chapter we analyze the observations at disposal and use them to build up the SFR functions at different redshifts up to $z \sim 10$.

3.1 Reconstructing the intrinsic SFR function

From an observational point of view, the intrinsic SFR function $N(\log\psi, z)$, namely the number of galaxies per logarithmic bin of SFR $[\log\psi, \log\psi + \mathrm{d}\log\psi]$ at given redshift z, is mainly determined from pure UV or pure far-IR selected samples; we recall that in both cases *corrections* come into play and must be taken into proper account to infer the intrinsic SFR function.

As mentioned in 2.2, for SFRs $\psi \gtrsim 30\,M_\odot$ yr^{-1}, when the UV attenuation becomes appreciable, the commonly used β_{UV}-IRX correlation is found to be extremely dispersed, resulting in a very uncertain estimate of the attenuation even in local samples (e.g. Howell et al., 2010; Reddy et al., 2015). On the other hand, the correlation is found to be less scattered for SFRs $\psi \lesssim 30\,M_\odot$ yr^{-1}, and the dust correction to UV luminosity gets more secure and relatively small on the average. This is also suggested by the UV attenuation inferred by combining Hα measurements with the Calzetti extinction curve (e.g. Mancuso et al., 2015; Reddy et al., 2015). For SFRs $\psi \gtrsim 10^2\,M_\odot$ yr^{-1} the cold diffuse IR emission from the dusty cirrus is not that important even at low z. The same conclusion holds for high redshift $z \sim 1.5 - 3$ star-forming galaxies with SFR $\psi \gtrsim 30\,M_\odot$ yr^{-1}, as it emerges from the analysis of the ALESS survey by Swinbank et al. (2014) and da Cunha et al. (2015, see their Fig. 10), who find dust temperatures in excess of 30 K.

Given that, we build up the intrinsic SFR function $N(\log\psi, z)$ as follows. We start from the most recent determinations of the luminosity functions at different redshifts from far-IR and UV data (the latter being dust-corrected according to the $\beta_{\rm UV}$-IRX relation, see Meurer et al. (1999); Bouwens et al. (2009, 2015); the outcome is illustrated in Fig. 3.1. The SFR ψ and the associated luminosity L_ψ reported on the upper and lower axis have been related assuming the calibration

$$\log\frac{\psi}{M_\odot\ \mathrm{yr}^{-1}} \approx -9.8 + \log\frac{L_\psi}{L_\odot}\,, \tag{3.1}$$

approximately holding both for far-IR and (intrinsic) UV luminosities (see Kennicutt and Evans, 2012b).

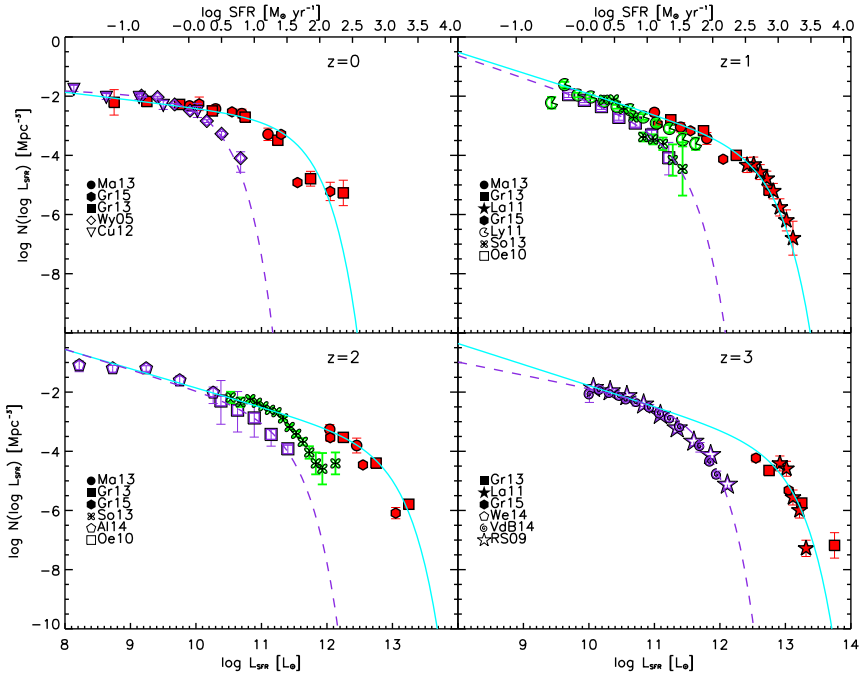

Figure 3.1 **The SFR function at redshifts $z\approx$ 0-3:** Solid cyan lines illustrate our fits to the global (IR+UV) SFR functions, while violet dashed lines refer to the purely UV-inferred SFR functions. UV data (dust-corrected; violet symbols) are from Wyder et al. (2005, open diamonds), Cucciati et al. (open inverse triangle 2012), Oesch et al. (open squares 2010), Alavi et al. (2014, open pentagons), Reddy and Steidel (2009, open stars), van der Burg et al. (2010, spirals), Hα data (green symbols) from Ly et al. (2011, pacmans), Sobral et al. (2013, clovers), and IR data (red symbols) from Magnelli et al. (2013, filled circles), Gruppioni et al. (2013, filled squares), Lapi et al. (2011, filled stars).

At redshift $z \lesssim 3$, we lack a robust determination of the SFR function at intermediate values of the SFR. On the one hand, UV data almost disappear for SFRs $\psi \gtrsim 30\,M_\odot$

Table 3.1 **SFR Function Parameters.** *Note:quoted uncertainties are at 1 σ level. Fits hold in the range SFR $\psi \sim 10^{-2} - 10^{4}$ and redshifts $z \sim$ 0-8.*

Parameter	Intrinsic				UV (dust-corrected)			
	p_0	p_1	p_2	p_3	p_0	p_1	p_2	p_3
$\log \mathcal{N}(z)$	-2.48 ± 0.06	-6.55 ± 1.17	12.98 ± 3.49	-8.19 ± 2.48	-1.96 ± 0.07	-1.60 ± 1.44	4.22 ± 3.66	-5.23 ± 2.48
$\log \psi_c(z)$	1.25 ± 0.05	5.14 ± 0.60	-3.22 ± 1.64	-1.81 ± 1.16	0.01 ± 0.05	2.85 ± 0.94	0.43 ± 2.40	-1.70 ± 1.61
$\alpha(z)$	1.27 ± 0.01	2.89 ± 0.23	-6.34 ± 0.66	4.33 ± 0.46	1.11 ± 0.02	2.85 ± 0.48	-6.18 ± 1.26	4.44 ± 0.83

yr^{-1} because of dust extinction (with dust corrections becoming progressively uncertain). On the other hand, far-IR data progressively disappear for SFRs $\lesssim 10^2\, M_\odot\ \mathrm{yr}^{-1}$ because of current observational limits. At higher redshift $z \gtrsim 4$, once more UV surveys can afford reliable estimate of the SFR function for SFRs $\psi \lesssim 30\, M_\odot\ \mathrm{yr}^{-1}$, but we lack far-IR data deep enough to statistically probe the high-SFR end.

To obtain an analytic rendition of the intrinsic SFR function in the full range of SFRs $\psi \sim 10^{-1}$ – several $10^3\, M_\odot\ \mathrm{yr}^{-1}$ and redshift $z \sim 0 - 10$, we perform a least χ^2-fit to the data with a standard Schechter functional shape

$$N(\log\psi) = \mathcal{N}(z) \left[\frac{\psi}{\psi_c(z)}\right]^{1-\alpha(z)} e^{-\psi/\psi_c(z)}\ . \tag{3.2}$$

The fit is educated, meaning that for redshift $z \lesssim 3$, where both UV and far-IR data are present, we consider as reliable the UV data (dust-corrected according the β_{UV}-IRX ratio) for SFRs $\psi \lesssim 30\, M_\odot\ \mathrm{yr}^{-1}$, and the far-IR data for SFRs $\psi \gtrsim 10^2\, M_\odot\ \mathrm{yr}^{-1}$. As for higher redshift, we make the assumption that at $z \gtrsim 8$ the (dust-corrected) UV data are reliable estimators of the intrinsic SFR function. This assumption relies on the fact that with an age of the Universe shorter than 6×10^8 yr, the amount of dust in a star-forming galaxy is expected to be rather small (see Sect. 4.2).

Equipped with such values of the Schechter parameters at redshift $z \lesssim 3$ and $z \gtrsim 8$, we fit their evolution with a polynomial in log-redshift; in other words, for any parameter $p(z)$ of the Schechter function, say $\mathcal{N}(z)$, $\psi_c(z)$, or $\alpha(z)$, we fit for the functional shape

$$p(z) = p_0 + p_1\,\xi + p_2\,\xi^2 + p_3\,\xi^3\ , \tag{3.3}$$

where $\xi \equiv \log(1+z)$. The outcomes of the fits are reported in Table 3.1.

This procedure, based on the assumption of analytical continuity of the intrinsic SFR function, yields a rendition that works pleasingly well for $z \lesssim 3$ and $z \gtrsim 8$, see Figs. 3.1 and 3.2; moreover, we end up with an estimate for the behavior of the SFR function at $z \sim 4 - 8$ where sampling by far-IR surveys is absent. In such a redshift range, this estimate implies a significant number density of dusty star-forming galaxies with SFR $\psi \gtrsim 10^2\, M_\odot\ \mathrm{yr}^{-1}$, currently missed by UV data (even corrected for dust extinction). To highlight more clearly this point, we also report in Figs. 3.1 and 3.2

the SFR function that would have been inferred basing solely on dust-corrected UV data over the full redshift range $z \approx 0 - 10$. Plainly, at any redshift $z \lesssim 7$ UV data, even corrected for dust extinction basing on the UV slope, strongly underestimate the intrinsic SFR function for SFRs $\psi \gtrsim 30\,M_\odot$ yr^{-1}.

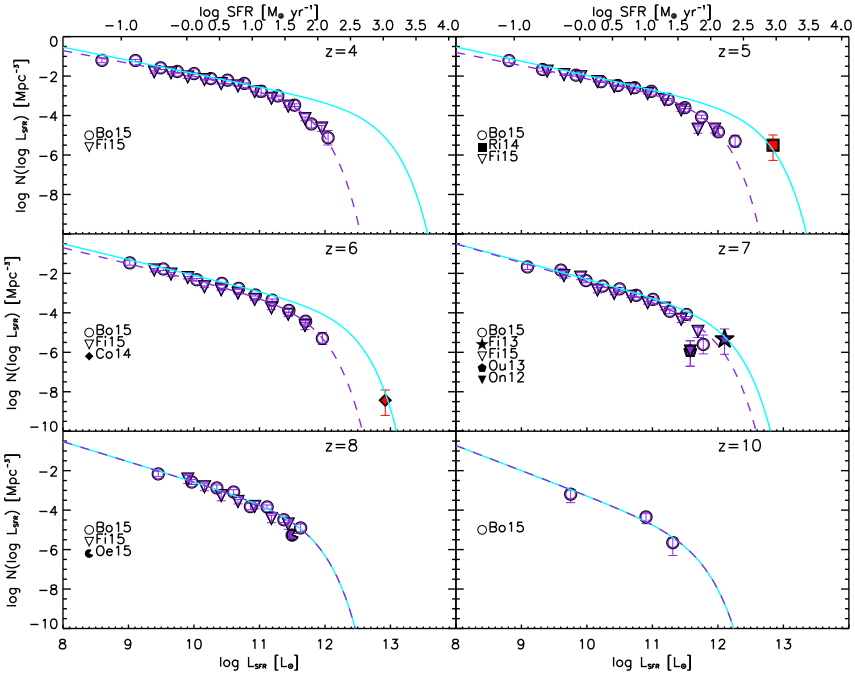

Figure 3.2 **The SFR function at redshifts $z \approx$ 4-10:** Solid cyan lines illustrate our determination of the the global (IR+UV) SFR functions, while violet dashed lines illustrate our fits to the SFR function from (dust-corrected) UV data. UV data (dust-corrected; violet symbols) are from Bouwens et al. (2015, open circles) and Finkelstein et al. (2015a, open inverse triangles). Filled symbols represent the number density associated to the detection of individual galaxies with spectroscopic redshift determination (see text for details): violet ones refer to galaxies selected in UV/Lyα from Finkelstein et al. (2013, star), Ouchi et al. (2013, pentagon), Ono et al. (2012, inverse triangle),Oesch et al. (2015, pacman); red ones refer to galaxies selected in IR/sub-mm from Riechers et al. (2014, square), Cooray et al. (2014, diamond).

Circumstantial evidence for such a population of dusty star-forming galaxies at $z \gtrsim 4$ is accumulating over the recent years. Riechers et al. (2014) detected a dust obscured galaxy at $z \approx 5.3$ with SFR $\psi \approx 1100\,M_\odot$ yr^{-1} and stellar mass $M_\star \approx 10^{10}\,M_\odot$. Cooray et al. (2014) detected a second one at $z \approx 6.34$ with SFR $\psi \approx 1320\,M_\odot$ yr^{-1} and stellar mass $M_\star \approx 5 \times 10^{10}\,M_\odot$. It is remarkable that the inferred number densities for these objects, though within the considerable uncertainties, agree with the prediction of our intrinsic SFR function, while being substantially higher than the expectations from the purely UV-inferred one (see Fig. 3.2).

At lower levels of SFRs, moderately dusty galaxies start to be selected even in the UV, especially at high redshift $z \gtrsim 7$. For example, Finkelstein et al. (2013) detected one at $z \approx 7.51$ with SFR $\psi \approx 200\,M_\odot\ \mathrm{yr}^{-1}$ and stellar mass $M_\star \approx 6 \times 10^8\,M_\odot$. Oesch et al. (2015) revealed one at $z \approx 7.73$ with SFR $\psi \approx 30 - 50\,M_\odot\ \mathrm{yr}^{-1}$ and stellar mass $M_\star \approx 5 \times 10^9\,M_\odot$. Ouchi et al. (2013) detected another one at $z \approx 6.6$ with SFR $\psi \approx 60\,M_\odot\ \mathrm{yr}^{-1}$ and stellar mass $M_\star \approx 10^{10}\,M_\odot$. Ono et al. (2012) detected one at $z \approx 7.2$ with SFR $\psi \approx 60\,M_\odot\ \mathrm{yr}^{-1}$ and stellar mass $M_\star \approx 3 \times 10^8\,M_\odot$. Intense search is currently going on, with an appreciable number of candidates being found (see Roberts-Borsani et al., 2016; Zitrin et al., 2015). The number densities of these galaxies are consistent with the UV-corrected SFR function, that at these high redshift approaches the intrinsic one.

We stress that while the focus of the present work is mainly on the bright portion of the intrinsic SFR function at high-redshift, the faint end as sampled by UV data is essential to understand important issues both in astrophysics/cosmology like the history of cosmic reionization (e.g. Cai et al., 2014; Robertson et al., 2015) and even in fundamental physics like the nature of dark matter (e.g. Lapi and Danese, 2015).

3.1.1 Validating the SFR functions via indirect observables

We decided to validate our intrinsic SFR function via comparison with the observed (sub-)mm counts, redshift distributions, and cosmic infrared background. We computed the counts according to the expression (see Lapi et al., 2011, see also the Appendix of this thesis)

$$\frac{\mathrm{d}N}{\mathrm{d}\log S_\nu\,\mathrm{d}\Omega}(S_\nu) = \int \mathrm{d}z\ \frac{\mathrm{d}V}{\mathrm{d}z\,\mathrm{d}\Omega}\ N(\log\psi)\ \frac{\mathrm{d}\log\psi}{\mathrm{d}\log S_\nu} \tag{3.4}$$

in terms of the flux

$$S_\nu = \frac{L_{\nu(1+z)}}{L_\psi}\ \frac{(1+z)}{4\pi\,D_L^2(z)}\ ; \tag{3.5}$$

in the above $N(\log\psi)$ is the SFR function, $\mathrm{d}V/\mathrm{d}z\,\mathrm{d}\Omega$ is the cosmological volume per redshift bin and unit solid angle, L_ψ is the bolometric luminosity associated to the SFR ψ according to Eq. (3.1), and $L_{\nu(1+z)}/L_\psi$ is the $K-$correction. The latter has been computed basing on the spectral energy distribution (SED) typical of a high-redshift, dust-obscured star-forming galaxy; specifically, we considered as a reference the SED of the 'Cosmic Eyelash' (SMM J2135+0102; see Swinbank et al., 2010; Ivison et al., 2010), but we shall show the impact of assuming a different SED. Actually, for the sources located at $z \lesssim 0.3$ and contributing only to the very bright counts probed by Planck Collaboration VII et al. (2013), we have adopted the warmest SED from the template library by Smith et al. (2012).

We have also evaluated the contribution to the counts from strong galaxy-scale

gravitational lensing, according to the SISSA model (cf. Lapi et al., 2012, see also the Appendix of this thesis); the lensed counts are computed as

$$\frac{\mathrm{d}N_{\rm lensed}}{\mathrm{d}\log S_\nu\,\mathrm{d}\Omega}(S_\nu) = \int \mathrm{d}z\,\frac{1}{\langle\mu\rangle}\int_2^{\mu_{\rm max}}\mathrm{d}\mu\,\frac{\mathrm{d}p}{\mathrm{d}\mu}(\mu,z)\,\frac{\mathrm{d}N_{\rm unlensed}}{\mathrm{d}\log S_\nu\,\mathrm{d}\Omega\,\mathrm{d}z}(S_\nu/\mu,z)\,. \qquad (3.6)$$

Here $\mathrm{d}p/\mathrm{d}\mu$ is the amplification distribution and $\langle\mu\rangle$ is its average (≈ 1 for a wide-area survey); a maximum amplification of $\mu_{\rm max}\approx 25$ has been adopted (see Cai et al., 2013; Bonato et al., 2014).

The Euclidean-normalized, differential counts at various wavelengths $\lambda\approx 500$, 850, 1100, and 1400 μm are plotted in Fig. 3.3. We find an excellent agreement of the counts derived from our intrinsic SFR function with various observational data (see details in the caption). By contrast, we also show that the counts expected from the UV-inferred SFR function considerably under-predict the data at the bright end. Note that, to make the contribution to the counts from the UV-inferred SFR function as large as possible, we have assumed that all the UV emission is reprocessed by dust and reradiated in the far-IR according to the coldest SED from the template library by Smith et al. (2012).

We remark that the counts at $\lambda\gtrsim 850\,\mu$m for fluxes $\gtrsim$ several mJy are substantially contributed by galaxies located at $z\gtrsim 3$. This is shown in detail by the redshift distributions presented in Fig. 3.4, that peak at $z\approx 3-4$ with a substantial tail at higher z. Specifically, we find a good agreement of our results based on the intrinsic SFR function with the 1400 μm *ALMA-SPT* data at a flux limit of $\gtrsim 20$ mJy, constructed from a sample of 26 galaxies with spectroscopic redshifts (Weiß et al., 2013). The redshift distribution is essentially contributed by gravitationally lensed sources, and it constitutes an extremely important test of the intrinsic SFR function up to $z\approx 6$. Note that the lensed counts would be strongly underestimated when basing on the (dust-corrected) UV-inferred SFR function (cf. Fig. 3.3, bottom right panel). We also find good agreement with the 850 μm data from *SCUBA-2* by Koprowski et al. (2016) at a limiting flux of $\gtrsim 2$ mJy, and from *AzTEC-LABOCA* data by Koprowski et al. (2014, see also Smolčić et al. (2012)) at a flux limit of $\gtrsim 8$ mJy, that constitute a sample of about 100 sources with mostly photometric redshifts. Note that, given the nonhomogeneous nature and the diverse systematics affecting the data sets exploited to build up the number counts and redshift distributions, a formal minimum χ^2 fit is not warranted.

In Fig. 3.5 we show that the cosmic infrared background at 500, 850, and 1400 μm as derived from our intrinsic SFR function is consistent with the measurements by Fixsen et al. (1998, see also Lagache et al. (1999), PlanckCollaborationXVIII, PlanckCollaborationXXX). As extensively discussed by Lapi et al. (2011, see their Fig. 19), the evolution with redshift of the background highlights that for $\lambda\gtrsim 500\,\mu$m it is mostly contributed by high-redshift galaxies down to $z\approx 2-3$. This trend strengthens as λ increases; in particular, at 1400 μm about 50% of the background is contributed by dusty

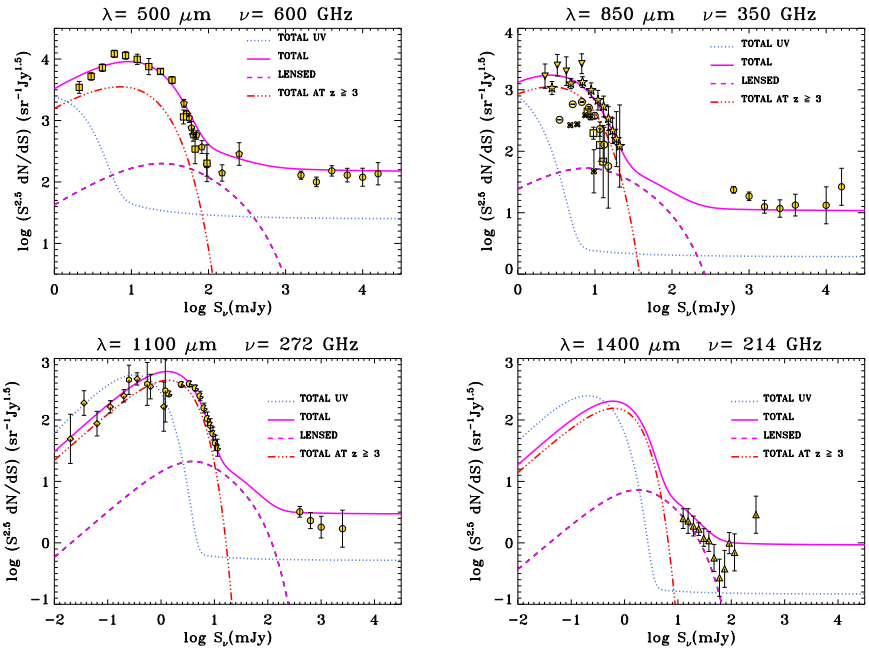

Figure 3.3 **Euclidean-normalized differential number counts at** 500 **(top left),** 850 **(top right),** 1100 **(bottom left), and** 1400 μ**m (bottom right):** Magenta lines refer to the counts derived from our intrinsic SFR function; the contribution to the total counts (solid) from strongly lensed galaxies (dashed) is highlighted. The triple dot-dashed red line is the contribution to unlensed counts from galaxies at $z \gtrsim 3$. The blue dotted line refers to the counts derived from the UV-inferred SFR function. Data (gold symbols) are from Planck Collaboration VII et al. (filled circles 2013), *Herschel*/HerMES by Béthermin et al. (2012, filled squares), *Herschel*/ATLAS by Clements et al. (2010, filled pentagons), *SCUBA* by Coppin et al. (2006, filled stars) and by Noble et al. (2012, filled reverse triangles), *LABOCA* by Weiß et al. (2009, open circles), *ALMA* by Karim et al. (2013, open clovers), Simpson et al. (2015, open squares), Hatsukade et al. (2016, exagons) and Fujimoto et al. (2016, filled diamonds), *AzTEC* by Scott et al. (2012, filled pacmans), and *SPT* by Mocanu et al. (2013, filled triangles).

galaxies at $z \gtrsim 3$; this fraction would drop dramatically to less than 10% basing on the (dust-corrected) UV-inferred SFR function.

All in all, the agreement with the observed counts, redshift distributions (including lensed sources), and cosmic infrared background constitutes a robust validation of our intrinsic SFR function in a range of SFRs and redshift where the far-IR data on the luminosity function are still not available.

Two remarks are in order. First, we have investigated the impact of using different SEDs typical of star-forming, dust-obscured galaxies, namely, the Cosmic Eyelash (our reference, see Sect. 2.3), the average from the ALESS sample (Swinbank et al., 2014; da Cunha et al., 2015; Rangwala et al., 2011), and the local ULIRG+Seyfert1 galaxy

Mrk231 (e.g. Polletta et al., 2007). In Fig. 3.6 we show that the effect on the steep part of the 850 μm counts (mostly contributed by $z \gtrsim 2-3$) is small when changing from the Eyelash to the ALESS (or Arp220) SED; the same holds at any $\lambda \gtrsim 500\,\mu$m, since for galaxies at $z \gtrsim 2-3$ the SEDs are quite similar in the corresponding range of rest-frame wavelengths (see Fig. 2.5). On the contrary, considering a SED shape like that of Mrk231, which exhibits more power in the mid-IR regime, would appreciably underpredict the (sub-)mm counts. Second, we point out that the contribution of active galactic nuclei (AGNs) is marginally relevant as to the above statistics. The argument have been extensively treated in Sect.2.3.

In this respect, an approach similar to the already mentioned one by Delvecchio et al. (2014) have been exploited by Gruppioni et al. (2015) in the COSMOS and GOODS-S fields of the PEP and HerMES/*Herschel* surveys: they subtracted the AGN emission on an object-by-object basis, and then reconstructed the bright end of the SFR function at $z \lesssim 3$ (cf. hexagons in Fig. 3.1); as a matter of fact, their outcomes agree with our SFR function, again indicating that the AGN contribution is irrelevant.

3.1.2 Validating the SFRF via the continuity equation

We now turn to validate our intrinsic SFR function by exploiting the observed stellar mass function at $z \gtrsim 4$. The SFR and stellar mass functions are naturally related via the continuity equation, along the lines already pursued for lower redshifts by Aversa et al. (2015, see also Leja et al. (2015)). The continuity equation has been originally devised for connecting the AGN statistics to the demographics of both active and dormant supermassive black holes; recently, it has been also applied with remarkable success to link the evolution of the galaxy SFR function $N(\psi, t)$ to the stellar mass functions $N(M_\star, t)$ of active and passively-evolving galaxies across cosmic times. We defer the reader to the paper by Aversa et al. (2015) and to the Appendix of this thesis for an extensive discussion of this approach.

In summary the continuity equation in integral formulation can be written as

$$N(\psi, t) = \int_0^\infty \mathrm{d}M_\star \; [\partial_t N(M_\star, t)] \; \frac{\mathrm{d}\tau}{\mathrm{d}\psi}(\psi | M_\star, t) \; ; \tag{3.7}$$

here t is the cosmological time corresponding to redshift z, τ is internal galactic time (i.e., the time elapsed since the triggering of significant star formation) and $\mathrm{d}\tau/\mathrm{d}\psi$ is the time spent by a galaxy with current stellar mass $M_\star$ in the SFR range $[\psi, \psi + \mathrm{d}\psi]$ given a star formation history $\psi = \psi(\tau | M_\star, t)$. Since we are mainly interested in the high-redshift $z \gtrsim 4$ evolution of the mass function, we have neglected any source term due to 'dry' merging, i.e., events adding the whole mass content in stars of merging galaxies without contributing significantly to luminosity associated with star formation.

As for the star formation history $\psi(\tau|M_\star, t)$, Aversa et al. (2015) have considered the standard, time-honored assumptions of a constant, or exponentially increasing/decreasing SFR. Here we follow the indications emerging from recent studies of SED-modeling (e.g. Papovich et al., 2011; Smit et al., 2012; Moustakas et al., 2013; Steinhardt et al., 2014) for a slow, power-law increase of the SFR with a characteristic time $\tau_\star$, in the form

$$\psi(\tau|M_\star, t) = \psi_\star \left(\frac{\tau}{\tau_\star}\right)^\kappa \qquad \psi_\star = \frac{M_\star\,(\kappa+1)}{\tau_\star}\,, \tag{3.8}$$

with $\kappa \approx 0.5$; the second equation above just links the normalization $\psi_\star$ of the SFR history to the current stellar mass $M_\star$. However, we checked that our results do not depend on this specific representation. The quantity $\mathrm{d}\tau/\mathrm{d}\psi$ entering the continuity equation reads

$$\frac{\mathrm{d}\tau}{\mathrm{d}\psi}(\psi|M_\star, t) = \frac{\tau_\star^{1+1/\kappa}}{\kappa}\,\frac{\psi^{-1+1/\kappa}}{[(1+\kappa)\,M_\star]^{1/\kappa}}\;\Theta_\mathrm{H}\left[\psi \leq \frac{(1+\kappa)\,M_\star}{\tau_\star}\right]\,; \tag{3.9}$$

the Heaviside function $\Theta_\mathrm{H}[\cdot]$ specifies that a galaxy with current mass $M_\star$ cannot have shone at a SFR ψ exceeding $M_\star\,(\kappa+1)/\tau_\star$.

At the high redshifts $z \gtrsim 4$, of interest here, the stellar mass function is dominated by actively star-forming galaxies; thus we adopt the star-formation timescale $\tau_\star$ inferred from the observed main-sequence $\psi - M_\star$ (e.g. Rodighiero et al., 2011, 2014; Whitaker et al., 2014; Renzini and Peng, 2015; Speagle et al., 2014). Such a timescale $\tau_\star = \tau_\star(\psi, t)$ is itself a function of the SFR/stellar mass and cosmic time.

We exploit the determination of the main sequence by Speagle et al. (2014), which takes into account many samples with different primary selections (UV, optical, far-IR; cf. their Table 3). This is a good representation of the statistical average relationships between SFR and stellar mass for galaxies over their lifetime (see also Koprowski et al., 2016). Note that in the Speagle et al. determination, 'off-main sequence' galaxies are accounted for by a scatter of 0.3 dex around the median relation, which is in turn dependent on redshift (see also Muñoz and Peeples, 2015; da Cunha et al., 2015).

We point out that at lower redshifts $z \lesssim 1.5$ it would be important to take the fraction of passively-evolving galaxies into account for obtaining sound estimates of the relic stellar mass function from the continuity equation (see Aversa et al., 2015; Leja et al., 2015). We also stress that $\tau_\star$ is in general different from the total duration of the star-formation episode over which most of the stellar mass is accumulated. More in detail, the two timescales are both quite close to a few 10^8 yr for massive galaxies, which typically formed their stars in a violent burst with SFR $\psi \gtrsim 10^2\,M_\odot\ \mathrm{yr}^{-1}$; but they can be appreciably different for less massive objects, which typically formed steadily their stars at much lower rates $\psi \lesssim 10\,M_\odot\ \mathrm{yr}^{-1}$ over several Gyrs. Thus the total

burst duration is an inverse function of the stellar mass in accord with the standard downsizing picture (e.g. Cowie et al., 1996), while the star-formation timescale from the main sequence $\psi \propto M_\star^{0.8}$ is a slow direct function of the stellar mass or of the time-averaged SFR, namely, $\tau_\star \propto M_\star^{0.2} \propto \langle\psi\rangle^{0.25}$. From a physical point of view, the latter dependence reflects the brevity of the condensation/dynamical timescales within the shallower potential wells of smaller mass halos, that are typically virialized earlier according to the standard structure formation paradigm (see Fan et al., 2010).

The solution of the continuity equation can be worked out under the same route followed in Aversa et al. (2015), to obtain

$$N(\log M_\star, t) = -\kappa\,(1+\kappa)^{1/\kappa}\,M_\star^{1/\kappa}\,\int_0^t \mathrm{d}t'\,\frac{\partial_{\ln\psi}}{f_{\tau_\star}}\left[\frac{N(\log\psi, t)\,\psi^{-1/\kappa}}{\tau_\star^{1+1/\kappa}}\right]\Bigg|_{\psi=(1+\kappa)\,M_\star/\tau_\star}\,, \quad (3.10)$$

with the shorthand $f_{\tau_\star} \equiv 1 + \partial_{\log\psi}[\log\tau_\star]$; this is in its stand a novel result, although we note that the differences in the outcome relative to a constant or exponential SFR are minor. Similarly, the value of the power-law index κ is marginally relevant if varied from the fiducial value $\kappa = 0.5$ within the range from 0 (constant SFR) to 1 (linearly increasing SFR).

In Fig. 3.7 we show the resulting stellar mass function at $z \gtrsim 4$ when using as input our intrinsic SFR functions. The outcome is compared with the determination of the mass function at $z \approx 4 - 8$ by (González et al., 2011; Grazian et al., 2015; Song et al., 2015; Stefanon et al., 2015). The agreement is particularly good with the near-IR selected samples based on HST/WFC3/IR and *Spitzer* data by Grazian et al. (2015, see also Duncan et al. (2014) and Caputi et al. (2015)), when the scatter of 0.3 dex around the median main sequence relation suggested by Speagle et al. (2014) is taken into account.

Notice that the stellar mass functions by González et al. (2011) and Song et al. (2015) are instead obtained from UV-selected samples by combining the observed UV luminosity function with the $M_{\rm UV} - M_\star$ relationship. Even including a scatter of 0.4 dex in the latter relation as adopted by Song et al. (2015), the stellar mass function is still appreciably lower at the high-mass end with respect to the determination based on near-IR samples; this is due to the underestimation of the luminosity function at the bright end by UV surveys, because of insufficient corrections for dust extinction.

We stress that the number density of massive galaxies $M_\star \approx 10^{11}\,M_\odot$ is still quite high at $z \approx 5$, amounting to about $\approx 10^{-5}$ Mpc^{-3}. Then this value is expected to drop around $\approx 5\times10^{-8}$ Mpc^{-3} at $z \approx 7$, to $\approx 2\times10^{-9}$ Mpc^{-3} at $z \approx 8$, and to less than 10^{-10} Mpc^{-3} at $z \approx 10$; this is mainly due to the rapid falloff of the halo mass function at these high redshifts. However, at $z \gtrsim 6$ data are still uncertain, but reliable measurements will become feasible with next generation instruments; in particular, the *JWST* will allow to determine stellar masses $M_\star \gtrsim 10^{10}\,M_\odot$ up to $z \sim 7$ (see Caputi, 2011). This will

eventually allow a detailed validation of the intrinsic SFR function via the continuity equation at these extremely high redshift.

On the other hand, the SFR functions inferred solely from UV data, even corrected for dust extinction, strongly underpredict the observed stellar mass function for $M_\star \gtrsim$ a few $10^{10}\,M_\odot$ at $z \lesssim 5$. This demonstrates that at these redshifts the strong suppression of the bright end in the UV-inferred SFR function with respect to the intrinsic one must be traced back to star formation in dust enshrouded environments, and cannot be related to any form of feedback, like that from SNe or AGNs, that instead would anyhow lower the stellar mass. In the redshift range $z \sim 6-8$ the intrinsic SFR function approaches the UV-inferred one, and particularly so at $z \gtrsim 7$ (cf. Fig. 3.1); as a consequence, the continuity equation implies that the stellar mass functions derived from the intrinsic or the UV (dust-corrected) SFR functions are both consistent with the observational determinations within their large uncertainties (cf. Fig. 3.7).

3.2 Linking to the halo mass via the abundance matching

We now connect the SFR and stellar mass function of active galaxies with the statistics of the underlying, gravitationally dominant DM halos. We exploit the abundance matching technique, a standard way of deriving a monotonic relationship between galaxy and halo properties by matching the corresponding integrated number densities (e.g. Vale and Ostriker, 2004; Shankar et al., 2006; Moster et al., 2013; Behroozi et al., 2013).

We derive the relationship $M_\star(M_{\rm H}, z)$ between the current stellar mass $M_\star$ and the halo mass $M_{\rm H}$ by solving the equation (see Aversa et al., 2015, for details, see also the Appendix to this thesis)

$$\int_{\log M_\star}^{\infty} {\rm d}\log M'_\star\, N(\log M'_\star, z) = \int_{-\infty}^{+\infty} {\rm d}\log M'_{\rm H}\, N(\log M'_{\rm H}, z)\, \frac{1}{2}\,{\rm erfc}\left\{\frac{\log[M_{\rm H}(M_\star)/M'_{\rm H}]}{\sqrt{2}\,\sigma_{\log M_\star}}\right\}, \tag{3.11}$$

which holds when a lognormal distribution of $M_\star$ at given $M_{\rm H}$ with dispersion $\sigma_{\log M_\star}$ is adopted; we follow previous studies based on the abundance matching technique (see references above) and fiducially take $\sigma_{\log M_\star} \approx 0.15$. In Eq. (3.11) the quantity $N(\log M_{\rm H}, z)$ is the galaxy halo mass function, i.e., the mass function of halos hosting one individual galaxy (see Aversa et al., 2015); actually, for $z \gtrsim 4$ and for the halo masses of interest here, it coincides with the standard halo mass function from cosmological $N-$body simulations (e.g. Tinker et al., 2008).

The same technique may also be applied to look for a relation $\psi(M_{\rm H}, z)$ specifying the typical SFR ψ in a halo of mass $M_{\rm H}$ at redshift z. However, when dealing with the SFR, one has to take into account that active galaxies shine with a characteristic star-formation timescale $\tau_\star(\psi, z)$ which may be smaller than the cosmic time $t(z)$. In practice, one can still rely on Eq. (3.11) by substituting: the current stellar mass with the SFR, i.e., $M_\star \rightarrow \psi$; the stellar mass function with the SFR function divided by the SFR timescale, i.e., $N(\log M_\star, z) \rightarrow N(\log \psi, z)/\tau_\star(\psi, z)$; and the halo mass function with the halo creation rate (see Lapi et al., 2013), i.e., $N(\log M_{\rm H}, z) \rightarrow \partial_t^+ N(\log M_{\rm H}, z)$.

In Fig. 3.8 (top panels) we show the resulting $M_\star - M_{\rm H}$ and $\psi - M_{\rm H}$ relationships. Note that these relationships refer to active star-forming galaxies, while Aversa et al. (2015) have presented the corresponding outcomes for the total population including objects in passive evolution; as expected, for active galaxies the SFR at given halo mass is higher.

The most remarkable feature of these relationships is the little if no evolution with redshift at given $M_{\rm H}$; this clearly indicates that the star formation in galaxies at high redshift $z \gtrsim 4$ is regulated by similar, *in-situ* processes (Moster et al., 2013; Aversa et al., 2015), and not by merging or gas infall from cosmological scales. The insets illustrate the sSFR= $\psi/M_\star$, and the star formation efficiency, i.e., the current stellar to baryon ratio $M_\star/(0.16 \times M_{\rm H})$, as a function of $M_{\rm H}$.

The latter highlights that star formation in galaxies is an extremely inefficient process, i.e., only a small amount of the available baryon content of a halo is converted into stars. From a physical point of view, this is usually interpreted in terms of competition between cooling and heating processes. In low-mass halos, heating is provided by energy feedback from SN explosions, that regulate star formation at slow rates $\psi \lesssim 10\, M_\odot\ {\rm yr}^{-1}$ over timescales of several Gyrs. In massive halos, cooling rates are not significantly offset by SN feedback, yielding the well-known overcooling problem (Cirasuolo et al., 2005; Dutton et al., 2015, for a recent discussion). This motivated a number of authors (Granato et al., 2004; Di Matteo et al., 2005; Lapi et al., 2006, 2014) to propose that the star formation can proceed at much higher levels $\psi \gtrsim 30\, M_\odot\ {\rm yr}^{-1}$ over several 10^8 yr, until the central AGN attains enough power to shine as a quasar, quenching the SFR abruptly and sweeping away most of the gas and dust content (e.g. Shankar et al., 2006; Aversa et al., 2015). On the contrary, neglecting quasar feedback in large halos would produce stellar masses well above the observed values.

We stress that the abundance matching relationships derived on the basis of the intrinsic and UV-inferred SFR function differ, marginally at $z \gtrsim 7$ but considerably at $z \approx 4$. It is extremely important to take such differences into account for a proper interpretation of the observational data in terms of galaxy formation scenarios. For example, consider a galaxy with stellar mass of $M_\star \approx 10^{11}\, M_\odot$ at $z \approx 5$, whose number density is of order $\approx 10^{-5}\ {\rm Mpc}^{-3}$ (see Duncan et al., 2014; Grazian et al., 2015). From

the $M_\star - M_\mathrm{H}$ relationship (cf. Fig. 3.8, top right), the host halo is seen to feature a mass of $M_\mathrm{H} \approx$ a few $10^{12}\,M_\odot$. Moreover, according to the $\psi - M_\mathrm{H}$ relationship with its 0.3 dex scatter (cf. Fig. 3.8, top left), the SFR turns out to be $\psi \approx 500 - 1000\,M_\odot$ yr^{-1} when basing on the intrinsic SFR function, but only of order $\psi_\mathrm{UV} \approx 50 - 100\,M_\odot$ yr^{-1} when relying on the UV-inferred one; the corresponding SFR timescales $M_\star/\psi$ amounts to $\approx 10^8$ yr and 10^9 yr, respectively. Given that the age of the Universe at $z \approx 5$ is of order 1.2 Gyr, the UV-inferred solution would require star formation to occur well in advance of the initial halo virialization, and/or extreme assumptions on the star formation efficiency or halo occupation (Steinhardt et al., 2016). On the other hand, the solution based on the intrinsic SFR function yields a formation redshift of the host halos $z_\mathrm{form} \approx 5.4$; the corresponding halo number density for $M_\mathrm{H} \approx$ a few $10^{12}\,M_\odot$ reads $\sim 10^{-5}$ Mpc^{-3}, in agreement with the stellar mass functions observed at $z \approx 5$ for $M_\star \approx 10^{11}\,M_\odot$ wherefrom the argument started.

The abundance matching relationships are also fundamental to interpret the clustering signal associated with high-z dusty galaxies (see Fig. 3.8, bottom panel). Specifically, we find that at $z \approx 4-5$ galaxies endowed with SFR $\psi \gtrsim 100-300\,M_\odot$ yr^{-1} and $M_\star \gtrsim 10^{11}\,M_\odot$ are typically hosted within halos of $M_\mathrm{H} \gtrsim$ a few $10^{12}\,M_\odot$, which are extremely biased and clustered. We note that on the basis of the observed clustering signal, Hildebrandt et al. (2009) and Bian et al. (2013) instead associate the same halo masses to galaxies selected with UV magnitudes $M_\mathrm{UV} \lesssim -21$; when using the dust correction based on the UV slope, they estimate a corresponding SFR $\psi \approx 30 - 50\,M_\odot$ yr^{-1}. This low value of the intrinsic SFR is underestimated because of an incomplete dust-correction applied to UV-selected samples (cf. Fig. 3.8, top left panel), and would raise again an issue on the star formation timescale (see above; Steinhardt et al., 2016).

From the top panels of Fig. 3.8 it is apparent that, when the abundance matching is performed by exploiting the intrinsic SFR function, the evolution with redshift of SFR and stellar mass at fixed halo mass is small and well within the errors determined by observations. On the other hand, the evolution is amplified when the abundance matching is performed by exploiting the (dust-corrected) UV-inferred SFR function. The latter case would imply an increasing star-formation efficiency with redshift, which is reminiscent of the claim by Finkelstein et al. (2015b). On the contrary, we find no evolution (within errors) of the star-formation efficiency when basing on the intrinsic SFR function.

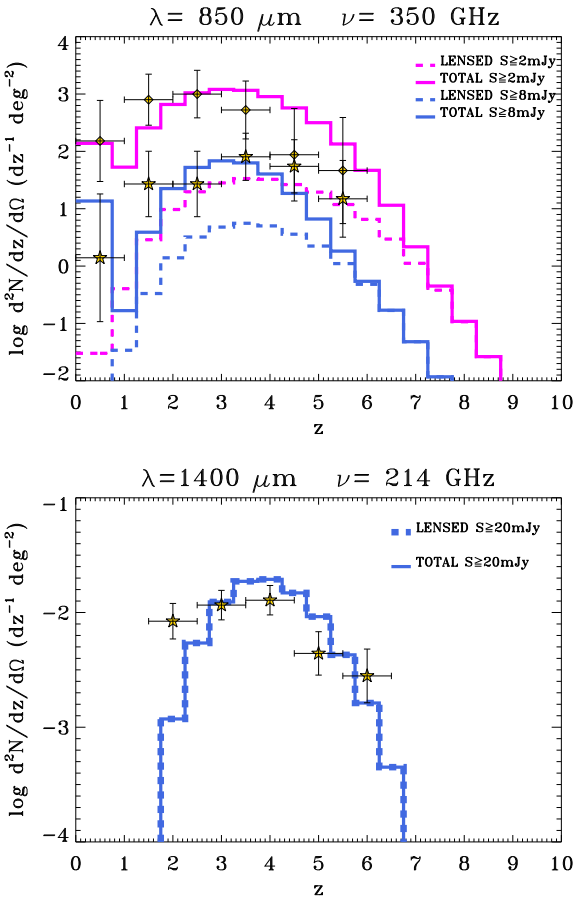

Figure 3.4 **Redshift distributions at** 850 **(top panel) and** 1400 μ**m (bottom panel):** At 850 μm magenta lines refer to a limiting flux of 2 mJy and blue lines to a limiting flux of 8 mJy, with the contribution to the total (solid) from strong galaxy-scale gravitational lensing (dashed) highlighted; data are from *AzTEC-LABOCA* by Koprowski et al. (2014, stars), and from *SCUBA-2* by Koprowski et al. (2016, diamond). At 1400 μm blue lines (solid and dashed are superimposed) refer to a limiting flux of 20 mJy; data are from *ALMA-SPT* by Weiß et al. (2013, stars) .

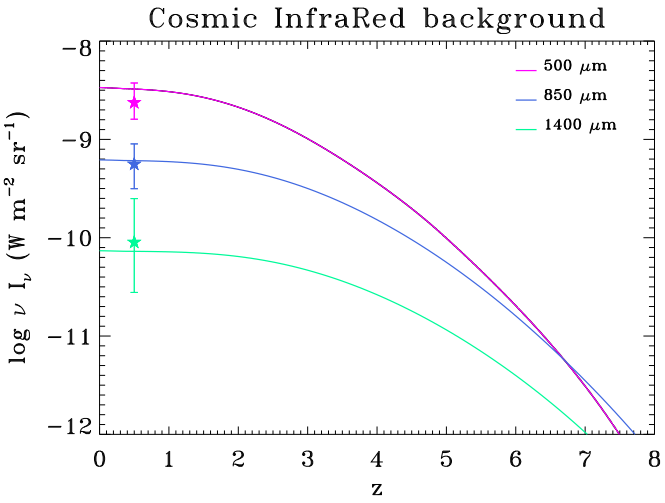

Figure 3.5 **Contribution to the the cosmic infrared background:** it is shown at 500 (magenta), 850 (blue), and 1400 μm (green) from redshift greater than z, as derived from our intrinsic SFR function, compared with the observational determinations at $z \approx 0$ (stars, slightly offset in redshift for clarity) by Fixsen et al. (1998, see also Lagache et al. (1999)).

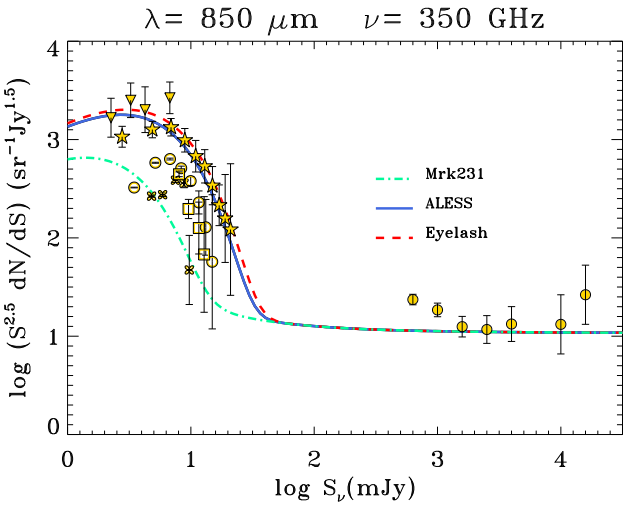

Figure 3.6 **Effect of varying the SED on the total** 850 μ**m counts:** data points as in Fig. 3.3.

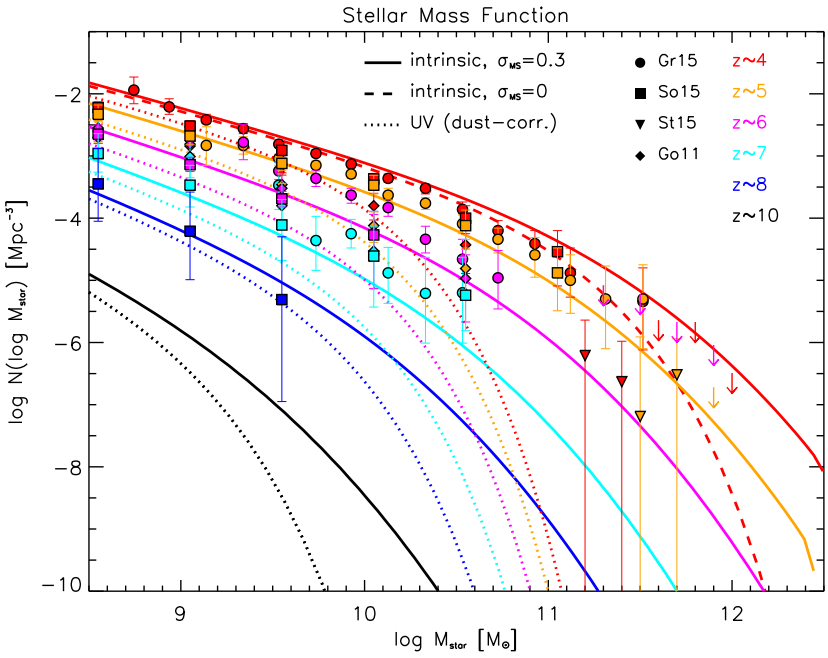

Figure 3.7 **The stellar mass function at redshifts $z\approx$ 4-10 (color-coded):** it has been obtained via the continuity equation from the intrinsic (solid) or UV-inferred (dotted) SFR function considering a scatter of $\sigma_{\rm MS} \approx 0.3$ dex around the median main sequence relationship; at $z \approx 4$ the outcome from the intrinsic SFR function with $\sigma_{\rm MS} \approx 0$ is highlighted by the dashed red line. Data of the stellar mass functions (see text for details) are from Grazian et al. (2015, circles), Song et al. (2015, squares), Stefanon et al. (2015, inverse triangles), Caputi et al. (2015, stars), and González et al. (2011, diamonds).

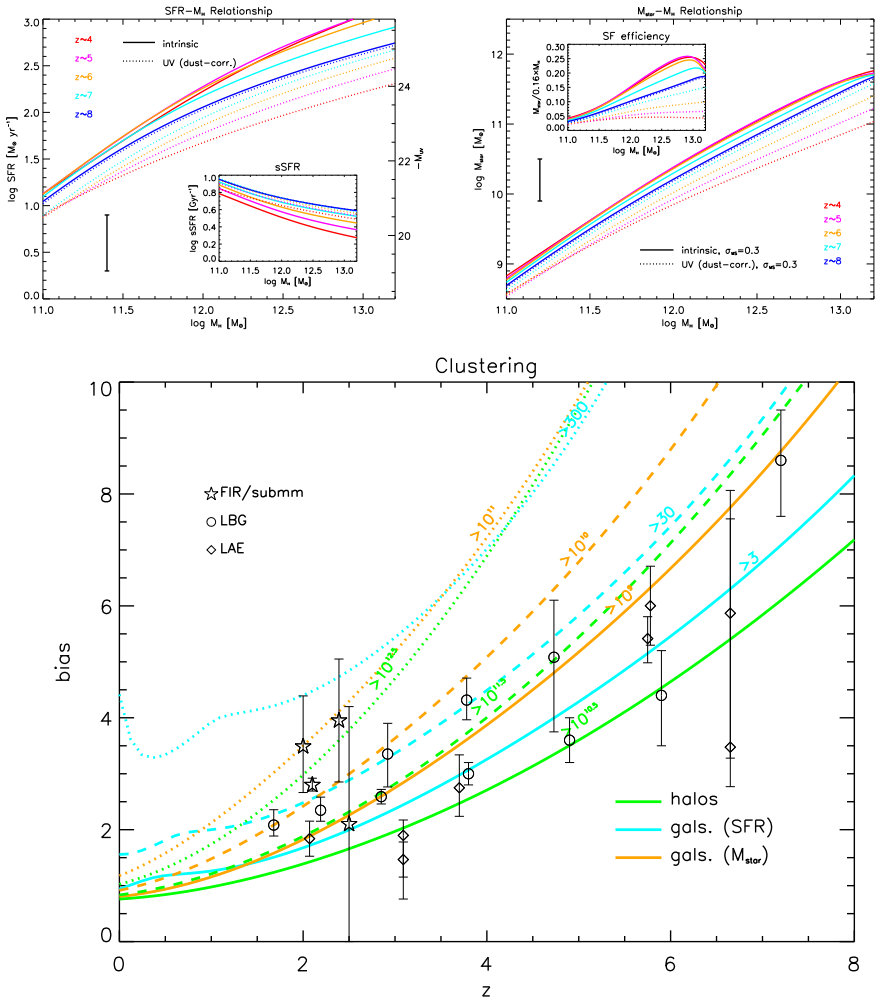

Figure 3.8 **The relationship $\psi - M_{\rm H}$ (top left panel):** it is the relation between SFR (right axis shows the corresponding uncorrected UV magnitude) and host halo mass at different redshift $z \approx 4-8$ (color-code), as derived from the abundance matching of the halo mass function to the intrinsic SFR function (solid lines) or to the SFR function inferred from (dust-corrected) UV data (dotted lines); the inset illustrates the corresponding sSFR= $\psi/M_\star$ vs. the halo mass. **The relationship $M_\star - M_{\rm H}$ (top right panel):** the same as before, this time between stellar mass and host halo mass. The inset illustrates the corresponding star-formation efficiency, i.e., the stellar to baryon fraction $M_\star/(0.16 \times M_{\rm H})$ vs. the halo mass. In both top panels, the error bars represent the typical uncertainty. **The evolution with redshift of the clustering bias (bottom panel):** the results are shown for halos (green) with DM mass exceeding $10^{10.5}$ (solid), $10^{11.5}$ (dashed) and $10^{12.5}$ $M_\odot$ (dotted), for galaxies (cyan) with SFR exceeding 3 (solid), 30 (dashed) and 300 $M_\odot$ yr^{-1} (dotted), and for galaxies (orange) with stellar masses exceeding 10^9 (solid), 10^{10} (dashed), and 10^{11} $M_\odot$ (dotted). Data for FIR/(sub-)mm galaxies (stars) are from Weiß et al. (2009), Hickox et al. (2012), Ono et al. (2014), Bianchini et al. (2015), for LBGs (circles) from Ouchi et al. (2004), Adelberger et al. (2005), Lee et al. (2006), Overzier et al. (2006), Bielby et al. (2013), Barone-Nugent et al. (2014), and for LAE (diamonds) from Gawiser et al. (2007), Ouchi et al. (2010), and Guaita et al. (2010).

Chapter 4

Hunting dusty star-forming galaxies at high-z

In previouses chapters we have stressed the relevance of probing the statistics of galaxies at $z \sim 4-6$ with SFRs $\psi \gtrsim 10^2\,M_\odot\,\mathrm{yr}^{-1}$, that contribute substantially to the high-mass end of the stellar mass function. Since most of these galaxies with high SFRs are likely dust-enshrouded, exploiting IR data is mandatory to fully assess the intrinsic SFR function. How to achieve this goal in practice, given the current and upcoming observational facilities in the far-IR/(sub-)mm and/or UV band, constitutes the issue addressed in this chapter.

4.1 Selecting dusty galaxies in the far-IR/(sub-)mm band

As a starting point, in Fig. 4.1 (top panel) we illustrate the redshift evolution for our reference SED (see Sect. 2.3). The SED has been normalized so that the far-IR emission in the range $3-1100\,\mu$m corresponds to a SFR of $\psi \approx 1\,M_\odot\,\mathrm{yr}^{-1}$.

We have illustrated the positions on the SED of the observational wavelengths for various instruments of interest here : 250, 350, and 500 μm for the SPIRE instrument on board of *Herschel*; 450 and 850 μm for the *SCUBA-2* instrument at the JCMT; $\sim$ 1100 μm for the *AzTEC* at the LMT; 1400 μm for the *SPT*; and 850, 1400 and 3000 μm for *ALMA*. We have also highlighted 5σ detection limits for such instruments (attained in the deepest large-scale surveys undertaken so far or upcoming): $S_{250} \approx 35$ mJy, $S_{350} \approx 40$ mJy, and $S_{500} \approx 50$ mJy for SPIRE; $S_{450} \approx 8$ mJy and $S_{850} \approx 2$ mJy for *SCUBA-2*; $S_{1100} \approx 1$ mJy for *AzTEC*; $S_{1400} \approx 20$ mJy for *SPT*; $S_{850} \approx 0.42$, $S_{1400} \approx 0.11$, and $S_{3000} \approx 0.02$ mJy for *ALMA* (500 hours on 100 arcmin^2).

The accurate determination of the spectroscopic redshift for a large sample of dusty

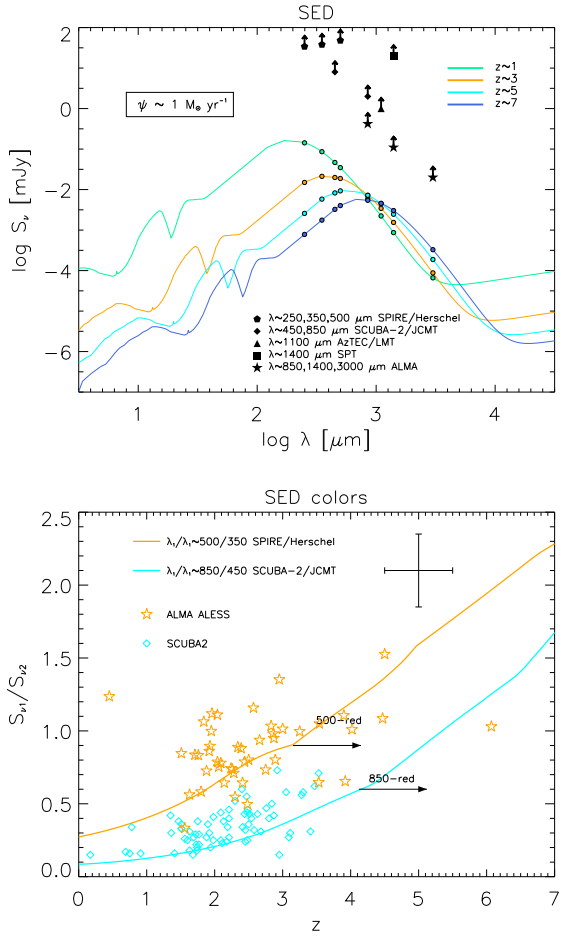

Figure 4.1 **The SED of a typical high-z, dust-obscured star-forming galaxy (top panel):** it is located at redshift $z \approx 1$ (green), 3 (orange), 5 (cyan), and 7 (blue), normalized to a SFR $\psi = 1\,M_{\odot}$ yr^{-1} in the range $\lambda \approx 3 - 1100\,\mu$m. Colored symbols illustrate the values of the SED at different operating wavelengths for various instruments: SPIRE/*Herschel* (circles), *SCUBA-2* (diamonds), *AzTEC* (triangles), *SPT* (squares), and *ALMA* (stars). The corresponding 5σ sensitivities are shown by the black symbols with arrows. **SED colors $S_{\nu,1}/S_{\nu,2}$ as a function of redshift (bottom panel):** they have been exploited for *Herschel* and *SCUBA-2* preselection of dusty galaxies; different lines refer to 500/350 (orange) and 850/450 (cyan) colors. Arrows indicate the redshift ranges where red galaxies are preferentially located. Data are from *ALMA*/ALESS by Swinbank et al. (orange stars 2014) and from *SCUBA-2* by Koprowski et al. (cyan diamonds 2016); in the upper right corner the typical data uncertainty on the median is reported.

galaxies is a major problem. In order to probe the bright end of the SFR function at $z \gtrsim 3$, a strategy could be to preselect high-redshift sources using flux/color criteria from surveys conducted with *Herschel* or *SCUBA-2*, and then perform a more accurate photometric (or even spectroscopic) redshift determination with observations on source by, e.g., *AzTEC* and *ALMA*.

Commonly used preselection criteria (e.g. Dowell et al., 2014; Asboth et al., 2016) for high-redshift sources based on *Herschel* photometry involve to look for '350−peakers' defined as sources with $S_{350}/S_{250} \gtrsim 1$ and $S_{500}/S_{350} \lesssim 1$, or '500−risers' defined as sources with $S_{350}/S_{250} \gtrsim 1$ and $S_{500}/S_{350} \gtrsim 1$. Actually, the uncertainties in the flux measurements make the distinction between peakers and risers quite loose; moreover, at $z \gtrsim 4$ the channel at $250\,\mu$m refers to restframe wavelengths $\lambda \lesssim 50\,\mu$m, where details of the SED due to different dust properties and a possible contribution from an AGN component can be relevant. Thus here we mainly focus on the color S_{500}/S_{350}. In Fig. 4.1 (bottom panel) we plot its evolution with redshift, and compare it with the measurements from *ALMA*/ALESS by Swinbank et al. (2014) finding a reasonable agreement within the large uncertainties. Sources with $S_{500}/S_{350} \gtrsim 0.8$ are high-redshift $z \gtrsim 3$ candidates.

However, the rather high limiting fluxes of *Herschel* cannot probe the SFR function much above $z \sim 5$, since even sources with SFR $\psi \gtrsim 10^3\,M_\odot\,\mathrm{yr}^{-1}$ are too faint to be detected. To go much beyond $z \gtrsim 4$, the preselection based on the color S_{850}/S_{450} from *SCUBA-2* photometry is much more efficient. In Fig. 4.1 (bottom panel) we plot its evolution with redshift, and compare it with the measurements from *SCUBA-2* by Koprowski et al. (2016) finding again a reasonable agreement. It is seen that the color condition $S_{850}/S_{450} \gtrsim 0.6$ can be exploited to preselect candidate galaxies at $z \gtrsim 4$.

In Fig. 4.2 we show our predictions for the differential counts at 500 and $850\,\mu$m for the red sources preselected according to the color criteria discussed above. At $500\,\mu$m the counts of unlensed red sources with $S_{500} \lesssim 100$ mJy agree with the determination by Asboth et al. (2016, see also Dowell et al. (2014)) while those of lensed red sources well compare with the candidate lenses in the *Herschel*/ATLAS survey selected via their red colors by Negrello, private communication; (see also Nayyeri et al. (2016) and Wardlow et al. (2013) for analogous studies in the *Herschel*-HeLMS+HerS and *Herschel*-HerMES surveys).

In Fig. 4.3 we present the corresponding redshift distributions. At $500\,\mu$m (top panel) red high-z candidates are mostly located at redshift $z \gtrsim 3$, featuring SFRs $\psi \gtrsim 300\,M_\odot\,\mathrm{yr}^{-1}$. Interestingly, strong gravitational lensing by foreground galaxies broadens the tail of their redshift distribution toward $z \approx 5-6$; we stress that most of the lensed sources are amplified by relatively modest factors $\langle\mu\rangle \approx 2-5$, so that they would on average feature SFRs still of $\psi \gtrsim 100\,M_\odot\,\mathrm{yr}^{-1}$. At $850\,\mu$m (bottom panel) the color selection based on 850 to 450 flux ratio picks up objects at $z \gtrsim 4$, with a tail ex-

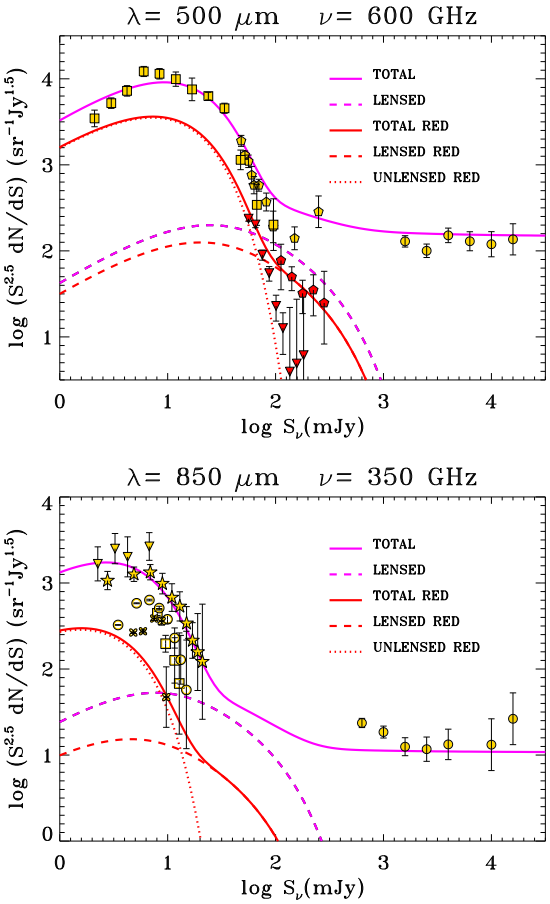

Figure 4.2 **Euclidean-normalized differential number counts at 500 (top panel) and 850 μm (bottom panel):** magenta lines refer to the counts derived from our intrinsic SFR function; the contribution to the total counts (solid) from strongly lensed galaxies (dashed) is highlighted. The counts of red galaxies are illustrated in red, with the solid lines referring to the total, the dotted lines to unlensed counts and the dashed lines to the gravitationally lensed sources. Data (gold symbols) are as in Fig. 3.3. At 500 μm data for red galaxies are from *Herschel*/HerMES by Asboth et al. (2016, red inverse triangles,see also Dowell et al. (2014)) and of candidate high-z lenses from *Herschel*/ATLAS by Negrello, private communication, red pentagons; see also Wardlow et al. (2013),Nayyeri et al. (2016).

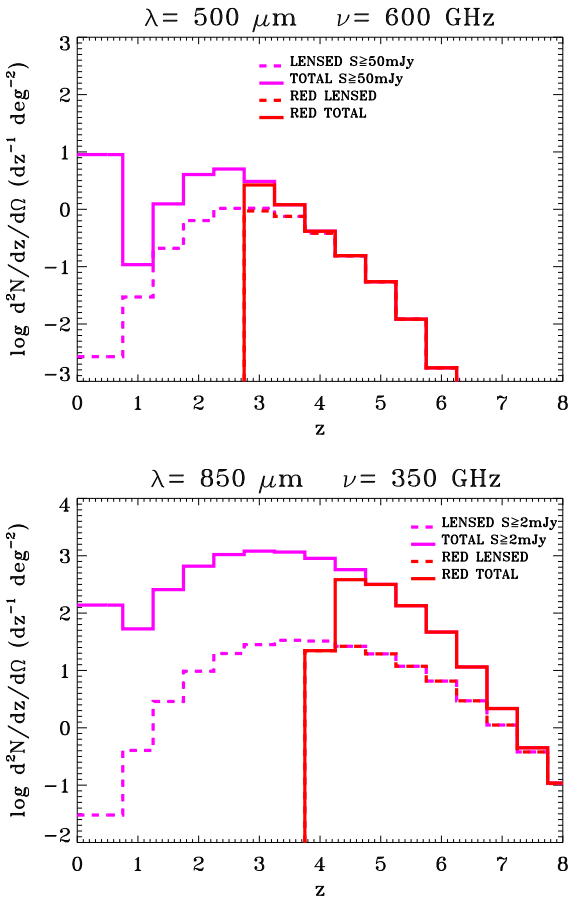

Figure 4.3 **Redshift distributions at** 500 **(top panel) and 850** μ**m (bottom panel):** at 500 μm magenta lines refer to the *Herschel* limiting flux of $\approx$ 50 mJy, with the contribution to the total (solid) from strong galaxy-scale gravitational lensing (dashed) highlighted; the same for red sources is shown in red. At 850 μm the magenta lines refer to a limiting flux of 2 mJy (again red lines refer to red sources).

tending out to $z \approx 7-8$. Since the *Herschel* surveys at 350 and 500 μm cover an overall area of ~ 1000 deg^{-2}, their data can be mined to pick out $\gtrsim 1000$ gravitationally lensed galaxies (see Gonzalez-Nuevo et al., 2012), which, in addition to their cosmological interest (e.g. Eales, 2015), can be also used to estimate the SFR distribution function up to $z \sim 6$.

Once the high$-z$ candidates have been preselected, the photometric data from *Herschel* or *SCUBA-2* have then to be supplemented with observations at longer wavelengths by, e.g., *AzTEC* and *ALMA*; the latter instrument can be also exploited to go for a spectroscopic redshift determination, but this plainly requires more observing time, and preferentially a precise estimate of the photometric redshift to choose the

most-suited observational band.

4.2 Dusty galaxies are not lost in the UV band

In Chapter 3 we have demonstrated that the intrinsic SFR functions as validated via the (sub-)mm counts and the continuity equation are largely underestimated by UV data, especially at the bright end for $z \lesssim 7$. However, next we show that such dusty galaxies can be efficiently probed by combining current UV surveys with upcoming far-IR/(sub-)mm and radio observations.

As a starting point, in Fig. 4.4 (top panel) we present the UV luminosity functions at $z \gtrsim 4$, as reconstructed from the intrinsic SFR function by using various prescriptions for dust extinction. We start by showing that the outcome when no correction is applied considerably overestimate the UV luminosity function for any redshift $z \lesssim 7$ at the bright end $M_{\rm UV} \lesssim -19$. This occurs even when the standard correction based on the $\beta_{\rm UV}$-IRX relation is adopted. This is because, as shown by several authors (e.g. Reddy et al., 2012; Davies et al., 2013; Fan et al., 2014; Coppin et al., 2015) thanks to mid-/far-IR observations of UV-selected galaxies at redshift $z \sim 2-4$, the attenuation values of galaxies with observed UV magnitude $M_{\rm UV} \lesssim -21$ are strongly in excess with respect to those estimated basing on the $\beta_{\rm UV}$-IRX relation, and feature a very large dispersion. The standard interpretation is that star formation occurs preferentially within heavily dust-enshrouded molecular clouds, while the UV slope mainly reflects the emission from stars obscured by the diffuse, cirrus dust component (see Silva et al., 1998; Coppin et al., 2015; Reddy et al., 2015). We notice that on approaching $z \approx 8$ the $\beta-$IRX corrected luminosity function converges toward the unextincted one, at least down to $M_{\rm UV} \gtrsim -21.5$, corresponding to an intrinsic SFR $\psi \lesssim 30\,M_\odot\ {\rm yr}^{-1}$; this suggests that for these galaxies the timescale required to accumulate substantial amount of dust becomes longer than their age.

All in all, for $z \lesssim 7$ and $M_{\rm UV} \lesssim -19$, an attenuation larger than that derived on the basis of the $\beta-$IRX relation is needed to recover the UV luminosity function from the intrinsic SFR function.

Observationally, at $z \sim 2$ the UV attenuation $A_{\rm UV}$ is found to directly correlate with the SFR, though with a large dispersion of about 1 mag (or 0.4 dex in log IRX; e.g., Reddy et al. (2010)); the attenuations are already significant with values $A_{\rm UV} \approx 1.5-2.5$ mag (or IRX values of $\approx 4-7$) for SFRs $\psi \approx 30-50\,M_\odot\ {\rm yr}^{-1}$. A heuristic rendition of such an observed correlation for $\psi \gtrsim 30\,M_\odot\ {\rm yr}^{-1}$ reads

$$A_{\rm UV} = \psi^{0.25}\ ; \tag{4.1}$$

Note that, via stacking analysis of 850 μm emission from Lyman Break Galaxies in the

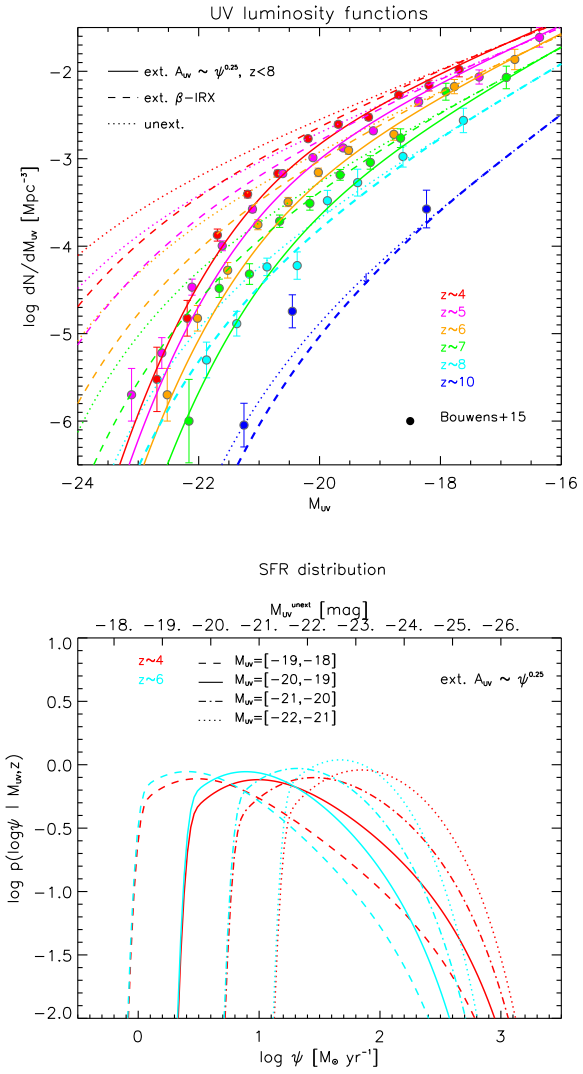

Figure 4.4 **UV luminosity function at different redshift** $z \approx 4-10$ **(color-coded, top panel):** it has been reconstructed from our intrinsic SFR function by not correcting for dust extinction (dotted lines), correcting via the standard $\beta_{\rm UV}$-IRX relation (dashed lines), and via the simple relationship $A_{\rm UV} = \psi^{0.25}$ (solid lines) with a scatter of 1 mag at given ψ (for $z < 8$). Data points (circles) are from Bouwens et al. (2015). **Normalized SFR distribution of galaxies in the observed UV magnitude bins (bottom panel):** it has been centered at $M_{\rm UV} \approx -18.5$ (dashed lines), -19.5 (solid), -20.5 (dot-dashed) and -21.5 (dotted) at redshifts $z \sim 4$ (red) and 6 (cyan). The upper axis refer to the unextincted UV magnitude $M_{\rm UV}^{\rm unext}$ associated to the intrinsic SFR ψ. The extinction law $A_{\rm UV} = \psi^{0.25}$ with a scatter of 1 mag at given ψ has been adopted.

SCUBA-2 Cosmology Legacy Survey, Coppin et al. (2015, cf their Table 2) finds at $z \sim 3-5$ average values of SFR $\psi \approx 70-130\,M_\odot$ yr^{-1} and UV attenuations $A_{\rm UV} \approx 2.3-2.5$, broadly consistent with Eq. (4.1). Note that the relation expressed by Eq. (4.1) represents an average UV attenuation defined as $A_{\rm UV} \equiv 2.5\,\log(1 + L_{\rm IR}/L_{\rm UV})$ in terms of the integrated UV and IR luminosities, and as such it is a basic quantity whose estimate does not require a full radiative transfer approach (e.g. Meurer et al., 1999; Reddy et al., 2015).

In Fig. 4.4 (top panel) we show this to map remarkably well the intrinsic SFR functions onto the observed UV luminosity function over the redshift range $z \approx 4-7$. The outcome on the luminosity function is mostly sensitive to the scatter of the above relation; the behavior at the bright end of the luminosity function constrains it to be within ± 0.2 of the best-fit value of 1 mag. We caveat that the above equation does not include a dependence on metallicity Z, which may well affect the dust abundance. As a matter of fact, Reddy et al. (2010) find a direct dependence between $A_{\rm UV}$ and the metallicity Z, with the former becoming appreciable when $Z \gtrsim Z_\odot/3$. A combined dependence $A_{\rm UV} \propto \psi^\alpha\,Z^\beta$ including both the SFR and metallicity has been considered by Mao et al. (2007) and Cai et al. (2014) basing on the $M_{\rm UV}$ vs. $E(B-V)$ relation by Shapley et al. (2001) and the UV luminosity functions at different redshift. Actually in their approach $\psi(\tau)$, $Z(\tau)$ and hence $A_{\rm UV}(\tau)$ are function of the galactic age τ, but for galaxies with quite robust SFR $\psi \gtrsim 30-50\,M_\odot$ yr^{-1} the SFR is roughly constant and the metallicity saturates rapidly for $\tau \gtrsim$ a few 10^7 yr to slightly subsolar values; all in all, their time-averaged relation is very close to Eq. (4.1).

In Fig. 4.4 (bottom panel), we represent the SFR distribution (areas under curves are normalized to 1) for galaxies selected with a given observed UV magnitude at redshift $z \sim 4-6$; the upper axis refers to the unextincted UV magnitude corresponding to a given SFR ψ. Plainly, the rapid truncation of the distributions to the left of the peak occurs because values of the SFRs yielding an unexctincted UV magnitude fainter than the observed are not allowed ($A_{\rm UV} > 0$ must hold). The decrease of the distributions to the right of the peak reflects the convolution between the intrinsic SFR function and the adopted attenuation law with its large dispersion. The distributions tend to be narrower at higher redshift and for brighter observed UV magnitudes, due to the evolution of the intrinsic SFR function at the high-SFR end, and to the decrease of the extinction with increasing redshift.

Basing on the star formation main sequence, we expect that most of the dusty galaxies with intrinsic SFR $\psi \gtrsim 100\,M_\odot$ yr^{-1} that appear as faint UV objects with $M_{\rm UV} \gtrsim -21$ also feature large stellar masses $M_\star \gtrsim$ a few $10^{10}\,M_\odot$. As such, they appear as upper outliers in the $M_\star - M_{\rm UV}$ diagram (see Duncan et al., 2014; Grazian et al., 2015; Song et al., 2015; Coppin et al., 2015). Note that a similar location could also be occupied by almost passively evolving galaxies, but their number at $z \gtrsim 4$ is

Table 4.1]
Number of dusty, UV-selected galaxies [in arcmin^{-2}]. For more details, see Sect. 4.2 and Fig. 4.4.

$M_{\rm UV}$	$\psi \gtrsim 100\,M_\odot$ yr^{-1}				$\psi \gtrsim 300\,M_\odot$ yr^{-1}				$\psi \gtrsim 1000\,M_\odot$ yr^{-1}			
observed	$z=3$	$z=4$	$z=5$	$z=6$	$z=3$	$z=4$	$z=5$	$z=6$	$z=3$	$z=4$	$z=5$	$z=6$
-17	0.14	0.09	0.04	0.01	0.03	0.02	0.006	0.0006	0.002	0.0008	0.00008	0.000001
-18	0.28	0.18	0.08	0.02	0.06	0.03	0.009	0.001	0.005	0.002	0.0002	0.000003
-19	0.28	0.18	0.08	0.02	0.06	0.03	0.009	0.001	0.005	0.002	0.0002	0.000003
-20	0.24	0.16	0.07	0.02	0.05	0.03	0.008	0.001	0.004	0.001	0.0001	0.000002
-21	0.12	0.08	0.03	0.01	0.03	0.01	0.004	0.0006	0.002	0.0006	0.00006	0.000001
-22	0.03	0.02	0.007	0.002	0.006	0.003	0.001	0.0001	0.0003	0.0001	0.00001	0.0000002

expected to be small, since the star formation timescales implied by the main sequence are close to the age of the Universe. As a consequence, a significant fraction of the outliers are expected to be highly star-forming, massive galaxies, and as such constitute particularly suited targets for far-IR and (sub-)mm observations. At redshift $z \gtrsim 6$ the same regime will be explored by *JWST*.

The broad shape of the SFR distributions implies that dusty, strongly star-forming galaxies with $\psi \gtrsim 30\,M_\odot$ yr^{-1} are not lost in the UV, but rather are moved by their strong attenuation $A_{\rm UV} \gtrsim 2.3$ at fainter magnitudes; although they are outnumbered by the intrinsically faint and poorly attenuated galaxies, nevertheless they can be singled out following the strategy proposed below. In Table 4.1 we present the number per sq. arcmin of dusty, UV-selected galaxies expected per observed magnitude bin, for a given threshold in SFR. The numbers decrease quite rapidly with increasing redshift and increasing SFR threshold. For example, considering that the current areas surveyed in the UV amount to $\approx 10^3$ arcmin^2 (see Bouwens et al., 2015, their Table 1), the expected numbers are around several hundreds of galaxies with SFR $\psi \gtrsim 100\,M_\odot$ yr^{-1} at $M_{\rm UV} \lesssim -17$ and $z \approx 4$; this number decreases to several tens at $z \approx 6$ for $\psi \gtrsim 100\,M_\odot$ yr^{-1}, and to a hundred at $z \approx 4$ for $\psi \gtrsim 300\,M_\odot$ yr^{-1}.

These UV data could be exploited in combination with (sub-)mm and/or radio observations (see Chapter 5 for a complete analysis) to reconstruct the bright end of the intrinsic SFR function (e.g. Barger et al., 2014). The strategy involves to observe the areas $\lesssim 10^3$ arcmin^2 of current UV surveys (see Bouwens et al., 2015) in the (sub-)mm and/or radio band. On one hand, this will allow to measure unbiasedly the intrinsic SFR of strongly dust-obscured galaxies from (sub-)mm/radio data; on the other hand, the cross matching with the positions from the UV maps will allow to associate to these galaxies reliable UV photometric redshifts. Note that the combination with UV photometric data will also help in removing from (sub-)mm and radio observations any contamination from low-luminosity, unobscured AGNs and low-z star-forming galaxies.

Specifically, given the areas covered by current or upcoming UV surveys (Bouwens

et al., 2015), in Fig. 4.5 we present the required sensitivity to detect at least 30 objects (to get sound statistics) with a given SFR threshold in a redshift bin of width $\Delta z \approx 1$. In particular, we focus on SFR $\psi \gtrsim 100$ and $1000\,M_\odot$ yr^{-1}, and consider three wavelengths: 850, $1400\,\mu$m of interest for *ALMA*, and 21 cm (1.4 GHz) of interest for *SKA*. The dots refer to redshift bins centered around $z \sim 1$, 3, 5, and 7, with the redshift increasing following the small colored arrows. The upward black arrows illustrate the 5σ sensitivity limits of *ALMA* and *SKA*, for a total integration time of 500 hours, on survey areas of 100, 1000 and 10000 arcmin^2 (from left to right). Here we have adopted as reference the following specifications: for *ALMA* (in survey-mode configuration, see `http://www.ioa.s.u-tokyo.ac.jp/~ytamura/Wiki/?plugin=attach&refer=ALMA&openfile=tamura-almawg-060302.pdf`) at $850-1400\,\mu$m, a field-of-view (FOV) of $0.02-0.04$ arcmin^2 and a 5σ sensitivity of $0.1-0.05$ mJy hr$^{-1/2}$; for *SKA* (configuration *SKA1-MID*; see Prandoni and Seymour (2015)) at 21 cm (1.4 GHz) a FOV of about 0.35 deg^2 and a 5σ sensitivity of 0.01 mJy hr$^{-1/2}$.

It is seen that on 100 arcmin^2, easily covered by subfields of current UV surveys, both *ALMA* and *SKA* can detect tens of galaxies at $z \approx 4-6$ with SFRs $\psi \gtrsim 100\,M_\odot$ yr^{-1}; on the other hand, on 1000 arcmin^2, the widest area currently surveyed in the UV, is needed to statistically sample galaxies with SFRs $\psi \gtrsim 300\,M_\odot$ yr^{-1}; finally, an area of 10000 arcmin^2, as possibly surveyed by the future *LSST* (e.g. Ivezic et al., 2008), will enable to detect, in the (sub-)mm/ radio band, an appreciable number of dusty galaxies with SFRs $\psi \gtrsim 1000\,M_\odot$ yr^{-1}. Notice that, at the flux limits and on the survey areas considered here, gravitational lensing is only marginally effective, even at the wavelengths $\lambda \gtrsim 1$ mm, where its effect on the counts is most relevant. For example, from Fig. 3.3 (upper panel) it is seen that at 1.4 mm for fluxes of 1 mJy the lensed sources are only a small fraction around a few percent of the total population.

On the (sub-)mm side, another interesting instrument that could be exploited for these observations is *NIKA2*; we adopt as reference specifications (see `http://ipag.osug.fr/ nika2/Instrument.html`) at 1.2 mm a FOV of about 40 arcmin^2 and a 5σ sensitivity around 1.3 mJy hr$^{-1/2}$. Then in 500 hours it can attain a 5σ sensitivity of 0.1 mJy on 100 arcmin^2, of 0.3 mJy on 1000 arcmin^2, and of 1 mJy on 10000 arcmin^2; thus *NIKA2* at 1.2 mm will perform similarly to *ALMA* at 1.4 mm. On the radio side, the *SKA* precursor *MeerKAT* is also interesting; we adopt as reference specifications (see Prandoni and Seymour, 2015) at 21 cm (1.4 GHz) a FOV of about 0.8 deg^2 and a 5σ sensitivity around 0.01 mJy hr$^{-1/2}$. In 500 hours it can attain a 5σ sensitivity of $0.5\,\mu$Jy on 100 arcmin^2, of $0.5\,\mu$Jy on 1000 arcmin^2, and of $0.8\,\mu$Jy on 10000 arcmin^2; thus it will perform similarly to *SKA*. However, we note that *NIKA2* and *MeerKAT*, differently from *ALMA* and *SKA*, in the surveys considered above would work close to their confusion limit. Both instruments feature a resolution around 10 arcsec, which

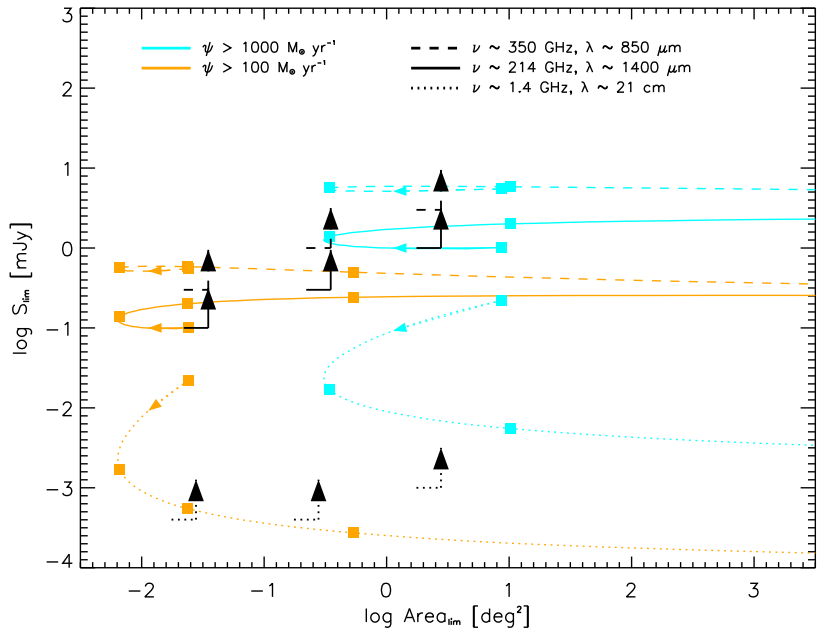

Figure 4.5 **Surveys to detect dusty galaxies:** the diagram is showing the limiting flux and the area of a (sub-)mm and radio survey required to detect at least 30 dusty galaxies per redshift bin $\Delta z \approx 1$. Results are shown for two different thresholds in intrinsic SFR $\psi \gtrsim 100$ (orange lines) and $\gtrsim 1000\,M_{\odot}$ yr^{-1} (cyan lines), at three wavelengths: 850 (dashed) and 1400 μm (solid) of interest for *ALMA*, and 21 cm (1.4 GHz, dotted) of interest for *SKA*. Along each curve redshift increases following the small colored arrows, with the dots referring to $z \approx 1$, 3 ,5, and 7. The black upward arrows illustrate the *ALMA* and *SKA* $5\,\sigma$ sensitivity limits (500 hours of integration time, see text for details) for surveys on 100, 1000, and 10000 arcmin^2.

implies, on considering the shape of the counts (cf. Fig. 3.3), a confusion limit around 0.1 mJy for *NIKA2* at 1.2 mm, and at the μJy level for *MeerKAT* at 21 cm (1.4 GHz).

Dust production

We stress that collecting large statistics of UV and far-IR selected galaxies at high redshift is extremely informative on timescales for dust production and destruction. For instance, in the case of AZTEC-3 at $z \approx 5.3$ (Riechers et al. 2014) and HLFS3 at $z \approx 6.3$ (Cooray et al. 2014) far-IR data indicate SFRs $\psi \sim 1000\,M_\odot\,\mathrm{yr}^{-1}$, stellar masses $M_\star \sim 1-5\times10^{10}\,M_\odot$, and dust masses $M_d \sim 3\times10^8\,M_\odot$. The star-formation timescale $\tau_\star = M_\star/\psi \sim 1 - 5 \times 10^7$ yr implies that a large amount of dust has been rapidly accumulated in these galaxies; adopting a Chabrier IMF and no dust destruction, for type-II SN explosion a dust mass yield of $m_d \sim 0.7 - 3\,M_\odot$ per SN is required. This yield is somewhat higher than the value found for SN 1987A $m_d \sim 0.8\,M_\odot$ per SN, possibly an upper bound (Matsuura et al. 2015).

On the other hand, the SN-driven shock waves destruct dust grains on a timescale $\tau_D = \tau_{\rm SN}\,M_{\rm ISM}/m_g$, where $\tau_{\rm SN}$ is the time between SN explosions, $M_{\rm ISM}$ is the mass of the ISM (gas and dust), and m_g is the mass of ISM cleared per SN explosion (e.g., Slavin et al. 2014). For the Milky Way, $\tau_{\rm SN} \sim 125$ yr, $M_{\rm ISM} \sim 5 \times 10^9\,M_\odot$ and $m_g \sim 600\,M_\odot$ hold, to yield $\tau_D \sim$ Gyr. Contrariwise, for the high-z galaxies mentioned above the extremely large SFRs $\psi \sim 1000\,M_\odot\,\mathrm{yr}^{-1}$ imply $\tau_{\rm SN} \sim 0.1$ yr, making $\tau_D \lesssim 10^7$ yr so short with respect to $\tau_\star$ as to exclude that destruction can be neglected. Additional stellar sources of dust may be at work, such as W-R stars, AGB stars and type-I SNe; the first are anyhow minor dust producers, while the second and the third can form significant dust amounts but over long timescales $\gtrsim$ a few $\times10^8$. Note that even accretion in molecular clouds can have an important role in dust formation (for a review, see Dwek & Cherchneff 2010).

These instances enlighten that the issues of dust formation in high-z galaxies and of dust production by type-II SN and AGB stars are still open problems (see, e.g., the discussion in Dwek & Cherchneff 2011; Dwek et al. 2015; Mancini et al. 2015; Wesson et al. 2015). Large statistical samples of dusty star-forming galaxies at $z \gtrsim 4$ will constitute key datasets for understanding the role of the physical processes involved in dust formation and destruction.

Chapter 5

Radio emission from star-forming galaxies

Another possibility to search for high-z dusty star-forming galaxies is to use the radio emission correlated to star formation to identify them. As already mentioned in Section 2.4.6, the deepest radio surveys on disposal, are not deep enough in flux, or have been carried out at frequencies that are too low, in order to be able to pinpoint the star-forming galaxies among the population of Radio Loud AGNs, that dominate the present number counts. The region where star-forming galaxies start to dominate the overall number counts at ν=1.4 GHz, for example, (see Fig. 5.1) has been, up to now, only briefly covered. The observations are still not able to properly separate the AGNs from star-forming (SF) galaxies, also given that the former are still present at mJy levels of flux in appreciable amount. In order to really disentangle the two populations, and hunt for dusty star forming galaxies in the radio band, it is necessary to investigate fluxes down to sub-mJy levels. This will be possible in the near future thanks to the SKA and its precursors.

5.1 The SFR-radio emission relations

In Section 2.4.6 we have briefly discussed the two radio components that trace the SFR in galaxies: they are the synchrotron emission and the free-free emission. The former is produced by supernovae, and it is the principal component of the overall radio emission related to star formation at low frequencies, while the free-free emission is related to the gas ionized by young massive stars, and it is the dominant component at higher frequencies (see Fig. 2.4). There are relationships between SFR and radio emission (both synchrotron and free-free), that can be exploited to the purpose of looking for

dusty galaxies at high-z.

5.1.1 Calibration of the relation between SFR and synchrotron emission

A calibration of the SFR-synchrotron luminosity relation was obtained by Murphy et al. (2011) using Starburst99 (Leitherer et al., 1999) with a Kroupa (2001) IMF and specific choices for the metallicity and the star formation history. We have slightly modified their relation including a steepening of the synchrotron spectrum by $\Delta\alpha = 0.5$ above a break frequency of 20 GHz to take into account electron ageing effects (Banday and Wolfendale, 1991). The SFR-synchrotron luminosity relation then writes:

$$\bar{L}_{\rm sync} \simeq 1.9 \times 10^{28} \left(\frac{\rm SFR}{\rm M_{\odot} yr^{-1}}\right)\left(\frac{\nu}{\rm GHz}\right)^{-0.85}\left[1+\left(\frac{\nu}{20\,\rm GHz}\right)^{0.5}\right]^{-1} \rm erg\,s^{-1}\,Hz^{-1}. \quad (5.1)$$

The high-frequency synchrotron emission can be further suppressed at high z because of the energy losses of relativistic electrons due to inverse Compton scattering off the Cosmic Microwave Background (CMB) photons, whose energy density increases as $(1+z)^4$ (Norris et al., 2013; Carilli et al., 2008; Murphy, 2009). We also highlight that, differently from free-free and UV emissions, which are a measure of the current SFR, the synchrotron emission is delayed by $\sim 10^7$ yr, that is the main sequence lifetime of massive stars that explode as supernovae, generating the relativistic electrons (Clemens et al., 2008). At high z the fraction of galaxies younger than $\sim 10^7$ yr, which are consequently lacking relativistic electrons, hence the synchrotron emission, increases.

These effects are not taken into account in our calculations, then we may overestimate the statistical properties that we derive, as the faint counts and the high-z tails of the redshift distributions. The overestimate of the total radio luminosity is however unlikely to be large because even at 1.4 GHz (and even more going at higher frequencies) the free-free contribution is comparable to the synchrotron one at flux densities below the current observational limits (see Fig. 5.1).

Applying the relation 5.1 to the redshift dependent SFR functions presented in Chapter 3, and exploiting them to produce predictions of radio counts at 1.4 GHz down to sub-mJy levels, where SF galaxies dominate the overall population, we find good agreement (see Fig. 5.1). The total counts are obtained adding those of radio-loud AGNs, yielded by the Massardi et al. (2010) model[1].

[1]Tabulations of the radio-loud AGN counts yielded by the model at several frequencies are publicly available at http://w1.ira.inaf.it/rstools/srccnt/srccnt_tables.html .

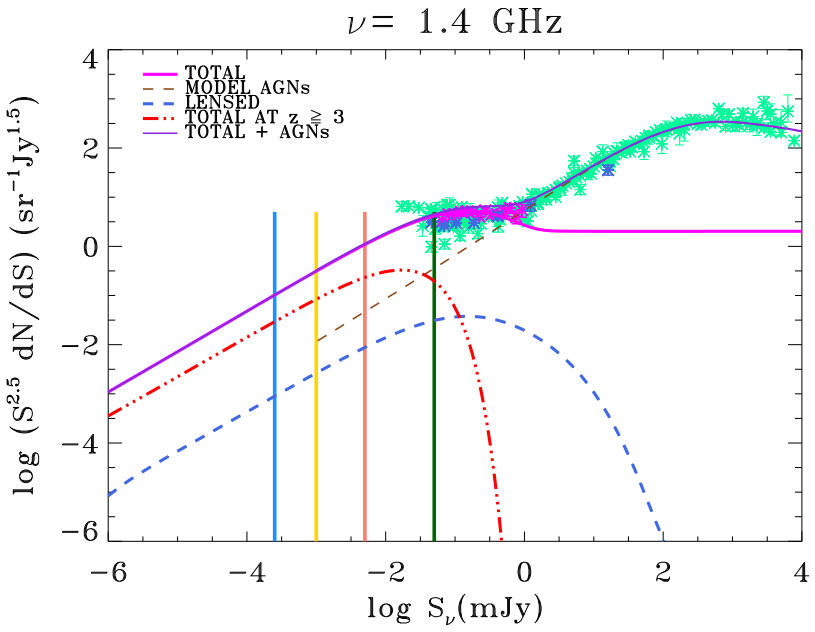

Figure 5.1 **Euclidean normalized differential number counts at 1.4 GHz:** they have been derived using our intrinsic (UV+FIR) SFR functions. Above ∼ 1 mJy the counts are dominated by canonical Radio Loud AGNs, while SF galaxies takes over at fainter fluxes. The dashed brown line shows the model for radio AGNs by Massardi et al. (2010). The triple dot-dashed red line shows the contribution of the sources that are located at z >3, while the blue dashed line represents the counts derived from strongly lensed SF galaxies. The solid magenta line shows the contribution of all SF galaxies, and the violet solid line is the total contribution (sum of all the components). The black polygon shows the ranges of 1.4 GHz counts consistent with the P(D) distributions by Vernstrom et al. (2014). The observational data are from the collection of de Zotti et al. (2010, green), from Bondi et al. (2008, magenta) and from the ECDFS of Padovani et al. (2015, blue) . The vertical lines represent, from left to right, the 5σ detection limits of the planned SKA1-MID surveys to unresolved sources: 0.25 μJy (blue), 1 μJy (yellow), 5μJy (pink). Given the resolution of these surveys ($\simeq$ 0.5″; Prandoni and Seymour, 2015) it is likely that a fraction of sources (especially bright, nearby galaxies) will be resolved out so that the surveys will not be 100% complete at the quoted limits. However, the array configuration proposed, which delivers an essentially flat point source sensitivity over a large range of synthesized beams, will overcome this problem. The 5 μJy limit applies also to the Tier 2 MIGHTEE survey (MeerKAT), while the dark green line shows the EMU (ASKAP) survey 5 σ limit. Again the limits refer to unresolved sources. The MIGHTEE and EMU surveys have a lower resolution than the SKA1-MID ones: 8.3″–3.5″ in the case of Tier 2 MIGHTEE (http://www.ast.uct.ac.za/arniston2011/vdheyden.pdf) and 10″ in the case of EMU (Norris et al., 2011).

5.1.2 Calibration of the relation between SFR and free-free emission

About the free-free emission, its relation with the SFR has been presented by Murphy et al. (2012): we have rewritten it as

$$L_{\rm ff} = 3.75 \times 10^{26} \left(\frac{\rm SFR}{M_\odot/{\rm yr}}\right) \left(\frac{T}{10^4\,{\rm K}}\right)^{0.3} {\rm g}(\nu, {\rm T})\, \exp\left(-\frac{h\nu}{k{\rm T}}\right) \tag{5.2}$$

where T is the temperature of the emitting plasma and g(ν, T) is the Gaunt factor for which we adopt the approximation of Draine (2011). It improves over earlier approximations, and looks like

$${\rm g}(\nu, {\rm T}) = \ln\left\{\exp\left[5.960 - \frac{\sqrt{3}}{\pi} \ln\left(Z_i \frac{\nu}{\rm GHz}\left(\frac{T}{10^4{\rm K}}\right)^{-1.5}\right)\right] + \exp(1)\right\}, \tag{5.3}$$

being Z_i the charge of ions and T their temperature. This equation reproduces the Murphy et al. (2012) calibration at the calibration frequency (33 GHz) for a pure hydrogen plasma ($Z_i = 1$) and $T = 10^4$ K. At the other frequencies relevant here the differences due to the different approximations for the Gaunt factor are small. We will adopt the above values of Z_i and T throughout the paper.

We have used eq. (5.2) to convert the redshift-dependent SFR functions to free-free luminosity functions. We then computed the counts of star-forming galaxies at 95 GHz, where an observational estimate has been obtained thanks to the SPT survey (Mocanu et al., 2013). In doing this we took into account that the measured flux densities include, in addition to the free-free emission, contributions from thermal dust and from the synchrotron emission (see Fig. 5.2).

To get down to any chosen frequency we used the SEDs for "warm" SF galaxies (those with a predominant component of warm dust, which are preferably located at z <0.4), and high-z SF galaxies (the typical cosmic Eyelash SED), adding the free-free and synchrotron emissions given by eqs. (5.2) and (5.1).

Our model independent counts at 95 GHz, turned out to be substantially below those estimated by Mocanu et al. (2013). To understand the origin of the discrepancy, we investigated further the approach used by these authors. They used the α_{220}^{150} spectral indices to classify their sources, taking $\alpha_{220}^{150} = 1.5$ as the boundary between dust-dominated galaxies ($\alpha_{220}^{150} > 1.5$) and radio-loud AGNs (synchrotron-dominated, in their terminology). They computed the probability that their posterior value for α_{220}^{150} was greater than the boundary value, and interpreted it as the probability for a source to be dust-dominated. The 95 GHz differential counts were calculated as the sum of the probabilities $P(\alpha_{220}^{150} > 1.5)$ that the sources in a given flux density ($S_{95{\rm GHz}}$) range are dusty. Since at 95 GHz the dusty galaxies are a small fraction of detected sources,

this approach may overestimate the counts because, due to the large uncertainties on α_{220}^{150}, many radio loud AGNs have a not-completely-zero probability of being dust-dominated. The sum of these low probabilities may give a count comparable to, or even larger than the count of the rare truly dusty galaxies.

We then checked the SEDs of all the galaxies in the catalogue with a 95 GHz flux brighter than 12.6 mJy (the 95% completeness limit of the survey). We collected the photometric data available in the NASA/IPAC Extragalactic Database (NED), in the Wide-field Infrared Survey Explorer (WISE; Wright et al., 2010) AllWISE[2] catalogue, in the Planck Catalogue of Compact Sources (Planck Collaboration XXVIII et al., 2014) and in the IRAS catalogue. We found that only 4 sources, all with $P(\alpha_{220}^{150} > 1.5) = 1$, show an SED typical of dusty galaxies. They are listed in Table 5.1 and their SEDs are shown in Fig. 5.2. A fifth source with $P(\alpha_{220}^{150} > 1.5) \simeq 1$, SJ043643 − 6204.4, is only 0.368 arcmin away from the very bright red giant Mira variable star R Doradus. Its SPT photometry may be then strongly contaminated by emission from dust shrouds that often form around this kind of stars. For this reason we have discarded this source.

For comparison, the Mocanu et al. (2013) approach yields $\simeq$ 12 dusty galaxies with $S_{95\mathrm{GHz}} \geq 12.6\,\mathrm{mJy}$. A substantial contribution to the difference with our result comes from sources with $P(\alpha_{220}^{150} > 1.5) \ll 1$. The re-assessed integral counts are shown in Fig. 5.4 (green asterisk), together with the value given by Mocanu et al. (2013) (magenta) for comparison. It is worth mentioning that 3 out of the 4 confirmed dusty galaxies have low frequency radio luminosity in excess of that expected from the mean relation between IR and 1.4 GHz luminosities. The difference is about twice the dispersion of the relation between the synchrotron luminosity and the SFR, yet within the range of values for star-forming galaxies according to Yun et al. (2001). It may thus be not statistically significant, especially taking into account a possible selection effect: the higher synchrotron luminosity helps bringing the sources above the detection limit at 95 GHz.

Galaxy	redshift	$S_{95\mathrm{GHz}}$ (mJy)
SJ041736-6246.8	0.00435	25.56
SJ041959-5456.2	0.005017	24.87
SJ044540-5914.7	0.00444	21.2
SJ213629-5433.4	0.002825	12.76

Table 5.1 Dusty galaxies in the Mocanu et al. (2013) 95 GHz sample.

The SEDs of all the other sources are consistent with the 95 GHz flux density being dominated by synchrotron emission and inconsistent with them being dusty galaxies. As illustrated by Fig. 5.3, this is the case also for the other 4 sources with $P(\alpha_{220}^{150} >$

[2] http://wise2.ipac.caltech.edu/docs/release/allwise/

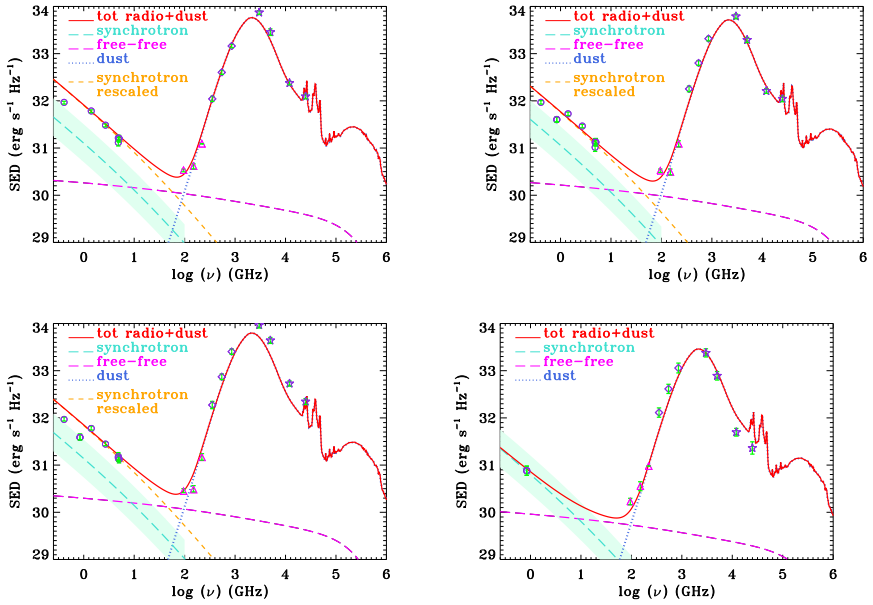

Figure 5.2 **SEDs of 95 GHz selected dusty galaxies in the SPT sample by Mocanu et al. (2013):** SPT-SJ041736-6246-8 (top left), SPT-SJ041959-5456-2 (top right), SPT-SJ044540-5914-7 (bottom left), SPT-SJ213629-5433-4 (bottom right). The red curve is a fit made by eye summing the Cai et al. (2013) SED of a cold late-type galaxy (dotted blue line), chosen because the 4 galaxies are all normal disc galaxies, with the free-free emission given by eq. (5.2) for the same SFR (long-dashed magenta line) and with the synchrotron emission matching the low frequency data. For three of the galaxies, such synchrotron emission (short-dashed orange line) is higher than that given by eq. (5.1), represented by the long-dashed green line. The difference is about twice the dispersion of the relation between the synchrotron luminosity and the SFR (shaded green band; see sub-sect. 5.1.1), yet within the range of values for star-forming galaxies according to Yun et al. (2001). It may thus be not statistically significant, especially taking into account a possible selection effect: the higher synchrotron luminosity helps bringing the sources above the detection limit at 95 GHz. However, we cannot rule out alternative explanations such as an additional contribution from a weak active nucleus or excess radio emission arising from radio continuum bridges and tidal tails not associated with star formation, similar to what is observed for so-called "taffy" galaxies (Condon et al., 2002; Murphy, 2013). Data points: low frequency radio flux densities from the NED (open circles); SPT flux densities (triangles); *Planck* flux densities (open diamonds); IRAS flux densities (open stars).

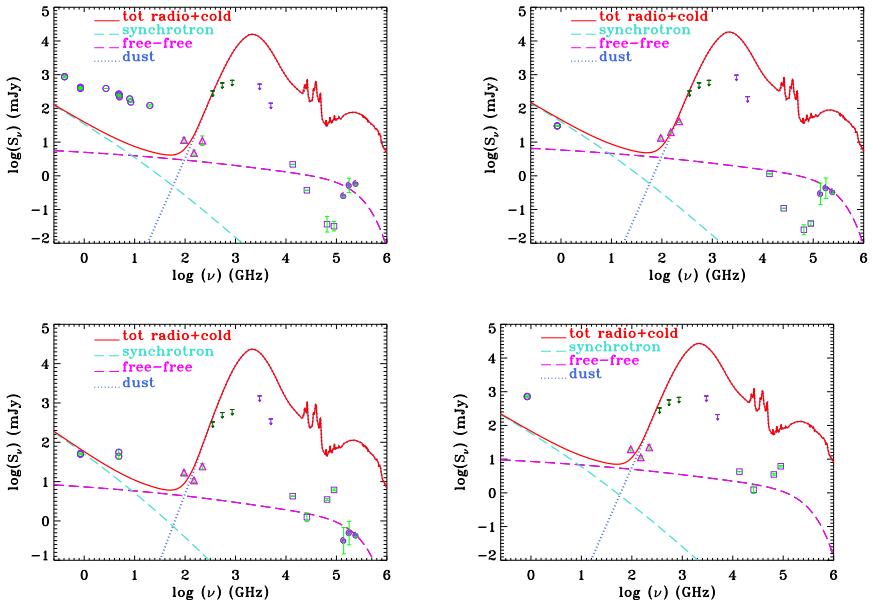

Figure 5.3 **SPT sources selected at 95 GHz that have** $1 > P(\alpha_{220}^{150} > 1.5) > 0.6$**:** SPT-SJ043651-5841-1 (top left), SPT-SJ203730-6513-3 (top right), SPT-SJ204101-5451-4 (bottom left), SPT-SJ213406-5334-3 (bottom right). Their SEDs are incompatible with those of star-forming galaxies, illustrated by the solid red line, and consistent with being radio sources. Data points: low frequency radio flux densities from the NED (open circles); SPT flux densities (triangles); WISE flux densities (open squares); 2MASS flux densities (spirals); in violet and dark green are IRAS and *Planck* upper limits, respectively. We have adopted as *Planck* upper limits the 90% completeness limits of the *Planck* Catalogue of Compact Sources (Planck Collaboration XXVIII et al., 2014) in the "extragalactic zone".

$1.5) > 0.6$, including the one with $P(\alpha_{220}^{150} > 1.5) = 0.91$. The radio-source nature of all objects with lower values of $P(\alpha_{220}^{150} > 1.5)$ is even clearer.

Figures 5.4 and 5.5 show that we obtain good agreement with the new determination of SPT counts of dusty galaxies at 95 GHz as well as with those by Mocanu et al. (2013) at 150 and 220 GHz. While the 95 GHz counts are dominated by nearby galaxies, those at the higher frequencies include a contribution from high-z strongly lensed galaxies; their contribution increases with decreasing flux density (in the ranges covered by the SPT surveys) to the point of becoming dominant at the SPT detection limits.

We also calculated predictions at 4.8, 8.4, 15 and 30 GHz (Fig. 5.6), that will be probably covered by the upcoming facilities. Not surprisingly, the free-free contribution becomes increasingly important at higher and higher frequencies. While at 1.4 GHz the dominant emission is synchrotron, at 8.4 GHz the free-free emission takes

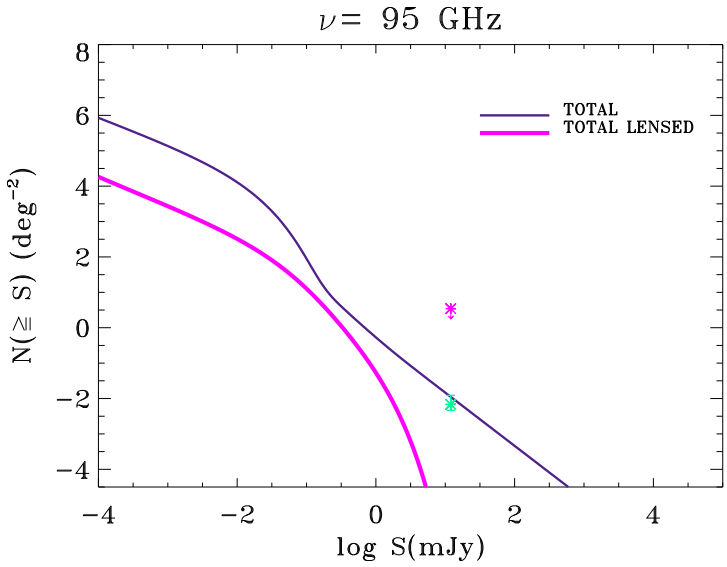

Figure 5.4 **Integral counts of dusty galaxies at ν=95 GHz (green asterisk with error bars):** they correspond to those remained after our analysis, and are compared with the predictions based on our model independent SFR functions. The magenta line show the contribution of the strongly lensed star forming galaxies, while the violet solid line represents the contribution of all SF galaxies. The former determination by Mocanu et al. (2013) is reported as magenta asterisk for comparison.

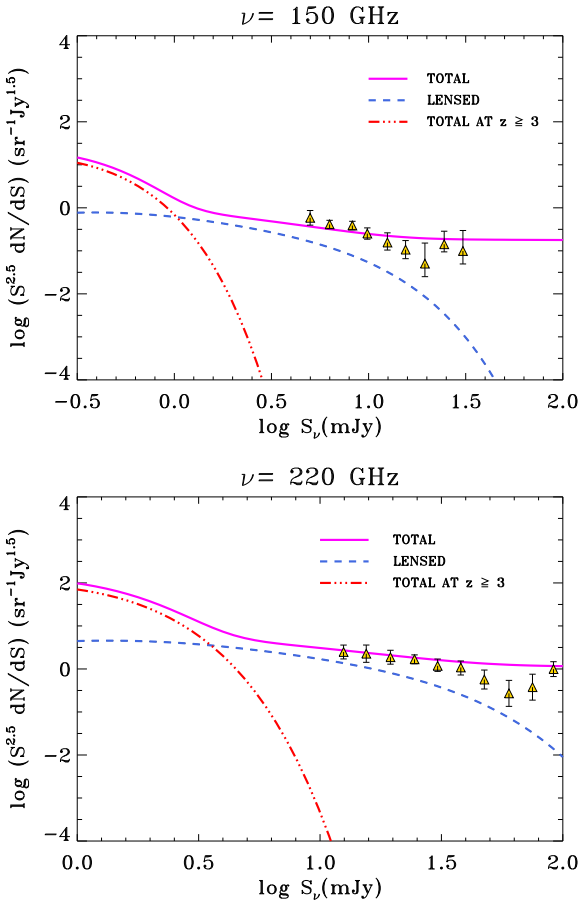

Figure 5.5 **Euclidean normalized differential counts of dusty galaxies at 150 and at 220 GHz (top and bottom panel, respectively):** the asterisks with error bars are the observational determinations by Mocanu et al. (2013). The solid magenta line represents all the SF galaxies, the triple dot-dashed red line shows the contribution of SF galaxies located at $z > 3$, and the blue dashed line represents the strongly lensed SF galaxies. Note that in the considered flux density ranges the counts of star-forming galaxies seen via their radio emission are made by nearby sources and have thus an Euclidean slope. On the contrary, counts of strongly lensed sources are due to strongly evolving high-z objects.

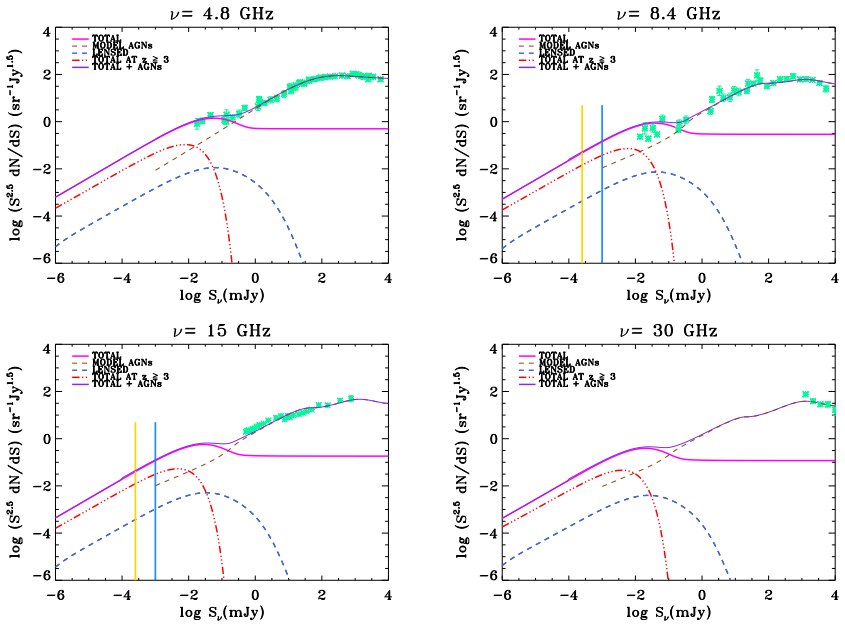

Figure 5.6 **Predicted versus observed counts at 4.8, 8.4, 15 and 30 GHz:** dusty galaxies come up at sub-mJy flux density levels and their counts are accounted for by the model independent approach. At higher flux densities the counts are dominated by canonical, AGN powered radio sources. The related models shown are from Massardi et al. (2010) at 1.4, and 4.8 GHz and from de Zotti et al. (2005) at 8.4 and 30 GHz. The various lines correspond to the contributions from the different source populations (dashed blue lines: strongly lensed galaxies; triple dot-dashed red lines: SF galaxies located at $z > 3$; dashed brown lines: radio-loud AGNs; solid magenta line: total SF galaxies; solid violet lines: total overall (SF galaxies + AGNs) objects). The solid vertical lines indicate the predicted flux density limits, for unresolved sources, of possible deep (yellow) and ultra-deep (blue) band 5 surveys with SKA1-MID.

over at sub-mJy levels.

5.2 Predictions for surveys with the Square Kilometer Array (SKA) and its precursors

The SKA and its precursors are going to revolutionize the future radio astronomy, making possible to reach flux limits never achieved before, and consequently to unbiasedly (with respect to dust extinction) probe the star formation process in galaxies up to high redshifts: in the following we give some predictions for such instruments, and try to give a glimpse of what could be the improvements for the galaxy evolution science.

5.2.1 Number counts and redshift distributions

The plans for SKA Phase 1 (SKA1-MID) will likely include three continuum surveys (in band 2), all at $\simeq$ 1–1.4 GHz: one over 1000 deg^2 with rms $\simeq$ 1 μJy/beam, a second one over 30 deg^2 with rms $\sim$ 0.2 μJy/beam, and a third over 1 deg^2 with rms $\sim$ 50 nJy/beam (Prandoni and Seymour, 2015). In addition there will possibly be a deep survey in band 5, at $\simeq$ 10 GHz, with rms $\simeq$ 0.3 μJy/beam over 1 deg^2, and an ultra-deep survey again in band 5, at $\simeq$ 10 GHz with rms $\simeq$ 0.03 μJy/beam over $\simeq$ 30 arcmin^2 (see also Murphy et al., 2015).

Deep surveys are also planned with the SKA precursors, like the Australian SKA Pathfinder (ASKAP) and the South African MeerKAT (Norris et al., 2013). The Evolutionary Map of the Universe (EMU) is a project that will use ASKAP to make a deep (5σ limit of 50 μJy beam^{-1}) radio continuum survey of the entire southern sky, extending as far north as +30°, i.e. covering about 30,000 deg^2 at $\sim$1.4 GHz. The MeerKAT International GigaHertz Tiered Extragalactic Exploration (MIGHTEE) Tier 2 will exploit the MeerKAT Phase 2 to observe over 35 deg^2 down to a 5σ limit of 5 μJy beam^{-1}, again at $\sim$ 1.4 GHz.

The SKA1-MID, EMU and MIGHTEE 5σ flux density limits for unresolved sources are indicated by vertical lines in Fig. 5.1. The contributions of the dusty SF galaxies are shown by the different lines: in particular the red triple dot-dashed line represents SF galaxies at $z > 3$, while the blue dashed one shows the contribution of strongly lensed sources. The "bump" at tens of μJy's is preferentially due to $z < 3$ galaxies , while the galaxies at higher z become increasingly important at lower flux densities, down to a few hundred nJy's.

The predicted redshift distributions for surveys at the flux density limits mentioned above are shown in Figs. 5.7 and 5.8. The surface density of galaxies at $z \geq 6$ increases rapidly with decreasing flux density. This means that such surveys will be able to detect a non negligible amount of galaxies up to high redshifts. This will also allow us to get a glimpse of the cosmic SFR across the re-ionization epoch, overcoming limitations by dust extinction.

As illustrated by Fig. 5.8, the planned band 5 surveys will also reach very high redshifts (see also Murphy et al., 2015). Dust emission is likely under-abundant in most galaxies at $z > 6$ (Munoz and Loeb, 2011; Cai et al., 2014; Capak et al., 2015): this is due to the small Age of the Universe, that does not allow to have substantial dust enrichment in the interstellar medium of the galaxies. Some detections of galaxies with high SFRs and substantial dust extinction have, in any case, been reported (Riechers et al., 2013; Watson et al., 2015), and we added them in Fig.3.2: they are single detections, so they are not that much significant from a statistical point of view. The SKA1-MID data will help in populating such redshifts regions, being unbiased with

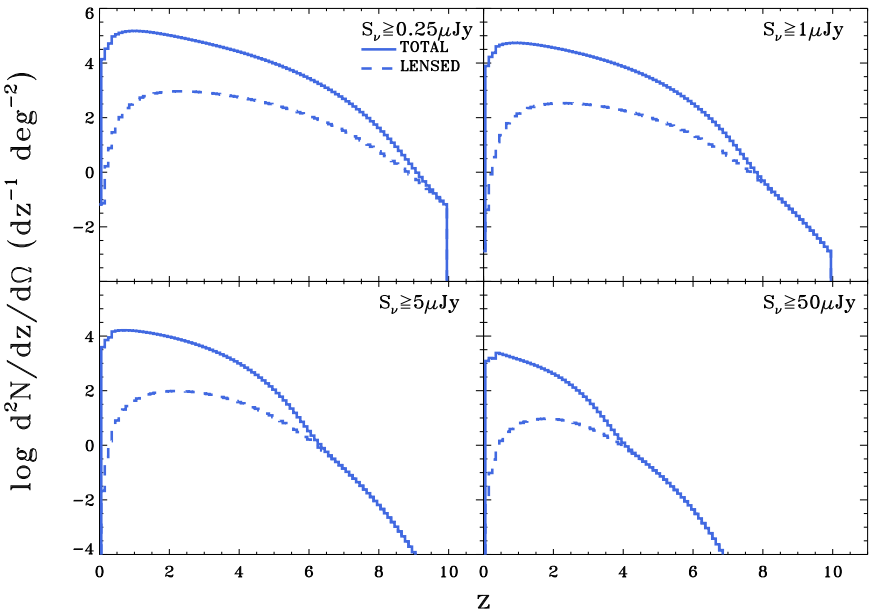

Figure 5.7 **Predicted redshift distributions at the** $5\,\sigma$ **detection limits of the deepest SKA1-MID, of the MIGHTEE (MeerKAT) and of the EMU (ASKAP) 1.4 GHz surveys (see text):** the lines show the contributions of the total population of SF galaxies (blue solid) and of the strongly lensed SF galaxies (blue dashed).

respect to the dust, thus providing a more complete view of the SFR functions at high z.

Figures 5.7 and 5.8 also show that a substantial fraction of the highest redshift galaxies that should be detected by the foreseen surveys are strongly lensed (magnification $\mu \geq 2$) galaxies. The strongly lensed fraction at high z increases with increasing flux density limit, while the total counts rapidly decrease.

5.2.2 Comparison between Herschel and SKA facilities

We want to point out how the upcoming radio facilities will be able to improve our knowledge about SFRFs at high-z, so in Fig. 5.9 we compare the SKA1-MID potential in measuring the evolution of the cosmic SFR to the results of *Herschel* and of the deepest UV and Hα surveys. The planned SKA1-MID surveys can detect galaxies with SFRs ranging from less than one $M_\odot$/yr for $z \lesssim 1$ to less than hundred $M_\odot$/yr for $z \lesssim 7$. This is an improvement by more than two orders of magnitude compared to *Herschel* results and will allow us to determine the dust-enshrouded star formation history up to much higher redshifts. The deepest rest frame UV surveys do better, but only for dust-free galaxies.

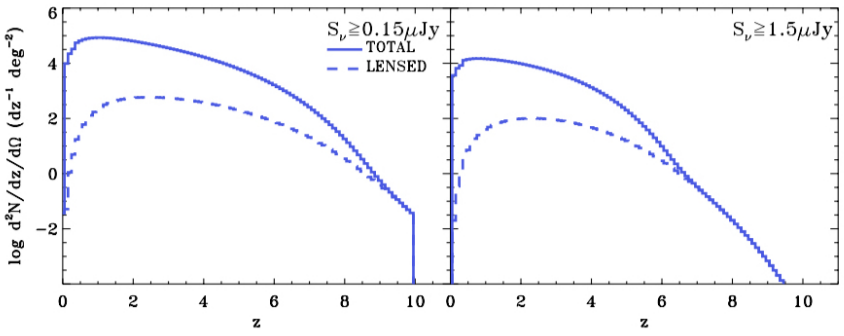

Figure 5.8 **Predicted redshift distributions at the 5σ detection limits of SKA1-MID 10 GHz surveys (see text):** the lines show the contributions of the total population of SF galaxies (blue solid) and of the strongly lensed SF galaxies (blue dashed).

5.3 Synergies with optical/near-IR surveys.

Also the radio detection of galaxies has some caveats in helping populating the bright end of the SFR function: in fact a full scientific exploitation of the data provided by the SKA surveys requires redshift determinations of the detected galaxies, especially of the most distant ones which carry information on the earliest stages of galaxy formation.

We then need to exploit some synergies with other instruments, capable to provide many observations to satisfactorily recover the SED of the single galaxy, and obtain in this way its photometric redshift. Several deep optical/near-IR imaging surveys covering substantial sky areas are ongoing or foreseen.

In Fig. 5.10 we show the minimum SFR of a dust-obscured galaxy detectable by the deepest SKA1-MID survey as a function of redshift (its SED is shown in the bottom panel of Fig. **??**), and compare it with those detectable by the following surveys:

- The *Euclid* deep survey covering an area of 40 deg^2 distributed over two fields close to the North and South ecliptic poles to 5σ magnitude limits for point source detection of 26 mag in the Y, H and J bands and of 27.5 mag in the VIS (Laureijs et al., 2014).

- The Subaru Hyper Suprime-Cam (HSC) ultra-deep survey[3] (Miyazaki et al., 2012) covering two fields of 1.8 deg^2 each to 5σ point source AB magnitude limits of g = 28.1, r = 27.7, i = 27.4, z = 26.8 and y = 26.3.

- The 4 Large Synoptic Survey Telescope (LSST; Ivezic et al., 2008) deep drilling fields of 9.6 deg^2 each, aimed at reaching 5σ point source AB magnitude limits

[3] www.subarutelescope.org/Projects/HSC/surveyplan.html

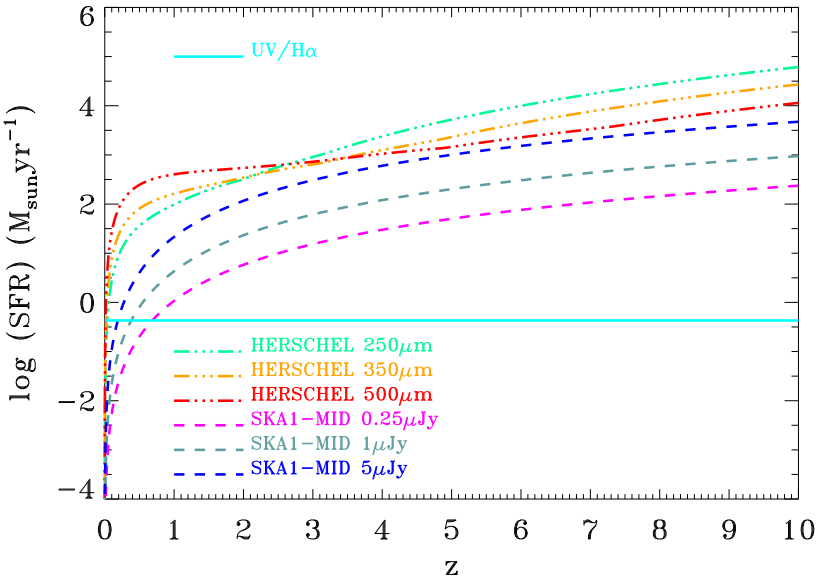

Figure 5.9 **Minimum SFR detectable by SKA1-MID surveys 1.4 GHz:** they have been computed down to 0.25 μJy (dashed magenta line), 1 μJy (dashed bottle green line) and 5 μJy (dashed blue line), as a function of z, compared with the minimum SFR detected by *Herschel*/SPIRE surveys, basically down to the confusion limits (dashed-dot-dot-dot lines, green for 250 μm, orange for 350 μm and red for 500 μm) and by UV/Hα surveys (horizontal cyan line). The latter line corresponds to the average minimum absolute magnitude reached by the deepest surveys, that turns out to be almost independent of redshift. Note that, while very deep in terms of SFR, the UV/Hα surveys miss the dust-enshrouded star formation.

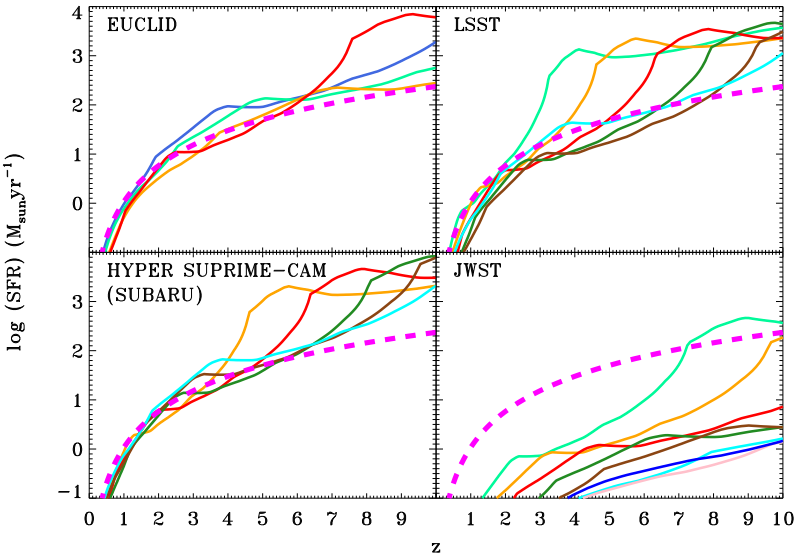

Figure 5.10 **Minimum SFR detectable by SKA1-MID vs other instruments:** we show the minimum SFR detectable by the deepest SKA1-MID survey at 1.4 GHz (down to 0.25 μJy, dashed magenta line), compared with the minimum SFR detectable in each spectral band by the *Euclid* deep survey, by the Subaru HSC ultra-deep survey, by the LSST deep drilling fields and by the JWST DWS for the obscured SED shown in the bottom panel of Fig. 5.11.

of 28 mag in the u, g, r, i and z bands and of 26.8 in the y band (see Sect. 9.8 of the LSST Science Book[4]).

- The Deep-Wide Survey (DWS; Windhorst et al., 2009) to be carried out with NIRCam on the James Webb Space Telescope (JWST). The DWS will image the sky with up to 8 filters. A severe limitation to the exploitation of the SKA1-MID/DWS synergy is the smallness of the DWS area, 100 arcmin^2, i.e. a factor of $1/36 \simeq 0.028$ smaller than the area of the deepest SKA1-MID survey (1 deg^2). We expect that the SKA1-MID will detect, within the DWS area, $\simeq 6,200$ galaxies at $z \leq 6$ but only $\simeq 14$ at $z \geq 6$.

The depth of the 4 LSST deep drilling fields is enough to detect all SKA1-MID dust-obscured galaxies in at least 3 bands up to $z \simeq 6$ and in at least one band up to $z \simeq 8$. Thus, photometric redshift estimates can be obtained up to $z \simeq 6$. With the obvious exception of the JWST/DWS the other surveys are somewhat less useful. In the case of the UV–bright SED (top panel of Fig. 5.11) all galaxies detected by the deepest SKA1-

[4] www.lsst.org/files/docs/sciencebook/SH_whole.pdf

MID survey are easily detected by the above optical/near-IR surveys in all bands, so that accurate photometric redshift estimates can be obtained. Since, as argued above, strong dust obscuration appears to affect only a minority of faint $z \geq 6$ galaxies, it may be expected that photometric redshift estimates will be missing only for a small fraction of SKA1-MID high-z galaxies.

Apart from the fact that the SFR inferred from SKA data are not affected by dust extinction, even in the case of no obscuration the SKA measurements are complementary to the optical/near-IR ones. In fact, while the rest frame UV emission measures the instantaneous SFR, the synchrotron emission measures the SFR $\sim 10^7$ yr earlier. Thus, in the absence of dust obscuration, the comparison of the SFR inferred from (rest-frame) UV photometry with that from low-frequency radio data, dominated by synchrotron, yields a measure of the starburst age (Clemens et al., 2008). Starbursts younger than $\sim 10^7$ yr have a synchrotron emission decreasing with the starburst age, so that the inferred SFR is lower and lower than that inferred from UV data. By the same token, the comparison of SFRs derived from UV and low-frequency radio measurements is informative on variations of the SFR on timescales of $\sim 10^7$ yr. Note that this comparison could not work at very high redshifts where the synchrotron emission may be highly suppressed due to the strong inverse Compton losses off the CMB (see sub-sect. 5.1.1 and Norris et al., 2013; Carilli et al., 2008; Murphy, 2009), so that even at relatively low frequencies the radio emission may not be synchrotron dominated.

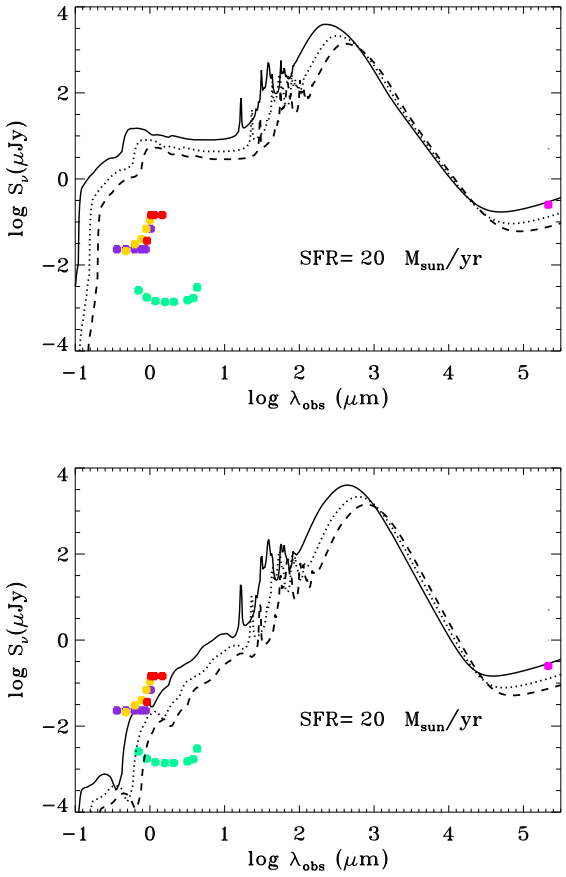

Figure 5.11 **Multiwavelength surveys detection limits on a UV bright SED (top panel) and on a dusty SED (bottom panel):** we show the detection limits of deep optical/near-IR surveys (left) and of the deepest SKA1-MID survey (magenta symbol on the right) compared with the spectral energy distribution of an UV-bright young galaxy with a SFR $= 20\,M_\odot\,\mathrm{yr}^{-1}$ at $z = 2$ (solid), 4 (dotted) and 6 (dashed). We have considered the following surveys (from top to bottom): *Euclid* deep (red), Subaru HSC ultra-deep (yellow), LSST deep drilling fields (violet) and JWST (green). The SED was computed using the GRASIL package (Silva et al., 1998) for a Chabrier (2003) Initial Mass Function (IMF), a galaxy age of 10 Myr and a metallicity of $0.1\,Z_\odot$. In the bottom panel we show the same as the top panel but for an obscured SED with the same IMF and SFR, a galactic age of 1 Gyr and a metallicity of $3\,Z_\odot$.

Chapter 6

The Main Sequence of star-forming galaxies

As already mentioned in the Introduction (see Chapter 1), the masses of star-forming galaxies seem to be strongly correlated with their SFR, following an almost linear relationship: here we give an estimation and analysis of such relationship, together with a novel interpretation that turns out to be in agreement with the *in − situ* star formation scenario.

Our analysis relies on two basic ingredients: the model-independent determination of the SFR functions at different redshifts, and the time dependence of the star formation rate within high-redshift star-forming galaxies, as inferred from observations and supported by simple physical arguments. The former has been presented in Chapter 3, we now describe the latter.

6.1 Star formation history

We now focus on the star formation history $\dot{M}_\star(\tau|M_\star, t)$; this quantity represents the behavior of the SFR ψ as a function of the internal galactic age τ (i.e., the time since the beginning of significant star formation) for a galaxy with stellar mass $M_\star$ at cosmological time t (corresponding to redshift z). We base on the indications emerging from many studies of SED-modeling for high $z \gtrsim 2$ star-forming galaxies (e.g. Papovich et al., 2011; Smit et al., 2012; Moustakas et al., 2013; Steinhardt et al., 2014; Citro et al., 2016; Cassará et al., 2016); these suggest a slow power law increase of the SFR ψ over a timescale τ_b, then followed by an exponential decline with timescale τ_SFR; in the literature a similar time evolution is sometimes referred to as 'delayed exponential

model' (see Lee et al., 2009). Such an overall behavior can be described as follows

$$\begin{aligned} \psi(\tau|M_\star, t) &= \dot{M}_{\star,\mathrm{b}}\,(\tau/\tau_\mathrm{b})^\kappa \quad 0 \le \tau \le \tau_\mathrm{b} \\ &= \dot{M}_{\star,\mathrm{b}}\,e^{-(\tau-\tau_\mathrm{b})/\tau_\mathrm{SFR}} \quad \tau \ge \tau_\mathrm{b} \end{aligned} \tag{6.1}$$

with $\kappa \approx 0.5$; the value of the SFR $\dot{M}_{\star,\mathrm{b}}$ at τ_b is easily related to the final stellar mass $M_\star$ by the relation $\dot{M}_{\star,\mathrm{b}} = M_\star\,[\tau_\mathrm{b}/(\kappa+1) + \tau_\mathrm{SFR}]^{-1}$.

As to the parameters involved in the above expressions, recent observations by *ALMA* have undoubtedly confirmed that the SFR in massive high-redshift galaxies must have proceeded over a timescale around $\tau_\mathrm{b} \lesssim 0.5 - 1$ Gyr at very high rates $\psi \gtrsim$ a few $10^2\,M_\odot\ \mathrm{yr}^{-1}$ under heavily dust-enshrouded conditions (e.g. Scoville et al., 2014, 2016).

A duration of the main star formation episode $\tau_\mathrm{b} \lesssim 0.5 - 1$ Gyr in massive high-redshift galaxies, which are thought to be the progenitors of local ellipticals, is indeed confirmed by observations of the $\alpha-$enhancement, i.e., iron underabundance compared to α elements. This occurs because star formation is stopped, presumably by AGN feedback, before type I*a* SN explosions can pollute the interstellar medium with substantial iron amounts (e.g. Thomas et al., 2005; Gallazzi et al., 2006; Renzini, 2006, for a review). Contrariwise, in low-mass galaxies with $M_\star \lesssim 10^{10}\,M_\odot$ longstanding data on stellar population and chemical abundances indicate that star formation has proceeded for longer times, regulated by type II SN feedback and galactic fountains (see reviews by Conroy, 2013; Courteau et al., 2014).

On this basis, following Aversa et al. (2015) we adopt a timescale for the duration of the main star-formation episode given by

$$\tau_\mathrm{b} = 1\,\mathrm{Gyr}\left(\frac{1+z}{3.5}\right)^{-3/2}\left[1 + 2\,\mathrm{erfc}\left(\frac{4}{3}\,\log\frac{\psi}{5\,M_\odot\ \mathrm{yr}^{-1}}\right)\right]. \tag{6.2}$$

The dependence on the cosmic time mirrors that of the dynamical time $t_c \propto 1/\sqrt{G\rho} \propto (1+z)^{-3/2}$, in turn reflecting the increase of the average density $\rho \propto (1+z)^3$ in the ambient medium. In addition, the erfc[1]-smoothing connects continuously the behavior for bright and faint objects expected from the discussion above; we have tested that our results are insensitive to the detailed shape of the smoothing function.

As to the quenching timescale τ_SFR, as confirmed by many works, the observed fraction of FIR-detected host galaxies in X-ray, (e.g. Mullaney et al., 2012b; Page et al., 2012; Rosario et al., 2012), and optically selected AGNs (e.g. Mor et al., 2012; Wang

[1] complementary error function: $\mathrm{erfc} = \frac{2}{\pi}\int_x^\infty e^{-t^2}\,\mathrm{d}t$

et al., 2013c; Willott et al., 2015) points toward an SFR abruptly shutting off, at least in massive galaxies, after $\tau_{\rm b}$ over a short timescale $\tau_{\rm SFR} \lesssim 10^8$ yr due to the action of AGN feedback. This little lifetime is derived by the chemistry inside the galaxies, that must not live longer that $\sim$1 Gyr in order to show the α-enhancement that is observed.

In Fig. 6.1 we show the ensuing star formation and BH accretion histories as a function of the galactic age. We test the adopted star formation history and timescales by connecting the SFR functions to the stellar mass function via the continuity equation.

In the absence of merging terms, the continuity equation can be written as

$$\frac{{\rm d}N}{{\rm d}\log\psi}(\psi,t) = \int {\rm d}\log M_\star \; \partial_t \left[\frac{{\rm d}N}{{\rm d}\log M_\star}(M_\star,t)\right] \frac{{\rm d}\tau}{{\rm d}\log\psi}(\psi|M_\star,t) \; ; \qquad (6.3)$$

here the term on the left hand side (l.h.s.) is the (known) SFR function, while under the integral on the right hand side (r.h.s.) the first term is the cosmic time derivative of the (unknown) stellar mass function, and the second is the time spent by a galaxy in a bin of SFR obtained from the star formation history after Eq. (6.1). We solve the continuity equation to derive the stellar mass function along the lines discussed by Aversa et al. (2015) and Mancuso et al. (2016). In Fig. 6.2 we compare the resulting stellar mass function to the recent observational data at various redshifts, finding an excellent agreement.

This result further substantiates our star formation history and timescales, and, can be interpreted as an evidence in favor of an in situ coevolution scenario of galaxy formation (e.g. Granato et al., 2004; Lapi et al., 2006, 2011, 2014; Lilly et al., 2013; Aversa et al., 2015). This envisages star formation in galaxies to be mainly a local process regulated by energy feedback from SNe and from the central supermassive BH. In the first stages of galaxy evolution the BH is still rather small and the nuclear luminosity is much less than that associated with the star formation in the host. The SFR is then regulated by feedback from SN explosions and slightly increases with time, while the AGN luminosity rises exponentially. After a fraction of Gyr in massive galaxies the nuclear luminosity becomes dominant, blowing away most of the gas and dust from the ambient medium and hence quenching abruptly the star formation in the host. Thereafter the stellar populations evolve passively and the galaxy becomes a 'red and dead' early-type.

We note that adopting a conceivable scatter 0.15 dex around the average star formation timescale changes only marginally the mass function at the high mass end. On the other hand, basing on the (dust-corrected) UV-inferred SFR function leads to strongly underpredict the high mass end of the stellar mass function; this just reflects the undersampling of galaxies with high SFRs by UV data (cf. Figs. 3.1,3.2).

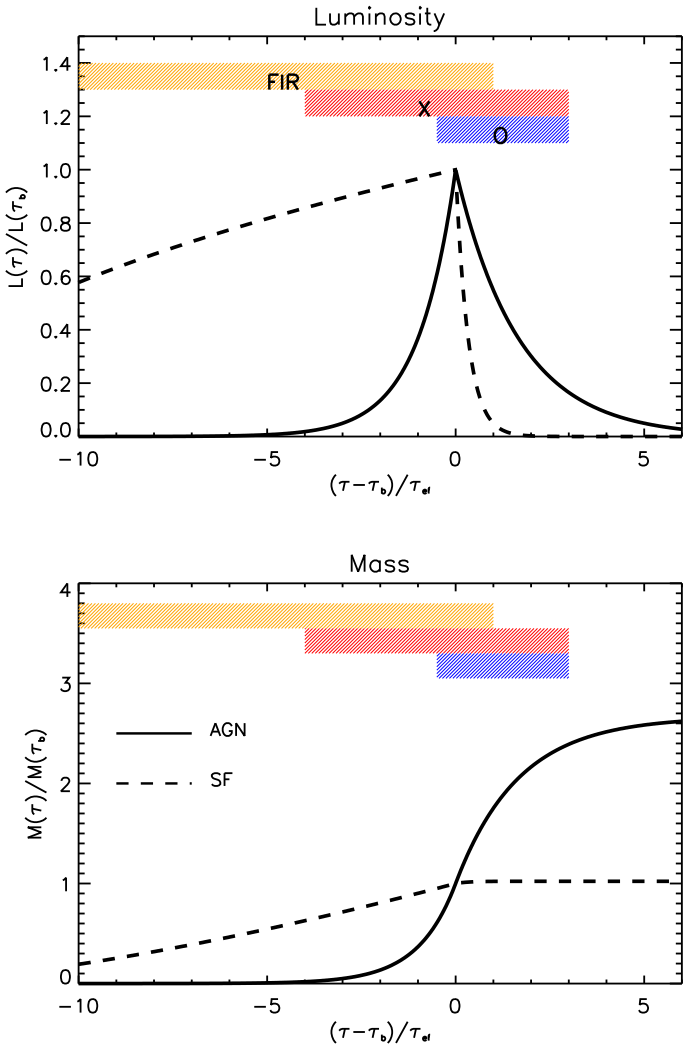

Figure 6.1 **Evolution with galactic age (in units of BH e−folding time $\tau_{\rm ef}$) of the luminosity (top panel) and mass (bottom panel):** they have been normalized at the time $\tau_{\rm b}$ when the AGN luminosity peaks and the star formation is quenched by the AGN feedback. Solid lines refer to AGN-related quantities and dashed lines to star formation-related quantities. The orange area sketches the stage when the star-forming galaxy is dust-enshrouded and appears as a far-IR bright source; the red area sketches the stage when the AGN X-ray (intrinsic) luminosity overwhelms that associated to star formation; the blue area sketches the optical phase, setting in when the quasar feedback removes gas and dust from the medium and quenches star formation in the host.

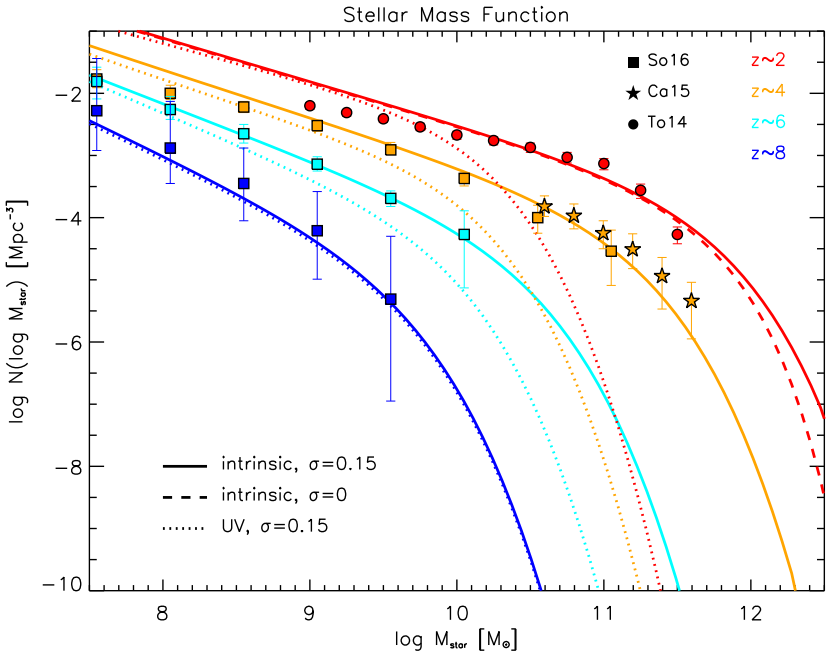

Figure 6.2 **The stellar mass function of star-forming galaxies with σ=0.15:** it has been computed at $z = 2$ (red), 4 (orange), 6 (cyan), and 8 (blue) as derived from the SFR functions and from the star formation timescale τ_b (cf. Eq. 6.2) via the continuity equation (cf. Eq. 6.3). Solid lines refer to the global (UV+far-IR) SFR functions with a scatter $\sigma = 0.15$ dex in the star-formation timescale τ_b, dashed line (only at $z = 2$ for clarity) refers to zero scatter, and dotted lines to the (dust-corrected) UV-inferred SFR functions. Data are from Tomczak et al. (2014; circles), Caputi et al. (2015; stars) and Song et al. (2016; squares).

6.2 Interpreting the galaxy main sequence

Given the ingredients above, we populate the SFR vs. $M_\star$ diagram as follows. The number of galaxies per logarithmic bins of SFR and stellar mass is given by

$$\frac{\mathrm{d}^2 N}{\mathrm{d}\log\psi\,\mathrm{d}\log M_\star} \simeq \frac{\mathrm{d}N}{\mathrm{d}\log\psi}\,\frac{\mathrm{d}\delta}{\mathrm{d}\log M_\star}\;; \tag{6.4}$$

this expression is actually an excellent approximation holding when the star formation $\psi(\tau) \propto \tau^\kappa$ increases slowly with the galaxy lifetime, and specifically milder than $\kappa \lesssim 1$; we recall that here $\kappa \approx 0.5$ is fiducially adopted on the basis of observations (cf. Sect. 6.1). In the above expression the factors on the r.h.s. are the SFR functions (cf. Chapter 3) and the relative time δ spent by the star-forming galaxy in a given logarithmic bin of $M_\star$; according to the star formation history (Eq. 6.1) the latter just reads

$$\frac{\mathrm{d}\delta}{\mathrm{d}\log M_\star} = \frac{M_\star}{\psi}\,\frac{1}{\tau_\mathrm{b} + \xi\,\tau_\mathrm{SFR}}\,\ln 10\;. \tag{6.5}$$

Here the total duration of the star formation period is taken as $\tau_\mathrm{b} + \xi\,\tau_\mathrm{SFR}$ with $\xi \approx 3$, since after that time the stellar luminosity is already decreased by a factor $e^{-\xi} \lesssim 0.05$ and the stellar mass has already attained its final value to a very good approximation; anyway, variations of this parameter do not affect appreciably our results.

The SFR vs. $M_\star$ diagram at the representative redshift $z \approx 2$ is presented in Fig. 6.3, where the color-code indicates the logarithmic number density of galaxies per unit comoving volume (in Mpc^{-3}) after Eq. (6.4). The lilac line with errorbars illustrates the number density-weighted mean relationship $\langle\psi\rangle$ at given $M_\star$ with its 2σ variance; this is the so called 'main sequence' of star-forming galaxies. We stress that averaging over the SFR function weighted by the relative time spent at given $M_\star$ is equivalent to perform a mass selection. In this respect, our outcome well compares with the observational determinations based on statistics of large multiwavelength (UV+IR), mass-selected samples by Rodighiero et al. (2011, 2014) and by Speagle et al. (2014).

We remark that the main sequence originates naturally in our approach as a statistical locus in the SFR vs. $M_\star$ plane. However, this by no means implies that an individual galaxy climbs along the main sequence during its lifetime. Typical evolutionary tracks followed by individual objects, as inspired by the in situ coevolution scenario (cf. Sect. 6.1), are illustrated by dotted lines; their shape is dictated by the slowly increasing SFR $\psi \propto \tau^{1/2}$ and appreciably rising stellar mass $M_\star \propto \tau^{3/2}$, which imply $\psi \propto M_\star^{1/3}$. Then the main sequence with its associated variance correspond to the portions of such tracks where galaxies spend most of their lifetime in logarithmic bins of $M_\star$ (see Eq. 6.5).

To highlight the relevance of observational selections different from the one based

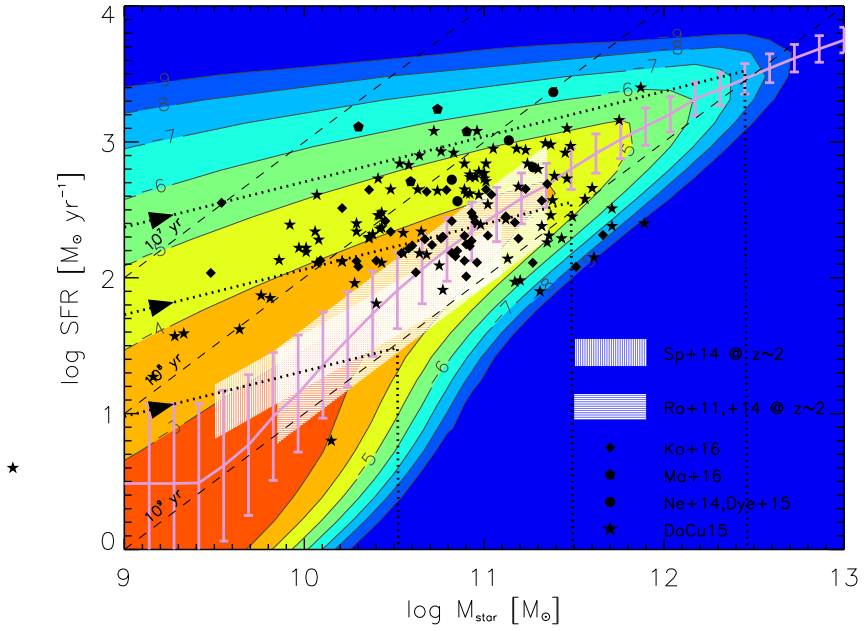

Figure 6.3 **The main sequence of star-forming galaxies at $z\approx$ 2 based on the intrinsic (UV+far-IR) SFR functions:** colored contours illustrate the number density of galaxies (labels are in log units of Mpc^{-3}) in the SFR vs. $M_\star$ plane. The lilac line with errorbars illustrates the mean relationship with its 2σ scatter. The dotted lines show three evolutionary tracks (forward time direction indicated by arrows) for galaxies with a given final stellar mass of about $10^{10.5}$, $10^{11.5}$, $10^{12.5}$ $M_\odot$. The dashed lines show the timescale $M_\star/\psi$ = 10^7, 10^8 and 10^9 yr as labeled. The white shaded areas are the observational determinations of the main sequence (based on statistics of large samples) by Rodighiero et al. (2011, 2014, horizontal line pattern), and by Speagle et al. (2014, vertical line pattern). Filled black symbols (error bars omitted for clarity) refer to far-IR data for individual objects by Koprowski et al. (2016, diamonds), Ma et al. (2015b, pentagons), Negrello et al. (2014) plus Dye et al. (2015, circles), and da Cunha et al. (2015, stars).

on stellar mass, in Fig. 6.3 we also report data points for individual, far-IR selected galaxies by Koprowski et al. (2016), Ma et al. (2015b), Negrello et al. (2014) plus Dye et al. (2015), and da Cunha et al. (2015) mainly at redshifts $1 \lesssim z \lesssim 3$. We note that the observations by Koprowski et al. are drawn from a *SCUBA2* survey area of 10^2 arcmin^2, while the other data are extracted from *Herschel* survey areas of 10^2 deg^2; as a consequence, the former sample can probe galaxies with SFRs of few $10^2\ M_\odot\ \mathrm{yr}^{-1}$ at most, while the latter samples can probe galaxies with more extreme SFR values up to few $10^3\ M_\odot\ \mathrm{yr}^{-1}$, whose number density is substantially lower. On the other hand, all these far-IR samples are limited by instrumental sensitivity to a minimum SFR around $10^2\ M_\odot\ \mathrm{yr}^{-1}$.

It is remarkable that an appreciable fraction of these individual, far-IR selected galaxies lie above the main sequence, i.e., at SFR values higher than expected on the basis of the average relationship at given $M_\star$. A common interpretation of these off main-sequence objects is that they are undergoing an episode of starburst triggered by a stochastic merger event. Although these instances may well occur especially at low redshift $z \lesssim 1$, our interpretation for the bulk of the objects at higher redshift $z \gtrsim 1$ differs substantially. On the basis of the evolutionary track of individual galaxies, we envisage off main sequence objects to be caught in an early evolutionary stage, and still accumulating their stellar mass. Since the SFR changes slowly during the evolution, far-IR selection is unbiased with respect to the stellar mass; thus young star-forming galaxies are found to be preferentially located above the main sequence, or better, to the left of it. As time goes by and stellar mass increases, the galaxy moves toward the average main sequence relationship, around which it will spend most of its lifetime. Afterwards, the SFR either slowly decreases because of gas exhaustion for galaxies with small final stellar mass, or is abruptly quenched by AGN feedback for galaxies with high final stellar mass. In particular, in the latter case the galaxy will then evolve passively to become a local early-type and will populate a region of the SFR vs. $M_\star$ diagram substantially below the main sequence. These loci of 'red and dead' galaxies are indeed observed locally (see Renzini and Peng, 2015), and start to be pinpointed even at high redshift (see Man et al., 2016).

Support to such an evolutionary picture comes from the estimates of the galaxy ages inferred from multiwavelength SED modeling by da Cunha et al. (2015) and Ma et al. (2015b). In Fig. 6.4 we report the data points from the latter authors, with the galaxy age highlighted in different colors. It can be seen that galaxies at $z \sim 2$ (data points with black contours) located above the main sequence are preferentially younger and less massive, with ages substantially below a few 10^8 yr; the ones more distant from the main sequence locus feature smaller and smaller ages.

In Fig. 6.5 we highlight that exploiting in Eq. (6.4) the UV-inferred SFR functions (dust corrected via the UV slope) originate a main sequence diagram in strong dis-

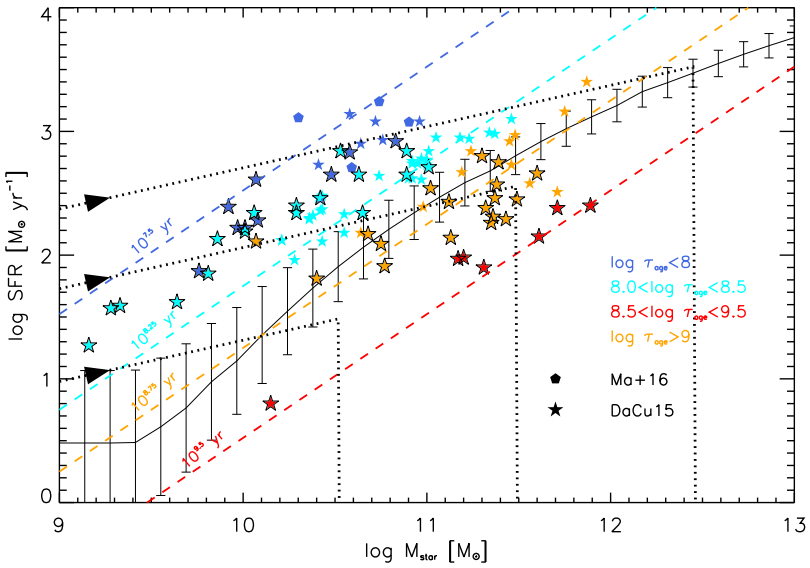

Figure 6.4 **The evolution in time of the main sequence of star-forming galaxies at $z \approx 2$, based on the intrinsic (UV+far-IR) SFR functions:** the solid line with errorbars illustrates the mean relationships with its 2σ scatter. The dotted lines show three evolutionary tracks (forward time direction indicated by arrows) for galaxies with a given final stellar mass of about $10^{10.5}$, $10^{11.5}$, $10^{12.5}$ $M_\odot$. The dashed lines shows the timescale $M_\star/\psi = 10^{7.5}$, $10^{8.25}$, $10^{8.75}$, and $10^{9.5}$ yr as labeled. Filled symbols (error bars omitted for clarity) refer to far-IR data for individual objects by Ma et al. (2015b; pentagons) and da Cunha et al. (2015, stars), color-coded according to the SED-inferred age $\tau_{\rm age}$ in bins $\tau_{\rm age} \lesssim 10^8$ (blue), $10^8 \lesssim \tau_{\rm age} \lesssim 10^{8.5}$ (cyan), $10^{8.5} \lesssim \tau_{\rm age} \lesssim 10^9$ (orange), and $\tau_{\rm age} \gtrsim 10^9$ (red). Data points for galaxies at $1 \lesssim z \lesssim 3$ are highlighted by a black contour.

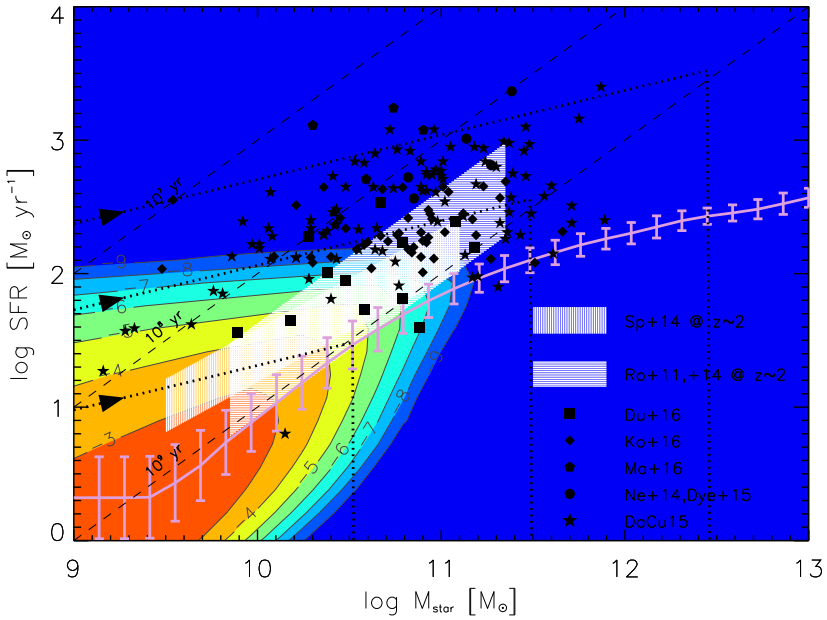

Figure 6.5 **The main sequence of star-forming galaxies at $z\approx$ 2 based on the (dust-corrected) UV-inferred SFR function.**

agreement with the observations at high SFRs and/or stellar masses, because the SFR and stellar mass functions are considerably undersampled in the UV, especially at the high SFR/stellar mass end.

In Fig. 6.6 we confront the outcome of our computation for the average main sequence of star-forming galaxies at different redshifts $z \sim 1$, 3, and 6 to the observational determinations by Speagle et al. (2014), finding good agreement. For comparison, the data points from individual observations presented in the previous Figures are also reported, with their estimated redshift highlighted in color. It is remarkable that the observed redshift evolution of the main sequence is in agreement with the in situ scenario of galaxy formation, which traces star formation in the galaxy back to local condensation processes. Specifically, at higher z and in massive galaxies, the ISM is on average denser $\rho \propto (1+z)^3$; both the dynamical $t_d \propto 1/\sqrt{\rho} \propto (1+z)^{-3/2}$ and the cooling $t_c \propto 1/\rho \propto (1+z)^{-3}$ timescales becomes shorter, and the SFR $\psi \propto M_\star/\max[t_d, t_c]$ associated to a galaxy of given stellar mass is higher, so making the main sequence locus to shift upwards. We stress that moving toward higher redshift the fraction of off-main sequence objects decreases appreciably; this is because, given the evolution of the SFR function and the shorter age of the Universe, it is more and more difficult to spot galaxies of appreciably different ages and featuring very high SFRs.

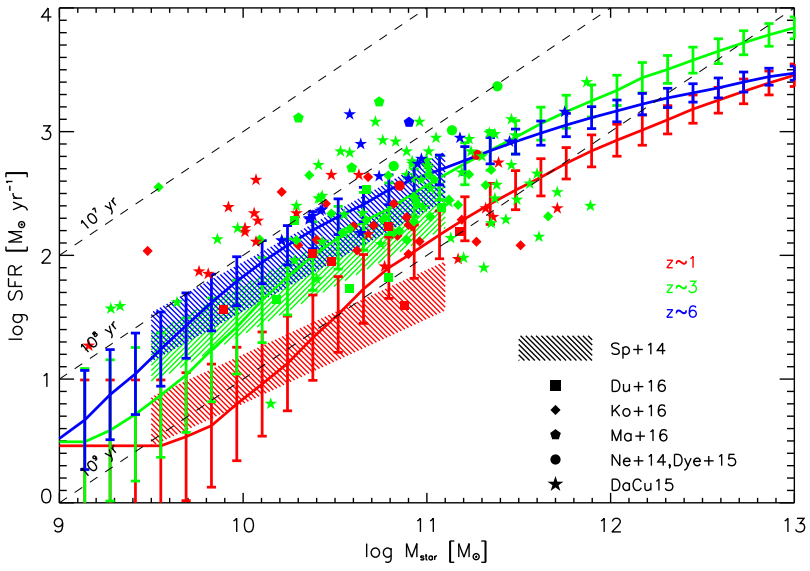

Figure 6.6 **The main sequence of star-forming galaxies at $z\approx$ 1 (red), 3 (green), and 6 (blue), based on the intrinsic (UV+far-IR) SFR functions:** the solid lines with errorbars illustrate the mean relationships with its 2σ scatter. The dashed lines shows the timescale $M_\star/\psi = 10^7$, 10^8 and 10^9 yr as labeled. The shaded areas are the observational determinations of the main sequence at different redshifts (based on statistics of large samples) by Speagle et al. (2014). Filled symbols (error bars omitted for clarity) refer to far-IR data for individual objects by Dunlop et al. (2016, squares), Koprowski et al. (2016, diamonds), Ma et al. (2015b, pentagons), Negrello et al. (2014) plus Dye et al. (2015, circles), and da Cunha et al. (2015, stars), color-coded according to redshift bins $z \lesssim 2$ (red), $2 \lesssim z \lesssim 4$ (green), and $z \gtrsim 4$ (blue).

Chapter 7

The Main Sequence of AGNs

As discussed in the Introduction (see Chapter. 1), nowadays it has been widely established that the mass of central BHs in massive, early-type galaxies is intimately linked to several properties of the hosts (e.g., velocity dispersion, stellar mass, etc.). However, a hot debate is still open on the physical origin of this link, in particular concerning the interplay between the star formation and BH accretion processes. Many studies pointed out the existence of an AGN main sequence, that relates the AGN luminosity to the SFR and/or stellar mass of the host star-forming galaxy. We stress that the AGN main sequence is actually a coevolution plane, since involves both AGN and host galaxy properties; as such it differs from the stellar main sequence, which relates only star related variables.

In the following we discuss the BH accretion history as inferred from a wealth of multiwavelength observations. We show that it can be exploited to map the SFR functions into AGN bolometric luminosity functions, in excellent agreement with recent determinations. Then we turn to interpret and physically understand the AGN main sequence.

7.1 BH accretion history

The BH accretion history in high-z star-forming galaxies can be robustly constrained from a wealth of multiwavelength observations concerning: (i) the fraction of X-ray detected AGNs in far-IR/K-band selected host galaxies (e.g. Alexander et al., 2005; Mullaney et al., 2012a; Wang et al., 2013a; Johnson et al., 2013) ; (ii) the fraction of far-IR detected galaxies in X-ray AGNs (e.g. Page et al., 2012; Mullaney et al., 2012b; Rosario et al., 2012) and optically selected quasars (e.g. Mor et al., 2012; Wang et al., 2013c; Willott et al., 2015); (iii) related statistics via stacking of undetected sources

(e.g. Basu-Zych et al., 2013).

Lapi et al. (2014) and Aversa et al. (2015) have interpreted these data in terms of a very basic physical scenario of in situ coevolution. In a nutshell, this envisages that the early growth of the nuclear BH in high redshift star-forming galaxies occurs under heavily dust enshrouded conditions. In the early stages $\tau \ll \tau_{\rm b}$, plenty of gas is available from the surroundings, and the BH accretes at substantial, mildly super-Eddington rates $\lambda_E \gtrsim 1$, so as to develop radiatively-inefficient slim-disk conditions (see Abramowicz et al., 1988; Watarai et al., 2000; Li, 2012; Madau et al., 2014; Volonteri et al., 2015). Since the BH mass is still small, the nuclear luminosity is much lower than that of the star-forming host galaxy, and the whole system behaves as a (sub-)mm bright galaxy with an X-ray nucleus. On the other hand, after a time $\tau \approx \tau_{\rm b} \lesssim$ Gyr, the BH mass has grown to large values and the nuclear emission becomes comparable or even overwhelms that of the surrounding galaxy. Strong winds from the nucleus remove gas and dust from the ambient medium stopping the star formation in the host, while the whole system shines as an optical quasar. If residual gas mass is still present in the central regions of the galaxy, it can be accreted onto the BH at progressively lower, sub-Eddington accretion rates; this phase corresponds to the onset of the standard thin disk accretion, which yields the observed SEDs of UV/optically-selected type-1 AGNs (Elvis et al., 1994; Hao et al., 2014).

In quantitative terms, the typical AGN lightcurve can be described as (Yu and Lu, 2004; Lapi et al., 2014; Aversa et al., 2015)

$$\begin{aligned} L_{\rm AGN}(\tau|M_{\rm BH},t) &= L_{\rm AGN,b}\, e^{(\tau-\tau_{\rm b})/\tau_{\rm ef}} \quad 0 \le \tau \le \tau_{\rm b} \\ &= L_{\rm AGN,b}\, e^{-(\tau-\tau_{\rm b})/\tau_{\rm AGN}} \quad \tau \ge \tau_{\rm b} \end{aligned} \tag{7.1}$$

that includes two phases: an early one up to the time $\tau_{\rm b}$ when the BH grows exponentially with a timescale $\tau_{\rm ef}$ to a mass $M_{\rm BH,b}$ and emits with an Eddington ratio $\lambda_E \gtrsim 1$ until it reaches a peak luminosity $L_{\rm AGN,b} = \lambda_E\, M_{\rm BH,b}\, c^2/t_{\rm Edd}$; a late phase when the luminosity declines exponentially on a timescale $\tau_{\rm AGN}$. The quantities λ_E and ϵ denote the average Eddington ratio and radiative efficiency during the early, ascending phase. The $e-$folding time associated to them is $\tau_{\rm ef} = \epsilon\, t_{\rm Edd}/\lambda_E\,(1-\epsilon)$.

As to the characteristic time $\tau_{\rm AGN}$ of the declining phase, the data concerning the fraction of star-forming galaxies in optically-selected quasars suggest a value $\tau_{\rm AGN} \approx 3\,\tau_{\rm ef}$ for AGNs with peak luminosities $L_{\rm AGN,b} \gtrsim 10^{13}\, L_\odot$; on the other hand, AGNs with lower peak luminosity are constrained to fade more drastically after the peak (Lapi et al., 2014; Aversa et al., 2015). To interpolate continuously between these behaviors

a standard erfc-function smoothing yields

$$\tau_{\rm AGN} = 3\,\tau_{\rm ef}\left[1-\frac{1}{2}\,{\rm erfc}\left(\frac{1}{2}\,\log\frac{L_{\rm AGN,b}}{10^{13}L_{\odot}}\right)\right]. \tag{7.2}$$

As to the Eddington ratio λ_E, its evolution with redshift is strongly constrained by various observations, including the bright end of the optical AGN luminosity function, the observed Eddington ratio function (see Vestergaard and Osmer, 2009; Kelly and Shen, 2013; Schulze et al., 2015), and the fraction of galaxies with given stellar mass hosting an AGN at a given Eddington ratio (see (see Aird et al., 2012; Bongiorno et al., 2012). The implied dependence of λ_E on redshift z can be rendered approximately as (see Lapi et al., 2014; Aversa et al., 2015)

$$\lambda_E(z) = 4\left[1-\frac{1}{2}\,{\rm erfc}\left(\frac{z-2}{3}\right)\right]. \tag{7.3}$$

where the coefficients are estimated considering the observational constraints at high-z ($\lambda_{\rm E}$ ~4), and at low-z ($\lambda_{\rm E}$ <1). Note that during the early, ascending phase of the lightcurve, λ_E exceeds the characteristic value $\lambda_{E\rm thin} \approx 0.3$ for the onset of a radiatively-inefficient slim accretion disc (Laor and Netzer, 1989). On the other hand, during the late, declining phase of the lightcurve, the Eddington ratio declines almost exponentially, so that after a time $\tau \approx \tau_{\rm AGN} \times \log \lambda_E/\lambda_{E\rm thin}$ the transition to a thin accretion disc takes place.

As to the radiative efficiency ϵ, several numerical simulations and analytic works (Abramowicz et al., 1988; Watarai et al., 2000; Blandford and Begelman, 2004; Li, 2012; Madau et al., 2014) indicate a simple prescription to relate the efficiency ϵ and the Eddington ratio λ_E in both slim and thin disc conditions

$$\epsilon = \frac{\epsilon_{\rm thin}}{2}\,\frac{\lambda_E}{e^{\lambda_E/2}-1}\,; \tag{7.4}$$

here $\epsilon_{\rm thin}$ is the efficiency during the thin disc phase, which may range from 0.057 for a non-rotating to 0.32 for a maximally rotating Kerr BH (Thorne, 1974). A fiducial value $\epsilon_{\rm thin} = 0.1$ is suggested by statistical investigations based on the continuity equation (e.g. Cao, 2010; Aversa et al., 2015) and from observations of individual systems (see Davis and Laor, 2011; Raimundo et al., 2012; Wu et al., 2013). In the early stages when mildly super-Eddington accretion occur with $\lambda_E \gtrsim$ a few, the radiative efficiency takes on small values $\epsilon \lesssim 0.3\,\epsilon_{\rm thin} \approx 0.03$, while in the late stages when sub-Eddington accretion occurs, it quickly approaches the thin disc value $\epsilon \approx \epsilon_{\rm thin}$.

The final BH mass $M_{\rm BH}$ is easily linked to the mass at the peak $M_{\rm BH,b}$ appearing in

Eq. (7.1) via $L_{\rm AGN,b}$. It results

$$M_{\rm BH} = \int_0^\infty d\tau' \frac{1-\epsilon}{\epsilon\, c^2} L_{\rm AGN}(\tau') = M_{\rm BH,b} \left[1 + f_\epsilon \frac{\tau_{\rm AGN}}{\tau_{\rm ef}}\right] . \tag{7.5}$$

The correction factor f_ϵ accounts for the modest change of the quantity $(1-\epsilon)/\epsilon$ along the declining phase, when $L_{\rm AGN}(\tau)$ and $\lambda_E(\tau)$ decrease almost exponentially and $\epsilon(\tau)$ increases according to Eq. (7.4); a value $f_\epsilon \approx 0.8$ applies to a good accuracy.

The evolution of the AGN luminosity and BH mass during the galaxy lifetime τ is illustrated in Fig. 6.1.

7.2 Mapping the SFR functions into the AGN luminosity functions

The above BH accretion history and timescales not only have been inferred from a plethora of observational data, but also have been validated in Aversa et al. (2015) by showing that the BH mass function obtained via the continuity equation approach well reproduces the current observational constraints at different redshifts (e.g. Vika et al., 2009; Shankar et al., 2009; Shankar, 2013; Willott et al., 2010; Li et al., 2011; Ueda et al., 2014).

In this work we provide a further validation, by examining the AGN statistics from a galaxy evolution viewpoint, basing on the SFR functions and on a deterministic BH accretion history consistent with the Eddington ratio distribution at various redshifts (cf. Figs. 8 and 9 in Aversa et al., 2015). This is similar in spirit with, but different operationally from, the approach by Caplar et al. (2015), who recovered the AGN luminosity functions from the stellar mass functions and from an ad hoc Eddington ratio distribution.

To relate the BH accretion and star formation histories, we impose that the final BH to stellar mass ratio $M_{\rm BH}/M_\star$ takes on average values $\approx 10^{-3}$ with a 0.4 dex scatter, as directly measured in the local Universe (see Shankar et al., 2016); actually, observational determinations at higher redshift and statistical estimates based on the abundance matching technique indicate that the $M_{\rm BH}/M_\star$ ratio weakly increases with redshift (e.g. Häring and Rix, 2004; Peng, 2007; Jahnke and Macciò, 2011; Kormendy and Ho, 2013; Aversa et al., 2015; Shankar et al., 2016). We describe this overall behavior as

$$\frac{M_{\rm BH}}{M_\star} = 1.5 \times 10^{-3} \left(\frac{1+z}{2}\right)^{1/2} . \tag{7.6}$$

The relative time spent by the AGN in a given logarithmic bin of luminosity $L_{\rm AGN}$,

i.e. the AGN duty cycle, just reads

$$\frac{\mathrm{d}\delta}{\mathrm{d}\log L_{\rm AGN}} = \frac{\tau_{\rm ef}+\tau_{\rm AGN}}{\tau_{\rm b}+\xi\,\tau_{\rm AGN}}\,\ln 10\;; \tag{7.7}$$

here the total duration of the AGN luminous phase is taken as $\tau_{\rm b}+\xi\,\tau_{\rm AGN}$ with $\xi\approx 3$, since after that time the luminosity is already decreased by a factor $e^{-\xi}\lesssim 0.05$ and the BH mass has already attained its final value to a very good approximation; anyway, variations of this parameter do not appreciably affect our results.

Then the AGN bolometric luminosity function can be straightforwardly computed as

$$\frac{\mathrm{d}N}{\mathrm{d}\log L_{\rm AGN}} = \int \mathrm{d}\log\psi\,\frac{\mathrm{d}N}{\mathrm{d}\log\psi}\,\frac{\mathrm{d}\delta}{\mathrm{d}\log L_{\rm AGN}}\;. \tag{7.8}$$

The outcome is illustrated in Fig. 7.1 at various redshifts, and pleasingly agrees with the most recent observational determinations. This further validates the proposed BH accretion history.

Basing on the UV-inferred SFR functions would clearly undersample the AGN luminosity functions at the bright end, since the number of galaxies with high SFR and high stellar mass, hence with high BH mass and AGN luminosity, is itself underestimated. Note that, as shown by the dotted lines in Fig. 9.3, AGNs with appreciable X-ray luminosity $L_X\gtrsim 10^{42}$ erg s^{-1} (bolometric corrections by Hopkins et al. (2007) are hosted by galaxies with SFRs $\psi\gtrsim 100\,M_\odot$ yr^{-1}, but their number density is smaller than that of the overall star-forming population by a factor $\lesssim 10^{-1}$; this is because of the duty cycle (cf. Eq. 7.7), which reflects the nearly constant behavior of the SFR vs. the exponential growth of the BH accretion rate during the galaxy lifetime.

7.3 Interpreting the AGN main sequence

Given consistent SFR functions, AGN duty cycles and luminosity functions, we can investigate the AGN main sequence. We start from discussing the $L_{\rm AGN}$ vs. SFR diagram. The number of objects per logarithmic bins of AGN luminosity and SFR is given by

$$\frac{\mathrm{d}^2N}{\mathrm{d}\log\psi\,\mathrm{d}\log L_{\rm AGN}} \simeq \frac{\mathrm{d}N}{\mathrm{d}\log\psi}\,\frac{\mathrm{d}\delta}{\mathrm{d}\log L_{\rm AGN}}\;. \tag{7.9}$$

The outcome at the representative redshift $z\approx 2$ is presented in Fig. 7.2, where the color-code indicates the logarithmic number density of objects per unit comoving volume (in Mpc^{-3}). The lilac line with errorbars illustrates the number density-weighted mean relationship $\langle\psi\rangle$ at given $L_{\rm AGN}$ with its 2σ variance when adopting, for a fair comparison with data, a SFR detection limit of $10^2\,M_\odot$ yr^{-1}. Our deterministic evolutionary tracks for the star formation and corresponding BH accretion history in individual galaxies

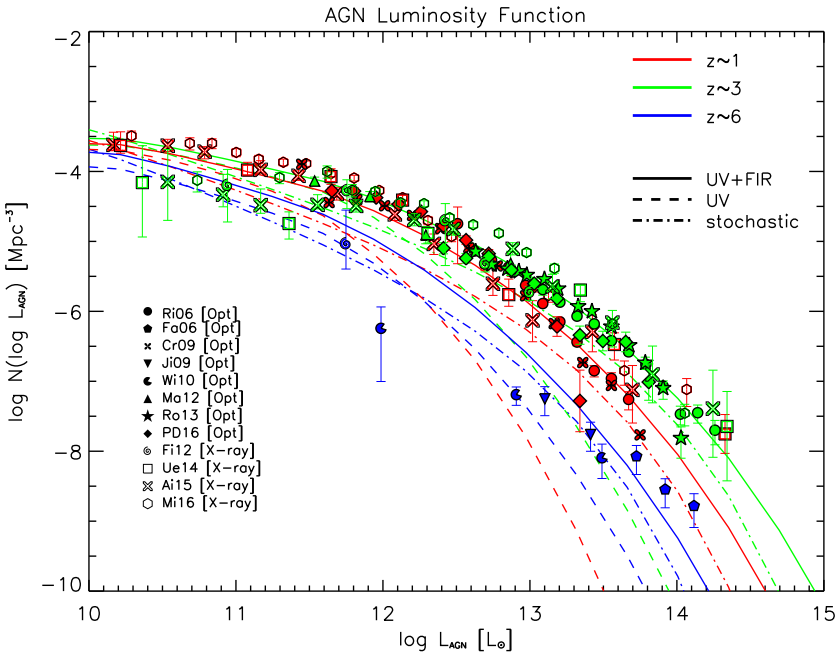

Figure 7.1 **The (bolometric) AGN luminosity functions at redshifts z=1 (red lines), 3 (green lines) and 6 (blue lines):** it has been reconstructed from the SFR functions and the AGN duty cycle associated to the deterministic BH accretion history of Sect. 7.1. Solid lines refer to our outcomes based on the intrinsic (UV+far-IR) SFR functions, while dashed lines refer to the (dust corrected) UV-inferred SFR functions. Dot-dashed lines are obtained by adopting the stochastic variability model by Hickox et al. (2014) and Stanley et al. (2015), inspired by the merger-driven scenario (see Eqs. 7.10 and 7.11). Optical data (filled symbols) are from Richards et al. (2006, circles), Fan et al. (2006, pentagons), Croom et al. (2009, crosses), Jiang et al. (2009, inverse triangles), Willott et al. (2010, pacmans), Masters et al. (2012, triangles), Ross et al. (2013, stars), and Palanque-Delabrouille et al. (2016, diamonds); X-ray data (empty symbols) are from Fiore et al. (2012, spirals), Ueda et al. (2014, squares), Aird et al. (2015, big cross), and Miyaji et al. (2015, hexagons). The optical and X-ray luminosities have been converted to bolometric by using the Hopkins et al. (2007, see their Figure 1) corrections, while the number densities have been corrected for the presence of obscured AGNs according to Ueda et al. (2003, 2014).

(dotted lines), and the locus where the AGN and SFR luminosities match (dashed line), are also illustrated.

For AGN luminosities $L_{\rm AGN} < L_{\rm SFR}$ lower than those associated with star formation, the tracks of individual objects and the mean relationships are flat; in fact, this occurs for galactic ages $\tau \lesssim \tau_{\rm b}$ when the SFR is roughly constant while the AGN luminosity grows exponentially. Then on moving toward higher AGN luminosities $L_{\rm AGN} \gtrsim L_{\rm SFR}$ that are attained for galactic ages $\tau \gtrsim \tau_{\rm b}$, the SFR gets rapidly suppressed and the AGN luminosity fades, so that the evolutionary tracks of individual objects move toward the bottom left region of the diagram. Contrariwise, the mean relationship starts to increase, being statistically dominated by objects with higher and higher SFR; this is because to achieve a higher AGN luminosity, the BH must reside in a galaxy with larger SFR.

In the diagram we illustrate for comparison data points from individual and stacked observations of X-ray selected AGNs (Page et al., 2012; Stanley et al., 2015; Harrison et al., 2016), mid-IR selected AGNs (Xu et al., 2015), and optically selected quasars (Netzer et al., 2016). The position on the diagram of these data points can be easily understood as a selection effect (cf. Fig. 6.1). Optical selection tends to pick up objects close to the peak of AGN luminosity when in the host dust has been partially removed and the SFR starts to be quenched; X-ray selection can pick up objects before or after the AGN peak, hence with SFR in the host still sustained or suppressed, respectively. Mid-IR selection with the current observational limits strikes an intermediate course between the former two.

For the sake of completeness, we also report data for a sample of far-IR selected galaxies, where the bolometric AGN luminosity has been estimated by stacking of X-ray fluxes (Delvecchio et al., 2015). In each of the SFR bins, the nuclear luminosity span a range of values, because the galaxy can be picked up at anytime before the peak, when the AGN luminosity can have vastly different values. Note that the contour levels reported in the figure apply if the primary selection is in AGN luminosity, and not in far-IR emission associated to star formation in the host.

In Fig. 7.2 the average result based on the variability model by Hickox et al. (2014) and Stanley et al. (2015) is also shown. These authors adopt an Eddington ratio (or AGN luminosity) distribution inspired by merger-driven models of galaxy formation, that translates into a duty cycle with shape

$$\frac{{\rm d}\delta}{{\rm d}\log L_{\rm AGN}} \propto \left(\frac{L_{\rm AGN}}{100\,\langle L_{\rm AGN}\rangle}\right)^{-\alpha} e^{-L_{\rm AGN}/100\,\langle L_{\rm AGN}\rangle}\,, \tag{7.10}$$

where $\alpha \approx 0.2$ (actually Hickox et al. 2004 adopt $\alpha \approx 0.6$, but the results change little); the distribution is normalized to unity over the range $L_{\rm AGN} > 10^{-2}\,\langle L_{\rm AGN}\rangle$.

The above authors also assume a constant ratio $\dot{M}_{\rm BH}/\psi \approx 1/3000$ between the BH

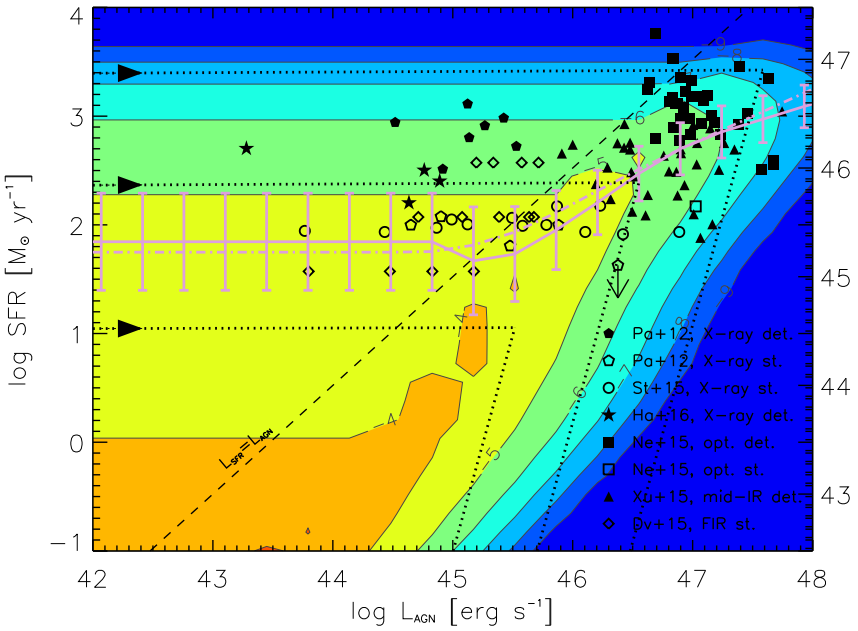

Figure 7.2 **Relationship between the SFR (left axis) or the far-IR luminosity (right axis) vs. the (bolometric) AGN luminosity at $z \approx 2$:** it is based on the intrinsic (UV+far-IR) SFR functions and the AGN duty cycle associated to the deterministic BH accretion history of Sect. 7.1. Colored contours illustrate the number density of galaxies plus AGNs (labels are in log units of Mpc^{-3}). The lilac line with errorbars illustrate the mean relationship with its 2σ scatter. The dashed line represents the locus where $L_{\rm SFR} = L_{\rm AGN}$. The dotted lines show three evolutionary tracks (forward time direction indicated by arrows) for objects with a given peak AGN luminosity of $10^{45.5}$, $10^{46.5}$, $10^{47.5}$ erg s^{-1}. Dot-dashed line is the average relationship obtained by adopting the variability model by Hickox et al. (2014) and Stanley et al. (2015), inspired by the merger-driven scenario (see Eqs. 7.10 and 7.11). Data are from: Page et al. (2012; pentagons) for both individual (filled symbols) and stacked (open symbols) X-ray selected sources; Stanley et al. (2015, circles) for stacked X-ray selected sources; Harrison et al. (2016, stars) for individual X-ray selected sources; Netzer et al. (2016, squares) for both individual and stacked optically selected sources; Xu et al. (2015, triangles) for individual mid-IR selected sources; Delvecchio et al. (2015, diamonds) for stacked far-IR selected sources.

accretion rate and the SFR, as observed in the local Universe (e.g. Chen et al., 2013); this provides a link between SFR and average AGN luminosity $\langle L_{\rm AGN}\rangle$ in the form

$$\langle L_{\rm AGN}\rangle \approx 2\times 10^{42}\,{\rm erg\ s^{-1}} \times \frac{\psi}{M_\odot\ {\rm yr^{-1}}} \tag{7.11}$$

Such a stochastic model produces a result (lilac dot dashed line) similar to our (lilac solid line) on the SFR vs. $L_{\rm AGN}$ diagram; however, as it is seen from Fig. 7.1 it considerably underpredicts the observed bolometric AGN luminosity functions at $z \gtrsim 1$, especially at the bright end; this is because Eq. (7.11) implies a too low normalization of the SFR to the BH accretion rate (1/3000) at high redshift, and Eq. (7.10) is not sufficiently broad at the bright end (cf. Bongiorno et al., 2012; Nobuta et al., 2012; Kelly and Shen, 2013).

We now turn to interpret the diagram L_X (or $L_{\rm AGN}$) vs. $M_\star$. The number of objects per logarithmic bins of AGN luminosity and stellar mass is given by

$$\frac{{\rm d}^2N}{{\rm d}\log M_\star\,{\rm d}\log L_{\rm AGN}} \simeq \int {\rm d}\log\psi\,\frac{{\rm d}N}{{\rm d}\log\psi}\,\frac{{\rm d}\delta}{{\rm d}\log L_{\rm AGN}}\,\frac{{\rm d}\delta}{{\rm d}\log M_\star}\,. \tag{7.12}$$

where the relative times spent by a galaxy with approximately constant SFR in a bin of AGN luminosity and stellar mass are given in Eqs. (7.7) and (6.5). The outcome at the representative redshift $z \approx 2$ is presented in Fig. 7.3, where the color-code indicates the logarithmic number density of objects per unit comoving volume (in ${\rm Mpc^{-3}}$). The lilac line with errorbars illustrates the number density-weighted mean relationship $\langle L_X\rangle$ (or $\langle L_{\rm AGN}\rangle$) at given $M_\star$ with its 2σ variance.

The evolutionary tracks for individual galaxies (dotted lines) feature a spiky behavior. This is because, as can be inferred from Fig. 6.1, both during the ascending and the declining part of the AGN lightcurve, the AGN luminosity increases or decreases exponentially, while the stellar mass varies little; e.g., before the AGN luminosity peak, the behavior $M_\star \propto \sqrt{\log L_{\rm AGN}}$ applies after Eqs. (6.1) and (7.1). This absence of correlation between $L_{\rm AGN}$ and $M_\star$ is consistent with the observations of X-ray selected AGNs by Mullaney et al. (2012b); as mentioned above, X-ray selection tends to pick up objects both before and after the AGN peak, when the AGN luminosity can be vastly different while the stellar mass changes little.

The mean relationship for detected galaxies (upper lilac dashed line) increases with stellar mass; this is because to achieve a high AGN luminosity, the BH must reside in a galaxy with rather high stellar mass, due to the constraint on the BH to stellar mass ratio at the end of the coevolution, that is pinpointed by a mass-selected sample (cf. Eq. 7.6). This well agrees with the average relationship for X-ray detected AGNs in the mass-selected galaxy sample by Rodighiero et al. (2015; upper empty circles).

However, the mean relationship when including stacked observations (Mullaney

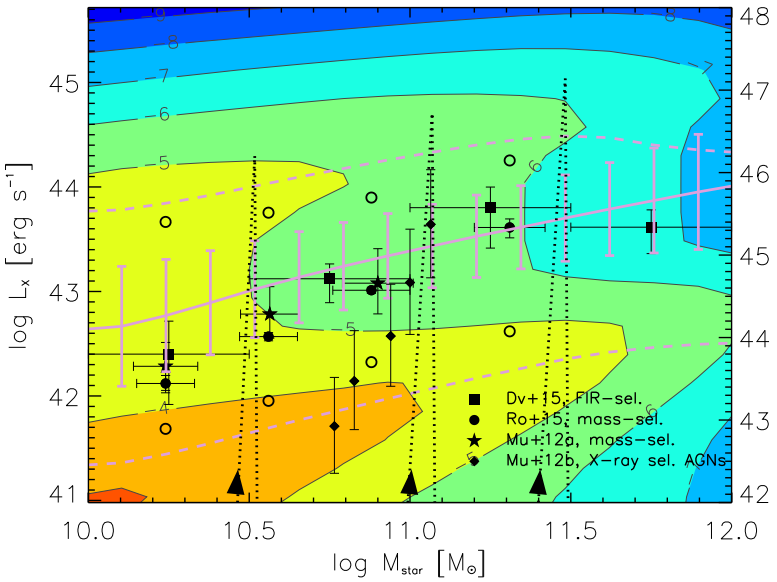

Figure 7.3 **Relationship between the X-ray luminosity (left axis) or the bolometric AGN luminosity (right axis, strictly valid only for detected sources; see text for details) vs. the host galaxy stellar mass at $z \approx 2$:** it is based on the intrinsic (UV+far-IR) SFR functions and the AGN duty cycle associated to the deterministic BH accretion history of Sect.7.1. Colored contours illustrate the number density of objects (labels are in log units of Mpc^{-3}). The lilac line with errorbars illustrates the relationship averaged over detected and stacked sources (dashed lines) with its 2σ variance, for a detection limit at $L_X \approx 10^{43}$ erg s^{-1}. The dotted lines show three evolutionary tracks (forward time direction indicated by arrows) for objects with a given peak AGN luminosity of 10^{46}, $10^{46.5}$, 10^{47} erg s^{-1}. Data are from Delvecchio et al. (2015, squares) for far-IR selected sources, from Mullaney et al. (2012b, diamonds) for X-ray selected sources, and from Mullaney et al. (2012a, stars) and Rodighiero et al. (2015, circles) for mass-selected samples; the open circles illustrate the average for detected (top) and stacked (bottom) sources in the Rodighiero et al. (2015) data.

et al., 2015; Rodighiero et al., 2015) lies substantially below, because of the contribution of undetected sources to the average. To compare with these data, it is essential to account for the contribution from star formation to the X-ray emission. In our computation we estimate the X-ray luminosity from star formation by the calibration

$$L_{X,\mathrm{SFR}} = 7 \times 10^{39}\ \mathrm{erg\ s^{-1}} \times \frac{\psi}{M_\odot\ \mathrm{yr^{-1}}} \tag{7.13}$$

of Vattakunnel et al. (2012).

We stress that the X-ray emission from star formation is usually negligible in individual detected sources with X-ray luminosity $L_X \gtrsim$ a few 10^{42} erg s^{-1}, corresponding for standard bolometric corrections to $L_{\mathrm{AGN}} \gtrsim 10^{44}$ erg s^{-1}. Contrariwise, when stacking sources with detection threshold $L_X \lesssim 10^{42}$ erg s^{-1}, the galaxy number density can be largely dominated by star-forming objects with negligible nuclear activity. As a consequence, the relation for undetected sources could just mirror the galaxy main sequence, with SFR converted in X-ray luminosity after Eq. (7.13). We find this is indeed the case, with the resulting average relationship for undetected sources (lower lilac dashed line) being a factor about 10^2 below that for detected AGNs, in agreement with Rodighiero et al. (2015, lower empty circles). We caution that, for such undetected sources, the conversion in bolometric luminosity via the standard X-ray correction for AGNs is somewhat misleading.

The average over detected and stacked sources (lilac solid line) strikes an intermediate course, and is found to be in excellent agreement with the observational determinations by Mullaney et al. (2015) and Rodighiero et al. (2015); however, its straight physical interpretation is hampered because the statistics of detected and undetected objects is contributed by different processes, i.e., either BH accretion or star formation, respectively.

In Fig. 7.4 we show the average ratio between the X-ray luminosity (or BH accretion rate) and the SFR vs. the stellar mass. Note that for a fair comparison with observational data by Mullaney et al. (2015) and Rodighiero et al. (2015), the BH accretion rate has been obtained from the X-ray luminosity by converting to bolometric with the standard X-ray correction for AGN and then using $\dot{M}_{\mathrm{BH}} = (1-\epsilon)\, L_{\mathrm{AGN}}/\epsilon\, c^2$ with $\epsilon \approx 0.1$. The result is another representation of the previous diagram, so our computation is again based on Eq. (7.9), and the same cautionary comments apply. Specifically, detected sources are truly AGN, while the undetected sources are mainly main sequence galaxies with negligible nuclear activity. The average relationship $L_X/\psi \propto M_\star^{0.5}$ weakly increases with the stellar mass, in agreement with the latest data from Rodighiero et al. (2015).

We stress that such a behavior of the average relationship (mean of detected plus stacked sources) between X-ray luminosity (or BH accretion rate, strictly holding only

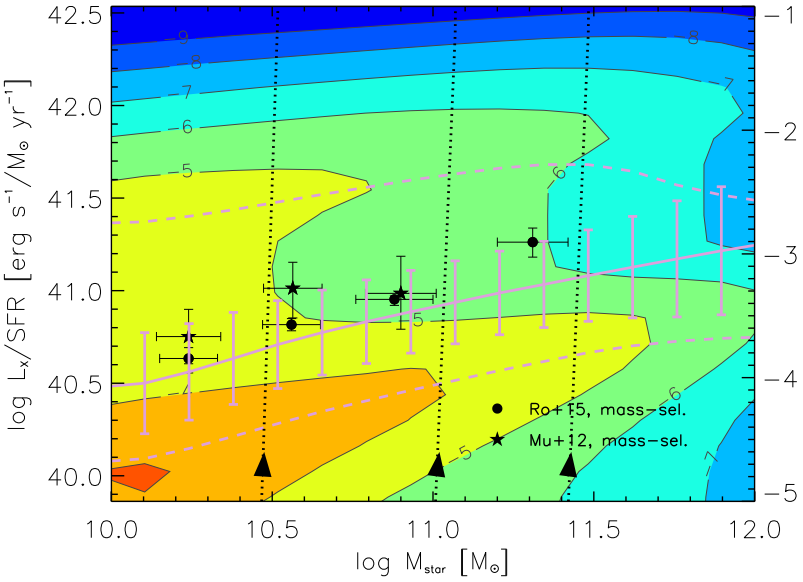

Figure 7.4 **Relationship between the ratio of the X-ray luminosity (left axis) or the BH accretion rate (right axis, strictly valid only for detected sources; see text for details) to the SFR vs. the host galaxy stellar mass at $z \approx 2$:** it is based on the intrinsic (UV+far-IR) SFR functions and the AGN duty cycle from the deterministic BH accretion history of Sect. 7.1. Colored contours illustrate the number density of objects (labels are in log units of Mpc^{-3}). The lilac line with errorbars illustrates the relationship averaged over detected and stacked sources (dashed lines), with its 2σ variance, for a detection limit at $L_X \approx 10^{43}$ erg s^{-1}. The dotted lines show three evolutionary tracks (forward time direction indicated by arrows) for objects with final stellar mass of about $10^{10.5}$, 10^{11}, $10^{11.5}$ $M_\odot$. Data are from Rodighiero et al. (2015, circles) and Mullaney et al. (2012a, stars) for mass-selected samples.

for detected sources) and the SFR does not mean that the quantities are proportional during the galaxy lifetime. In fact, the evolutionary tracks for individual objects are characterized by a very steep trend; this is because, during the ascending phase, the AGN luminosity increases exponentially, while the SFR is roughly constant and the stellar mass increases mildly with time. It is only in statistical sense that the weakly increasing behavior with $M_\star$ emerges.

Finally, we note that the normalization of the average ratio around a few 10^{-4} at $M_\star \approx 10^{11}\,M_\odot$ is driven by the statistics of stacked sources, that is mainly contributed by star-forming galaxies with negligible nuclear activity. In fact, the relationship for detected X-ray AGNs lies a factor around 10 above, with normalization increased to a few 10^{-3} at $M_\star \approx 10^{11}\,M_\odot$; indeed this reflects the value of the BH to stellar mass ratio at the end of the coevolution, as pinpointed by a mass selection.

Chapter 8

Conclusions

The history of star formation in massive galaxies (the host of high-redshift quasars) is a fundamental problem in galaxy evolution. There are important issues still concerning such topic, as: *is star formation in galaxies mainly regulated by in-situ processes or by merging ? How does the presence of dust affect the statistics of the star formation rate in galaxies at high redshift* $z \gtrsim 3$ *?*

To cast light on these issues, we have designed a method (see Chapter 3) to build up the intrinsic SFR function at different redshifts up to $z \lesssim 10$. In detail, at $z \lesssim 3$ we have fitted a Schechter function to the UV data for SFRs $\psi \lesssim 30\,M_{\odot}$ yr^{-1} and to the far-IR data for SFRs $\psi \gtrsim 100\,M_{\odot}$ yr^{-1}. We have further imposed that at $z \gtrsim 8$ the UV-inferred SFR function is representative of the intrinsic one, since we expect small attenuation by dust due to the short age of the Universe. This allows us to set the redshift evolution of the Schechter parameters, and hence to work out specific predictions for the SFR functions over the full range $z \sim 0 - 10$.

We have found that for $z \lesssim 7$ the UV-inferred SFR function, even when corrected for dust-absorption according to the standard prescriptions based on the UV slope, strongly underestimate the intrinsic SFR function for SFRs $\psi \gtrsim 30\,M_{\odot}$ yr^{-1}. Thus our result on the SFR function implies the existence of a galaxy population at $z \gtrsim 4$ featuring large star formation rates SFR $\psi \gtrsim 10^2\,M_{\odot}$ yr^{-1} in heavily dust-obscured conditions. These galaxies constitute the high-redshift counterparts of the dusty star-forming population already surveyed for $z \lesssim 3$ in the far-IR band by the *Herschel* space observatory. A number of these objects have been discovered thanks to spectroscopic follow-up of high-redshift candidates identified in UV or IR surveys, and their corresponding number densities are well reproduced by our intrinsic SFR function. We have further validated the latter by comparison with the observed (sub-)mm counts, redshift distributions, and cosmic infrared background (see Sect. 3.1.1), finding an excellent agreement.

We have exploited the continuity equation approach and the 'main sequence' star-formation observed timescales to show that our intrinsic SFR function is fully consistent with the stellar mass function of active, star-forming galaxies observed at redshift $z \gtrsim 4$ (see Sect. 3.1.2). In particular, we reproduce the considerable abundance of galaxies with stellar masses in excess of a few $10^{10}\,M_{\odot}$ at redshift $z \gtrsim 4$, and even their still substantial number densities out to $z \sim 6$. On the contrary, we show that the UV-inferred SFR function would produce a strong deficit of galaxies with such large stellar masses.

We have computed average relationships between intrinsic SFR and stellar mass vs. halo mass via the abundance matching technique (see Sect. 3.2). We find that such relationships show little if no evolution with redshift at given $M_{\rm H}$; this clearly indicates that the star formation in galaxies at high redshift $z \gtrsim 4$ is regulated by similar, *in-situ* processes, and not by merging or gas infall from cosmological scales. We have pointed out that our results on the intrinsic SFR functions straightforwardly overcome the 'impossibly early galaxy problem' recently pointed out by Steinhardt et al. (2015).

In order to probe the bright end of the SFR functions at $z \gtrsim 4$, we have computed the expected galaxy number counts and redshift distributions (including galaxy-scale gravitational lensing) of dusty star-forming galaxies. We have also designed an observational strategy (see Chapter. 4) to hunt these galaxies based on a preselection in the far-IR or (sub-)mm band with *Herschel* and *SCUBA-2*, possibly supplemented by on source observations with mm instruments like *AzTEC* and *ALMA*, aimed at recovering photometric (or even spectroscopic) redshifts (see Sect. 4.1).

We have investigated (see Sect. 4.2) the nature of the UV-selected galaxies at $z \gtrsim 4$, finding that their attenuation properties are strongly in excess with respect to those routinely estimated from the UV slope, i.e., via the $\beta_{\rm UV}-$IRX correlation. This is because star formation preferentially occurs within molecular clouds, i.e., cocooned environments extremely rich in dust; on the other hand, the UV slope mostly refers to the milder attenuation of the emission from relatively older stars by the diffuse cirrus dust component. We have shown that a simple, power-law representation of the UV attenuation due to molecular clouds in terms of the SFR, maps the intrinsic SFR function onto the observed UV luminosity function.

We have shown that dusty, strongly star-forming galaxies with $\psi \gtrsim 30\,M_{\odot}$ yr^{-1} are not lost in the UV, but rather are moved by their strong attenuation $A_{\rm UV} \gtrsim 2.3$ at fainter magnitudes, where they are outnumbered by the intrinsically faint and poorly attenuated galaxies. Such a highly star-forming, dust-obscured and massive galaxies are expected to be located on the high side of the $M_{\rm UV} - M_{\star}$ relationship; as such these constitute particularly suitable targets for far-IR and (sub-)mm observations with current instruments, and for near/mid-IR observations with the *JWST*.

We have also discussed (see Sect. 4.2) how the intrinsic SFR function at high-

redshift could be probed by combining current UV surveys with observations from (sub-)mm instruments like *ALMA* and *NIKA2*, and upcoming radio facilities like *SKA* and its precursors.

In particular, in Chapter 5, we produced detailed predictions for the counts and the redshift distributions for planned surveys with the SKA1-MID and its precursors, starting from our SFR functions and allowing for the effect of gravitational lensing.

The SFR functions were converted into radio luminosity functions taking into account both the synchrotron and the free-free emissions, exploiting the calibrations present in literature.

We have been able to reproduce the available source counts in the range 1.4–30 GHz, with some caveats for the published SPT counts of dusty galaxies at 95 GHz (Mocanu et al., 2013), solved thanks to a multiwavelength approach.

The highest redshift tails of the distributions at the detection limits of planned SKA1-MID surveys were found to include a substantial fraction of strongly lensed galaxies. We predict that a survey down to $0.25\,\mu$Jy will detect a non negligible amount of strongly lensed galaxies per square degree, at redshifts of up to 10.

The redshift distributions also show that the SKA1-MID surveys, and to some extent surveys with the SKA precursors, ASKAP and MeerKAT, will allow us to probe the star formation history through the re-ionization epoch without being affected by dust extinction. The deepest SKA1-MID surveys, down to $0.25\,\mu$Jy, will extend the determination of the SFR function by about two orders of magnitude compared to *Herschel* surveys up to the highest redshifts.

We have also discussed the synergies between the deepest SKA1 -MID survey and deep ongoing or planned optical/near-IR surveys. We find that the LSST deep drilling fields reach faint enough magnitudes to detect essentially all SKA1-MID galaxies in at least 3 bands, allowing reliable photometric redshift estimates. Exceptions may be heavily obscured $z > 6$ galaxies that are however expected to be rare. The JWST/DWS can detect also those in at least 6 filters, but its small area is a serious limitation.

We have finally provided a novel, unifying physical interpretation on the origin, the average shape, the scatter, and the cosmic evolution for the main sequences of star-forming galaxies and AGNs at high redshift $z \gtrsim 1$. We have achieved this goal in a *model-independent* way by exploiting: (i) our redshift-dependent SFR functions, (ii) deterministic evolutionary tracks for the history of star formation and black hole accretion, gauged on a wealth of multiwavelength observations.

We found that the galaxy main sequence and its scatter originate naturally as a statistical relationship from the SFR functions and a deterministic star formation history. The existence of the main sequence by no means implies that individual galaxies evolve along it. Specifically, we envisage young objects to be preferentially located

to the left of the main sequence at given SFR. As the time goes by they will move at nearly constant SFR toward the main sequence locus, spending there most of their lifetime. Afterwards, their SFR will be reduced and the galaxy will move below the main sequence, occupying the locus of 'red and dead' objects, as observed locally. Such a picture provides, again, strong support to an in situ scenario for star formation in galaxies.

The off-main sequence galaxies are interpreted as young objects, that have still to accumulate most of their stellar mass. In this respect, the interpretation of their peculiar position in the SFR vs. $M_\star$ diagram is not to be *above* the main sequence at given stellar mass, but rather to be to the *left* of it at given SFR. Mass-selected galaxies tends to preferentially lie on the main sequence, while far-IR selected ones are unbiasedly picked up on it or to the left of it. The age estimates via SED modeling of far-IR selected galaxies support our interpretation, showing a tendency for objects more distant from the main sequence locus to feature smaller and smaller ages. Note that this is in contrast to the interpretation of off-main sequence objects as starbursts triggered by mergers or cosmological inflows.

We are also able to explain the redshift evolution of the main sequence toward higher SFRs at given stellar mass, tracing star formation in galaxies back to in situ condensation processes. At higher z these are typically more efficient, yielding more violent SFRs, and so making the main sequence locus to shift upwards. We also expect that going toward higher redshift, the number of off-main sequence objects decreases appreciably.

The AGN main sequence is globally understood in terms of star formation and BH accretion histories. As to the SFR vs. $L_{\rm AGN}$ relationship, we expect a flat behavior for AGN luminosities lower than those associated with star formation, reflecting the individual evolutionary tracks of young galaxies. Then on moving toward higher AGN luminosities, the SFR gets rapidly suppressed by feedback processes, and the AGN luminosity itself slowly fades, so that the evolutionary tracks of individual objects move toward the bottom left region of the diagram. Contrariwise, the mean SFR increases with AGN luminosity, being statistically dominated by more massive objects that feature higher and higher SFRs.

As to the L_X vs. $M_\star$ relationship, we expect that the evolutionary tracks for individual galaxies feature a spiky behavior, because the AGN luminosity increases or decreases exponentially with the galactic age, while the stellar mass varies little. This absence of correlation is consistent with the observations of X-ray selected AGNs. On the other hand, the mean L_X for detected galaxies increases almost linearly with $M_\star$, being statistically dominated by objects with higher stellar and BH masses. The resulting relation well agrees with the average relationship for X-ray detected AGNs in mass-selected galaxy samples. However, when including stacked observations the

mean L_X is substantially lower, because of the contribution of undetected sources to the mean. We have highlighted that the statistics of undetected sources is dominated by star-forming galaxies with negligible AGN emission, and so it reflects the galaxy main sequence, with SFR converted in X-ray luminosity. As such, a straight physical interpretation of the mean relationship is hampered because the statistics of detected and undetected objects is contributed by different processes, i.e., either BH accretion or star formation, respectively.

Finally, we have discussed the increase of the average ratio between BH accretion rate and the SFR as a function of galaxy stellar mass. This does not imply that the BH accretion rate and SFR are proportional during the entire galaxy lifetime, because the average relationship holds only for detected sources in a statistical sense.

We remark that the star formation and BH accretion histories emerging from the above observational landscape constitute a testbed for galaxy and AGN evolution models; in particular, they provide a guide to gauge subgrid physics in numerical simulations.

We have shown that to properly interpret the main sequences for star-forming galaxies and AGNs at high redshift $z \gtrsim 2$ future observations should aim at: (i) exploiting different selections for galaxies and AGNs to fully populate the main sequence diagrams, especially for detected sources; (ii) measuring with improved accuracy the ages of stellar populations for extended samples of star-forming galaxies and AGN hosts; (iii) determining via spectroscopic observations the gas content of star-forming galaxies and AGN hosts located on and above the main sequences. To study off-main sequence objects, an important issue concerns the stellar mass determination of far-IR selected galaxies at high-redshift, that will become feasible in the near future thanks to the *JWST*.

To sum up we have provided an unified view on galaxy and supermassive BH evolution. In fact, while there is a large consensus on BH evolution via in situ accretion processes, debate is still open on the role of mergers or cosmological gas inflows in the assembly of stellar mass within galaxies. Our analysis highlights that the present data strongly support an in situ nature of both star formation and BH accretion processes, and it specifies in detail how they are coordinated in time. All in all, a framework of *in situ coevolution* is emerging, and it strongly demands to be further tested via future observations.

Chapter 9

Future Plans

Here we give an overview of our future plans for research.

9.1 An holistic view of galaxy evolution at high-z

In the future we plan to provide an holistic view of galaxy evolution at high redshift, reconciling constraints from various astrophysical/cosmological probes, such as the estimate of the cosmic SFR density from UV/IR surveys and long GRB rates, the cosmic reionization history after the latest *Planck* measurements, and the missing satellite problem.

We will use the global model-independent SFR functions to compute the cosmic SFR density down to an UV magnitude limit $M_{\rm UV} \lesssim -12$ (corresponding to a SFR limit of a few $10^{-3}\,M_{\odot}\ {\rm yr}^{-1}$, see Fig. 9.1) to test its agreement with recent determinations from IR surveys, and, taking into account a metallicity threshold, also against the estimates from long GRBs rates: they provide, in fact, an unbiased (with respect to dust extinction) view of the star formation processes at very high redshifts, being connected with the explosions of SNe.

We also plan to exploit such analysis to reproduce the electron scattering optical depth as recently measured by *Planck*, testing the underlying galaxy formation scenario against cosmic reionization.

All these results will let us put some constraints also on the efficiency of galaxy formation within dark matter halos, making it possible to analyze if there is a mass limit for dark matter halos that can form galaxies inside: remarkably, such a limit is also required not to run into the missing satellite problem in the local Universe.

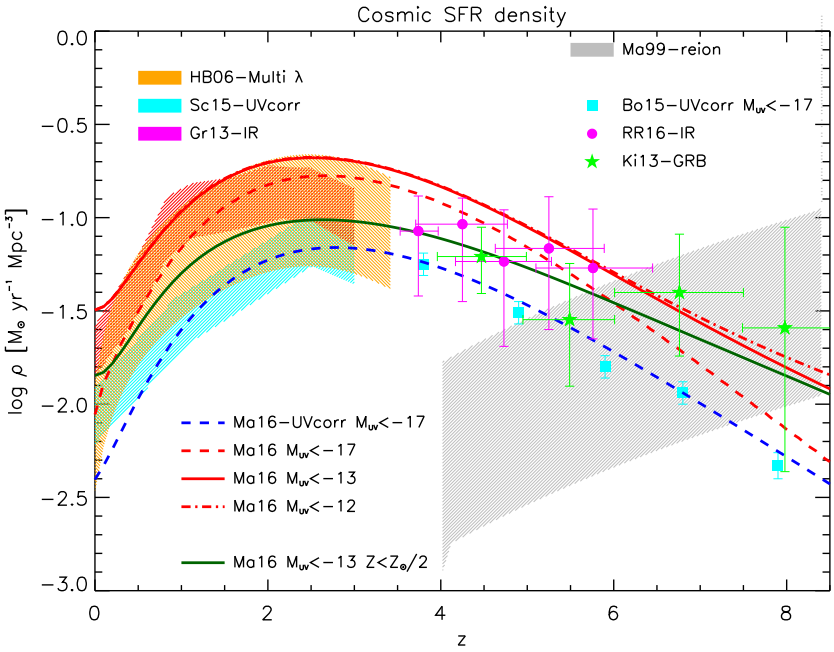

Figure 9.1 **PRELIMINARY! Madau Plot:** cosmic SFR density from the global model-independent SFR functions

9.2 The Radio Quiet AGNs contribution to SF galaxies in Radio Surveys

The radio emission of the so called radio-quiet (RQ) AGNs is still an open issue. We plan to investigate whether the statistical properties of galaxies detected by the Extended Chandra Deep Field-South (E-CDFS) VLA survey and found to host an RQ AGN are consistent with the radio emission being dominated by star-formation in the host galaxy.

We will achieve this goal using the global model-independent SFR functions and the SFR-radio emission relations presented in this thesis, and provide also redshift dependent radio luminosity functions for both SF galaxies and for the fraction of these galaxies that hosts a RQ AGN (See 9.2). We plan to calculate the latter exploiting our knowledge about the AGNs duty cycles and bolometric luminosity functions, obtaining in the end a probability for the SF galaxy to contain an (RQ) AGN.

We would like to check our results with existent and upcoming observations of luminosity functions of SF galaxies (See Fig. 9.2) and RQ AGNs, as well as provide predictions for number counts and redshift distributions for the upcoming radio facilities.

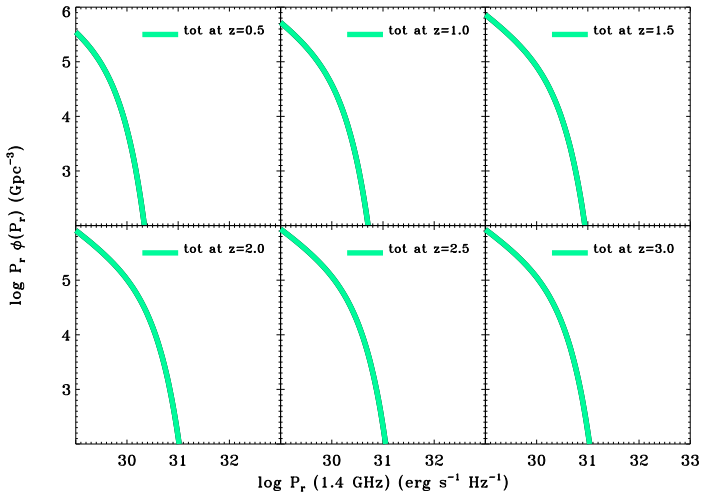

Figure 9.2 **PRELIMINARY! SFGs radio luminosity functions:** Luminosity functions of Star-Forming galaxies as derived from the global model-independent SFR functions in the radio band.

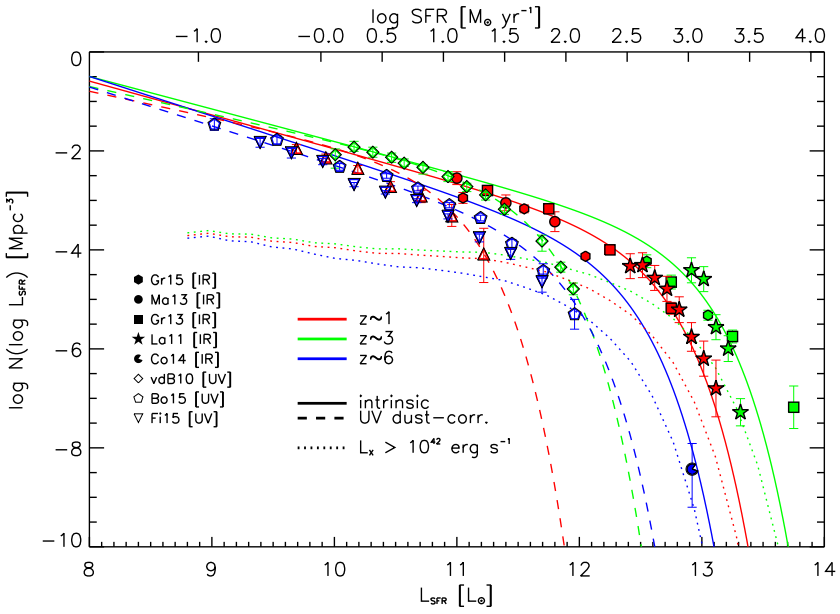

Figure 9.3 **PRELIMINARY! SF galaxies bolometric luminosity functions:** Bolometric luminosity functions of Star-Forming galaxies hosting an active nucleus with $L_X > 10^{42}$ (dotted lines), derived as a fraction of the bolometric luminosity function of all SF galaxies as inferred from global, model-independent, SFR functions (solid lines)
.

Appendix A

Computing number counts

Here we give all the extensive formulae used to compute differential, integral and Euclidean number counts and redshift distributions along the whole presented work.

As already mentioned in Chapter 3, the equation that computes the differential number counts is the following:

$$\frac{\mathrm{d}N}{\mathrm{d}\log S_\nu \mathrm{d}\Omega}(S_\nu) = \int \mathrm{d}z \frac{\mathrm{dV}}{\mathrm{d}z\mathrm{d}\Omega} N(\log\psi) \frac{\mathrm{d}\log\psi}{\mathrm{d}\log S_\nu} \tag{A.1}$$

where the flux is given as

$$S_\nu = \frac{L_{\nu(1+z)}}{L_\psi} \frac{1+z}{4\pi D_L^2(z)}, \tag{A.2}$$

while the comoving volume per unit solid angle is

$$\frac{dV}{dz d\Omega} = \frac{c}{H_0} \frac{(1+z)^2 D_\mathrm{A}^2(z)}{E(z)} \tag{A.3}$$

with $D_\mathrm{L} = (1+z)^2 D_\mathrm{A}$.

The Euclidean number counts are simply

$$S_\nu^{2.5} \frac{\mathrm{d}N}{\mathrm{d}S_\nu \mathrm{d}\Omega}(S_\nu) \tag{A.4}$$

and translated using $\mathrm{dN/dlog}\, S_\nu\, \mathrm{d}\Omega$ with $\mathrm{d}S_\nu = S_\nu \ln 10\, \mathrm{d}\log S_\nu$, after some simplifications they read

$$S_\nu^{1.5} \frac{\mathrm{d}N}{\mathrm{d}\log S_\nu \mathrm{d}\Omega \ln 10}(S_\nu). \tag{A.5}$$

The integral number counts per unit volume, instead, can be simply obtained by

integrating over the flux Eq. A.1 in the following way:

$$N(>S) \equiv \frac{\mathrm{d}N}{\mathrm{d}\Omega} = \int_{S_{\nu,inf}}^{\infty} \mathrm{d}S_\nu \int \mathrm{d}z \frac{\mathrm{dV}}{\mathrm{d}z\,\mathrm{d}\Omega} N(\log\psi) \frac{\mathrm{d}\log\psi}{\mathrm{d}\log S_\nu}. \tag{A.6}$$

Finally the redshift distributions are computed as follows:

$$\frac{\mathrm{d}N}{\mathrm{d}z\,\mathrm{d}\Omega}(z, S_\nu > S_{\nu,inf}) = \int_{\log S_{\nu,inf}}^{\infty} \mathrm{d}\log S_\nu [\frac{\mathrm{dV}}{\mathrm{d}z\,\mathrm{d}\Omega} N(\log\psi) \frac{\mathrm{d}\log\psi}{\mathrm{d}\log S_\nu}] S_\nu \ln 10 \tag{A.7}$$

Appendix B

The continuity equation

The continuity equation approach is useful in linking the luminosity function N(L,t) to the corresponding final mass function N(M,t) of a galaxy by tracing a generic form of baryonic accretion, for example the one that regulates the accretion onto the central BH or the stellar content in the host galaxy itself. The standard approach (Small and Blandford, 1992; Yu and Lu, 2004) in the integral formulation has been exploited by Aversa et al. (2015) in the following way: they started from the equation

$$\mathrm{N(L,t)} = \int_0^\infty dM[\partial_t \mathrm{N(M,t)} - \mathrm{S(M,t)}] \sum_i \frac{d\tau_i}{dL}(\mathrm{L|M,t}) \tag{B.1}$$

where τ is the time elapsed since the triggering of the activity (a sort of internal clock, not the cosmological time t), and dτ/dL is the time spent by an object with final mass M in the luminosity bin [L, L+dL] considering a defined lightcurve L(τ | M, t). There could be multiple solutions τ_i for the equation L=L(τ | M, t) thanks to the sum. The source term S(M, t) is due to "dry" merging, so it account for the mass content in stars or BHs derived from merging processes that do not contribute significantly to the star formation or BH accretion processes. Aversa et al. (2015, see their Appendix B for details) demonstrates that the impact of dry mergers on the mass functions is apparent only at the high mass end, in fact their effect is to increase the space density of BHs with mass $\mathrm{M_{BH}} \gtrsim 10^9 M_\odot$ and boost that of stellar masses $\mathrm{M_*} \gtrsim 10^{12} M_\odot$: in this intervals the data are still statistically uncertain of affected by large systematics. The authors then set the dry merging term to zero to solve Eq. B.1. Starting from it, a Soltan (1982) argument, concerning the equivalence between the integrated luminosity density and the local, final mass density, can be recovered: assuming that the timescales τ_i (that encase the mass-to-energy conversion efficiency) are constant in redshift and luminosity, neglecting the source term, multiplying by L and integrating over both L

and t the authors obtain:

$$\int_0^{t_0} dt \int_0^{\infty} d\mathrm{LLN(L,t)} = \int_0^{\infty} d\mathrm{L} \times \sum_i \frac{d\tau_i}{dL} = const \times \int_0^{\infty} d\mathrm{MN(M,t)}, \qquad \text{(B.2)}$$

given that $\sum_i \int d\tau_i \mathrm{L} \equiv \mathrm{const} \times \mathrm{M}$. For the BHs $const = \epsilon c^2/(1-\epsilon)$ given a radiative efficiency $\epsilon \sim 0.1$, and according to Aversa et al. (2015) the same expression holds also for the stellar components.

In practice Eq. B.1 is an integro-differential equation in the unknown function N(M, t), and it can be solved if the input luminosity function and the lightcurve (N(L, t) and L(τ | M, t), respectively) are specified. On Aversa et al. (2015) basis we use them to derive the mass function of supermassive black holes and stellar component in galaxies throughout the history of the Universe.

Appendix C

Modeling strong lensing

To compute the galaxy-galaxy lensing for the predictions of number counts and redshift distributions we adopt a two component model, made of a stellar component with a Sersic profile plus a DM halo with a Navarro-Frenk-White (NFW) profile (see Lapi et al., 2012), referred to as "SISSA model" (an example is given in Fig. C). For an extensive treatment of the topic we defer to the work by Lapi et al. (2012), here we just present the equations which are useful for computing the number counts.

The lensing optical depth is computed as

$$\tau(z_s| > \mu) = \int_0^{z_s} \mathrm{d}z_l \times \int \mathrm{dM_H} \frac{\mathrm{d}^2\mathrm{N}}{\mathrm{dM_H dV}} \frac{\mathrm{d}^2\mathrm{V}}{\mathrm{d}z_l \mathrm{d}\Omega} \sigma(>\mu, \mathrm{M_H}, z_s, z_l), \qquad \text{(C.1)}$$

where $\mathrm{d}^2\mathrm{V}/\mathrm{d}z\mathrm{d}\Omega$ is the comoving volume per unit z-interval and solid angle, while $\mathrm{d}^2\mathrm{N}/\mathrm{dM_H}$ is the galaxy halo mass function, (the statistics of halos containing one single galaxy, (see Shankar et al., 2006, for details). The galaxy halo mass function is computed from the standard Sheth and Tormen (1999, 2002) mass function, accounting for the possibility that an halo can contain multiple subhalos, and removing halos corresponding to galaxy systems. The latter characteristic is obtained cutting off the halo mass function at $\mathrm{M}=10^{13.5}\mathrm{M}_\odot$, in fact beyond this limit the probability of having multiple galaxies within a halo becomes very high. As for the subhalo, in Lapi et al. (2012) they point out that for masses in the range $11.4 \lesssim \log(\mathrm{M_H}/\mathrm{M}_\odot) \lesssim 13.5$ and redshift $z \gtrsim 1.5$, for which the lensing effect becomes important, the total (halo+subhalo) mass function differs from the halo mass function by less than 5%.

The inner integral in Eq.C.1 gives the lens redshift distribution, in other words the surface density per unit redshift interval of lenses located at z_l that can produce a strong lensing event with total magnification $> \mu$ on a source at redshift z_s: $dp(z_l| > \mu, z_s)/dz_l$.

To obtain the number counts of lensed galaxies it is necessary to start from the number density of unlensed galaxies $d^2N/dS\,dz_s$, to multiply by the amplification dis-

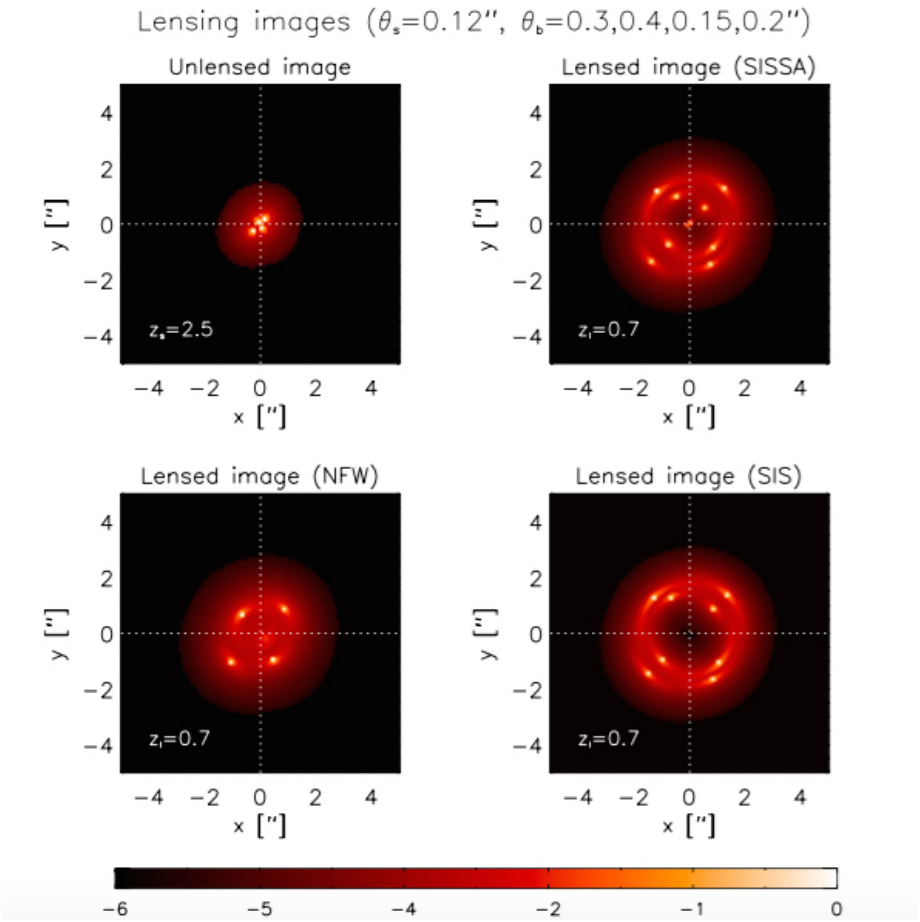

Figure C.1 **Ray-tracing simulation of the gravitational lensing for an extended source at z_s = 2.5 with a Sersic profile (n = 4) and effective (half light) angular radius θ_s = 0.”12, and a lens at z' = 0.7 from Lapi et al. (2012)**. The impact parameter θ_b (i.e., the angular separation between the source and the optical axis) is 0.”3, 0.”4, 0.”15, 0.”2, respectively. The unlensed source is shown in the top left panel, while the lensed image for the SISSA model is in the top right panel, for the NFW model is in the bottom left panel, and for the SIS model is in the bottom right panel. In all panels the origin of coordinates marks the position of the optical axis, while the color scale represents in logarithmic units the surface brightness relative to the central value of the unlensed image. Note that the centra lpixels in the SISSA and NFW panels correspond to the strongly demagnified image, and appear in the figure owing to the finite resolution of the simulations.

tribution $dp/d\mu$, and to integrate as follows:

$$\frac{\mathrm{d}N}{\mathrm{d}\log S}(s) = \int \mathrm{d}z_s \frac{1}{\langle\mu\rangle} \int \mathrm{d}\mu \frac{\mathrm{d}p}{\mathrm{d}\mu}(\mu|z_s) \frac{\mathrm{d}^2N}{\mathrm{d}\log S\,\mathrm{d}} z_s(S\,|\mu). \tag{C.2}$$

The factor $\frac{1}{\langle\mu\rangle}$ can be approximated with 1 in the case of large area surveys.

The redshift distributions are computed as in Eq.C.2, without integrating over z.

Appendix D

Abundance Matching technique

As introduced in Chapter 3 the abundance matching technique is a standard way of deriving monotonic relationships between galaxy and halo properties by matching the corresponding number densities (Vale and Ostriker, 2004; Shankar et al., 2006; Moster et al., 2010, 2013; Behroozi et al., 2013).

In order to derive the relation between the stellar or BH mass M and the corresponding Halo mass $M_{\rm H}$, it is necessary to solve the following equation (e.g. White et al., 2008; Shankar et al., 2010):

$$\begin{aligned} \int_{\log M}^{\infty} d\log M' N(\log M', z) = \\ = \int_{-\infty}^{+\infty} d\log M'_{\rm H} N \times (\log M'_{\rm H}, z) \times \\ \times \frac{1}{2}{\rm erfc}\left\{\frac{\log[M_{\rm H}(M)/M'_{\rm H}]}{\sqrt{2}\widetilde{\sigma}_{\log {\rm M}}}\right\} \end{aligned} \tag{D.1}$$

which holds when using a lognormal distribution of M at a given $M_{\rm H}$, with a dispersion $\sigma_{\log {\rm M}}$. In Eq.D.1 we have defined $\widetilde{\sigma}_{\log {\rm M}} = \sigma_{\log {\rm M}}/\mu$, where $\mu = d\log M/d\log M_{\rm H}$.

The quantity N(log $M_{\rm H}$) is the galaxy halo mass function, in other words the mass function of the halos hosting one individual galaxy. Since we would like to have relationships which are valid for a single galaxy, and not for a galaxy system, we do not rely on the halo mass function. We use the Aversa et al. (2015) approach: they build the galaxy halo mass function by correcting the overall halo mass function from cosmological N-body simulations, adding the contribution of subhalos after having removed, on probabilistic considerations, the contribution of halos corresponding to galaxy systems. In practice, they first account for the possibility that an halo contains many subhalos, and secondly they exclude halos corresponding to galaxy systems.

They start from the subhalo mass function as determined by Jiang and van den Bosch (2014): the subhalos having mass between m and $m + dm$ in an halo of mass $M_{\rm H}$ at a given redshift z are distributed as

$$N(\log\psi) = \gamma\psi^{\alpha}\exp^{-\beta\psi^{\omega}}\ln 10 \tag{D.2}$$

where $\psi = M/M_{\rm H}$; m is considered to be the mass of the self-bound entity at redshift z, that has survived after that mass stripping and dynamical friction reduced the initial mass. The parameters to be inserted in Eq. D.1 to describe the evolved subhalo mass function are given by Aversa et al. (2015) as $[\gamma, \alpha, \beta, \omega]$=[0.31$f_s$, -0.82, 50.00,4.00], where f_s accounts for the dependance from the host halo mass and the redshift. It can be written as $f_s = 0.3563 N_{\tau}^{-0.6} - 0.075$, where $N_{\tau} = \int_{t(z)}^{t(z_{0.5})} dt/\tau_{dyn}(t)$, τ_{dyn} is the halo dynamical time. We defer the reader to the paper by Aversa et al. (2015) for detailed figures and the outcome at different redshifts.

Having all those ingredients, then it is possible to compute the overall subhalo contribution to the halo mass function in a mass bin $\mathrm{M_H}$-$\mathrm{M_H}$+$d\mathrm{M_H}$ as

$$\mathrm{N_{subH}}(\log \mathrm{M_H}) = \int_0^{\infty} d\log \mathrm{M'_H N_H}(\log \mathrm{M'_H}) \times \mathrm{N}(\log\psi)_{|\psi=\mathrm{M_H/M'_H}} \tag{D.3}$$

where $\mathrm{N_H}(\log \mathrm{M_H})$ is the standard Halo mass function (see Sheth and Tormen, 1999; Tinker et al., 2008). The total halo+subhalo mass function then reads

$$\mathrm{N_{H+subH}}(\log \mathrm{M_H}) = \mathrm{N_H}(\log \mathrm{M_H}) + \mathrm{N_{subH}}(\log \mathrm{M_H}). \tag{D.4}$$

.

It turns out that the contribution of the subhalo is in general negligible for any redshift in the mass interval of interest.

The probability distribution for an halo to contain one individual galaxy is computed as follows: the first step consists in obtaining the halo occupation number, in other words the average number of subhalos inside a host halo with mass $\mathrm{M_H}$, given by

$$\langle N\rangle(\mathrm{M_H}, z)0 \int_{\log m_{min}/M_H}^{0} d\log\psi N(\log\psi) \tag{D.5}$$

with m_{min} the minimum mass for an halo to avoid divergence in the integral. The value of m_{min} has been set by comparison with observational datasets and numerical simulations. For high masses $\mathrm{M_H} \gg m_{min}$, the halo occupation number is well represented by a power law with logarithmic slope $\lesssim 1$, again according to Aversa et al. (2015), going into an abrupt cutoff for masses $\mathrm{M_H} \lesssim 3 - 5\, m_{min}$.

Since numerical simulations and HOD models in literature, indicate the Poissonian

distribution as the best one to represent the probability of having N subhalos given the average number $\langle N \rangle(\mathrm{M_H}, z)$, the second step consists in writing:

$$\mathrm{P}(< \mathrm{N}|\langle \mathrm{N} \rangle) = \frac{\Gamma(\underline{\mathrm{N}+1}), \langle \mathrm{N} \rangle}{\underline{\mathrm{N}!}} \tag{D.6}$$

where $\Gamma(a, x) = \int_x^\infty dt t^{a-1} e^{-t}$ is the incomplete complementary gamma function, $\underline{\mathrm{x}}$ is the floor function (the closer integer lower than x), and n! is the factorial function.

In the end, the galactic halo mass function can be computed as

$$\mathrm{N_{GHMF}}(\log \mathrm{M_H}) = \mathrm{N_{H+subH}}(\log \mathrm{M_H}) \times \mathrm{P}(< \mathrm{N} = 1|\langle \mathrm{N} \rangle). \tag{D.7}$$

In general, Aversa et al. (2015) pointed out that the galactic halo mass function shows a cutoff for host halo masses $\mathrm{M_H} \gtrsim 10^{13} M_\odot$, more pronounced at lower redshifts: this occurs because the larger halos are more likely to host a galaxy group or cluster, rather than an individual galaxy. The lower ($\sim$ afew$10^{11} M_\odot$, for satellite halos) and the upper ($\sim$ afew$10^{13} M_\odot$, for a halo to host an individual galaxy) limits for the halo mass, are suggested by galaxy weak lensing observations.
An example of Galaxy Halo Mass function vs Halo Mass Function at different redshifts is given in Fig. D.

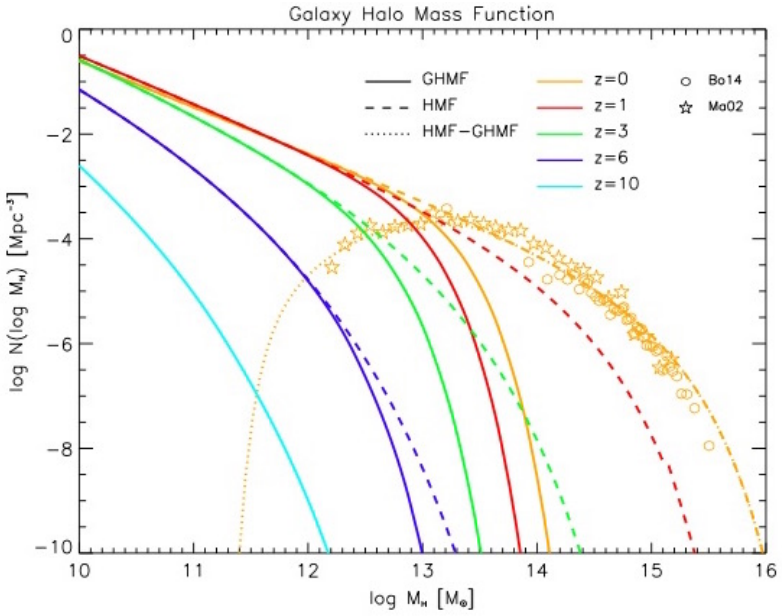

Figure D.1 **Galaxy halo mass function N (**log $\mathbf{M}_H$ **) (solid lines) at redshift z = 0 (orange), 1 (red), 3 (green), 6 (blue), and 10 (cyan), vs. the halo mass** $\mathbf{M}_H$ **in solar units from Aversa et al. (2015)**. This is obtained from the halo mass function (dashed lines) by adding the global subhalo mass function and subtracting the mass function of multiply occupied halos (or equivalently multiplying by the probability of single occupation). At z = 0 they also report as a dotted line the resulting cluster and group halo mass function (obtained by subtraction of the solid from the dashed line); this is compared with the determinations by Boehringer et al. (2014, circles) from X-ray observations of groups and clusters and by Martínez et al. (2002, stars) from optical observations of loose groups.

Acknowledgments

First af all I would like to thank my supervisors, prof. Andrea Lapi, prof. Gianfranco De Zotti and prof. Luigi Danese, for these four years of intense and dedicated work, and for all the extremely useful discussions we had toghether. To Andrea and Gigi goes a very special thanks, for having showed me how to go home, after an intense day of hard work, with a smile of satisfaction on my lips.
Thanks to the external referees, I. Prandoni and M. Béthermin, for having read the thesis and provided useful comments.
Another thanks goes to Francesca Perrotta, for all the support she gave me in these years, to profs. Sandro Bressan and Carlo Baccigalupi and to all the staff, students and postdocs of the astrophysics sector, for the scientific (and not only) chats we had in this time. Xiaoting, Federico, Marco, Alessio, Elena, Giovanni, Mauro, Guillaume and Eolo deserve a special mention, for having been actively part of my life here in Trieste, as well as all the students' representatives who served under my presidency, thank you for having shared with me this incredible adventure.
A very special thanks, from the deepest of my heart, goes to Serena and Kate, the best officemates ever, for having been my "family" here in Trieste.
Another very big thank you goes to Giorgio and Alice, for having been the best dance partners ever, and for their true friendship, as well as to the whole group of Trieste Folk, for having taught me how to dance a waltz.
Thanks also to Simona, Olga, Enrico and the SISSA Medialab, for having involved me in the outreach activities, I've had a lot of fun with you, and learned so much.
I would also acknowledge the Students' Secretariat, namely Riccardo and Federica, as well as Lorena, for all the help they gave me in my stay here at SISSA, as well as in my job trips around the world. Thank you also to JingJing and Zhen-Yi, for their warm hospitality in China, and to my cousin Caterina, for having hosted me in my very first week in Trieste.
I cannot forget Romy, Laura, Sabino and Simone, thank you for the special moments spent in Turin during the weekends, and the Friend of a Lifetime, Veronica, who never let me feel the geographical distance between us.
Last but not least, the biggest thank you goes to my family, for all the support, the help,

and for having always believed that I could have arrived until the end of this fantastic journey. In particular to my fiancé Federico, for having waited me so long, to Gaia and Luna, for all their love, and to my sister Ilaria and my mother Ennia, for having always pushed me to take the train back: whitout you I simply would not be here.

Bibliography

Abramowicz, M. A., Czerny, B., Lasota, J. P., and Szuszkiewicz, E. (1988). Slim accretion disks. *The Astrophysical Journal*, 332:646–658.

Adelberger, K. L., Steidel, C. C., Pettini, M., Shapley, A. E., Reddy, N. A., and Erb, D. K. (2005). The Spatial Clustering of Star-forming Galaxies at Redshifts 1.4 < z < 3.5. *The Astrophysical Journal*, 619:697.

Aird, J., Coil, A. L., Georgakakis, A., Nandra, K., Barro, G., and Pérez-González, P. G. (2015). The evolution of the X-ray luminosity functions of unabsorbed and absorbed AGNs out to z∼ 5. *MNRAS*, 451:1892–1927.

Aird, J., Coil, A. L., Moustakas, J., Blanton, M. R., Burles, S. M., Cool, R. J., Eisenstein, D. J., Smith, M. S. M., Wong, K. C., and Zhu, G. (2012). PRIMUS: The Dependence of AGN Accretion on Host Stellar Mass and Color. *The Astrophysical Journal*, 746:90.

Aird, J., Coil, A. L., Moustakas, J., Diamond-Stanic, A. M., Blanton, M. R., Cool, R. J., Eisenstein, D. J., Wong, K. C., and Zhu, G. (2013). PRIMUS: An Observationally Motivated Model to Connect the Evolution of the Active Galactic Nucleus and Galaxy Populations out to z ∼ 1. *The Astrophysical Journal*, 775:41.

Alavi, A., Siana, B., Richard, J., Stark, D. P., Scarlata, C., Teplitz, H. I., Freeman, W. R., Dominguez, A., Rafelski, M., Robertson, B., and Kewley, L. (2014). Ultra-faint Ultraviolet Galaxies at z 2 behind the Lensing Cluster A1689: The Luminosity Function, Dust Extinction, and Star Formation Rate Density. *The Astrophysical Journal*, 780:143.

Alexander, D. M., Bauer, F. E., Chapman, S. C., Smail, I., Blain, A. W., Brandt, W. N., and Ivison, R. J. (2005). The X-Ray Spectral Properties of SCUBA Galaxies. *The Astrophysical Journal*, 632:736–750.

Alexander, D. M., Brandt, W. N., Smail, I., Swinbank, A. M., Bauer, F. E., Blain, A. W., Chapman, S. C., Coppin, K. E. K., Ivison, R. J., and Menendez-Delmestre,

K. (2008). Weighing the Black Holes in z $\sim$ 2 Submillimeter-Emitting Galaxies Hosting Active Galactic Nuclei. *Astronomic. J.*, 135:1968–1981.

Alexander, D. M. and Hickox, R. C. (2012). What drives the growth of black holes? *New Astron. Rev.*, 56:93–121.

Asboth, V., Conley, A., Sayers, J., Bethermin, M., Chapman, S. C., Clements, D. L., Cooray, A., Dannerbauer, H., Farrah, D., Glenn, J., Golwala, S. R., Halpern, M., Ibar, E., Ivison, R. J., Maloney, P. R., Marques-Chaves, R., Martinez-Navajas, P. I., Oliver, S. J., Perez-Fournon, I., Riechers, D. A., Rowan-Robinson, M., Scott, D., Siegel, S. R., Vieira, J. D., Viero, M., Wang, L., Wardlow, J., and Wheeler, J. (2016). HerMES: A search for high-redshift dusty galaxies in the HerMES Large Mode Survey - Catalogue, number counts and early results. *ArXiv e-prints*.

Aversa, R., Lapi, A., de Zotti, G., Shankar, F., and Danese, L. (2015). Black Hole and Galaxy Coevolution from Continuity Equation and Abundance Matching. *The Astrophysical Journal*, 810:74.

Azadi, M., Aird, J., Coil, A. L., Moustakas, J., Mendez, A. J., Blanton, M. R., Cool, R. J., Eisenstein, D. J., Wong, K. C., and Zhu, G. (2015). PRIMUS: The Relationship between Star Formation and AGN Accretion. *The Astrophysical Journal*, 806:187.

Baldry, I. K. and Glazebrook, K. (2003). Constraints on a Universal Stellar Initial Mass Function from Ultraviolet to Near-Infrared Galaxy Luminosity Densities. *The Astrophysical Journal*, 593:258–271.

Banday, A. J. and Wolfendale, A. W. (1991). Fluctuations in the galactic synchrotron radiation. I - Implications for searches for fluctuations of cosmological origin. *MNRAS*, 248:705–714.

Barger, A. J., Cowie, L. L., Chen, C.-C., Owen, F. N., Wang, W.-H., Casey, C. M., Lee, N., Sanders, D. B., and Williams, J. P. (2014). Is There a Maximum Star Formation Rate in High-redshift Galaxies? *The Astrophysical Journal*, 784:9.

Barger, A. J., Cowie, L. L., Owen, F. N., Chen, C.-C., Hasinger, G., Hsu, L.-Y., and Li, Y. (2015). The Host Galaxies of X-Ray Quasars are Not Strong Star Formers. *The Astrophysical Journal*, 801:87.

Barone-Nugent, R. L., Trenti, M., Wyithe, J. S. B., Bouwens, R. J., Oesch, P. A., Illingworth, G. D., Carollo, C. M., Su, J., Stiavelli, M., Labbe, I., and van Dokkum, P. G. (2014). Measurement of Galaxy Clustering at z 7.2 and the Evolution of Galaxy Bias from 3.8 < z < 8 in the XDF, GOODS-S, and GOODS-N. *The Astrophysical Journal*, 793:17.

Basu-Zych, A. R., Lehmer, B. D., Hornschemeier, A. E., Bouwens, R. J., Fragos, T., Oesch, P. A., Belczynski, K., Brandt, W. N., Kalogera, V., Luo, B., Miller, N., Mullaney, J. R., Tzanavaris, P., Xue, Y., and Zezas, A. (2013). The X-Ray Star Formation Story as Told by Lyman Break Galaxies in the 4 Ms CDF-S. *The Astrophysical Journal*, 762:45.

Bauer, F. E., Alexander, D. M., Brandt, W. N., Hornschemeier, A. E., Vignali, C., Garmire, G. P., and Schneider, D. P. (2002). The Chandra Deep Field North Survey. XII. The Link between Faint X-Ray and Radio Source Populations. *Astronomic. J.*, 124:2351–2363.

Behroozi, P. S., Wechsler, R. H., and Conroy, C. (2013). The Average Star Formation Histories of Galaxies in Dark Matter Halos from z = 0-8. *The Astrophysical Journal*, 770:57.

Beifiori, A., Courteau, S., Corsini, E. M., and Zhu, Y. (2012). On the correlations between galaxy properties and supermassive black hole mass. *MNRAS*, 419:2497–2528.

Bell, E. F. (2003). Estimating Star Formation Rates from Infrared and Radio Luminosities: The Origin of the Radio-Infrared Correlation. *The Astrophysical Journal*, 586:794–813.

Bernardi, M., Meert, A., Sheth, R. K., Vikram, V., Huertas-Company, M., Mei, S., and Shankar, F. (2013). The massive end of the luminosity and stellar mass functions: dependence on the fit to the light profile. *MNRAS*, 436:697–704.

Béthermin, M., Le Floc'h, E., Ilbert, O., Conley, A., Lagache, G., Amblard, A., Arumugam, V., Aussel, H., Berta, S., Bock, J., Boselli, A., Buat, V., Casey, C. M., Castro-Rodríguez, N., Cava, A., Clements, D. L., Cooray, A., Dowell, C. D., Eales, S., Farrah, D., Franceschini, A., Glenn, J., Griffin, M., Hatziminaoglou, E., Heinis, S., Ibar, E., Ivison, R. J., Kartaltepe, J. S., Levenson, L., Magdis, G., Marchetti, L., Marsden, G., Nguyen, H. T., O'Halloran, B., Oliver, S. J., Omont, A., Page, M. J., Panuzzo, P., Papageorgiou, A., Pearson, C. P., Pérez-Fournon, I., Pohlen, M., Rigopoulou, D., Roseboom, I. G., Rowan-Robinson, M., Salvato, M., Schulz, B., Scott, D., Seymour, N., Shupe, D. L., Smith, A. J., Symeonidis, M., Trichas, M., Tugwell, K. E., Vaccari, M., Valtchanov, I., Vieira, J. D., Viero, M., Wang, L., Xu, C. K., and Zemcov, M. (2012). HerMES: deep number counts at 250 μm, 350 μm and 500 μm in the COSMOS and GOODS-N fields and the build-up of the cosmic infrared background. *Astron. Astrophys.*, 542:A58.

Bian, F., Fan, X., Jiang, L., McGreer, I., Dey, A., Green, R. F., Maiolino, R., Walter, F., Lee, K.-S., and Davé, R. (2013). The LBT Boötes Field Survey. I. The Rest-frame

Ultraviolet and Near-infrared Luminosity Functions and Clustering of Bright Lyman Break Galaxies at Z 3. *The Astrophysical Journal*, 774:28.

Bianchini, F., Bielewicz, P., Lapi, A., Gonzalez-Nuevo, J., Baccigalupi, C., de Zotti, G., Danese, L., Bourne, N., Cooray, A., Dunne, L., Dye, S., Eales, S., Ivison, R., Maddox, S., Negrello, M., Scott, D., Smith, M. W. L., and Valiante, E. (2015). Cross-correlation between the CMB Lensing Potential Measured by Planck and High-z Submillimeter Galaxies Detected by the Herschel-Atlas Survey. *The Astrophysical Journal*, 802:64.

Bielby, R., Hill, M. D., Shanks, T., Crighton, N. H. M., Infante, L., Bornancini, C. G., Francke, H., Héraudeau, P., Lambas, D. G., Metcalfe, N., Minniti, D., Padilla, N., Theuns, T., Tummuangpak, P., and Weilbacher, P. (2013). The VLT LBG Redshift Survey - III. The clustering and dynamics of Lyman-break galaxies at z $\sim$ 3. *MNRAS*, 430:425–449.

Blandford, R. D. and Begelman, M. C. (2004). Two-dimensional adiabatic flows on to a black hole - I. Fluid accretion. *MNRAS*, 349:68–86.

Boehringer, H., Chon, G., and Collins, C. A. (2014). The extended ROSAT-ESO Flux Limited X-ray Galaxy Cluster Survey (REFLEX II). IV. X-ray luminosity function and first constraints on cosmological parameters. *Astron. Astrophys.*, 570:A31.

Bolton, J. S., Haehnelt, M. G., Warren, S. J., Hewett, P. C., Mortlock, D. J., Venemans, B. P., McMahon, R. G., and Simpson, C. (2011). How neutral is the intergalactic medium surrounding the redshift z = 7.085 quasar ULAS J1120+0641? *MNRAS*, 416:L70–L74.

Bonato, M., Negrello, M., Cai, Z.-Y., De Zotti, G., Bressan, A., Lapi, A., Gruppioni, C., Spinoglio, L., and Danese, L. (2014). Exploring the early dust-obscured phase of galaxy formation with blind mid-/far-infrared spectroscopic surveys. *MNRAS*, 438:2547–2564.

Bondi, M., Ciliegi, P., Schinnerer, E., Smolcic, V., Jahnke, K., Carilli, C., and Zamorani, G. (2008). The VLA-COSMOS Survey. III. Further Catalog Analysis and the Radio Source Counts. *The Astrophysical Journal*, 681:1129–1135.

Bonfield, D. G., Jarvis, M. J., Hardcastle, M. J., Cooray, A., Hatziminaoglou, E., Ivison, R. J., Page, M. J., Stevens, J. A., de Zotti, G., Auld, R., Baes, M., Buttiglione, S., Cava, A., Dariush, A., Dunlop, J. S., Dunne, L., Dye, S., Eales, S., Fritz, J., Hopwood, R., Ibar, E., Maddox, S. J., Michalowski, M. J., Pascale, E., Pohlen, M., Rigby, E. E., Rodighiero, G., Serjeant, S., Smith, D. J. B., Temi, P., and van der Werf, P. (2011). Herschel-ATLAS: the link between accretion luminosity and star formation in quasar host galaxies. *MNRAS*, 416:13–21.

Bongiorno, A., Merloni, A., Brusa, M., Magnelli, B., Salvato, M., Mignoli, M., Zamorani, G., Fiore, F., Rosario, D., Mainieri, V., Hao, H., Comastri, A., Vignali, C., Balestra, I., Bardelli, S., Berta, S., Civano, F., Kampczyk, P., Le Floc'h, E., Lusso, E., Lutz, D., Pozzetti, L., Pozzi, F., Riguccini, L., Shankar, F., and Silverman, J. (2012). Accreting supermassive black holes in the COSMOS field and the connection to their host galaxies. *MNRAS*, 427:3103–3133.

Borys, C., Smail, I., Chapman, S. C., Blain, A. W., Alexander, D. M., and Ivison, R. J. (2005). The Relationship between Stellar and Black Hole Mass in Submillimeter Galaxies. *The Astrophysical Journal*, 635:853–863.

Bournaud, F., Dekel, A., Teyssier, R., Cacciato, M., Daddi, E., Juneau, S., and Shankar, F. (2011). Black Hole Growth and Active Galactic Nuclei Obscuration by Instability-driven Inflows in High-redshift Disk Galaxies Fed by Cold Streams. *The Astrophysical Journal Letters*, 741:L33.

Bourne, N., Dunne, L., Ivison, R. J., Maddox, S. J., Dickinson, M., and Frayer, D. T. (2011). Evolution of the far-infrared-radio correlation and infrared spectral energy distributions of massive galaxies over z= 0-2. *MNRAS*, 410:1155–1173.

Bouwens, R. J., Illingworth, G. D., Franx, M., Chary, R.-R., Meurer, G. R., Conselice, C. J., Ford, H., Giavalisco, M., and van Dokkum, P. (2009). UV Continuum Slope and Dust Obscuration from z 6 to z 2: The Star Formation Rate Density at High Redshift. *The Astrophysical Journal*, 705:936–961.

Bouwens, R. J., Illingworth, G. D., Oesch, P. A., Franx, M., Labbé, I., Trenti, M., van Dokkum, P., Carollo, C. M., González, V., Smit, R., and Magee, D. (2012). UV-continuum Slopes at z $\sim$ 4-7 from the HUDF09+ERS+CANDELS Observations: Discovery of a Well-defined UV Color-Magnitude Relationship for z $\geq$ 4 Star-forming Galaxies. *The Astrophysical Journal*, 754:83.

Bouwens, R. J., Illingworth, G. D., Oesch, P. A., Labbé, I., van Dokkum, P. G., Trenti, M., Franx, M., Smit, R., Gonzalez, V., and Magee, D. (2014). UV-continuum Slopes of >4000 z 4-8 Galaxies from the HUDF/XDF, HUDF09, ERS, CANDELS-South, and CANDELS-North Fields. *The Astrophysical Journal*, 793:115.

Bouwens, R. J., Illingworth, G. D., Oesch, P. A., Trenti, M., Labbé, I., Bradley, L., Carollo, M., van Dokkum, P. G., Gonzalez, V., Holwerda, B., Franx, M., Spitler, L., Smit, R., and Magee, D. (2015). UV Luminosity Functions at Redshifts z $\sim$ 4 to z $\sim$ 10: 10,000 Galaxies from HST Legacy Fields. *The Astrophysical Journal*, 803:34.

Bouwens, R. J., Oesch, P. A., Illingworth, G. D., Labbé, I., van Dokkum, P. G., Brammer, G., Magee, D., Spitler, L. R., Franx, M., Smit, R., Trenti, M., Gonzalez, V.,

and Carollo, C. M. (2013). Photometric Constraints on the Redshift of z ∼ 10 Candidate UDFj-39546284 from Deeper WFC3/IR+ACS+IRAC Observations over the HUDF. *The Astrophysical Journal Letters*, 765:L16.

Bower, R. G., Benson, A. J., Malbon, R., Helly, J. C., Frenk, C. S., Baugh, C. M., Cole, S., and Lacey, C. G. (2006). Breaking the hierarchy of galaxy formation. *MNRAS*, 370:645–655.

Bowler, R. A. A., Dunlop, J. S., McLure, R. J., McCracken, H. J., Milvang-Jensen, B., Furusawa, H., Taniguchi, Y., Le Fèvre, O., Fynbo, J. P. U., Jarvis, M. J., and Häußler, B. (2015). The galaxy luminosity function at z ≃ 6 and evidence for rapid evolution in the bright end from z ≃ 7 to 5. *MNRAS*, 452:1817–1840.

Boyle, B. J. and Terlevich, R. J. (1998). The cosmological evolution of the QSO luminosity density and of the star formation rate. *MNRAS*, 293:L49–L51.

Bressan, A., Chiosi, C., and Fagotto, F. (1994). Spectrophotometric evolution of elliptical galaxies. 1: Ultraviolet excess and color-magnitude-redshift relations. *The Astrophysical Journal Supp. Series*, 94:63–115.

Bressan, A., Granato, G. L., and Silva, L. (1998). Modelling intermediate age and old stellar populations in the Infrared. *Astron. Astrophys.*, 332:135–148.

Bressan, A., Silva, L., and Granato, G. L. (2002). Far infrared and radio emission in dusty starburst galaxies. *Astron. Astrophys.*, 392:377–391.

Bruzual A., G. and Charlot, S. (1993). Spectral evolution of stellar populations using isochrone synthesis. *The Astrophysical Journal*, 405:538–553.

Buat, V. (1992). Global recent star formation in normal galaxies from a multiwavelength study - Comparison with their gas content. *Astron. Astrophys.*, 264:444–454.

Buat, V., Iglesias-Páramo, J., Seibert, M., Burgarella, D., Charlot, S., Martin, D. C., Xu, C. K., Heckman, T. M., Boissier, S., Boselli, A., Barlow, T., Bianchi, L., Byun, Y.-I., Donas, J., Forster, K., Friedman, P. G., Jelinski, P., Lee, Y.-W., Madore, B. F., Malina, R., Milliard, B., Morissey, P., Neff, S., Rich, M., Schiminovitch, D., Siegmund, O., Small, T., Szalay, A. S., Welsh, B., and Wyder, T. K. (2005). Dust Attenuation in the Nearby Universe: A Comparison between Galaxies Selected in the Ultraviolet and in the Far-Infrared. *The Astrophysical Journal Letters*, 619:L51–L54.

Buat, V. and Xu, C. (1996). Star formation and dust extinction in disk galaxies. Comparison between the UV non-ionizing and the FIR emissions. *Astron. Astrophys.*, 306:61.

Burgarella, D., Buat, V., and Iglesias-Páramo, J. (2005). Star formation and dust attenuation properties in galaxies from a statistical ultraviolet-to-far-infrared analysis. *MNRAS*, 360:1413–1425.

Cai, Z.-Y., Lapi, A., Bressan, A., De Zotti, G., Negrello, M., and Danese, L. (2014). A Physical Model for the Evolving Ultraviolet Luminosity Function of High Redshift Galaxies and their Contribution to the Cosmic Reionization. *The Astrophysical Journal*, 785:65.

Cai, Z.-Y., Lapi, A., Xia, J.-Q., De Zotti, G., Negrello, M., Gruppioni, C., Rigby, E., Castex, G., Delabrouille, J., and Danese, L. (2013). A Hybrid Model for the Evolution of Galaxies and Active Galactic Nuclei in the Infrared. *The Astrophysical Journal*, 768:21.

Calzetti, D. (1999). UV Emission and bust properties of high redshift galaxies. *Ap&SS*, 266:243–253.

Calzetti, D., Armus, L., Bohlin, R. C., Kinney, A. L., Koornneef, J., and Storchi-Bergmann, T. (2000). The Dust Content and Opacity of Actively Star-forming Galaxies. *The Astrophysical Journal*, 533:682–695.

Calzetti, D., Kinney, A. L., and Storchi-Bergmann, T. (1994). Dust extinction of the stellar continua in starburst galaxies: The ultraviolet and optical extinction law. *The Astrophysical Journal*, 429:582–601.

Cao, X. (2010). Cosmological Evolution of Massive Black Holes: Effects of Eddington Ratio Distribution and Quasar Lifetime. *The Astrophysical Journal*, 725:388–393.

Capak, P. L., Carilli, C., Jones, G., Casey, C. M., Riechers, D., Sheth, K., Carollo, C. M., Ilbert, O., Karim, A., Lefevre, O., Lilly, S., Scoville, N., Smolcic, V., and Yan, L. (2015). Galaxies at redshifts 5 to 6 with systematically low dust content and high [C II] emission. *Nature*, 522:455–458.

Caplar, N., Lilly, S. J., and Trakhtenbrot, B. (2015). AGN Evolution from a Galaxy Evolution Viewpoint. *The Astrophysical Journal*, 811:148.

Caputi, K., I. (2011). in frontier science with the james webb space telescope. Available on line, http://realserver4v.stsci.edu/t/data/2011/06/2611/KarinaCaputi.pdf.

Caputi, K. I., Ilbert, O., Laigle, C., McCracken, H. J., Le Fèvre, O., Fynbo, J., Milvang-Jensen, B., Capak, P., Salvato, M., and Taniguchi, Y. (2015). Spitzer Bright, UltraVISTA Faint Sources in COSMOS: The Contribution to the Overall Population of Massive Galaxies at z = 3-7. *The Astrophysical Journal*, 810:73.

Carilli, C. L., Bertoldi, F., Rupen, M. P., Fan, X., Strauss, M. A., Menten, K. M., Kreysa, E., Schneider, D. P., Bertarini, A., Yun, M. S., and Zylka, R. (2001). A 250 GHz Survey of High-Redshift Quasars from the Sloan Digital Sky Survey. *The Astrophysical Journal*, 555:625–632.

Carilli, C. L., Lee, N., Capak, P., Schinnerer, E., Lee, K.-S., McCraken, H., Yun, M. S., Scoville, N., Smolčić, V., Giavalisco, M., Datta, A., Taniguchi, Y., and Urry, C. M. (2008). Star Formation Rates in Lyman Break Galaxies: Radio Stacking of LBGs in the COSMOS Field and the Sub-μJy Radio Source Population. *The Astrophysical Journal*, 689:883–888.

Carilli, C. L., Riechers, D., Walter, F., Maiolino, R., Wagg, J., Lentati, L., McMahon, R., and Wolfe, A. (2013). The Anatomy of an Extreme Starburst within 1.3 Gyr of the Big Bang Revealed by ALMA. *The Astrophysical Journal*, 763:120.

Carrera, F. J., Page, M. J., Stevens, J. A., Ivison, R. J., Dwelly, T., Ebrero, J., and Falocco, S. (2011). A strongly star-forming group: three massive galaxies associated with a quasi-stellar object. *MNRAS*, 413:2791–2807.

Casey, C. M., Narayanan, D., and Cooray, A. (2014). Dusty star-forming galaxies at high redshift. *Phys. Rep.*, 541:45–161.

Cassará, L. P., Maccagni, D., Garilli, B., Scodeggio, M., Thomas, R., Le Fèvre, O., Zamorani, G., Schaerer, D., Lemaux, B. C., Cassata, P., Le Brun, V., Pentericci, L., Tasca, L. A. M., Vanzella, E., Zucca, E., Amorín, R., Bardelli, S., Castellano, M., Cimatti, A., Cucciati, O., Durkalec, A., Fontana, A., Giavalisco, M., Grazian, A., Hathi, N. P., Ilbert, O., Paltani, S., Ribeiro, B., Sommariva, V., Talia, M., Tresse, L., Vergani, D., Capak, P., Charlot, S., Contini, T., de la Torre, S., Dunlop, J., Fotopoulou, S., Guaita, L., Koekemoer, A., Lopez-Sanjuan, C., Mellier, Y., Pforr, J., Salvato, M., Scoville, N., Taniguchi, Y., and Wang, P. W. (2016). The impact of the Star Formation Histories on the SFR-M_$*$ relation at z$\geq$2. *ArXiv e-prints*.

Chabrier, G. (2003). Galactic Stellar and Substellar Initial Mass Function. *PASP*, 115:763–795.

Chapman, S. C., Scott, D., Steidel, C. C., Borys, C., Halpern, M., Morris, S. L., Adelberger, K. L., Dickinson, M., Giavalisco, M., and Pettini, M. (2000). A search for the submillimetre counterparts to Lyman break galaxies. *MNRAS*, 319:318–330.

Charlot, S. and Bruzual, A. G. (1991). Stellar population synthesis revisited. *The Astrophysical Journal*, 367:126–140.

Charlot, S. and Fall, S. M. (2000). A Simple Model for the Absorption of Starlight by Dust in Galaxies. *The Astrophysical Journal*, 539:718–731.

Chen, C.-T. J., Hickox, R. C., Alberts, S., Brodwin, M., Jones, C., Murray, S. S., Alexander, D. M., Assef, R. J., Brown, M. J. I., Dey, A., Forman, W. R., Gorjian, V., Goulding, A. D., Le Floc'h, E., Jannuzi, B. T., Mullaney, J. R., and Pope, A. (2013). A Correlation between Star Formation Rate and Average Black Hole Accretion in Star-forming Galaxies. *The Astrophysical Journal*, 773:3.

Cirasuolo, M., Shankar, F., Granato, G. L., De Zotti, G., and Danese, L. (2005). Dynamical and Photometric Imprints of Feedback Processes on the Formation and Evolution of E/S0 Galaxies. *The Astrophysical Journal*, 629:816–824.

Citro, A., Pozzetti, L., Moresco, M., and Cimatti, A. (2016). Inferring the star-formation histories of the most massive and passive early-type galaxies at z < 0.3. *Astron. Astrophys.*, 592:A19.

Clemens, M. S., Negrello, M., De Zotti, G., Gonzalez-Nuevo, J., Bonavera, L., Cosco, G., Guarese, G., Boaretto, L., Salucci, P., Baccigalupi, C., Clements, D. L., Danese, L., Lapi, A., Mandolesi, N., Partridge, R. B., Perrotta, F., Serjeant, S., Scott, D., and Toffolatti, L. (2013). Dust and star formation properties of a complete sample of local galaxies drawn from the Planck Early Release Compact Source Catalogue. *MNRAS*, 433:695–711.

Clemens, M. S., Vega, O., Bressan, A., Granato, G. L., Silva, L., and Panuzzo, P. (2008). Modeling the spectral energy distribution of ULIRGs. I. The radio spectra. *Astron. Astrophys.*, 477:95–104.

Clements, D. L., Rigby, E., Maddox, S., Dunne, L., Mortier, A., Pearson, C., Amblard, A., Auld, R., Baes, M., Bonfield, D., Burgarella, D., Buttiglione, S., Cava, A., Cooray, A., Dariush, A., de Zotti, G., Dye, S., Eales, S., Frayer, D., Fritz, J., Gardner, J. P., Gonzalez-Nuevo, J., Herranz, D., Ibar, E., Ivison, R., Jarvis, M. J., Lagache, G., Leeuw, L., Lopez-Caniego, M., Negrello, M., Pascale, E., Pohlen, M., Rodighiero, G., Samui, S., Serjeant, S., Sibthorpe, B., Scott, D., Smith, D. J. B., Temi, P., Thompson, M., Valtchanov, I., van der Werf, P., and Verma, A. (2010). Herschel-ATLAS: Extragalactic number counts from 250 to 500 microns. *Astron. Astrophys.*, 518:L8.

Colbert, E. J. M., Heckman, T. M., Ptak, A. F., Strickland, D. K., and Weaver, K. A. (2004). Old and Young X-Ray Point Source Populations in Nearby Galaxies. *The Astrophysical Journal*, 602:231–248.

Condon, J. J. (1992). Radio emission from normal galaxies. *Annu. Rev. Astron. Astrophys.*, 30:575–611.

Condon, J. J., Helou, G., and Jarrett, T. H. (2002). A Second "Taffy" Galaxy Pair. *Astronomic. J.*, 123:1881–1891.

Conroy, C. (2013). Modeling the Panchromatic Spectral Energy Distributions of Galaxies. *Annu. Rev. Astron. Astrophys.*, 51:393–455.

Cooray, A., Calanog, J., Wardlow, J. L., Bock, J., Bridge, C., Burgarella, D., Bussmann, R. S., Casey, C. M., Clements, D., Conley, A., Farrah, D., Fu, H., Gavazzi, R., Ivison, R. J., La Porte, N., Lo Faro, B., Ma, B., Magdis, G., Oliver, S. J., Osage, W. A., Pérez-Fournon, I., Riechers, D., Rigopoulou, D., Scott, D., Viero, M., and Watson, D. (2014). HerMES: The Rest-frame UV Emission and a Lensing Model for the z = 6.34 Luminous Dusty Starburst Galaxy HFLS3. *The Astrophysical Journal*, 790:40.

Coppin, K., Chapin, E. L., Mortier, A. M. J., Scott, S. E., Borys, C., Dunlop, J. S., Halpern, M., Hughes, D. H., Pope, A., Scott, D., Serjeant, S., Wagg, J., Alexander, D. M., Almaini, O., Aretxaga, I., Babbedge, T., Best, P. N., Blain, A., Chapman, S., Clements, D. L., Crawford, M., Dunne, L., Eales, S. A., Edge, A. C., Farrah, D., Gaztañaga, E., Gear, W. K., Granato, G. L., Greve, T. R., Fox, M., Ivison, R. J., Jarvis, M. J., Jenness, T., Lacey, C., Lepage, K., Mann, R. G., Marsden, G., Martinez-Sansigre, A., Oliver, S., Page, M. J., Peacock, J. A., Pearson, C. P., Percival, W. J., Priddey, R. S., Rawlings, S., Rowan-Robinson, M., Savage, R. S., Seigar, M., Sekiguchi, K., Silva, L., Simpson, C., Smail, I., Stevens, J. A., Takagi, T., Vaccari, M., van Kampen, E., and Willott, C. J. (2006). The SCUBA Half-Degree Extragalactic Survey - II. Submillimetre maps, catalogue and number counts. *MNRAS*, 372:1621–1652.

Coppin, K. E. K., Geach, J. E., Almaini, O., Arumugam, V., Dunlop, J. S., Hartley, W. G., Ivison, R. J., Simpson, C. J., Smith, D. J. B., Swinbank, A. M., Blain, A. W., Bourne, N., Bremer, M., Conselice, C., Harrison, C. M., Mortlock, A., Chapman, S. C., Davies, L. J. M., Farrah, D., Gibb, A., Jenness, T., Karim, A., Knudsen, K. K., Ibar, E., Michalowski, M. J., Peacock, J. A., Rigopoulou, D., Robson, E. I., Scott, D., Stevens, J., and van der Werf, P. P. (2015). The SCUBA-2 Cosmology Legacy Survey: the submillimetre properties of Lyman-break galaxies at z = 3-5. *MNRAS*, 446:1293–1304.

Cortese, L., Boselli, A., Buat, V., Gavazzi, G., Boissier, S., Gil de Paz, A., Seibert, M., Madore, B. F., and Martin, D. C. (2006). UV Dust Attenuation in Normal Star-Forming Galaxies. I. Estimating the L_{TIR}/L_{FUV} Ratio. *The Astrophysical Journal*, 637:242–254.

Cortese, L., Boselli, A., Franzetti, P., Decarli, R., Gavazzi, G., Boissier, S., and Buat, V. (2008). Ultraviolet dust attenuation in star-forming galaxies - II. Calibrating the A(UV) versus L_{TIR}/L_{UV} relation. *MNRAS*, 386:1157–1168.

Courteau, S., Cappellari, M., de Jong, R. S., Dutton, A. A., Emsellem, E., Hoekstra, H., Koopmans, L. V. E., Mamon, G. A., Maraston, C., Treu, T., and Widrow, L. M. (2014). Galaxy masses. *Reviews of Modern Physics*, 86:47–119.

Cowie, L. L., Songaila, A., Hu, E. M., and Cohen, J. G. (1996). New Insight on Galaxy Formation and Evolution From Keck Spectroscopy of the Hawaii Deep Fields. *Astronomic. J.*, 112:839.

Croom, S. M., Richards, G. T., Shanks, T., Boyle, B. J., Strauss, M. A., Myers, A. D., Nichol, R. C., Pimbblet, K. A., Ross, N. P., Schneider, D. P., Sharp, R. G., and Wake, D. A. (2009). The 2dF-SDSS LRG and QSO survey: the QSO luminosity function at $0.4 < z < 2.6$. *MNRAS*, 399:1755–1772.

Croton, D. J., Springel, V., White, S. D. M., De Lucia, G., Frenk, C. S., Gao, L., Jenkins, A., Kauffmann, G., Navarro, J. F., and Yoshida, N. (2006). The many lives of active galactic nuclei: cooling flows, black holes and the luminosities and colours of galaxies. *MNRAS*, 365:11–28.

Croton, D. J., Stevens, A. R. H., Tonini, C., Garel, T., Bernyk, M., Bibiano, A., Hodkinson, L., Mutch, S. J., Poole, G. B., and Shattow, G. M. (2016). Semi-Analytic Galaxy Evolution (SAGE): Model Calibration and Basic Results. *The Astrophysical Journal Supp. Series*, 222:22.

Cucciati, O., Tresse, L., Ilbert, O., Le Fèvre, O., Garilli, B., Le Brun, V., Cassata, P., Franzetti, P., Maccagni, D., Scodeggio, M., Zucca, E., Zamorani, G., Bardelli, S., Bolzonella, M., Bielby, R. M., McCracken, H. J., Zanichelli, A., and Vergani, D. (2012). The star formation rate density and dust attenuation evolution over 12 Gyr with the VVDS surveys. *Astron. Astrophys.*, 539:A31.

da Cunha, E., Charlot, S., and Elbaz, D. (2008). A simple model to interpret the ultraviolet, optical and infrared emission from galaxies. *MNRAS*, 388:1595–1617.

da Cunha, E., Walter, F., Smail, I. R., Swinbank, A. M., Simpson, J. M., Decarli, R., Hodge, J. A., Weiss, A., van der Werf, P. P., Bertoldi, F., Chapman, S. C., Cox, P., Danielson, A. L. R., Dannerbauer, H., Greve, T. R., Ivison, R. J., Karim, A., and Thomson, A. (2015). An ALMA Survey of Sub-millimeter Galaxies in the Extended Chandra Deep Field South: Physical Properties Derived from Ultraviolet-to-radio Modeling. *The Astrophysical Journal*, 806:110.

Daddi, E., Dickinson, M., Morrison, G., Chary, R., Cimatti, A., Elbaz, D., Frayer, D., Renzini, A., Pope, A., Alexander, D. M., Bauer, F. E., Giavalisco, M., Huynh, M., Kurk, J., and Mignoli, M. (2007). Multiwavelength Study of Massive Galaxies at z∼2. I. Star Formation and Galaxy Growth. *The Astrophysical Journal*, 670:156–172.

Davies, L. J. M., Bremer, M. N., Stanway, E. R., and Lehnert, M. D. (2013). The detection of FIR emission from high-redshift star-forming galaxies in the ECDF-S. *MNRAS*, 433:2588–2603.

Davis, S. W. and Laor, A. (2011). The Radiative Efficiency of Accretion Flows in Individual Active Galactic Nuclei. *The Astrophysical Journal*, 728:98.

de Zotti, G., Massardi, M., Negrello, M., and Wall, J. (2010). Radio and millimeter continuum surveys and their astrophysical implications. *The Astronomy and Astrophysics Rev.*, 18:1–65.

de Zotti, G., Ricci, R., Mesa, D., Silva, L., Mazzotta, P., Toffolatti, L., and González-Nuevo, J. (2005). Predictions for high-frequency radio surveys of extragalactic sources. *Astron. Astrophys.*, 431:893–903.

Dekel, A., Sari, R., and Ceverino, D. (2009). Formation of Massive Galaxies at High Redshift: Cold Streams, Clumpy Disks, and Compact Spheroids. *The Astrophysical Journal*, 703:785–801.

Delvecchio, I., Gruppioni, C., Pozzi, F., Berta, S., Zamorani, G., Cimatti, A., Lutz, D., Scott, D., Vignali, C., Cresci, G., Feltre, A., Cooray, A., Vaccari, M., Fritz, J., Le Floc'h, E., Magnelli, B., Popesso, P., Oliver, S., Bock, J., Carollo, M., Contini, T., Le Févre, O., Lilly, S., Mainieri, V., Renzini, A., and Scodeggio, M. (2014). Tracing the cosmic growth of supermassive black holes to z $\sim$ 3 with Herschel. *MNRAS*, 439:2736–2754.

Delvecchio, I., Lutz, D., Berta, S., Rosario, D. J., Zamorani, G., Pozzi, F., Gruppioni, C., Vignali, C., Brusa, M., Cimatti, A., Clements, D. L., Cooray, A., Farrah, D., Lanzuisi, G., Oliver, S., Rodighiero, G., Santini, P., and Symeonidis, M. (2015). Mapping the average AGN accretion rate in the SFR-M_* plane for Herschel-selected galaxies at $0 < z \leq 2.5$. *MNRAS*, 449:373–389.

Devriendt, J. E. G., Guiderdoni, B., and Sadat, R. (1999). Galaxy modelling. I. Spectral energy distributions from far-UV to sub-mm wavelengths. *Astron. Astrophys.*, 350:381–398.

Di Matteo, T., Springel, V., and Hernquist, L. (2005). Energy input from quasars regulates the growth and activity of black holes and their host galaxies. *Nature*, 433:604–607.

Diemand, J., Kuhlen, M., and Madau, P. (2007). Formation and Evolution of Galaxy Dark Matter Halos and Their Substructure. *The Astrophysical Journal*, 667:859–877.

Dowell, C. D., Conley, A., Glenn, J., Arumugam, V., Asboth, V., Aussel, H., Bertoldi, F., Béthermin, M., Bock, J., Boselli, A., Bridge, C., Buat, V., Burgarella, D., Cabrera-Lavers, A., Casey, C. M., Chapman, S. C., Clements, D. L., Conversi, L., Cooray, A., Dannerbauer, H., De Bernardis, F., Ellsworth-Bowers, T. P., Farrah, D., Franceschini, A., Griffin, M., Gurwell, M. A., Halpern, M., Hatziminaoglou, E., Heinis, S., Ibar, E., Ivison, R. J., Laporte, N., Marchetti, L., Martínez-Navajas, P., Marsden, G., Morrison, G. E., Nguyen, H. T., O'Halloran, B., Oliver, S. J., Omont, A., Page, M. J., Papageorgiou, A., Pearson, C. P., Petitpas, G., Pérez-Fournon, I., Pohlen, M., Riechers, D., Rigopoulou, D., Roseboom, I. G., Rowan-Robinson, M., Sayers, J., Schulz, B., Scott, D., Seymour, N., Shupe, D. L., Smith, A. J., Streblyanska, A., Symeonidis, M., Vaccari, M., Valtchanov, I., Vieira, J. D., Viero, M., Wang, L., Wardlow, J., Xu, C. K., and Zemcov, M. (2014). HerMES: Candidate High-redshift Galaxies Discovered with Herschel/SPIRE. *The Astrophysical Journal*, 780:75.

Draine, B. T. (2011). *Physics of the Interstellar and Intergalactic Medium*.

Draine, B. T. and Lazarian, A. (1998). Diffuse Galactic Emission from Spinning Dust Grains. *The Astrophysical Journal Letters*, 494:L19–L22.

Dubois, Y., Volonteri, M., Silk, J., Devriendt, J., and Slyz, A. (2014). Black hole evolution - II. Spinning black holes in a supernova-driven turbulent interstellar medium. *MNRAS*, 440:2333–2346.

Duncan, K., Conselice, C. J., Mortlock, A., Hartley, W. G., Guo, Y., Ferguson, H. C., Davé, R., Lu, Y., Ownsworth, J., Ashby, M. L. N., Dekel, A., Dickinson, M., Faber, S., Giavalisco, M., Grogin, N., Kocevski, D., Koekemoer, A., Somerville, R. S., and White, C. E. (2014). The mass evolution of the first galaxies: stellar mass functions and star formation rates at $4 < z < 7$ in the CANDELS GOODS-South field. *MNRAS*, 444:2960–2984.

Dunlop, J. S., McLure, R. J., Biggs, A. D., Geach, J. E., Michalowski, M. J., Ivison, R. J., Rujopakarn, W., van Kampen, E., Kirkpatrick, A., Pope, A., Scott, D., Swinbank, A. M., Targett, T. A., Aretxaga, I., Austermann, J. E., Best, P. N., Bruce, V. A., Chapin, E. L., Charlot, S., Cirasuolo, M., Coppin, K. E. K., Ellis, R. S., Finkelstein, S. L., Hayward, C. C., Hughes, D. H., Ibar, E., Khochfar, S., Koprowski, M. P., Narayanan, D., Papovich, C., Peacock, J. A., Robertson, B., Vernstrom, T., van der Werf, P. P., Wilson, G. W., and Yun, M. (2016). A deep ALMA image of the Hubble Ultra Deep Field. *ArXiv e-prints*.

Dutton, A. A., Macciò, A. V., Stinson, G. S., Gutcke, T. A., Penzo, C., and Buck, T. (2015). The response of dark matter haloes to elliptical galaxy formation: a new test for quenching scenarios. *MNRAS*, 453:2447–2464.

Dye, S., Furlanetto, C., Swinbank, A. M., Vlahakis, C., Nightingale, J. W., Dunne, L., Eales, S. A., Smail, I., Oteo, I., Hunter, T., Negrello, M., Dannerbauer, H., Ivison, R. J., Gavazzi, R., Cooray, A., and van der Werf, P. (2015). Revealing the complex nature of the strong gravitationally lensed system H-ATLAS J090311.6+003906 using ALMA. *MNRAS*, 452:2258–2268.

Eales, S. A. (2015). Practical cosmology with lenses. *MNRAS*, 446:3224–3234.

Elbaz, D., Daddi, E., Le Borgne, D., Dickinson, M., Alexander, D. M., Chary, R.-R., Starck, J.-L., Brandt, W. N., Kitzbichler, M., MacDonald, E., Nonino, M., Popesso, P., Stern, D., and Vanzella, E. (2007). The reversal of the star formation-density relation in the distant universe. *Astron. Astrophys.*, 468:33–48.

Elvis, M., Wilkes, B. J., McDowell, J. C., Green, R. F., Bechtold, J., Willner, S. P., Oey, M. S., Polomski, E., and Cutri, R. (1994). Atlas of quasar energy distributions. *The Astrophysical Journal Supp. Series*, 95:1–68.

Erfanianfar, G., Popesso, P., Finoguenov, A., Wilman, D., Wuyts, S., Biviano, A., Salvato, M., Mirkazemi, M., Morselli, L., Ziparo, F., Nandra, K., Lutz, D., Elbaz, D., Dickinson, M., Tanaka, M., Altieri, M. B., Aussel, H., Bauer, F., Berta, S., Bielby, R. M., Brandt, N., Cappelluti, N., Cimatti, A., Cooper, M. C., Fadda, D., Ilbert, O., Le Floc'h, E., Magnelli, B., Mulchaey, J. S., Nordon, R., Newman, J. A., Poglitsch, A., and Pozzi, F. (2016). Non-linearity and environmental dependence of the star-forming galaxies main sequence. *MNRAS*, 455:2839–2851.

Fabian, A. C. (1999). The obscured growth of massive black holes. *MNRAS*, 308:L39–L43.

Fan, L., Lapi, A., Bressan, A., Bernardi, M., De Zotti, G., and Danese, L. (2010). Cosmic Evolution of Size and Velocity Dispersion for Early-type Galaxies. *The Astrophysical Journal*, 718:1460–1475.

Fan, L.-L., Lapi, A., Bressan, A., Nonino, M., De Zotti, G., and Danese, L. (2014). The star formation history of redshift z 2 galaxies: the role of the infrared prior. *Research in Astronomy and Astrophysics*, 14:15–34.

Fan, X., Strauss, M. A., Richards, G. T., Hennawi, J. F., Becker, R. H., White, R. L., Diamond-Stanic, A. M., Donley, J. L., Jiang, L., Kim, J. S., Vestergaard, M., Young, J. E., Gunn, J. E., Lupton, R. H., Knapp, G. R., Schneider, D. P., Brandt, W. N., Bahcall, N. A., Barentine, J. C., Brinkmann, J., Brewington, H. J., Fukugita, M., Harvanek, M., Kleinman, S. J., Krzesinski, J., Long, D., Neilsen, Jr., E. H., Nitta, A., Snedden, S. A., and Voges, W. (2006). A Survey of z>5.7 Quasars in the Sloan Digital Sky Survey. IV. Discovery of Seven Additional Quasars. *Astronomic. J.*, 131:1203–1209.

Fanidakis, N., Baugh, C. M., Benson, A. J., Bower, R. G., Cole, S., Done, C., and Frenk, C. S. (2011). Grand unification of AGN activity in the ΛCDM cosmology. *MNRAS*, 410:53–74.

Fanidakis, N., Baugh, C. M., Benson, A. J., Bower, R. G., Cole, S., Done, C., Frenk, C. S., Hickox, R. C., Lacey, C., and Del P. Lagos, C. (2012). The evolution of active galactic nuclei across cosmic time: what is downsizing? *MNRAS*, 419:2797–2820.

Ferrarese, L. and Ford, H. (2005). Supermassive Black Holes in Galactic Nuclei: Past, Present and Future Research. *Space Science Rev.*, 116:523–624.

Ferrarese, L. and Merritt, D. (2000). A Fundamental Relation between Supermassive Black Holes and Their Host Galaxies. *The Astrophysical Journal Letters*, 539:L9–L12.

Finkelstein, S. L., Papovich, C., Dickinson, M., Song, M., Tilvi, V., Koekemoer, A. M., Finkelstein, K. D., Mobasher, B., Ferguson, H. C., Giavalisco, M., Reddy, N., Ashby, M. L. N., Dekel, A., Fazio, G. G., Fontana, A., Grogin, N. A., Huang, J.-S., Kocevski, D., Rafelski, M., Weiner, B. J., and Willner, S. P. (2013). A galaxy rapidly forming stars 700 million years after the Big Bang at redshift 7.51. *Nature*, 502:524–527.

Finkelstein, S. L., Ryan, Jr., R. E., Papovich, C., Dickinson, M., Song, M., Somerville, R. S., Ferguson, H. C., Salmon, B., Giavalisco, M., Koekemoer, A. M., Ashby, M. L. N., Behroozi, P., Castellano, M., Dunlop, J. S., Faber, S. M., Fazio, G. G., Fontana, A., Grogin, N. A., Hathi, N., Jaacks, J., Kocevski, D. D., Livermore, R., McLure, R. J., Merlin, E., Mobasher, B., Newman, J. A., Rafelski, M., Tilvi, V., and Willner, S. P. (2015a). The Evolution of the Galaxy Rest-frame Ultraviolet Luminosity Function over the First Two Billion Years. *The Astrophysical Journal*, 810:71.

Finkelstein, S. L., Song, M., Behroozi, P., Somerville, R. S., Papovich, C., Milosavljević, M., Dekel, A., Narayanan, D., Ashby, M. L. N., Cooray, A., Fazio, G. G., Ferguson, H. C., Koekemoer, A. M., Salmon, B., and Willner, S. P. (2015b). An Increasing Stellar Baryon Fraction in Bright Galaxies at High Redshift. *The Astrophysical Journal*, 814:95.

Fioc, M. and Rocca-Volmerange, B. (1997). PEGASE: a UV to NIR spectral evolution model of galaxies. Application to the calibration of bright galaxy counts. *Astron. Astrophys.*, 326:950–962.

Fiore, F., Puccetti, S., Grazian, A., Menci, N., Shankar, F., Santini, P., Piconcelli, E., Koekemoer, A. M., Fontana, A., Boutsia, K., Castellano, M., Lamastra, A., Malacaria, C., Feruglio, C., Mathur, S., Miller, N., and Pannella, M. (2012). Faint

high-redshift AGN in the Chandra deep field south: the evolution of the AGN luminosity function and black hole demography. *Astron. Astrophys.*, 537:A16.

Fixsen, D. J., Dwek, E., Mather, J. C., Bennett, C. L., and Shafer, R. A. (1998). The Spectrum of the Extragalactic Far-Infrared Background from the COBE FIRAS Observations. *The Astrophysical Journal*, 508:123–128.

Franceschini, A., Hasinger, G., Miyaji, T., and Malquori, D. (1999). On the relationship between galaxy formation and quasar evolution. *MNRAS*, 310:L5–L9.

Frenk, C. S. and White, S. D. M. (2012). Dark matter and cosmic structure. *Annalen der Physik*, 524:507–534.

Fujimoto, S., Ouchi, M., Ono, Y., Shibuya, T., Ishigaki, M., Nagai, H., and Momose, R. (2016). ALMA Census of Faint 1.2 mm Sources Down to 0.02 mJy: Extragalactic Background Light and Dust-poor, High-z Galaxies. *The Astrophysical Journal Supp. Series*, 222:1.

Gallazzi, A., Charlot, S., Brinchmann, J., and White, S. D. M. (2006). Ages and metallicities of early-type galaxies in the Sloan Digital Sky Survey: new insight into the physical origin of the colour-magnitude and the Mg_2-σ_V relations. *MNRAS*, 370:1106–1124.

Gawiser, E., Francke, H., Lai, K., Schawinski, K., Gronwall, C., Ciardullo, R., Quadri, R., Orsi, A., Barrientos, L. F., Blanc, G. A., Fazio, G., Feldmeier, J. J., Huang, J.-s., Infante, L., Lira, P., Padilla, N., Taylor, E. N., Treister, E., Urry, C. M., van Dokkum, P. G., and Virani, S. N. (2007). Lyα-Emitting Galaxies at z = 3.1: L* Progenitors Experiencing Rapid Star Formation. *The Astrophysical Journal*, 671:278–284.

Gebhardt, K., Bender, R., Bower, G., Dressler, A., Faber, S. M., Filippenko, A. V., Green, R., Grillmair, C., Ho, L. C., Kormendy, J., Lauer, T. R., Magorrian, J., Pinkney, J., Richstone, D., and Tremaine, S. (2000). A Relationship between Nuclear Black Hole Mass and Galaxy Velocity Dispersion. *The Astrophysical Journal Letters*, 539:L13–L16.

Georgantopoulos, I., Rovilos, E., Akylas, A., Comastri, A., Ranalli, P., Vignali, C., Balestra, I., Gilli, R., and Cappelluti, N. (2011). On the L_x - L_{6m} ratio as a diagnostic for Compton-thick AGN. *Astron. Astrophys.*, 534:A23.

Goldader, J. D., Meurer, G., Heckman, T. M., Seibert, M., Sanders, D. B., Calzetti, D., and Steidel, C. C. (2002). Far-Infrared Galaxies in the Far-Ultraviolet. *The Astrophysical Journal*, 568:651–678.

González, V., Labbé, I., Bouwens, R. J., Illingworth, G., Franx, M., and Kriek, M. (2011). Evolution of Galaxy Stellar Mass Functions, Mass Densities, and Mass-to-light Ratios from z 7 to z 4. *The Astrophysical Journal Letters*, 735:L34.

Gonzalez-Nuevo, J., Lapi, A., Fleuren, S., Bressan, S., Danese, L., De Zotti, G., Negrello, M., Cai, Z.-Y., Fan, L., Sutherland, W., Baes, M., Baker, A. J., Clements, D. L., Cooray, A., Dannerbauer, H., Dunne, L., Dye, S., Eales, S., Frayer, D. T., Harris, A. I., Ivison, R., Jarvis, M. J., Michalowski, M. J., Lopez-Caniego, M., Rodighiero, G., Rowlands, K., Serjeant, S., Scott, D., van der Werf, P., Auld, R., Buttiglione, S., Cava, A., Dariush, A., Fritz, J., Hopwood, R., Ibar, E., Maddox, S., Pascale, E., Pohlen, M., Rigby, E., Smith, D., and Temi, P. (2012). Herschel-ATLAS: Toward a Sample of ˜1000 Strongly Lensed Galaxies. *The Astrophysical Journal*, 749:65.

Gordon, K. D., Clayton, G. C., Witt, A. N., and Misselt, K. A. (2000). The Flux Ratio Method for Determining the Dust Attenuation of Starburst Galaxies. *The Astrophysical Journal*, 533:236–244.

Graham, A. W. (2007). The black hole mass - spheroid luminosity relation. *MNRAS*, 379:711–722.

Graham, A. W., Onken, C. A., Athanassoula, E., and Combes, F. (2011). An expanded M_{bh}-σ diagram, and a new calibration of active galactic nuclei masses. *MNRAS*, 412:2211–2228.

Granato, G. L., De Zotti, G., Silva, L., Bressan, A., and Danese, L. (2004). A Physical Model for the Coevolution of QSOs and Their Spheroidal Hosts. *The Astrophysical Journal*, 600:580–594.

Grazian, A., Fontana, A., Santini, P., Dunlop, J. S., Ferguson, H. C., Castellano, M., Amorin, R., Ashby, M. L. N., Barro, G., Behroozi, P., Boutsia, K., Caputi, K. I., Chary, R. R., Dekel, A., Dickinson, M. E., Faber, S. M., Fazio, G. G., Finkelstein, S. L., Galametz, A., Giallongo, E., Giavalisco, M., Grogin, N. A., Guo, Y., Kocevski, D., Koekemoer, A. M., Koo, D. C., Lee, K.-S., Lu, Y., Merlin, E., Mobasher, B., Nonino, M., Papovich, C., Paris, D., Pentericci, L., Reddy, N., Renzini, A., Salmon, B., Salvato, M., Sommariva, V., Song, M., and Vanzella, E. (2015). The galaxy stellar mass function at 3.5 *leqz leq* 7.5 in the CANDELS/UDS, GOODS-South, and HUDF fields. *Astron. Astrophys.*, 575:A96.

Greene, J. E. and Ho, L. C. (2007). The Mass Function of Active Black Holes in the Local Universe. *The Astrophysical Journal*, 667:131–148.

Groves, B., Dopita, M. A., Sutherland, R. S., Kewley, L. J., Fischera, J., Leitherer, C., Brandl, B., and van Breugel, W. (2008). Modeling the Pan-Spectral Energy Distribution of Starburst Galaxies. IV. The Controlling Parameters of the Starburst SED. *The Astrophysical Journal Supp. Series*, 176:438–456.

Gruppioni, C., Calura, F., Pozzi, F., Delvecchio, I., Berta, S., De Lucia, G., Fontanot, F., Franceschini, A., Marchetti, L., Menci, N., Monaco, P., and Vaccari, M. (2015). Star formation in Herschel's Monsters versus semi-analytic models. *MNRAS*, 451:3419–3426.

Gruppioni, C., Pozzi, F., Rodighiero, G., Delvecchio, I., Berta, S., Pozzetti, L., Zamorani, G., Andreani, P., Cimatti, A., Ilbert, O., Le Floc'h, E., Lutz, D., Magnelli, B., Marchetti, L., Monaco, P., Nordon, R., Oliver, S., Popesso, P., Riguccini, L., Roseboom, I., Rosario, D. J., Sargent, M., Vaccari, M., Altieri, B., Aussel, H., Bongiovanni, A., Cepa, J., Daddi, E., Domínguez-Sánchez, H., Elbaz, D., Förster Schreiber, N., Genzel, R., Iribarrem, A., Magliocchetti, M., Maiolino, R., Poglitsch, A., Pérez García, A., Sanchez-Portal, M., Sturm, E., Tacconi, L., Valtchanov, I., Amblard, A., Arumugam, V., Bethermin, M., Bock, J., Boselli, A., Buat, V., Burgarella, D., Castro-Rodríguez, N., Cava, A., Chanial, P., Clements, D. L., Conley, A., Cooray, A., Dowell, C. D., Dwek, E., Eales, S., Franceschini, A., Glenn, J., Griffin, M., Hatziminaoglou, E., Ibar, E., Isaak, K., Ivison, R. J., Lagache, G., Levenson, L., Lu, N., Madden, S., Maffei, B., Mainetti, G., Nguyen, H. T., O'Halloran, B., Page, M. J., Panuzzo, P., Papageorgiou, A., Pearson, C. P., Pérez-Fournon, I., Pohlen, M., Rigopoulou, D., Rowan-Robinson, M., Schulz, B., Scott, D., Seymour, N., Shupe, D. L., Smith, A. J., Stevens, J. A., Symeonidis, M., Trichas, M., Tugwell, K. E., Vigroux, L., Wang, L., Wright, G., Xu, C. K., Zemcov, M., Bardelli, S., Carollo, M., Contini, T., Le Févre, O., Lilly, S., Mainieri, V., Renzini, A., Scodeggio, M., and Zucca, E. (2013). The Herschel PEP/HerMES luminosity function - I. Probing the evolution of PACS selected Galaxies to z $\simeq$ 4. *MNRAS*, 432:23–52.

Guaita, L., Gawiser, E., Padilla, N., Francke, H., Bond, N. A., Gronwall, C., Ciardullo, R., Feldmeier, J. J., Sinawa, S., Blanc, G. A., and Virani, S. (2010). Lyα-emitting Galaxies at z = 2.1 in ECDF-S: Building Blocks of Typical Present-day Galaxies? *The Astrophysical Journal*, 714:255–269.

Gültekin, K., Richstone, D. O., Gebhardt, K., Lauer, T. R., Tremaine, S., Aller, M. C., Bender, R., Dressler, A., Faber, S. M., Filippenko, A. V., Green, R., Ho, L. C., Kormendy, J., Magorrian, J., Pinkney, J., and Siopis, C. (2009). The M-σ and M-L Relations in Galactic Bulges, and Determinations of Their Intrinsic Scatter. *The Astrophysical Journal*, 698:198–221.

Guo, Q., White, S., Boylan-Kolchin, M., De Lucia, G., Kauffmann, G., Lemson, G., Li, C., Springel, V., and Weinmann, S. (2011). From dwarf spheroidals to cD galaxies: simulating the galaxy population in a ΛCDM cosmology. *MNRAS*, 413:101–131.

Hao, C.-N., Kennicutt, R. C., Johnson, B. D., Calzetti, D., Dale, D. A., and Moustakas, J. (2011). Dust-corrected Star Formation Rates of Galaxies. II. Combinations of Ultraviolet and Infrared Tracers. *The Astrophysical Journal*, 741:124.

Hao, H., Elvis, M., Civano, F., Zamorani, G., Ho, L. C., Comastri, A., Brusa, M., Bongiorno, A., Merloni, A., Trump, J. R., Salvato, M., Impey, C. D., Koekemoer, A. M., Lanzuisi, G., Celotti, A., Jahnke, K., Vignali, C., Silverman, J. D., Urry, C. M., Schawinski, K., and Capak, P. (2014). Spectral energy distributions of type 1 AGN in XMM-COSMOS - II. Shape evolution. *MNRAS*, 438:1288–1304.

Häring, N. and Rix, H.-W. (2004). On the Black Hole Mass-Bulge Mass Relation. *The Astrophysical Journal Letters*, 604:L89–L92.

Harris, K., Farrah, D., Schulz, B., Hatziminaoglou, E., Viero, M., Anderson, N., Béthermin, M., Chapman, S., Clements, D. L., Cooray, A., Efstathiou, A., Feltre, A., Hurley, P., Ibar, E., Lacy, M., Oliver, S., Page, M. J., Pérez-Fournon, I., Petty, S. M., Pitchford, L. K., Rigopoulou, D., Scott, D., Symeonidis, M., Vieira, J., and Wang, L. (2016). Star formation rates in luminous quasars at $2 < z < 3$. *MNRAS*, 457:4179–4194.

Harrison, C. M., Alexander, D. M., Mullaney, J. R., Altieri, B., Coia, D., Charmandaris, V., Daddi, E., Dannerbauer, H., Dasyra, K., Del Moro, A., Dickinson, M., Hickox, R. C., Ivison, R. J., Kartaltepe, J., Le Floc'h, E., Leiton, R., Magnelli, B., Popesso, P., Rovilos, E., Rosario, D., and Swinbank, A. M. (2012). No Clear Submillimeter Signature of Suppressed Star Formation among X-Ray Luminous Active Galactic Nuclei. *The Astrophysical Journal Letters*, 760:L15.

Harrison, C. M., Simpson, J. M., Stanley, F., Alexander, D. M., Daddi, E., Mullaney, J. R., Pannella, M., Rosario, D. J., and Smail, I. (2016). ALMA resolves extended star formation in high-z AGN host galaxies. *MNRAS*, 457:L122–L126.

Hatsukade, B., Kohno, K., Umehata, H., Aretxaga, I., Caputi, K. I., Dunlop, J. S., Ikarashi, S., Iono, D., Ivison, R. J., Lee, M., Makiya, R., Matsuda, Y., Motohara, K., Nakanishi, K., Ohta, K., Tadaki, K.-i., Tamura, Y., Wang, W.-H., Wilson, G. W., Yamaguchi, Y., and Yun, M. S. (2016). SXDF-ALMA 2-arcmin^2 deep survey: 1.1-mm number counts. *Publ. Astron. Soc. Japan*, 68:36.

Heckman, T. M., Kauffmann, G., Brinchmann, J., Charlot, S., Tremonti, C., and White, S. D. M. (2004). Present-Day Growth of Black Holes and Bulges: The Sloan Digital Sky Survey Perspective. *The Astrophysical Journal*, 613:109–118.

Heckman, T. M., Robert, C., Leitherer, C., Garnett, D. R., and van der Rydt, F. (1998). The Ultraviolet Spectroscopic Properties of Local Starbursts: Implications at High Redshift. *The Astrophysical Journal*, 503:646–661.

Helou, G., Soifer, B. T., and Rowan-Robinson, M. (1985). Thermal infrared and non-thermal radio - Remarkable correlation in disks of galaxies. *The Astrophysical Journal Letters*, 298:L7–L11.

Hickox, R. C., Mullaney, J. R., Alexander, D. M., Chen, C.-T. J., Civano, F. M., Goulding, A. D., and Hainline, K. N. (2014). Black Hole Variability and the Star Formation-Active Galactic Nucleus Connection: Do All Star-forming Galaxies Host an Active Galactic Nucleus? *The Astrophysical Journal*, 782:9.

Hickox, R. C., Wardlow, J. L., Smail, I., Myers, A. D., Alexander, D. M., Swinbank, A. M., Danielson, A. L. R., Stott, J. P., Chapman, S. C., Coppin, K. E. K., Dunlop, J. S., Gawiser, E., Lutz, D., van der Werf, P., and Weiß, A. (2012). The LABOCA survey of the Extended Chandra Deep Field-South: clustering of submillimetre galaxies. *MNRAS*, 421:284–295.

Hildebrandt, H., Pielorz, J., Erben, T., van Waerbeke, L., Simon, P., and Capak, P. (2009). CARS: the CFHTLS-Archive-Research Survey. II. Weighing dark matter halos of Lyman-break galaxies at z = 3-5. *Astron. Astrophys.*, 498:725–736.

Hirashita, H., Inoue, A. K., Kamaya, H., and Shibai, H. (2001). Emission from dust in galaxies: Metallicity dependence. *Astron. Astrophys.*, 366:83–90.

Ho, L. C. and Kim, M. (2014). The Black Hole Mass Scale of Classical and Pseudo Bulges in Active Galaxies. *The Astrophysical Journal*, 789:17.

Hopkins, A. M., Connolly, A. J., Haarsma, D. B., and Cram, L. E. (2001). Toward a Resolution of the Discrepancy between Different Estimators of Star Formation Rate. *Astronomic. J.*, 122:288–296.

Hopkins, P. F., Cox, T. J., Hernquist, L., Narayanan, D., Hayward, C. C., and Murray, N. (2013). Star formation in galaxy mergers with realistic models of stellar feedback and the interstellar medium. *MNRAS*, 430:1901–1927.

Hopkins, P. F. and Hernquist, L. (2009). Quasars Are Not Light Bulbs: Testing Models of Quasar Lifetimes with the Observed Eddington Ratio Distribution. *The Astrophysical Journal*, 698:1550–1569.

Hopkins, P. F., Hernquist, L., Martini, P., Cox, T. J., Robertson, B., Di Matteo, T., and Springel, V. (2005). A Physical Model for the Origin of Quasar Lifetimes. *The Astrophysical Journal Letters*, 625:L71–L74.

Hopkins, P. F., Richards, G. T., and Hernquist, L. (2007). An Observational Determination of the Bolometric Quasar Luminosity Function. *The Astrophysical Journal*, 654:731–753.

Hopkins, P. F., Somerville, R. S., Hernquist, L., Cox, T. J., Robertson, B., and Li, Y. (2006). The Relation between Quasar and Merging Galaxy Luminosity Functions and the Merger-driven Star Formation History of the Universe. *The Astrophysical Journal*, 652:864–888.

Hopkins, P. F., Torrey, P., Faucher-Giguere, C.-A., Quataert, E., and Murray, N. (2016). Stellar and quasar feedback in concert: effects on AGN accretion, obscuration, and outflows. *MNRAS*, 458:816–831.

Howarth, I. D. (1983). LMC and galactic extinction. *MNRAS*, 203:301–304.

Howell, J. H., Armus, L., Mazzarella, J. M., Evans, A. S., Surace, J. A., Sanders, D. B., Petric, A., Appleton, P., Bothun, G., Bridge, C., Chan, B. H. P., Charmandaris, V., Frayer, D. T., Haan, S., Inami, H., Kim, D.-C., Lord, S., Madore, B. F., Melbourne, J., Schulz, B., U, V., Vavilkin, T., Veilleux, S., and Xu, K. (2010). The Great Observatories All-sky LIRG Survey: Comparison of Ultraviolet and Far-infrared Properties. *The Astrophysical Journal*, 715:572–588.

Ikarashi, S., Ivison, R. J., Caputi, K. I., Aretxaga, I., Dunlop, J. S., Hatsukade, B., Hughes, D. H., Iono, D., Izumi, T., Kawabe, R., Kohno, K., Lagos, C. D. P., Motohara, K., Nakanishi, K., Ohta, K., Tamura, Y., Umehata, H., Wilson, G. W., Yabe, K., and Yun, M. S. (2015). Compact Starbursts in z ∼ 3-6 Submillimeter Galaxies Revealed by ALMA. *The Astrophysical Journal*, 810:133.

Ilbert, O., McCracken, H. J., Le Fèvre, O., Capak, P., Dunlop, J., Karim, A., Renzini, M. A., Caputi, K., Boissier, S., Arnouts, S., Aussel, H., Comparat, J., Guo, Q., Hudelot, P., Kartaltepe, J., Kneib, J. P., Krogager, J. K., Le Floc'h, E., Lilly, S., Mellier, Y., Milvang-Jensen, B., Moutard, T., Onodera, M., Richard, J., Salvato, M., Sanders, D. B., Scoville, N., Silverman, J. D., Taniguchi, Y., Tasca, L., Thomas, R., Toft, S., Tresse, L., Vergani, D., Wolk, M., and Zirm, A. (2013). Mass assembly in quiescent and star-forming galaxies since z ≃ 4 from UltraVISTA. *Astron. Astrophys.*, 556:A55.

Ivezic, Z., Tyson, J. A., Abel, B., Acosta, E., Allsman, R., AlSayyad, Y., Anderson, S. F., Andrew, J., Angel, R., Angeli, G., Ansari, R., Antilogus, P., Arndt, K. T., Astier, P., Aubourg, E., Axelrod, T., Bard, D. J., Barr, J. D., Barrau, A., Bartlett, J. G., Bauman, B. J., Beaumont, S., Becker, A. C., Becla, J., Beldica, C., Bellavia, S., Blanc, G., Blandford, R. D., Bloom, J. S., Bogart, J., Borne, K., Bosch, J. F., Boutigny, D., Brandt, W. N., Brown, M. E., Bullock, J. S., Burchat, P., Burke, D. L., Cagnoli, G., Calabrese, D., Chandrasekharan, S., Chesley, S., Cheu, E. C., Chiang, J., Claver, C. F., Connolly, A. J., Cook, K. H., Cooray, A., Covey, K. R., Cribbs, C., Cui, W., Cutri, R., Daubard, G., Daues, G., Delgado, F., Digel, S., Doherty, P., Dubois, R., Dubois-Felsmann, G. P., Durech, J., Eracleous, M., Ferguson, H., Frank, J., Freemon, M., Gangler, E., Gawiser, E., Geary, J. C., Gee, P., Geha, M., Gibson, R. R., Gilmore, D. K., Glanzman, T., Goodenow, I., Gressler, W. J., Gris, P., Guyonnet, A., Hascall, P. A., Haupt, J., Hernandez, F., Hogan, C., Huang, D., Huffer, M. E., Innes, W. R., Jacoby, S. H., Jain, B., Jee, J., Jernigan, J. G., Jevremovic, D.,

Johns, K., Jones, R. L., Juramy-Gilles, C., Juric, M., Kahn, S. M., Kalirai, J. S., Kallivayalil, N., Kalmbach, B., Kantor, J. P., Kasliwal, M. M., Kessler, R., Kirkby, D., Knox, L., Kotov, I., Krabbendam, V. L., Krughoff, S., Kubanek, P., Kuczewski, J., Kulkarni, S., Lambert, R., Le Guillou, L., Levine, D., Liang, M., Lim, K., Lintott, C., Lupton, R. H., Mahabal, A., Marshall, P., Marshall, S., May, M., McKercher, R., Migliore, M., Miller, M., Mills, D. J., Monet, D. G., Moniez, M., Neill, D. R., Nief, J., Nomerotski, A., Nordby, M., O'Connor, P., Oliver, J., Olivier, S. S., Olsen, K., Ortiz, S., Owen, R. E., Pain, R., Peterson, J. R., Petry, C. E., Pierfederici, F., Pietrowicz, S., Pike, R., Pinto, P. A., Plante, R., Plate, S., Price, P. A., Prouza, M., Radeka, V., Rajagopal, J., Rasmussen, A., Regnault, N., Ridgway, S. T., Ritz, S., Rosing, W., Roucelle, C., Rumore, M. R., Russo, S., Saha, A., Sassolas, B., Schalk, T. L., Schindler, R. H., Schneider, D. P., Schumacher, G., Sebag, J., Sembroski, G. H., Seppala, L. G., Shipsey, I., Silvestri, N., Smith, J. A., Smith, R. C., Strauss, M. A., Stubbs, C. W., Sweeney, D., Szalay, A., Takacs, P., Thaler, J. J., Van Berg, R., Vanden Berk, D., Vetter, K., Virieux, F., Xin, B., Walkowicz, L., Walter, C. W., Wang, D. L., Warner, M., Willman, B., Wittman, D., Wolff, S. C., Wood-Vasey, W. M., Yoachim, P., Zhan, H., and for the LSST Collaboration (2008). LSST: from Science Drivers to Reference Design and Anticipated Data Products. *ArXiv e-prints*.

Ivison, R. J., Swinbank, A. M., Swinyard, B., Smail, I., Pearson, C. P., Rigopoulou, D., Polehampton, E., Baluteau, J.-P., Barlow, M. J., Blain, A. W., Bock, J., Clements, D. L., Coppin, K., Cooray, A., Danielson, A., Dwek, E., Edge, A. C., Franceschini, A., Fulton, T., Glenn, J., Griffin, M., Isaak, K., Leeks, S., Lim, T., Naylor, D., Oliver, S. J., Page, M. J., Pérez Fournon, I., Rowan-Robinson, M., Savini, G., Scott, D., Spencer, L., Valtchanov, I., Vigroux, L., and Wright, G. S. (2010). Herschel and SCUBA-2 imaging and spectroscopy of a bright, lensed submillimetre galaxy at z = 2.3. *Astron. Astrophys.*, 518:L35.

Jahnke, K. and Macciò, A. V. (2011). The Non-causal Origin of the Black-hole-galaxy Scaling Relations. *The Astrophysical Journal*, 734:92.

Jarvis, M. J., Smith, D. J. B., Bonfield, D. G., Hardcastle, M. J., Falder, J. T., Stevens, J. A., Ivison, R. J., Auld, R., Baes, M., Baldry, I. K., Bamford, S. P., Bourne, N., Buttiglione, S., Cava, A., Cooray, A., Dariush, A., de Zotti, G., Dunlop, J. S., Dunne, L., Dye, S., Eales, S., Fritz, J., Hill, D. T., Hopwood, R., Hughes, D. H., Ibar, E., Jones, D. H., Kelvin, L., Lawrence, A., Leeuw, L., Loveday, J., Maddox, S. J., Michalowski, M. J., Negrello, M., Norberg, P., Pohlen, M., Prescott, M., Rigby, E. E., Robotham, A., Rodighiero, G., Scott, D., Sharp, R., Temi, P., Thompson, M. A., van der Werf, P., van Kampen, E., Vlahakis, C., and White, G. (2010). Herschel-ATLAS: the far-infrared-radio correlation at $z < 0.5$. *MNRAS*, 409:92–101.

Jiang, F. and van den Bosch, F. C. (2014). Statistics of Dark Matter Substructure: I. Model and Universal Fitting Functions. *ArXiv e-prints*.

Jiang, L., Fan, X., Bian, F., Annis, J., Chiu, K., Jester, S., Lin, H., Lupton, R. H., Richards, G. T., Strauss, M. A., Malanushenko, V., Malanushenko, E., and Schneider, D. P. (2009). A Survey of z $\sim$ 6 Quasars in the Sloan Digital Sky Survey Deep Stripe. II. Discovery of Six Quasars at z $_{AB}$>21. *Astronomic. J.*, 138:305–311.

Johnson, S. P., Wilson, G. W., Wang, Q. D., Williams, C. C., Scott, K. S., Yun, M. S., Pope, A., Lowenthal, J., Aretxaga, I., Hughes, D., Kim, M. J., Kim, S., Tamura, Y., Kohno, K., Ezawa, H., Kawabe, R., and Oshima, T. (2013). X-ray detections of submillimetre galaxies: active galactic nuclei versus starburst contribution. *MNRAS*, 431:662–682.

Karim, A., Swinbank, A. M., Hodge, J. A., Smail, I. R., Walter, F., Biggs, A. D., Simpson, J. M., Danielson, A. L. R., Alexander, D. M., Bertoldi, F., de Breuck, C., Chapman, S. C., Coppin, K. E. K., Dannerbauer, H., Edge, A. C., Greve, T. R., Ivison, R. J., Knudsen, K. K., Menten, K. M., Schinnerer, E., Wardlow, J. L., Weiß, A., and van der Werf, P. (2013). An ALMA survey of submillimetre galaxies in the Extended Chandra Deep Field South: high-resolution 870 μm source counts. *MNRAS*, 432:2–9.

Kaviraj, S., Laigle, C., Kimm, T., Devriendt, J. E. G., Dubois, Y., Pichon, C., Slyz, A., Chisari, E., and Peirani, S. (2016). The Horizon-AGN simulation: evolution of galaxy properties over cosmic time. *ArXiv e-prints*.

Kelly, B. C. and Shen, Y. (2013). The Demographics of Broad-line Quasars in the Mass-Luminosity Plane. II. Black Hole Mass and Eddington Ratio Functions. *The Astrophysical Journal*, 764:45.

Kennicutt, R. C. and Evans, N. J. (2012a). Star Formation in the Milky Way and Nearby Galaxies. *Annu. Rev. Astron. Astrophys.*, 50:531–608.

Kennicutt, R. C. and Evans, N. J. (2012b). Star Formation in the Milky Way and Nearby Galaxies. *Annu. Rev. Astron. Astrophys.*, 50:531–608.

Kennicutt, Jr., R. C. (1983). The rate of star formation in normal disk galaxies. *The Astrophysical Journal*, 272:54–67.

Kennicutt, Jr., R. C. (1998). Star Formation in Galaxies Along the Hubble Sequence. *Annu. Rev. Astron. Astrophys.*, 36:189–232.

Kennicutt, Jr., R. C., Hao, C.-N., Calzetti, D., Moustakas, J., Dale, D. A., Bendo, G., Engelbracht, C. W., Johnson, B. D., and Lee, J. C. (2009). Dust-corrected Star

Formation Rates of Galaxies. I. Combinations of Hα and Infrared Tracers. *The Astrophysical Journal*, 703:1672–1695.

Khandai, N., Di Matteo, T., Croft, R., Wilkins, S., Feng, Y., Tucker, E., DeGraf, C., and Liu, M.-S. (2015). The MassiveBlack-II simulation: the evolution of haloes and galaxies to z $\sim$ 0. *MNRAS*, 450:1349–1374.

King, A. (2003). Black Holes, Galaxy Formation, and the M_{BH}-σ Relation. *The Astrophysical Journal Letters*, 596:L27–L29.

King, A. (2014). The Supermassive Black Hole-Galaxy Connection. *Space Science Rev.*, 183:427–451.

Koprowski, M. P., Dunlop, J. S., Michalowski, M. J., Cirasuolo, M., and Bowler, R. A. A. (2014). A reassessment of the redshift distribution and physical properties of luminous (sub-)millimetre galaxies. *MNRAS*, 444:117–128.

Koprowski, M. P., Dunlop, J. S., Michalowski, M. J., Roseboom, I., Geach, J. E., Cirasuolo, M., Aretxaga, I., Bowler, R. A. A., Banerji, M., Bourne, N., Coppin, K. E. K., Chapman, S., Hughes, D. H., Jenness, T., McLure, R. J., Symeonidis, M., and Werf, P. v. d. (2016). The SCUBA-2 Cosmology Legacy Survey: galaxies in the deep 850 μm survey, and the star-forming 'main sequence'. *MNRAS*, 458:4321–4344.

Kormendy, J. and Bender, R. (2009). Correlations between Supermassive Black Holes, Velocity Dispersions, and Mass Deficits in Elliptical Galaxies with Cores. *The Astrophysical Journal Letters*, 691:L142–L146.

Kormendy, J. and Ho, L. C. (2013). Coevolution (Or Not) of Supermassive Black Holes and Host Galaxies. *Annu. Rev. Astron. Astrophys.*, 51:511–653.

Kormendy, J. and Richstone, D. (1995). Inward Bound—The Search For Supermassive Black Holes In Galactic Nuclei. *Annu. Rev. Astron. Astrophys.*, 33:581.

Kroupa, P. (2001). On the variation of the initial mass function. *MNRAS*, 322:231–246.

Kroupa, P., Tout, C. A., and Gilmore, G. (1993). The distribution of low-mass stars in the Galactic disc. *MNRAS*, 262:545–587.

Kurczynski, P., Gawiser, E., Acquaviva, V., Bell, E. F., Dekel, A., de Mello, D. F., Ferguson, H. C., Gardner, J. P., Grogin, N. A., Guo, Y., Hopkins, P. F., Koekemoer, A. M., Koo, D. C., Lee, S.-K., Mobasher, B., Primack, J. R., Rafelski, M., Soto, E., and Teplitz, H. I. (2016). Evolution of Intrinsic Scatter in the SFR-Stellar Mass Correlation at 0.5 < z < 3. *The Astrophysical Journal Letters*, 820:L1.

Lacki, B. C., Thompson, T. A., and Quataert, E. (2010). The Physics of the Far-infrared-Radio Correlation. I. Calorimetry, Conspiracy, and Implications. *The Astrophysical Journal*, 717:1–28.

Lagache, G., Abergel, A., Boulanger, F., Désert, F. X., and Puget, J.-L. (1999). First detection of the warm ionised medium dust emission. Implication for the cosmic far-infrared background. *Astron. Astrophys.*, 344:322–332.

Laird, E. S., Nandra, K., Adelberger, K. L., Steidel, C. C., and Reddy, N. A. (2005). X-ray properties of UV-selected star-forming galaxies at z˜ 1 in the Hubble Deep Field North. *MNRAS*, 359:47–56.

Laird, E. S., Nandra, K., Hobbs, A., and Steidel, C. C. (2006). The X-ray emission of Lyman break galaxies. *MNRAS*, 373:217–230.

Laird, E. S., Nandra, K., Pope, A., and Scott, D. (2010). On the X-ray properties of sub-mm-selected galaxies. *MNRAS*, 401:2763–2772.

Laor, A. and Netzer, H. (1989). Massive thin accretion discs. I - Calculated spectra. *MNRAS*, 238:897–916.

Lapi, A. and Cavaliere, A. (2011). Self-similar Dynamical Relaxation of Dark Matter Halos in an Expanding Universe. *The Astrophysical Journal*, 743:127.

Lapi, A. and Danese, L. (2015). Cold or warm? Constraining dark matter with primeval galaxies and cosmic reionization after Planck. *JCAP*, 9:003.

Lapi, A., González-Nuevo, J., Fan, L., Bressan, A., De Zotti, G., Danese, L., Negrello, M., Dunne, L., Eales, S., Maddox, S., Auld, R., Baes, M., Bonfield, D. G., Buttiglione, S., Cava, A., Clements, D. L., Cooray, A., Dariush, A., Dye, S., Fritz, J., Herranz, D., Hopwood, R., Ibar, E., Ivison, R., Jarvis, M. J., Kaviraj, S., López-Caniego, M., Massardi, M., Michalowski, M. J., Pascale, E., Pohlen, M., Rigby, E., Rodighiero, G., Serjeant, S., Smith, D. J. B., Temi, P., Wardlow, J., and van der Werf, P. (2011). Herschel-ATLAS Galaxy Counts and High-redshift Luminosity Functions: The Formation of Massive Early-type Galaxies. *The Astrophysical Journal*, 742:24.

Lapi, A., Negrello, M., González-Nuevo, J., Cai, Z.-Y., De Zotti, G., and Danese, L. (2012). Effective Models for Statistical Studies of Galaxy-scale Gravitational Lensing. *The Astrophysical Journal*, 755:46.

Lapi, A., Raimundo, S., Aversa, R., Cai, Z.-Y., Negrello, M., Celotti, A., De Zotti, G., and Danese, L. (2014). The Coevolution of Supermassive Black Holes and Massive Galaxies at High Redshift. *The Astrophysical Journal*, 782:69.

Lapi, A., Salucci, P., and Danese, L. (2013). Statistics of Dark Matter Halos from the Excursion Set Approach. *The Astrophysical Journal*, 772:85.

Lapi, A., Shankar, F., Mao, J., Granato, G. L., Silva, L., De Zotti, G., and Danese, L. (2006). Quasar Luminosity Functions from Joint Evolution of Black Holes and Host Galaxies. *The Astrophysical Journal*, 650:42–56.

Lauer, T. R., Gebhardt, K., Faber, S. M., Richstone, D., Tremaine, S., Kormendy, J., Aller, M. C., Bender, R., Dressler, A., Filippenko, A. V., Green, R., and Ho, L. C. (2007). The Centers of Early-Type Galaxies with Hubble Space Telescope. VI. Bimodal Central Surface Brightness Profiles. *The Astrophysical Journal*, 664:226–256.

Laureijs, R., Hoar, J., Buenadicha, G., Mellier, Y., Pasian, F., Dabin, C., Sauvage, M., and Euclid Collaboration (2014). The Euclid Mission: Cosmology Data Processing and Much More. In Manset, N. and Forshay, P., editors, *Astronomical Data Analysis Software and Systems XXIII*, volume 485 of *Astronomical Society of the Pacific Conference Series*, page 495.

Lee, K.-S., Alberts, S., Atlee, D., Dey, A., Pope, A., Jannuzi, B. T., Reddy, N., and Brown, M. J. I. (2012). Herschel Detection of Dust Emission from UV-luminous Star-forming Galaxies at $3.3 < z < 4.3$. *The Astrophysical Journal Letters*, 758:L31.

Lee, K.-S., Giavalisco, M., Gnedin, O. Y., Somerville, R. S., Ferguson, H. C., Dickinson, M., and Ouchi, M. (2006). The Large-Scale and Small-Scale Clustering of Lyman Break Galaxies at 3.5<=z<=5.5 from the GOODS Survey. *The Astrophysical Journal*, 642:63–80.

Lee, S.-K., Idzi, R., Ferguson, H. C., Somerville, R. S., Wiklind, T., and Giavalisco, M. (2009). Biases and Uncertainties in Physical Parameter Estimates of Lyman Break Galaxies from Broadband Photometry. *The Astrophysical Journal Supp. Series*, 184:100–132.

Lehmer, B. D., Alexander, D. M., Bauer, F. E., Brandt, W. N., Goulding, A. D., Jenkins, L. P., Ptak, A., and Roberts, T. P. (2010). A Chandra Perspective on Galaxy-wide X-ray Binary Emission and its Correlation with Star Formation Rate and Stellar Mass: New Results from Luminous Infrared Galaxies. *The Astrophysical Journal*, 724:559–571.

Lehmer, B. D., Brandt, W. N., Alexander, D. M., Bauer, F. E., Conselice, C. J., Dickinson, M. E., Giavalisco, M., Grogin, N. A., Koekemoer, A. M., Lee, K.-S., Moustakas, L. A., and Schneider, D. P. (2005). X-Ray Properties of Lyman Break Galaxies in the Great Observatories Origins Deep Survey. *Astronomic. J.*, 129:1–8.

Leitherer, C., Schaerer, D., Goldader, J. D., Delgado, R. M. G., Robert, C., Kune, D. F., de Mello, D. F., Devost, D., and Heckman, T. M. (1999). Starburst99: Synthesis Models for Galaxies with Active Star Formation. *The Astrophysical Journal Supp. Series*, 123:3–40.

Leja, J., van Dokkum, P. G., Franx, M., and Whitaker, K. E. (2015). Reconciling the Observed Star-forming Sequence with the Observed Stellar Mass Function. *The Astrophysical Journal*, 798:115.

Li, L.-X. (2012). Accretion, growth of supermassive black holes, and feedback in galaxy mergers. *MNRAS*, 424:1461–1470.

Li, Y.-R., Ho, L. C., and Wang, J.-M. (2011). Cosmological Evolution of Supermassive Black Holes. I. Mass Function at $0 < z <\sim 2$. *The Astrophysical Journal*, 742:33.

Lilly, S. J., Carollo, C. M., Pipino, A., Renzini, A., and Peng, Y. (2013). Gas Regulation of Galaxies: The Evolution of the Cosmic Specific Star Formation Rate, the Metallicity-Mass-Star-formation Rate Relation, and the Stellar Content of Halos. *The Astrophysical Journal*, 772:119.

Lutz, D., Mainieri, V., Rafferty, D., Shao, L., Hasinger, G., Weiß, A., Walter, F., Smail, I., Alexander, D. M., Brandt, W. N., Chapman, S., Coppin, K., Forster Schreiber, N. M., Gawiser, E., Genzel, R., Greve, T. R., Ivison, R. J., Koekemoer, A. M., Kurczynski, P., Menten, K. M., Nordon, R., Popesso, P., Schinnerer, E., Silverman, J. D., Wardlow, J., and Xue, Y. Q. (2010). The LABOCA Survey of the Extended Chandra Deep Field South: Two Modes of Star Formation in Active Galactic Nucleus Hosts? *The Astrophysical Journal*, 712:1287–1301.

Ly, C., Lee, J. C., Dale, D. A., Momcheva, I., Salim, S., Staudaher, S., Moore, C. A., and Finn, R. (2011). The Hα Luminosity Function and Star Formation Rate Volume Density at z = 0.8 from the NEWFIRM Hα Survey. *The Astrophysical Journal*, 726:109.

Ma, B., Cooray, A., Calanog, J. A., Nayyeri, H., Timmons, N., Casey, C., Baes, M., Chapman, S., Dannerbauer, H., da Cunha, E., De Zotti, G., Dunne, L., Farrah, D., Fu, H., Gonzalez-Nuevo, J., Magdis, G., Michalowski, M. J., Oteo, I., Riechers, D. A., Scott, D., Smith, M. W. L., Wang, L., Wardlow, J., Vaccari, M., Viaene, S., and Vieira, J. D. (2015a). Spitzer Imaging of Strongly lensed Herschel-selected Dusty Star-forming Galaxies. *The Astrophysical Journal*, 814:17.

Ma, J., Gonzalez, A. H., Spilker, J. S., Strandet, M., Ashby, M. L. N., Aravena, M., Béthermin, M., Bothwell, M. S., de Breuck, C., Brodwin, M., Chapman, S. C., Fassnacht, C. D., Greve, T. R., Gullberg, B., Hezaveh, Y., Malkan, M., Marrone, D. P., Saliwanchik, B. R., Vieira, J. D., Weiss, A., and Welikala, N. (2015b). Stellar

Masses and Star Formation Rates of Lensed, Dusty, Star-forming Galaxies from the SPT Survey. *The Astrophysical Journal*, 812:88.

Madau, P. and Dickinson, M. (2014a). Cosmic Star-Formation History. *Annu. Rev. Astron. Astrophys.*, 52:415–486.

Madau, P. and Dickinson, M. (2014b). Cosmic Star-Formation History. *Annu. Rev. Astron. Astrophys.*, 52:415–486.

Madau, P., Haardt, F., and Dotti, M. (2014). Super-critical Growth of Massive Black Holes from Stellar-mass Seeds. *The Astrophysical Journal Letters*, 784:L38.

Magnelli, B., Popesso, P., Berta, S., Pozzi, F., Elbaz, D., Lutz, D., Dickinson, M., Altieri, B., Andreani, P., Aussel, H., Béthermin, M., Bongiovanni, A., Cepa, J., Charmandaris, V., Chary, R.-R., Cimatti, A., Daddi, E., Förster Schreiber, N. M., Genzel, R., Gruppioni, C., Harwit, M., Hwang, H. S., Ivison, R. J., Magdis, G., Maiolino, R., Murphy, E., Nordon, R., Pannella, M., Pérez García, A., Poglitsch, A., Rosario, D., Sanchez-Portal, M., Santini, P., Scott, D., Sturm, E., Tacconi, L. J., and Valtchanov, I. (2013). The deepest Herschel-PACS far-infrared survey: number counts and infrared luminosity functions from combined PEP/GOODS-H observations. *Astron. Astrophys.*, 553:A132.

Magorrian, J., Tremaine, S., Richstone, D., Bender, R., Bower, G., Dressler, A., Faber, S. M., Gebhardt, K., Green, R., Grillmair, C., Kormendy, J., and Lauer, T. (1998). The Demography of Massive Dark Objects in Galaxy Centers. *Astronomic. J.*, 115:2285–2305.

Mainieri, V., Bongiorno, A., Merloni, A., Aller, M., Carollo, M., Iwasawa, K., Koekemoer, A. M., Mignoli, M., Silverman, J. D., Bolzonella, M., Brusa, M., Comastri, A., Gilli, R., Halliday, C., Ilbert, O., Lusso, E., Salvato, M., Vignali, C., Zamorani, G., Contini, T., Kneib, J.-P., Le Fevre, O., Lilly, S., Renzini, A., Scodeggio, M., Balestra, I., Bardelli, S., Caputi, K., Coppa, G., Cucciati, O., de la Torre, S., de Ravel, L., Franzetti, P., Garilli, B., Iovino, A., Kampczyk, P., Knobel, C., Kovač, K., Lamareille, F., Le Borgne, J.-F., Le Brun, V., Maier, C., Nair, P., Pello, R., Peng, Y., Perez Montero, E., Pozzetti, L., Ricciardelli, E., Tanaka, M., Tasca, L., Tresse, L., Vergani, D., Zucca, E., Aussel, H., Capak, P., Cappelluti, N., Elvis, M., Fiore, F., Hasinger, G., Impey, C., Le Floc'h, E., Scoville, N., Taniguchi, Y., and Trump, J. (2011). Black hole accretion and host galaxies of obscured quasars in XMM-COSMOS. *Astron. Astrophys.*, 535:A80.

Man, A. W. S., Greve, T. R., Toft, S., Magnelli, B., Karim, A., Ilbert, O., Salvato, M., Le Floc'h, E., Bertoldi, F., Casey, C. M., Lee, N., Li, Y., Navarrete, F., Sheth, K., Smolčić, V., Sanders, D. B., Schinnerer, E., and Zirm, A. W. (2016). Confirming

the Existence of a Quiescent Galaxy Population out to z=3: A Stacking Analysis of Mid-, Far-Infrared and Radio Data. *The Astrophysical Journal*, 820:11.

Mancuso, C., Lapi, A., Cai, Z.-Y., Negrello, M., De Zotti, G., Bressan, A., Bonato, M., Perrotta, F., and Danese, L. (2015). Predictions for Ultra-deep Radio Counts of Star-forming Galaxies. *The Astrophysical Journal*, 810:72.

Mancuso, C., Lapi, A., Shi, J., Gonzalez-Nuevo, J., Aversa, R., and Danese, L. (2016). The Quest for Dusty Star-forming Galaxies at High Redshift z $\gtrsim$ 4. *The Astrophysical Journal*, 823:128.

Mao, J., Lapi, A., Granato, G. L., de Zotti, G., and Danese, L. (2007). The Role of the Dust in Primeval Galaxies: A Simple Physical Model for Lyman Break Galaxies and Lyα Emitters. *The Astrophysical Journal*, 667:655–666.

Mao, M. Y., Huynh, M. T., Norris, R. P., Dickinson, M., Frayer, D., Helou, G., and Monkiewicz, J. A. (2011). No Evidence for Evolution in the Far-infrared-Radio Correlation out to z ~2 in the Extended Chandra Deep Field South. *The Astrophysical Journal*, 731:79.

Maraston, C. (1998). Evolutionary synthesis of stellar populations: a modular tool. *MNRAS*, 300:872–892.

Maraston, C. (2005). Evolutionary population synthesis: models, analysis of the ingredients and application to high-z galaxies. *MNRAS*, 362:799–825.

Marconi, A. and Hunt, L. K. (2003). The Relation between Black Hole Mass, Bulge Mass, and Near-Infrared Luminosity. *The Astrophysical Journal Letters*, 589:L21–L24.

Marconi, A., Risaliti, G., Gilli, R., Hunt, L. K., Maiolino, R., and Salvati, M. (2004). Local supermassive black holes, relics of active galactic nuclei and the X-ray background. *MNRAS*, 351:169–185.

Marcum, P. M., O'Connell, R. W., Fanelli, M. N., Cornett, R. H., Waller, W. H., Bohlin, R. C., Neff, S. G., Roberts, M. S., Smith, A. M., Cheng, K.-P., Collins, N. R., Hennessy, G. S., Hill, J. K., Hill, R. S., Hintzen, P., Landsman, W. B., Ohl, R. G., Parise, R. A., Smith, E. P., Freedman, W. L., Kuchinski, L. E., Madore, B., Angione, R., Palma, C., Talbert, F., and Stecher, T. P. (2001). An Ultraviolet/Optical Atlas of Bright Galaxies. *The Astrophysical Journal Supp. Series*, 132:129–198.

Martin, D. C., Seibert, M., Buat, V., Iglesias-Páramo, J., Barlow, T. A., Bianchi, L., Byun, Y.-I., Donas, J., Forster, K., Friedman, P. G., Heckman, T. M., Jelinsky, P. N., Lee, Y.-W., Madore, B. F., Malina, R. F., Milliard, B., Morrissey, P. F., Neff, S. G., Rich, R. M., Schiminovich, D., Siegmund, O. H. W., Small, T., Szalay, A. S., Welsh,

B. Y., and Wyder, T. K. (2005). The Star Formation Rate Function of the Local Universe. *The Astrophysical Journal Letters*, 619:L59–L62.

Martínez, H. J., Zandivarez, A., Merchán, M. E., and Domínguez, M. J. L. (2002). Galaxy groups in the 2dF Galaxy Redshift Survey: luminosity and mass statistics. *MNRAS*, 337:1441–1449.

Mashian, N., Oesch, P. A., and Loeb, A. (2016). An empirical model for the galaxy luminosity and star formation rate function at high redshift. *MNRAS*, 455:2101–2109.

Mason, K. O., Breeveld, A., Much, R., Carter, M., Cordova, F. A., Cropper, M. S., Fordham, J., Huckle, H., Ho, C., Kawakami, H., Kennea, J., Kennedy, T., Mittaz, J., Pandel, D., Priedhorsky, W. C., Sasseen, T., Shirey, R., Smith, P., and Vreux, J.-M. (2001). The XMM-Newton optical/UV monitor telescope. *Astron. Astrophys.*, 365:L36–L44.

Massardi, M., Bonaldi, A., Negrello, M., Ricciardi, S., Raccanelli, A., and de Zotti, G. (2010). A model for the cosmological evolution of low-frequency radio sources. *MNRAS*, 404:532–544.

Masters, D., Capak, P., Salvato, M., Civano, F., Mobasher, B., Siana, B., Hasinger, G., Impey, C. D., Nagao, T., Trump, J. R., Ikeda, H., Elvis, M., and Scoville, N. (2012). Evolution of the Quasar Luminosity Function over $3 < z < 5$ in the COSMOS Survey Field. *The Astrophysical Journal*, 755:169.

Mawatari, K., Yamada, T., Fazio, G. G., Huang, J.-S., and Ashby, M. L. N. (2016). Possible identification of massive and evolved galaxies at $z \gtrsim 5$. *Publ. Astron. Soc. Japan*, 68:46.

McConnell, N. J. and Ma, C.-P. (2013). Revisiting the Scaling Relations of Black Hole Masses and Host Galaxy Properties. *The Astrophysical Journal*, 764:184.

McLure, R. J. and Dunlop, J. S. (2004). The cosmological evolution of quasar black hole masses. *MNRAS*, 352:1390–1404.

Melbourne, J., Peng, C. Y., Soifer, B. T., Urrutia, T., Desai, V., Armus, L., Bussmann, R. S., Dey, A., and Matthews, K. (2011). The Black Hole Masses and Star Formation Rates of z>1 Dust Obscured Galaxies: Results from Keck OSIRIS Integral Field Spectroscopy. *Astronomic. J.*, 141:141.

Menci, N., Fiore, F., and Lamastra, A. (2012). Galaxy formation in warm dark matter cosmology. *MNRAS*, 421:2384–2394.

Meurer, G. R., Heckman, T. M., and Calzetti, D. (1999). Dust Absorption and the Ultraviolet Luminosity Density at z ∼3 as Calibrated by Local Starburst Galaxies. *The Astrophysical Journal*, 521:64–80.

Miller, G. E. and Scalo, J. M. (1979). The initial mass function and stellar birthrate in the solar neighborhood. *The Astrophysical Journal Supp. Series*, 41:513–547.

Miyaji, T., Hasinger, G., Salvato, M., Brusa, M., Cappelluti, N., Civano, F., Puccetti, S., Elvis, M., Brunner, H., Fotopoulou, S., Ueda, Y., Griffiths, R. E., Koekemoer, A. M., Akiyama, M., Comastri, A., Gilli, R., Lanzuisi, G., Merloni, A., and Vignali, C. (2015). Detailed Shape and Evolutionary Behavior of the X-Ray Luminosity Function of Active Galactic Nuclei. *The Astrophysical Journal*, 804:104.

Miyazaki, S., Komiyama, Y., Nakaya, H., Kamata, Y., Doi, Y., Hamana, T., Karoji, H., Furusawa, H., Kawanomoto, S., Morokuma, T., Ishizuka, Y., Nariai, K., Tanaka, Y., Uraguchi, F., Utsumi, Y., Obuchi, Y., Okura, Y., Oguri, M., Takata, T., Tomono, D., Kurakami, T., Namikawa, K., Usuda, T., Yamanoi, H., Terai, T., Uekiyo, H., Yamada, Y., Koike, M., Aihara, H., Fujimori, Y., Mineo, S., Miyatake, H., Yasuda, N., Nishizawa, J., Saito, T., Tanaka, M., Uchida, T., Katayama, N., Wang, S.-Y., Chen, H.-Y., Lupton, R., Loomis, C., Bickerton, S., Price, P., Gunn, J., Suzuki, H., Miyazaki, Y., Muramatsu, M., Yamamoto, K., Endo, M., Ezaki, Y., Itoh, N., Miwa, Y., Yokota, H., Matsuda, T., Ebinuma, R., and Takeshi, K. (2012). Hyper Suprime-Cam. In *Ground-based and Airborne Instrumentation for Astronomy IV*, volume 8446 of *Spie Proc.*, page 84460Z.

Mocanu, L. M., Crawford, T. M., Vieira, J. D., Aird, K. A., Aravena, M., Austermann, J. E., Benson, B. A., Béthermin, M., Bleem, L. E., Bothwell, M., Carlstrom, J. E., Chang, C. L., Chapman, S., Cho, H.-M., Crites, A. T., de Haan, T., Dobbs, M. A., Everett, W. B., George, E. M., Halverson, N. W., Harrington, N., Hezaveh, Y., Holder, G. P., Holzapfel, W. L., Hoover, S., Hrubes, J. D., Keisler, R., Knox, L., Lee, A. T., Leitch, E. M., Lueker, M., Luong-Van, D., Marrone, D. P., McMahon, J. J., Mehl, J., Meyer, S. S., Mohr, J. J., Montroy, T. E., Natoli, T., Padin, S., Plagge, T., Pryke, C., Rest, A., Reichardt, C. L., Ruhl, J. E., Sayre, J. T., Schaffer, K. K., Shirokoff, E., Spieler, H. G., Spilker, J. S., Stalder, B., Staniszewski, Z., Stark, A. A., Story, K. T., Switzer, E. R., Vanderlinde, K., and Williamson, R. (2013). Extragalactic Millimeter-wave Point-source Catalog, Number Counts and Statistics from 771 $\deg^2$ of the SPT-SZ Survey. *The Astrophysical Journal*, 779:61.

Mor, R., Netzer, H., Trakhtenbrot, B., Shemmer, O., and Lira, P. (2012). Extreme Star Formation in the Host Galaxies of the Fastest Growing Supermassive Black Holes at z = 4.8. *The Astrophysical Journal Letters*, 749:L25.

Moster, B. P., Naab, T., and White, S. D. M. (2013). Galactic star formation and accretion histories from matching galaxies to dark matter haloes. *MNRAS*, 428:3121–3138.

Moster, B. P., Somerville, R. S., Maulbetsch, C., van den Bosch, F. C., Macciò, A. V., Naab, T., and Oser, L. (2010). Constraints on the Relationship between Stellar Mass and Halo Mass at Low and High Redshift. *The Astrophysical Journal*, 710:903–923.

Moustakas, J., Coil, A. L., Aird, J., Blanton, M. R., Cool, R. J., Eisenstein, D. J., Mendez, A. J., Wong, K. C., Zhu, G., and Arnouts, S. (2013). PRIMUS: Constraints on Star Formation Quenching and Galaxy Merging, and the Evolution of the Stellar Mass Function from z = 0-1. *The Astrophysical Journal*, 767:50.

Muñoz, J. A. and Peeples, M. S. (2015). A framework for empirical galaxy phenomenology: the scatter in galaxy ages and stellar metallicities. *MNRAS*, 448:1430–1445.

Mullaney, J. R., Alexander, D. M., Aird, J., Bernhard, E., Daddi, E., Del Moro, A., Dickinson, M., Elbaz, D., Harrison, C. M., Juneau, S., Liu, D., Pannella, M., Rosario, D., Santini, P., Sargent, M., Schreiber, C., Simpson, J., and Stanley, F. (2015). ALMA and Herschel reveal that X-ray-selected AGN and main-sequence galaxies have different star formation rate distributions. *MNRAS*, 453:L83–L87.

Mullaney, J. R., Daddi, E., Béthermin, M., Elbaz, D., Juneau, S., Pannella, M., Sargent, M. T., Alexander, D. M., and Hickox, R. C. (2012a). The Hidden "AGN Main Sequence": Evidence for a Universal Black Hole Accretion to Star Formation Rate Ratio since z $\sim$ 2 Producing an M $_{BH}$-M $_{*}$ Relation. *The Astrophysical Journal Letters*, 753:L30.

Mullaney, J. R., Pannella, M., Daddi, E., Alexander, D. M., Elbaz, D., Hickox, R. C., Bournaud, F., Altieri, B., Aussel, H., Coia, D., Dannerbauer, H., Dasyra, K., Dickinson, M., Hwang, H. S., Kartaltepe, J., Leiton, R., Magdis, G., Magnelli, B., Popesso, P., Valtchanov, I., Bauer, F. E., Brandt, W. N., Del Moro, A., Hanish, D. J., Ivison, R. J., Juneau, S., Luo, B., Lutz, D., Sargent, M. T., Scott, D., and Xue, Y. Q. (2012b). GOODS-Herschel: the far-infrared view of star formation in active galactic nucleus host galaxies since z $\sim$ 3. *MNRAS*, 419:95–115.

Munoz, J. A. and Loeb, A. (2011). Constraining the Minimum Mass of High-redshift Galaxies and their Contribution to the Ionization State of the Intergalactic Medium. *The Astrophysical Journal*, 729:99.

Murphy, E., Sargent, M., Beswick, R., Dickinson, C., Heywood, I., Hunt, L., Huynh, M., Jarvis, M., Karim, A., Krause, M., Prandoni, I., Seymour, N., Schinnerer, E., Tabatabaei, F., and Wagg, J. (2015). The Astrophysics of Star Formation Across

Cosmic Time at >10 GHz with the Square Kilometre Array. *Advancing Astrophysics with the Square Kilometre Array (AASKA14)*, page 85.

Murphy, E. J. (2009). The Far-Infrared-Radio Correlation at High Redshifts: Physical Considerations and Prospects for the Square Kilometer Array. *The Astrophysical Journal*, 706:482–496.

Murphy, E. J. (2013). The Role of Merger Stage on Galaxy Radio Spectra in Local Infrared-bright Starburst Galaxies. *The Astrophysical Journal*, 777:58.

Murphy, E. J., Bremseth, J., Mason, B. S., Condon, J. J., Schinnerer, E., Aniano, G., Armus, L., Helou, G., Turner, J. L., and Jarrett, T. H. (2012). The Star Formation in Radio Survey: GBT 33 GHz Observations of Nearby Galaxy Nuclei and Extranuclear Star-forming Regions. *The Astrophysical Journal*, 761:97.

Murphy, E. J., Condon, J. J., Schinnerer, E., Kennicutt, R. C., Calzetti, D., Armus, L., Helou, G., Turner, J. L., Aniano, G., Beirão, P., Bolatto, A. D., Brandl, B. R., Croxall, K. V., Dale, D. A., Donovan Meyer, J. L., Draine, B. T., Engelbracht, C., Hunt, L. K., Hao, C.-N., Koda, J., Roussel, H., Skibba, R., and Smith, J.-D. T. (2011). Calibrating Extinction-free Star Formation Rate Diagnostics with 33 GHz Free-free Emission in NGC 6946. *The Astrophysical Journal*, 737:67.

Nayyeri, H., Keele, M., Cooray, A., Riechers, D. A., Ivison, R. J., Harris, A. I., Frayer, D. T., Baker, A. J., Chapman, S. C., Eales, S., Farrah, D., Fu, H., Marchetti, L., Marques-Chaves, R., Martinez-Navajas, P. I., Oliver, S. J., Omont, A., Perez-Fournon, I., Scott, D., Vaccari, M., Vieira, J., Viero, M., Wang, L., and Wardlow, J. (2016). Candidate Gravitationally Lensed Dusty Star-forming Galaxies in the Herschel Wide Area Surveys. *The Astrophysical Journal*, 823:17.

Negrello, M., Hopwood, R., Dye, S., Cunha, E. d., Serjeant, S., Fritz, J., Rowlands, K., Fleuren, S., Bussmann, R. S., Cooray, A., Dannerbauer, H., Gonzalez-Nuevo, J., Lapi, A., Omont, A., Amber, S., Auld, R., Baes, M., Buttiglione, S., Cava, A., Danese, L., Dariush, A., De Zotti, G., Dunne, L., Eales, S., Ibar, E., Ivison, R. J., Kim, S., Leeuw, L., Maddox, S., Michalowski, M. J., Massardi, M., Pascale, E., Pohlen, M., Rigby, E., Smith, D. J. B., Sutherland, W., Temi, P., and Wardlow, J. (2014). Herschel *-ATLAS: deep HST/WFC3 imaging of strongly lensed submillimetre galaxies. *MNRAS*, 440:1999–2012.

Neri, R., Downes, D., Cox, P., and Walter, F. (2014). High-resolution C^+ imaging of HDF850.1 reveals a merging galaxy at z = 5.185. *Astron. Astrophys.*, 562:A35.

Netzer, H., Lani, C., Nordon, R., Trakhtenbrot, B., Lira, P., and Shemmer, O. (2016). Star Formation Black Hole Growth and Dusty Tori in the Most Luminous AGNs at z=2-3.5. *The Astrophysical Journal*, 819:123.

Noble, A. G., Webb, T. M. A., Ellingson, E., Faloon, A. J., Gal, R. R., Gladders, M. D., Hicks, A. K., Hoekstra, H., Hsieh, B. C., Ivison, R. J., Lemaux, B. C., Lubin, L. M., O'Donnell, D. V., and Yee, H. K. C. (2012). Submillimetre source counts in the fields of high-redshift galaxy clusters. *MNRAS*, 419:1983–2013.

Nobuta, K., Akiyama, M., Ueda, Y., Watson, M. G., Silverman, J., Hiroi, K., Ohta, K., Iwamuro, F., Yabe, K., Tamura, N., Moritani, Y., Sumiyoshi, M., Takato, N., Kimura, M., Maihara, T., Dalton, G., Lewis, I., Bonfield, D., Lee, H., Curtis-Lake, E., Macaulay, E., Clarke, F., Sekiguchi, K., Simpson, C., Croom, S., Ouchi, M., Hanami, H., and Yamada, T. (2012). Black Hole Mass and Eddington Ratio Distribution Functions of X-Ray-selected Broad-line AGNs at z $\sim$ 1.4 in the Subaru XMM-Newton Deep Field. *The Astrophysical Journal*, 761:143.

Noll, S., Burgarella, D., Giovannoli, E., Buat, V., Marcillac, D., and Muñoz-Mateos, J. C. (2009). Analysis of galaxy spectral energy distributions from far-UV to far-IR with CIGALE: studying a SINGS test sample. *Astron. Astrophys.*, 507:1793–1813.

Norris, R. P., Afonso, J., Bacon, D., Beck, R., Bell, M., Beswick, R. J., Best, P., Bhatnagar, S., Bonafede, A., Brunetti, G., Budavári, T., Cassano, R., Condon, J. J., Cress, C., Dabbech, A., Feain, I., Fender, R., Ferrari, C., Gaensler, B. M., Giovannini, G., Haverkorn, M., Heald, G., Van der Heyden, K., Hopkins, A. M., Jarvis, M., Johnston-Hollitt, M., Kothes, R., Van Langevelde, H., Lazio, J., Mao, M. Y., Martinez-Sansigre, A., Mary, D., Mcalpine, K., Middelberg, E., Murphy, E., Padovani, P., Paragi, Z., Prandoni, I., Raccanelli, A., Rigby, E., Roseboom, I. G., Rottgering, H., Sabater, J., Salvato, M., Scaife, A. M. M., Schilizzi, R., Seymour, N., Smith, D. J. B., Umana, G., Zhao, G.-B., and Zinn, P.-C. (2013). Radio Continuum Surveys with Square Kilometre Array Pathfinders. *Publ Astron. Soc. Austr.*, 30:e020.

Norris, R. P., Hopkins, A. M., Afonso, J., Brown, S., Condon, J. J., Dunne, L., Feain, I., Hollow, R., Jarvis, M., Johnston-Hollitt, M., Lenc, E., Middelberg, E., Padovani, P., Prandoni, I., Rudnick, L., Seymour, N., Umana, G., Andernach, H., Alexander, D. M., Appleton, P. N., Bacon, D., Banfield, J., Becker, W., Brown, M. J. I., Ciliegi, P., Jackson, C., Eales, S., Edge, A. C., Gaensler, B. M., Giovannini, G., Hales, C. A., Hancock, P., Huynh, M. T., Ibar, E., Ivison, R. J., Kennicutt, R., Kimball, A. E., Koekemoer, A. M., Koribalski, B. S., Lopez-Sanchez, A. R., Mao, M. Y., Murphy, T., Messias, H., Pimbblet, K. A., Raccanelli, A., Randall, K. E., Reiprich, T. H., Roseboom, I. G., Rottgering, H., Saikia, D. J., Sharp, R. G., Slee, O. B., Smail, I., Thompson, M. A., Urquhart, J. S., Wall, J. V., and Zhao, G.-B. (2011). EMU: Evolutionary Map of the Universe. *Publ Astron. Soc. Austr.*, 28:215–248.

Novak, G. S., Ostriker, J. P., and Ciotti, L. (2011). Feedback from Central Black Holes

in Elliptical Galaxies: Two-dimensional Models Compared to One-dimensional Models. *The Astrophysical Journal*, 737:26.

Oesch, P. A., Bouwens, R. J., Carollo, C. M., Illingworth, G. D., Magee, D., Trenti, M., Stiavelli, M., Franx, M., Labbé, I., and van Dokkum, P. G. (2010). The Evolution of the Ultraviolet Luminosity Function from z 0.75 to z 2.5 Using HST ERS WFC3/UVIS Observations. *The Astrophysical Journal Letters*, 725:L150–L155.

Oesch, P. A., van Dokkum, P. G., Illingworth, G. D., Bouwens, R. J., Momcheva, I., Holden, B., Roberts-Borsani, G. W., Smit, R., Franx, M., Labbé, I., González, V., and Magee, D. (2015). A Spectroscopic Redshift Measurement for a Luminous Lyman Break Galaxy at z = 7.730 Using Keck/MOSFIRE. *The Astrophysical Journal Letters*, 804:L30.

Omont, A., Beelen, A., Bertoldi, F., Cox, P., Carilli, C. L., Priddey, R. S., McMahon, R. G., and Isaak, K. G. (2003). A 1.2 mm MAMBO/IRAM-30 m study of dust emission from optically luminous z ∼ 2 quasars. *Astron. Astrophys.*, 398:857–865.

Omont, A., Cox, P., Bertoldi, F., McMahon, R. G., Carilli, C., and Isaak, K. G. (2001). A 1.2 mm MAMBO/IRAM-30 m survey of dust emission from the highest redshift PSS quasars. *Astron. Astrophys.*, 374:371–381.

Omont, A., McMahon, R. G., Cox, P., Kreysa, E., Bergeron, J., Pajot, F., and Storrie-Lombardi, L. J. (1996). Continuum millimetre observations of high-redshift radio-quiet QSOs II. Five new detections at z>4. *Astron. Astrophys.*, 315:1–10.

Ono, Y., Ouchi, M., Kurono, Y., and Momose, R. (2014). Faint Submillimeter Galaxies Revealed by Multifield Deep ALMA Observations: Number Counts, Spatial Clustering, and a Dark Submillimeter Line Emitter. *The Astrophysical Journal*, 795:5.

Ono, Y., Ouchi, M., Mobasher, B., Dickinson, M., Penner, K., Shimasaku, K., Weiner, B. J., Kartaltepe, J. S., Nakajima, K., Nayyeri, H., Stern, D., Kashikawa, N., and Spinrad, H. (2012). Spectroscopic Confirmation of Three z-dropout Galaxies at z = 6.844-7.213: Demographics of Lyα Emission in z 7 Galaxies. *The Astrophysical Journal*, 744:83.

Ouchi, M., Ellis, R., Ono, Y., Nakanishi, K., Kohno, K., Momose, R., Kurono, Y., Ashby, M. L. N., Shimasaku, K., Willner, S. P., Fazio, G. G., Tamura, Y., and Iono, D. (2013). An Intensely Star-forming Galaxy at z 7 with Low Dust and Metal Content Revealed by Deep ALMA and HST Observations. *The Astrophysical Journal*, 778:102.

Ouchi, M., Shimasaku, K., Furusawa, H., Saito, T., Yoshida, M., Akiyama, M., Ono, Y., Yamada, T., Ota, K., Kashikawa, N., Iye, M., Kodama, T., Okamura, S., Simpson, C., and Yoshida, M. (2010). Statistics of 207 Lyα Emitters at a Redshift Near 7:

Constraints on Reionization and Galaxy Formation Models. *The Astrophysical Journal*, 723:869–894.

Ouchi, M., Shimasaku, K., Okamura, S., Furusawa, H., Kashikawa, N., Ota, K., Doi, M., Hamabe, M., Kimura, M., Komiyama, Y., Miyazaki, M., Miyazaki, S., Nakata, F., Sekiguchi, M., Yagi, M., and Yasuda, N. (2004). Subaru Deep Survey. VI. A Census of Lyman Break Galaxies at z=4 and 5 in the Subaru Deep Fields: Clustering Properties. *The Astrophysical Journal*, 611:685–702.

Overzier, R. A., Bouwens, R. J., Illingworth, G. D., and Franx, M. (2006). Clustering of i_{775} Dropout Galaxies at z 6 in GOODS and the UDF. *The Astrophysical Journal Letters*, 648:L5–L8.

Overzier, R. A., Heckman, T. M., Wang, J., Armus, L., Buat, V., Howell, J., Meurer, G., Seibert, M., Siana, B., Basu-Zych, A., Charlot, S., Gonçalves, T. S., Martin, D. C., Neill, J. D., Rich, R. M., Salim, S., and Schiminovich, D. (2011). Dust Attenuation in UV-selected Starbursts at High Redshift and Their Local Counterparts: Implications for the Cosmic Star Formation Rate Density. *The Astrophysical Journal Letters*, 726:L7.

Padovani, P., Bonzini, M., Kellermann, K. I., Miller, N., Mainieri, V., and Tozzi, P. (2015). Radio-faint AGN: a tale of two populations. *MNRAS*, 452:1263–1279.

Page, M. J., Stevens, J. A., Ivison, R. J., and Carrera, F. J. (2004). The Evolutionary Sequence of Active Galactic Nuclei and Galaxy Formation Revealed. *The Astrophysical Journal Letters*, 611:L85–L88.

Page, M. J., Symeonidis, M., Vieira, J. D., Altieri, B., Amblard, A., Arumugam, V., Aussel, H., Babbedge, T., Blain, A., Bock, J., Boselli, A., Buat, V., Castro-Rodríguez, N., Cava, A., Chanial, P., Clements, D. L., Conley, A., Conversi, L., Cooray, A., Dowell, C. D., Dubois, E. N., Dunlop, J. S., Dwek, E., Dye, S., Eales, S., Elbaz, D., Farrah, D., Fox, M., Franceschini, A., Gear, W., Glenn, J., Griffin, M., Halpern, M., Hatziminaoglou, E., Ibar, E., Isaak, K., Ivison, R. J., Lagache, G., Levenson, L., Lu, N., Madden, S., Maffei, B., Mainetti, G., Marchetti, L., Nguyen, H. T., O'Halloran, B., Oliver, S. J., Omont, A., Panuzzo, P., Papageorgiou, A., Pearson, C. P., Pérez-Fournon, I., Pohlen, M., Rawlings, J. I., Rigopoulou, D., Riguccini, L., Rizzo, D., Rodighiero, G., Roseboom, I. G., Rowan-Robinson, M., Portal, M. S., Schulz, B., Scott, D., Seymour, N., Shupe, D. L., Smith, A. J., Stevens, J. A., Trichas, M., Tugwell, K. E., Vaccari, M., Valtchanov, I., Viero, M., Vigroux, L., Wang, L., Ward, R., Wright, G., Xu, C. K., and Zemcov, M. (2012). The suppression of star formation by powerful active galactic nuclei. *Nature*, 485:213–216.

Palanque-Delabrouille, N., Magneville, C., Yeche, C., Paris, I., Petitjean, P., Burtin, E., Dawson, K., McGreer, I., Myers, A. D., Rossi, G., Schlegel, D., Schneider, D., Stre-

blyanska, A., and Tinker, J. (2016). The extended Baryon Oscillation Spectroscopic Survey: Variability selection and quasar luminosity function. *Astron. Astrophys.*, 587:A41.

Pannella, M., Carilli, C. L., Daddi, E., McCracken, H. J., Owen, F. N., Renzini, A., Strazzullo, V., Civano, F., Koekemoer, A. M., Schinnerer, E., Scoville, N., Smolčić, V., Taniguchi, Y., Aussel, H., Kneib, J. P., Ilbert, O., Mellier, Y., Salvato, M., Thompson, D., and Willott, C. J. (2009). Star Formation and Dust Obscuration at z $\sim$ 2: Galaxies at the Dawn of Downsizing. *The Astrophysical Journal Letters*, 698:L116–L120.

Pannella, M., Elbaz, D., Daddi, E., Dickinson, M., Hwang, H. S., Schreiber, C., Strazzullo, V., Aussel, H., Bethermin, M., Buat, V., Charmandaris, V., Cibinel, A., Juneau, S., Ivison, R. J., Le Borgne, D., Le Floc'h, E., Leiton, R., Lin, L., Magdis, G., Morrison, G. E., Mullaney, J., Onodera, M., Renzini, A., Salim, S., Sargent, M. T., Scott, D., Shu, X., and Wang, T. (2015). GOODS-Herschel: Star Formation, Dust Attenuation, and the FIR-radio Correlation on the Main Sequence of Star-forming Galaxies up to z $\simeq$4. *The Astrophysical Journal*, 807:141.

Papovich, C., Finkelstein, S. L., Ferguson, H. C., Lotz, J. M., and Giavalisco, M. (2011). The rising star formation histories of distant galaxies and implications for gas accretion with time. *MNRAS*, 412:1123–1136.

Peng, C. Y. (2007). How Mergers May Affect the Mass Scaling Relation between Gravitationally Bound Systems. *The Astrophysical Journal*, 671:1098–1107.

Peng, Y.-j., Lilly, S. J., Kovač, K., Bolzonella, M., Pozzetti, L., Renzini, A., Zamorani, G., Ilbert, O., Knobel, C., Iovino, A., Maier, C., Cucciati, O., Tasca, L., Carollo, C. M., Silverman, J., Kampczyk, P., de Ravel, L., Sanders, D., Scoville, N., Contini, T., Mainieri, V., Scodeggio, M., Kneib, J.-P., Le Fèvre, O., Bardelli, S., Bongiorno, A., Caputi, K., Coppa, G., de la Torre, S., Franzetti, P., Garilli, B., Lamareille, F., Le Borgne, J.-F., Le Brun, V., Mignoli, M., Perez Montero, E., Pello, R., Ricciardelli, E., Tanaka, M., Tresse, L., Vergani, D., Welikala, N., Zucca, E., Oesch, P., Abbas, U., Barnes, L., Bordoloi, R., Bottini, D., Cappi, A., Cassata, P., Cimatti, A., Fumana, M., Hasinger, G., Koekemoer, A., Leauthaud, A., Maccagni, D., Marinoni, C., McCracken, H., Memeo, P., Meneux, B., Nair, P., Porciani, C., Presotto, V., and Scaramella, R. (2010). Mass and Environment as Drivers of Galaxy Evolution in SDSS and zCOSMOS and the Origin of the Schechter Function. *The Astrophysical Journal*, 721:193–221.

Perez-Gonzalez, P. G., Rieke, G. H., Villar, V., Barro, G., Blaylock, M., Egami, E., Gallego, J., Gil de Paz, A., Pascual, S., Zamorano, J., and Donley, J. L. (2008). The Stellar Mass Assembly of Galaxies from z = 0 to z = 4: Analysis of a Sample

Selected in the Rest-Frame Near-Infrared with Spitzer. *The Astrophysical Journal*, 675:234–261.

Persic, M., Rephaeli, Y., Braito, V., Cappi, M., Della Ceca, R., Franceschini, A., and Gruber, D. E. (2004). 2-10 keV luminosity of high-mass binaries as a gauge of ongoing star-formation rate. *Astron. Astrophys.*, 419:849–862.

Planck Collaboration VII, Ade, P. A. R., Aghanim, N., Argüeso, F., Arnaud, M., Ashdown, M., Atrio-Barandela, F., Aumont, J., Baccigalupi, C., Balbi, A., Banday, A. J., Barreiro, R. B., Battaner, E., Benabed, K., Benoît, A., Bernard, J.-P., Bersanelli, M., Bethermin, M., Bhatia, R., Bonaldi, A., Bond, J. R., Borrill, J., Bouchet, F. R., Burigana, C., Cabella, P., Cardoso, J.-F., Catalano, A., Cayón, L., Chamballu, A., Chary, R.-R., Chen, X., Chiang, L.-Y., Christensen, P. R., Clements, D. L., Colafrancesco, S., Colombi, S., Colombo, L. P. L., Coulais, A., Crill, B. P., Cuttaia, F., Danese, L., Davis, R. J., de Bernardis, P., de Gasperis, G., de Zotti, G., Delabrouille, J., Dickinson, C., Diego, J. M., Dole, H., Donzelli, S., Doré, O., Dörl, U., Douspis, M., Dupac, X., Efstathiou, G., Enßlin, T. A., Eriksen, H. K., Finelli, F., Forni, O., Fosalba, P., Frailis, M., Franceschi, E., Galeotta, S., Ganga, K., Giard, M., Giardino, G., Giraud-Héraud, Y., González-Nuevo, J., Górski, K. M., Gregorio, A., Gruppuso, A., Hansen, F. K., Harrison, D., Henrot-Versillé, S., Hernández-Monteagudo, C., Herranz, D., Hildebrandt, S. R., Hivon, E., Hobson, M., Holmes, W. A., Jaffe, T. R., Jaffe, A. H., Jagemann, T., Jones, W. C., Juvela, M., Keihänen, E., Kisner, T. S., Kneissl, R., Knoche, J., Knox, L., Kunz, M., Kurinsky, N., Kurki-Suonio, H., Lagache, G., Lähteenmäki, A., Lamarre, J.-M., Lasenby, A., Lawrence, C. R., Leonardi, R., Lilje, P. B., López-Caniego, M., Macías-Pérez, J. F., Maino, D., Mandolesi, N., Maris, M., Marshall, D. J., Martínez-González, E., Masi, S., Massardi, M., Matarrese, S., Mazzotta, P., Melchiorri, A., Mendes, L., Mennella, A., Mitra, S., Miville-Deschènes, M.-A., Moneti, A., Montier, L., Morgante, G., Mortlock, D., Munshi, D., Murphy, J. A., Naselsky, P., Nati, F., Natoli, P., Nørgaard-Nielsen, H. U., Noviello, F., Novikov, D., Novikov, I., Osborne, S., Pajot, F., Paladini, R., Paoletti, D., Partridge, B., Pasian, F., Patanchon, G., Perdereau, O., Perotto, L., Perrotta, F., Piacentini, F., Piat, M., Pierpaoli, E., Plaszczynski, S., Pointecouteau, E., Polenta, G., Ponthieu, N., Popa, L., Poutanen, T., Pratt, G. W., Prunet, S., Puget, J.-L., Rachen, J. P., Reach, W. T., Rebolo, R., Reinecke, M., Renault, C., Ricciardi, S., Riller, T., Ristorcelli, I., Rocha, G., Rosset, C., Rowan-Robinson, M., Rubiño-Martín, J. A., Rusholme, B., Sajina, A., Sandri, M., Savini, G., Scott, D., Smoot, G. F., Starck, J.-L., Sudiwala, R., Suur-Uski, A.-S., Sygnet, J.-F., Tauber, J. A., Terenzi, L., Toffolatti, L., Tomasi, M., Tristram, M., Tucci, M., Türler, M., Valenziano, L., Van Tent, B., Vielva, P., Villa, F., Vittorio, N., Wade, L. A., Wandelt, B. D., White, M., Yvon, D., Zacchei, A., and Zonca, A. (2013). Planck intermediate results. VII. Statistical properties of infrared and radio extragalactic sources from the

Planck Early Release Compact Source Catalogue at frequencies between 100 and 857 GHz. *Astron. Astrophys.*, 550:A133.

Planck Collaboration XX, Ade, P. A. R., Aghanim, N., Arnaud, M., Ashdown, M., Aumont, J., Baccigalupi, C., Balbi, A., Banday, A. J., Barreiro, R. B., and et al. (2011). Planck early results. XX. New light on anomalous microwave emission from spinning dust grains. *Astron. Astrophys.*, 536:A20.

Planck Collaboration XXV, Ade, P. A. R., Aghanim, N., Arnaud, M., Ashdown, M., Aumont, J., Baccigalupi, C., Banday, A. J., Barreiro, R. B., Bartolo, N., and et al. (2015). Planck intermediate results. XXV. The Andromeda galaxy as seen by Planck. *Astron. Astrophys.*, 582:A28.

Planck Collaboration XXVIII, Ade, P. A. R., Aghanim, N., Argüeso, F., Armitage-Caplan, C., Arnaud, M., Ashdown, M., Atrio-Barandela, F., Aumont, J., Baccigalupi, C., and et al. (2014). Planck 2013 results. XXVIII. The Planck Catalogue of Compact Sources. *Astron. Astrophys.*, 571:A28.

Polletta, M., Tajer, M., Maraschi, L., Trinchieri, G., Lonsdale, C. J., Chiappetti, L., Andreon, S., Pierre, M., Le Fèvre, O., Zamorani, G., Maccagni, D., Garcet, O., Surdej, J., Franceschini, A., Alloin, D., Shupe, D. L., Surace, J. A., Fang, F., Rowan-Robinson, M., Smith, H. E., and Tresse, L. (2007). Spectral Energy Distributions of Hard X-Ray Selected Active Galactic Nuclei in the XMM-Newton Medium Deep Survey. *The Astrophysical Journal*, 663:81–102.

Pozzetti, L., Bolzonella, M., Lamareille, F., Zamorani, G., Franzetti, P., Le FÃl'vre, O., Iovino, A., Temporin, S., Ilbert, O., Arnouts, S., Charlot, S., Brinchmann, J., Zucca, E., Tresse, L., Scodeggio, M., Guzzo, L., Bottini, D., Garilli, B., Le Brun, V., Maccagni, D., Picat, J. P., Scaramella, R., Vettolani, G., Zanichelli, A., Adami, C., Bardelli, S., Cappi, A., Ciliegi, P., Contini, T., Foucaud, S., Gavignaud, I., McCracken, H. J., Marano, B., Marinoni, C., Mazure, A., Meneux, B., Merighi, R., Paltani, S., PellÃš, R., Pollo, A., Radovich, M., Bondi, M., Bongiorno, A., Cucciati, O., de la Torre, S., Gregorini, L., Mellier, Y., Merluzzi, P., Vergani, D., and Walcher, C. J. (2007). The VIMOS VLT Deep Survey. The assembly history of the stellar mass in galaxies: from the young to the old universe. *Astron. Astrophys.*, 474:443–459.

Prandoni, I. and Seymour, N. (2015). Revealing the Physics and Evolution of Galaxies and Galaxy Clusters with SKA Continuum Surveys. *Advancing Astrophysics with the Square Kilometre Array (AASKA14)*, page 67.

Priddey, R. S., Isaak, K. G., McMahon, R. G., and Omont, A. (2003). The SCUBA Bright Quasar Survey (SBQS) - II. Unveiling the quasar epoch at submillimetre wavelengths. *MNRAS*, 339:1183–1188.

Prouton, O. R., Bressan, A., Clemens, M., Franceschini, A., Granato, G. L., and Silva, L. (2004). Modelling the Spectral Energy Distribution of compact luminous infrared galaxies: Constraints from high frequency radio data. *Astron. Astrophys.*, 421:115–127.

Rafferty, D. A., Brandt, W. N., Alexander, D. M., Xue, Y. Q., Bauer, F. E., Lehmer, B. D., Luo, B., and Papovich, C. (2011). Supermassive Black Hole Growth in Starburst Galaxies over Cosmic Time: Constraints from the Deepest Chandra Fields. *The Astrophysical Journal*, 742:3.

Raimundo, S. I., Fabian, A. C., Vasudevan, R. V., Gandhi, P., and Wu, J. (2012). Can we measure the accretion efficiency of active galactic nuclei? *MNRAS*, 419:2529–2544.

Ranalli, P., Comastri, A., and Setti, G. (2003). The 2-10 keV luminosity as a Star Formation Rate indicator. *Astron. Astrophys.*, 399:39–50.

Rangwala, N., Maloney, P. R., Glenn, J., Wilson, C. D., Rykala, A., Isaak, K., Baes, M., Bendo, G. J., Boselli, A., Bradford, C. M., Clements, D. L., Cooray, A., Fulton, T., Imhof, P., Kamenetzky, J., Madden, S. C., Mentuch, E., Sacchi, N., Sauvage, M., Schirm, M. R. P., Smith, M. W. L., Spinoglio, L., and Wolfire, M. (2011). Observations of Arp 220 Using Herschel-SPIRE: An Unprecedented View of the Molecular Gas in an Extreme Star Formation Environment. *The Astrophysical Journal*, 743:94.

Rawle, T. D., Egami, E., Bussmann, R. S., Gurwell, M., Ivison, R. J., Boone, F., Combes, F., Danielson, A. L. R., Rex, M., Richard, J., Smail, I., Swinbank, A. M., Altieri, B., Blain, A. W., Clement, B., Dessauges-Zavadsky, M., Edge, A. C., Fazio, G. G., Jones, T., Kneib, J.-P., Omont, A., Pérez-González, P. G., Schaerer, D., Valtchanov, I., van der Werf, P. P., Walth, G., Zamojski, M., and Zemcov, M. (2014). [C II] and ^{12}CO(1-0) Emission Maps in HLSJ091828.6+514223: A Strongly Lensed Interacting System at z = 5.24. *The Astrophysical Journal*, 783:59.

Reddy, N., Dickinson, M., Elbaz, D., Morrison, G., Giavalisco, M., Ivison, R., Papovich, C., Scott, D., Buat, V., Burgarella, D., Charmandaris, V., Daddi, E., Magdis, G., Murphy, E., Altieri, B., Aussel, H., Dannerbauer, H., Dasyra, K., Hwang, H. S., Kartaltepe, J., Leiton, R., Magnelli, B., and Popesso, P. (2012). GOODS-Herschel Measurements of the Dust Attenuation of Typical Star-forming Galaxies at High Redshift: Observations of Ultraviolet-selected Galaxies at z 2. *The Astrophysical Journal*, 744:154.

Reddy, N. A., Erb, D. K., Pettini, M., Steidel, C. C., and Shapley, A. E. (2010). Dust Obscuration and Metallicity at High Redshift: New Inferences from UV, Hα, and 8 μm Observations of z 2 Star-forming Galaxies. *The Astrophysical Journal*, 712:1070–1091.

Reddy, N. A., Kriek, M., Shapley, A. E., Freeman, W. R., Siana, B., Coil, A. L., Mobasher, B., Price, S. H., Sanders, R. L., and Shivaei, I. (2015). The MOSDEF Survey: Measurements of Balmer Decrements and the Dust Attenuation Curve at Redshifts z 1.4-2.6. *The Astrophysical Journal*, 806:259.

Reddy, N. A. and Steidel, C. C. (2004). X-Ray and Radio Emission from Ultraviolet-selected Star-forming Galaxies at Redshifts $1.5 \lesssim z \lesssim 3.0$ in the GOODS-North Field. *The Astrophysical Journal Letters*, 603:L13–L16.

Reddy, N. A. and Steidel, C. C. (2009). A Steep Faint-End Slope of the UV Luminosity Function at z 2-3: Implications for the Global Stellar Mass Density and Star Formation in Low-Mass Halos. *The Astrophysical Journal*, 692:778–803.

Reddy, N. A., Steidel, C. C., Fadda, D., Yan, L., Pettini, M., Shapley, A. E., Erb, D. K., and Adelberger, K. L. (2006). Star Formation and Extinction in Redshift $z \sim 2$ Galaxies: Inferences from Spitzer MIPS Observations. *The Astrophysical Journal*, 644:792–812.

Renzini, A. (2006). Stellar Population Diagnostics of Elliptical Galaxy Formation. *Annu. Rev. Astron. Astrophys.*, 44:141–192.

Renzini, A. and Peng, Y.-j. (2015). An Objective Definition for the Main Sequence of Star-forming Galaxies. *The Astrophysical Journal Letters*, 801:L29.

Richards, G. T., Strauss, M. A., Fan, X., Hall, P. B., Jester, S., Schneider, D. P., Vanden Berk, D. E., Stoughton, C., Anderson, S. F., Brunner, R. J., Gray, J., Gunn, J. E., Ivezić, Ž., Kirkland, M. K., Knapp, G. R., Loveday, J., Meiksin, A., Pope, A., Szalay, A. S., Thakar, A. R., Yanny, B., York, D. G., Barentine, J. C., Brewington, H. J., Brinkmann, J., Fukugita, M., Harvanek, M., Kent, S. M., Kleinman, S. J., Krzesiński, J., Long, D. C., Lupton, R. H., Nash, T., Neilsen, Jr., E. H., Nitta, A., Schlegel, D. J., and Snedden, S. A. (2006). The Sloan Digital Sky Survey Quasar Survey: Quasar Luminosity Function from Data Release 3. *Astronomic. J.*, 131:2766–2787.

Riechers, D. A., Bradford, C. M., Clements, D. L., Dowell, C. D., Perez-Fournon, I., Ivison, R. J., Bridge, C., Conley, A., Fu, H., Vieira, J. D., Wardlow, J., Calanog, J., Cooray, A., Hurley, P., Neri, R., Kamenetzky, J., Aguirre, J. E., Altieri, B., Arumugam, V., Benford, D. J., Béthermin, M., Bock, J., Burgarella, D., Cabrera-Lavers, A., Chapman, S. C., Cox, P., Dunlop, J. S., Earle, L., Farrah, D., Ferrero, P., Franceschini, A., Gavazzi, R., Glenn, J., Solares, E. A. G., Gurwell, M. A., Halpern, M., Hatziminaoglou, E., Hyde, A., Ibar, E., Kovács, A., Krips, M., Lupu, R. E., Maloney, P. R., Martinez-Navajas, P., Matsuhara, H., Murphy, E. J., Naylor, B. J., Nguyen, H. T., Oliver, S. J., Omont, A., Page, M. J., Petitpas, G., Rangwala, N., Roseboom, I. G., Scott, D., Smith, A. J., Staguhn, J. G., Streblyanska, A., Thomson,

A. P., Valtchanov, I., Viero, M., Wang, L., Zemcov, M., and Zmuidzinas, J. (2013). A dust-obscured massive maximum-starburst galaxy at a redshift of 6.34. *Nature*, 496:329–333.

Riechers, D. A., Carilli, C. L., Capak, P. L., Scoville, N. Z., Smolčić, V., Schinnerer, E., Yun, M., Cox, P., Bertoldi, F., Karim, A., and Yan, L. (2014). ALMA Imaging of Gas and Dust in a Galaxy Protocluster at Redshift 5.3: [C II] Emission in "Typical" Galaxies and Dusty Starbursts ≈ 1 Billion Years after the Big Bang. *The Astrophysical Journal*, 796:84.

Roberts-Borsani, G. W., Bouwens, R. J., Oesch, P. A., Labbe, I., Smit, R., Illingworth, G. D., van Dokkum, P., Holden, B., Gonzalez, V., Stefanon, M., Holwerda, B., and Wilkins, S. (2016). z ≳ 7 Galaxies with Red Spitzer/IRAC [3.6]-[4.5] Colors in the Full CANDELS Data Set: The Brightest-Known Galaxies at z 7-9 and a Probable Spectroscopic Confirmation at z = 7.48. *The Astrophysical Journal*, 823:143.

Robertson, B. E., Ellis, R. S., Furlanetto, S. R., and Dunlop, J. S. (2015). Cosmic Reionization and Early Star-forming Galaxies: A Joint Analysis of New Constraints from Planck and the Hubble Space Telescope. *The Astrophysical Journal Letters*, 802:L19.

Rodighiero, G., Brusa, M., Daddi, E., Negrello, M., Mullaney, J. R., Delvecchio, I., Lutz, D., Renzini, A., Franceschini, A., Baronchelli, I., Pozzi, F., Gruppioni, C., Strazzullo, V., Cimatti, A., and Silverman, J. (2015). Relationship between Star Formation Rate and Black Hole Accretion At Z = 2: the Different Contributions in Quiescent, Normal, and Starburst Galaxies. *The Astrophysical Journal Letters*, 800:L10.

Rodighiero, G., Daddi, E., Baronchelli, I., Cimatti, A., Renzini, A., Aussel, H., Popesso, P., Lutz, D., Andreani, P., Berta, S., Cava, A., Elbaz, D., Feltre, A., Fontana, A., Förster Schreiber, N. M., Franceschini, A., Genzel, R., Grazian, A., Gruppioni, C., Ilbert, O., Le Floc'h, E., Magdis, G., Magliocchetti, M., Magnelli, B., Maiolino, R., McCracken, H., Nordon, R., Poglitsch, A., Santini, P., Pozzi, F., Riguccini, L., Tacconi, L. J., Wuyts, S., and Zamorani, G. (2011). The Lesser Role of Starbursts in Star Formation at z = 2. *The Astrophysical Journal Letters*, 739:L40.

Rodighiero, G., Renzini, A., Daddi, E., Baronchelli, I., Berta, S., Cresci, G., Franceschini, A., Gruppioni, C., Lutz, D., Mancini, C., Santini, P., Zamorani, G., Silverman, J., Kashino, D., Andreani, P., Cimatti, A., Sánchez, H. D., Le Floc'h, E., Magnelli, B., Popesso, P., and Pozzi, F. (2014). A multiwavelength consensus on the main sequence of star-forming galaxies at z ∼ 2. *MNRAS*, 443:19–30.

Roming, P. W. A., Kennedy, T. E., Mason, K. O., Nousek, J. A., Ahr, L., Bingham, R. E., Broos, P. S., Carter, M. J., Hancock, B. K., Huckle, H. E., Hunsberger, S. D.,

Kawakami, H., Killough, R., Koch, T. S., McLelland, M. K., Smith, K., Smith, P. J., Soto, J. C., Boyd, P. T., Breeveld, A. A., Holland, S. T., Ivanushkina, M., Pryzby, M. S., Still, M. D., and Stock, J. (2005). The Swift Ultra-Violet/Optical Telescope. *Space Science Rev.*, 120:95–142.

Rosario, D. J., Santini, P., Lutz, D., Shao, L., Maiolino, R., Alexander, D. M., Altieri, B., Andreani, P., Aussel, H., Bauer, F. E., Berta, S., Bongiovanni, A., Brandt, W. N., Brusa, M., Cepa, J., Cimatti, A., Cox, T. J., Daddi, E., Elbaz, D., Fontana, A., Förster Schreiber, N. M., Genzel, R., Grazian, A., Le Floc'h, E., Magnelli, B., Mainieri, V., Netzer, H., Nordon, R., Pérez Garcia, I., Poglitsch, A., Popesso, P., Pozzi, F., Riguccini, L., Rodighiero, G., Salvato, M., Sanchez-Portal, M., Sturm, E., Tacconi, L. J., Valtchanov, I., and Wuyts, S. (2012). The mean star formation rate of X-ray selected active galaxies and its evolution from z $\sim$ 2.5: results from PEP-Herschel. *Astron. Astrophys.*, 545:A45.

Ross, N. P., McGreer, I. D., White, M., Richards, G. T., Myers, A. D., Palanque-Delabrouille, N., Strauss, M. A., Anderson, S. F., Shen, Y., Brandt, W. N., Yeche, C., Swanson, M. E. C., Aubourg, E., Bailey, S., Bizyaev, D., Bovy, J., Brewington, H., Brinkmann, J., DeGraf, C., Di Matteo, T., Ebelke, G., Fan, X., Ge, J., Malanushenko, E., Malanushenko, V., Mandelbaum, R., Maraston, C., Muna, D., Oravetz, D., Pan, K., aris, I., Petitjean, P., Schawinski, K., Schlegel, D. J., Schneider, D. P., Silverman, J. D., Simmons, A., Snedden, S., Streblyanska, A., Suzuki, N., Weinberg, D. H., and York, D. (2013). The SDSS-III Baryon Oscillation Spectroscopic Survey: The Quasar Luminosity Function from Data Release Nine. *The Astrophysical Journal*, 773:14.

Rovilos, E., Comastri, A., Gilli, R., Georgantopoulos, I., Ranalli, P., Vignali, C., Lusso, E., Cappelluti, N., Zamorani, G., Elbaz, D., Dickinson, M., Hwang, H. S., Charmandaris, V., Ivison, R. J., Merloni, A., Daddi, E., Carrera, F. J., Brandt, W. N., Mullaney, J. R., Scott, D., Alexander, D. M., Del Moro, A., Morrison, G., Murphy, E. J., Altieri, B., Aussel, H., Dannerbauer, H., Kartaltepe, J., Leiton, R., Magdis, G., Magnelli, B., Popesso, P., and Valtchanov, I. (2012). GOODS-Herschel: ultra-deep XMM-Newton observations reveal AGN/star-formation connection. *Astron. Astrophys.*, 546:A58.

Rowlands, K., Dunne, L., Dye, S., Aragón-Salamanca, A., Maddox, S., da Cunha, E., Smith, D. J. B., Bourne, N., Eales, S., Gomez, H. L., Smail, I., Alpaslan, M., Clark, C. J. R., Driver, S., Ibar, E., Ivison, R. J., Robotham, A., Smith, M. W. L., and Valiante, E. (2014). Herschel-ATLAS: properties of dusty massive galaxies at low and high redshifts. *MNRAS*, 441:1017–1039.

Salmon, B., Papovich, C., Finkelstein, S. L., Tilvi, V., Finlator, K., Behroozi, P., Dahlen, T., Davé, R., Dekel, A., Dickinson, M., Ferguson, H. C., Giavalisco, M.,

Long, J., Lu, Y., Mobasher, B., Reddy, N., Somerville, R. S., and Wechsler, R. H. (2015). The Relation between Star Formation Rate and Stellar Mass for Galaxies at 3.5 <= z <= 6.5 in CANDELS. *The Astrophysical Journal*, 799:183.

Salpeter, E. E. (1955). The Luminosity Function and Stellar Evolution. *The Astrophysical Journal*, 121:161.

Sani, E., Davies, R. I., Sternberg, A., Graciá-Carpio, J., Hicks, E. K. S., Krips, M., Tacconi, L. J., Genzel, R., Vollmer, B., Schinnerer, E., García-Burillo, S., Usero, A., and Orban de Xivry, G. (2012). Physical properties of dense molecular gas in centres of Seyfert galaxies. *MNRAS*, 424:1963–1976.

Santini, P., Fontana, A., Grazian, A., Salimbeni, S., Fontanot, F., Paris, D., Boutsia, K., Castellano, M., Fiore, F., Gallozzi, S., Giallongo, E., Koekemoer, A. M., Menci, N., Pentericci, L., and Somerville, R. S. (2012a). The evolving slope of the stellar mass function at 0.6 *leq* z < 4.5 from deep WFC3 data. *Astron. Astrophys.*, 538:A33.

Santini, P., Rosario, D. J., Shao, L., Lutz, D., Maiolino, R., Alexander, D. M., Altieri, B., Andreani, P., Aussel, H., Bauer, F. E., Berta, S., Bongiovanni, A., Brandt, W. N., Brusa, M., Cepa, J., Cimatti, A., Daddi, E., Elbaz, D., Fontana, A., Forster Schreiber, N. M., Genzel, R., Grazian, A., Le Floc'h, E., Magnelli, B., Mainieri, V., Nordon, R., Perez Garcia, A. M., Poglitsch, A., Popesso, P., Pozzi, F., Riguccini, L., Rodighiero, G., Salvato, M., Sanchez-Portal, M., Sturm, E., Tacconi, L. J., Valtchanov, I., and Wuyts, S. (2012b). Enhanced star formation rates in AGN hosts with respect to inactive galaxies from PEP-Herschel observations. *Astron. Astrophys.*, 540:A109.

Sauvage, M. and Thuan, T. X. (1992). On the use of far-infrared luminosity as a star formation indicator in galaxies. *The Astrophysical Journal Letters*, 396:L69–L73.

Scalo, J. M. (1986). The initial mass function of massive stars in galaxies Empirical evidence. In De Loore, C. W. H., Willis, A. J., and Laskarides, P., editors, *Luminous Stars and Associations in Galaxies*, volume 116 of *IAU Symposium*, pages 451–466.

Scannapieco, C., Wadepuhl, M., Parry, O. H., Navarro, J. F., Jenkins, A., Springel, V., Teyssier, R., Carlson, E., Couchman, H. M. P., Crain, R. A., Dalla Vecchia, C., Frenk, C. S., Kobayashi, C., Monaco, P., Murante, G., Okamoto, T., Quinn, T., Schaye, J., Stinson, G. S., Theuns, T., Wadsley, J., White, S. D. M., and Woods, R. (2012). The Aquila comparison project: the effects of feedback and numerical methods on simulations of galaxy formation. *MNRAS*, 423:1726–1749.

Schady, P., Savaglio, S., Muller, T., Kruhler, T., Dwelly, T., Palazzi, E., Hunt, L. K., Greiner, J., Linz, H., Michalowski, M. J., Pierini, D., Piranomonte, S., Vergani, S. D., and Gear, W. K. (2014). Herschel observations of gamma-ray burst host galaxies:

implications for the topology of the dusty interstellar medium. *Astron. Astrophys.*, 570:A52.

Schmidt, M. (1968). Space Distribution and Luminosity Functions of Quasi-Stellar Radio Sources. *The Astrophysical Journal*, 151:393.

Schulze, A., Bongiorno, A., Gavignaud, I., Schramm, M., Silverman, J., Merloni, A., Zamorani, G., Hirschmann, M., Mainieri, V., Wisotzki, L., Shankar, F., Fiore, F., Koekemoer, A. M., and Temporin, G. (2015). The cosmic growth of the active black hole population at 1 <z <2 in zCOSMOS, VVDS and SDSS. *MNRAS*, 447:2085–2111.

Scott, K. S., Wilson, G. W., Aretxaga, I., Austermann, J. E., Chapin, E. L., Dunlop, J. S., Ezawa, H., Halpern, M., Hatsukade, B., Hughes, D. H., Kawabe, R., Kim, S., Kohno, K., Lowenthal, J. D., Montaña, A., Nakanishi, K., Oshima, T., Sanders, D., Scott, D., Scoville, N., Tamura, Y., Welch, D., Yun, M. S., and Zeballos, M. (2012). The source counts of submillimetre galaxies detected at λ= 1.1 mm. *MNRAS*, 423:575–589.

Scoville, N., Aussel, H., Sheth, K., Scott, K. S., Sanders, D., Ivison, R., Pope, A., Capak, P., Vanden Bout, P., Manohar, S., Kartaltepe, J., Robertson, B., and Lilly, S. (2014). The Evolution of Interstellar Medium Mass Probed by Dust Emission: ALMA Observations at z = 0.3-2. *The Astrophysical Journal*, 783:84.

Scoville, N., Sheth, K., Aussel, H., Vanden Bout, P., Capak, P., Bongiorno, A., Casey, C. M., Murchikova, L., Koda, J., Álvarez-Márquez, J., Lee, N., Laigle, C., McCracken, H. J., Ilbert, O., Pope, A., Sanders, D., Chu, J., Toft, S., Ivison, R. J., and Manohar, S. (2016). ISM Masses and the Star formation Law at Z=1 to 6: ALMA Observations of Dust Continuum in 145 Galaxies in the COSMOS Survey Field. *The Astrophysical Journal*, 820:83.

Seaton, M. J. (1979). Interstellar extinction in the UV. *MNRAS*, 187:73P–76P.

Serjeant, S., Bertoldi, F., Blain, A. W., Clements, D. L., Cooray, A., Danese, L., Dunlop, J., Dunne, L., Eales, S., Falder, J., Hatziminaoglou, E., Hughes, D. H., Ibar, E., Jarvis, M. J., Lawrence, A., Lee, M. G., Michalowski, M., Negrello, M., Omont, A., Page, M., Pearson, C., van der Werf, P. P., White, G., Amblard, A., Auld, R., Baes, M., Bonfield, D. G., Burgarella, D., Buttiglione, S., Cava, A., Dariush, A., de Zotti, G., Dye, S., Frayer, D., Fritz, J., Gonzalez-Nuevo, J., Herranz, D., Ivison, R. J., Lagache, G., Leeuw, L., Lopez-Caniego, M., Maddox, S., Pascale, E., Pohlen, M., Rigby, E., Rodighiero, G., Samui, S., Sibthorpe, B., Smith, D. J. B., Temi, P., Thompson, M., Valtchanov, I., and Verma, A. (2010). Herschel ATLAS: The cosmic star formation history of quasar host galaxies. *Astron. Astrophys.*, 518:L7.

Shankar, F. (2013). Black hole demography: from scaling relations to models. *Classical and Quantum Gravity*, 30(24):244001.

Shankar, F., Bernardi, M., Sheth, R. K., Ferrarese, L., Graham, A. W., Savorgnan, G., Allevato, V., Marconi, A., Läsker, R., and Lapi, A. (2016). Selection bias in dynamically measured supermassive black hole samples: its consequences and the quest for the most fundamental relation. *MNRAS*, 460:3119–3142.

Shankar, F., Lapi, A., Salucci, P., De Zotti, G., and Danese, L. (2006). New Relationships between Galaxy Properties and Host Halo Mass, and the Role of Feedbacks in Galaxy Formation. *The Astrophysical Journal*, 643:14–25.

Shankar, F., Weinberg, D. H., and Miralda-Escude, J. (2009). Self-Consistent Models of the AGN and Black Hole Populations: Duty Cycles, Accretion Rates, and the Mean Radiative Efficiency. *The Astrophysical Journal*, 690:20–41.

Shankar, F., Weinberg, D. H., and Shen, Y. (2010). Constraints on black hole duty cycles and the black hole-halo relation from SDSS quasar clustering. *MNRAS*, 406:1959–1966.

Shao, L., Lutz, D., Nordon, R., Maiolino, R., Alexander, D. M., Altieri, B., Andreani, P., Aussel, H., Bauer, F. E., Berta, S., Bongiovanni, A., Brandt, W. N., Brusa, M., Cava, A., Cepa, J., Cimatti, A., Daddi, E., Dominguez-Sanchez, H., Elbaz, D., Förster Schreiber, N. M., Geis, N., Genzel, R., Grazian, A., Gruppioni, C., Magdis, G., Magnelli, B., Mainieri, V., Perez Garcia, A. M., Poglitsch, A., Popesso, P., Pozzi, F., Riguccini, L., Rodighiero, G., Rovilos, E., Saintonge, A., Salvato, M., Sanchez Portal, M., Santini, P., Sturm, E., Tacconi, L. J., Valtchanov, I., Wetzstein, M., and Wieprecht, E. (2010). Star formation in AGN hosts in GOODS-N. *Astron. Astrophys.*, 518:L26.

Shapley, A. E., Steidel, C. C., Adelberger, K. L., Dickinson, M., Giavalisco, M., and Pettini, M. (2001). The Rest-Frame Optical Properties of z=3 Galaxies. *The Astrophysical Journal*, 562:95–123.

Sheth, R. K. and Tormen, G. (1999). Large-scale bias and the peak background split. *MNRAS*, 308:119–126.

Sheth, R. K. and Tormen, G. (2002). An excursion set model of hierarchical clustering: ellipsoidal collapse and the moving barrier. *MNRAS*, 329:61–75.

Siebenmorgen, R., Heymann, F., and Efstathiou, A. (2015). Self-consistent two-phase AGN torus models. SED library for observers. *Astron. Astrophys.*, 583:A120.

Silk, J. and Rees, M. J. (1998). Quasars and galaxy formation. *Astron. Astrophys.*, 331:L1–L4.

Silva, L., Granato, G. L., Bressan, A., and Danese, L. (1998). Modeling the Effects of Dust on Galactic Spectral Energy Distributions from the Ultraviolet to the Millimeter Band. *The Astrophysical Journal*, 509:103–117.

Silverman, J. D., Lamareille, F., Maier, C., Lilly, S. J., Mainieri, V., Brusa, M., Cappelluti, N., Hasinger, G., Zamorani, G., Scodeggio, M., Bolzonella, M., Contini, T., Carollo, C. M., Jahnke, K., Kneib, J.-P., Le Fevre, O., Merloni, A., Bardelli, S., Bongiorno, A., Brunner, H., Caputi, K., Civano, F., Comastri, A., Coppa, G., Cucciati, O., de la Torre, S., de Ravel, L., Elvis, M., Finoguenov, A., Fiore, F., Franzetti, P., Garilli, B., Gilli, R., Iovino, A., Kampczyk, P., Knobel, C., Kovač, K., Le Borgne, J.-F., Le Brun, V., Mignoli, M., Pello, R., Peng, Y., Perez Montero, E., Ricciardelli, E., Tanaka, M., Tasca, L., Tresse, L., Vergani, D., Vignali, C., Zucca, E., Bottini, D., Cappi, A., Cassata, P., Fumana, M., Griffiths, R., Kartaltepe, J., Koekemoer, A., Marinoni, C., McCracken, H. J., Memeo, P., Meneux, B., Oesch, P., Porciani, C., and Salvato, M. (2009). Ongoing and Co-Evolving Star Formation in zCOSMOS Galaxies Hosting Active Galactic Nuclei. *The Astrophysical Journal*, 696:396–410.

Simpson, J. M., Smail, I., Swinbank, A. M., Chapman, S. C., Geach, J. E., Ivison, R. J., Thomson, A. P., Aretxaga, I., Blain, A. W., Cowley, W. I., Chen, C.-C., Coppin, K. E. K., Dunlop, J. S., Edge, A. C., Farrah, D., Ibar, E., Karim, A., Knudsen, K. K., Meijerink, R., Michalowski, M. J., Scott, D., Spaans, M., and van der Werf, P. P. (2015). The SCUBA-2 Cosmology Legacy Survey: ALMA Resolves the Bright-end of the Sub-millimeter Number Counts. *The Astrophysical Journal*, 807:128.

Small, T. A. and Blandford, R. D. (1992). Quasar evolution and the growth of black holes. *MNRAS*, 259:725–737.

Smit, R., Bouwens, R. J., Franx, M., Illingworth, G. D., Labbé, I., Oesch, P. A., and van Dokkum, P. G. (2012). The Star Formation Rate Function for Redshift z 4-7 Galaxies: Evidence for a Uniform Buildup of Star-forming Galaxies during the First 3 Gyr of Cosmic Time. *The Astrophysical Journal*, 756:14.

Smith, D. J. B., Dunne, L., da Cunha, E., Rowlands, K., Maddox, S. J., Gomez, H. L., Bonfield, D. G., Charlot, S., Driver, S. P., Popescu, C. C., Tuffs, R. J., Dunlop, J. S., Jarvis, M. J., Seymour, N., Symeonidis, M., Baes, M., Bourne, N., Clements, D. L., Cooray, A., De Zotti, G., Dye, S., Eales, S., Scott, D., Verma, A., van der Werf, P., Andrae, E., Auld, R., Buttiglione, S., Cava, A., Dariush, A., Fritz, J., Hopwood, R., Ibar, E., Ivison, R. J., Kelvin, L., Madore, B. F., Pohlen, M., Rigby, E. E., Robotham, A., Seibert, M., and Temi, P. (2012). Herschel-ATLAS: multi-wavelength SEDs and physical properties of 250 μm selected galaxies at z < 0.5. *MNRAS*, 427:703–727.

Smolčić, V., Aravena, M., Navarrete, F., Schinnerer, E., Riechers, D. A., Bertoldi, F., Feruglio, C., Finoguenov, A., Salvato, M., Sargent, M., McCracken, H. J., Albrecht,

M., Karim, A., Capak, P., Carilli, C. L., Cappelluti, N., Elvis, M., Ilbert, O., Kartaltepe, J., Lilly, S., Sanders, D., Sheth, K., Scoville, N. Z., and Taniguchi, Y. (2012). Millimeter imaging of submillimeter galaxies in the COSMOS field: redshift distribution. *Astron. Astrophys.*, 548:A4.

Sobral, D., Smail, I., Best, P. N., Geach, J. E., Matsuda, Y., Stott, J. P., Cirasuolo, M., and Kurk, J. (2013). A large Hα survey at z = 2.23, 1.47, 0.84 and 0.40: the 11 Gyr evolution of star-forming galaxies from HiZELS. *MNRAS*, 428:1128–1146.

Soltan, A. (1982). Masses of quasars. *MNRAS*, 200:115–122.

Somerville, R. S. and Davé, R. (2015). Physical Models of Galaxy Formation in a Cosmological Framework. *Annu. Rev. Astron. Astrophys.*, 53:51–113.

Somerville, R. S., Gilmore, R. C., Primack, J. R., and Domínguez, A. (2012). Galaxy properties from the ultraviolet to the far-infrared: Λ cold dark matter models confront observations. *MNRAS*, 423:1992–2015.

Song, M., Finkelstein, S. L., Ashby, M. L. N., Grazian, A., Lu, Y., Papovich, C., Salmon, B., Somerville, R. S., Dickinson, M., Duncan, K., Faber, S. M., Fazio, G. G., Ferguson, H. C., Fontana, A., Guo, Y., Hathi, N., Lee, S.-K., Merlin, E., and Willner, S. P. (2015). The Evolution of the Galaxy Stellar Mass Function at z= 4-8: A Steepening Low-mass-end Slope with Increasing Redshift. *ArXiv e-prints*.

Song, M., Finkelstein, S. L., Ashby, M. L. N., Grazian, A., Lu, Y., Papovich, C., Salmon, B., Somerville, R. S., Dickinson, M., Duncan, K., Faber, S. M., Fazio, G. G., Ferguson, H. C., Fontana, A., Guo, Y., Hathi, N., Lee, S.-K., Merlin, E., and Willner, S. P. (2016). The Evolution of the Galaxy Stellar Mass Function at z = 4-8: A Steepening Low-mass-end Slope with Increasing Redshift. *The Astrophysical Journal*, 825:5.

Speagle, J. S., Steinhardt, C. L., Capak, P. L., and Silverman, J. D. (2014). A Highly Consistent Framework for the Evolution of the Star-Forming "Main Sequence" from z 0-6. *The Astrophysical Journal Supp. Series*, 214:15.

Springel, V., Wang, J., Vogelsberger, M., Ludlow, A., Jenkins, A., Helmi, A., Navarro, J. F., Frenk, C. S., and White, S. D. M. (2008). The Aquarius Project: the subhaloes of galactic haloes. *MNRAS*, 391:1685–1711.

Stadel, J., Potter, D., Moore, B., Diemand, J., Madau, P., Zemp, M., Kuhlen, M., and Quilis, V. (2009). Quantifying the heart of darkness with GHALO - a multibillion particle simulation of a galactic halo. *MNRAS*, 398:L21–L25.

Stanley, F., Harrison, C. M., Alexander, D. M., Swinbank, A. M., Aird, J. A., Del Moro, A., Hickox, R. C., and Mullaney, J. R. (2015). A remarkably flat relationship

between the average star formation rate and AGN luminosity for distant X-ray AGN. *MNRAS*, 453:591–604.

Stark, D. P., Ellis, R. S., Bunker, A., Bundy, K., Targett, T., Benson, A., and Lacy, M. (2009). The Evolutionary History of Lyman Break Galaxies Between Redshift 4 and 6: Observing Successive Generations of Massive Galaxies in Formation. *The Astrophysical Journal*, 697:1493–1511.

Stecher, T. P., Cornett, R. H., Greason, M. R., Landsman, W. B., Hill, J. K., Hill, R. S., Bohlin, R. C., Chen, P. C., Collins, N. R., Fanelli, M. N., Hollis, J. I., Neff, S. G., O'Connell, R. W., Offenberg, J. D., Parise, R. A., Parker, J., Roberts, M. S., Smith, A. M., and Waller, W. H. (1997). The Ultraviolet Imaging Telescope: Instrument and Data Characteristics. *PASP*, 109:584–599.

Stefanon, M., Marchesini, D., Muzzin, A., Brammer, G., Dunlop, J. S., Franx, M., Fynbo, J. P. U., Labbé, I., Milvang-Jensen, B., and van Dokkum, P. G. (2015). Stellar Mass Functions of Galaxies At $4 < z < 7$ from an IRAC-selected Sample in Cosmos/Ultravista: Limits on the Abundance of Very Massive Galaxies. *The Astrophysical Journal*, 803:11.

Steinhardt, C. L., Capak, P., Masters, D., and Speagle, J. S. (2016). The Impossibly Early Galaxy Problem. *The Astrophysical Journal*, 824:21.

Steinhardt, C. L., Speagle, J. S., Capak, P., Silverman, J. D., Carollo, M., Dunlop, J., Hashimoto, Y., Hsieh, B.-C., Ilbert, O., Le Fevre, O., Le Floc'h, E., Lee, N., Lin, L., Lin, Y.-T., Masters, D., McCracken, H. J., Nagao, T., Petric, A., Salvato, M., Sanders, D., Scoville, N., Sheth, K., Strauss, M. A., and Taniguchi, Y. (2014). Star Formation at $4 < z < 6$ from the Spitzer Large Area Survey with Hyper-Suprime-Cam (SPLASH). *The Astrophysical Journal Letters*, 791:L25.

Stevens, J. A., Page, M. J., Ivison, R. J., Carrera, F. J., Mittaz, J. P. D., Smail, I., and McHardy, I. M. (2005). Submillimetre photometry of X-ray absorbed quasi-stellar objects: their formation and evolutionary status. *MNRAS*, 360:610–618.

Swinbank, A. M., Simpson, J. M., Smail, I., Harrison, C. M., Hodge, J. A., Karim, A., Walter, F., Alexander, D. M., Brandt, W. N., de Breuck, C., da Cunha, E., Chapman, S. C., Coppin, K. E. K., Danielson, A. L. R., Dannerbauer, H., Decarli, R., Greve, T. R., Ivison, R. J., Knudsen, K. K., Lagos, C. D. P., Schinnerer, E., Thomson, A. P., Wardlow, J. L., Weiß, A., and van der Werf, P. (2014). An ALMA survey of sub-millimetre Galaxies in the Extended Chandra Deep Field South: the far-infrared properties of SMGs. *MNRAS*, 438:1267–1287.

Swinbank, A. M., Smail, I., Longmore, S., Harris, A. I., Baker, A. J., De Breuck, C., Richard, J., Edge, A. C., Ivison, R. J., Blundell, R., Coppin, K. E. K., Cox, P.,

Gurwell, M., Hainline, L. J., Krips, M., Lundgren, A., Neri, R., Siana, B., Siringo, G., Stark, D. P., Wilner, D., and Younger, J. D. (2010). Intense star formation within resolved compact regions in a galaxy at z = 2.3. *Nature*, 464:733–736.

Symeonidis, M., Georgakakis, A., Seymour, N., Auld, R., Bock, J., Brisbin, D., Buat, V., Burgarella, D., Chanial, P., Clements, D. L., Cooray, A., Eales, S., Farrah, D., Franceschini, A., Glenn, J., Griffin, M., Hatziminaoglou, E., Ibar, E., Ivison, R. J., Mortier, A. M. J., Oliver, S. J., Page, M. J., Papageorgiou, A., Pearson, C. P., Pérez-Fournon, I., Pohlen, M., Rawlings, J. I., Raymond, G., Rodighiero, G., Roseboom, I. G., Rowan-Robinson, M., Scott, D., Smith, A. J., Tugwell, K. E., Vaccari, M., Vieira, J. D., Vigroux, L., Wang, L., and Wright, G. (2011). Herschel/HerMES: the X-ray-infrared correlation for star-forming galaxies at z∼1. *MNRAS*, 417:2239–2252.

Symeonidis, M., Rosario, D., Georgakakis, A., Harker, J., Laird, E. S., Page, M. J., and Willmer, C. N. A. (2010). The central energy source of 70 μm-selected galaxies: starburst or AGN? *MNRAS*, 403:1474–1490.

Tasca, L. A. M., Le Fevre, O., Hathi, N. P., Schaerer, D., Ilbert, O., Zamorani, G., Lemaux, B. C., Cassata, P., Garilli, B., Le Brun, V., Maccagni, D., Pentericci, L., Thomas, R., Vanzella, E., Zucca, E., Amorin, R., Bardelli, S., Cassará, L. P., Castellano, M., Cimatti, A., Cucciati, O., Durkalec, A., Fontana, A., Giavalisco, M., Grazian, A., Paltani, S., Ribeiro, B., Scodeggio, M., Sommariva, V., Talia, M., Tresse, L., Vergani, D., Capak, P., Charlot, S., Contini, T., de la Torre, S., Dunlop, J., Fotopoulou, S., Koekemoer, A., Lopez-Sanjuan, C., Mellier, Y., Pforr, J., Salvato, M., Scoville, N., Taniguchi, Y., and Wang, P. W. (2015). The evolving star formation rate: M_* relation and sSFR since z $\simeq$ 5 from the VUDS spectroscopic survey. *Astron. Astrophys.*, 581:A54.

Thomas, D., Maraston, C., Bender, R., and Mendes de Oliveira, C. (2005). The Epochs of Early-Type Galaxy Formation as a Function of Environment. *The Astrophysical Journal*, 621:673–694.

Thorne, K. S. (1974). Disk-Accretion onto a Black Hole. II. Evolution of the Hole. *The Astrophysical Journal*, 191:507–520.

Tinker, J., Kravtsov, A. V., Klypin, A., Abazajian, K., Warren, M., Yepes, G., Gottlöber, S., and Holz, D. E. (2008). Toward a Halo Mass Function for Precision Cosmology: The Limits of Universality. *The Astrophysical Journal*, 688:709–728.

Tomczak, A. R., Quadri, R. F., Tran, K.-V. H., Labbé, I., Straatman, C. M. S., Papovich, C., Glazebrook, K., Allen, R., Brammer, G. B., Kacprzak, G. G., Kawinwanichakij, L., Kelson, D. D., McCarthy, P. J., Mehrtens, N., Monson, A. J., Persson, S. E.,

Spitler, L. R., Tilvi, V., and van Dokkum, P. (2014). Galaxy Stellar Mass Functions from ZFOURGE/CANDELS: An Excess of Low-mass Galaxies since z = 2 and the Rapid Buildup of Quiescent Galaxies. *The Astrophysical Journal*, 783:85.

Tremaine, S., Gebhardt, K., Bender, R., Bower, G., Dressler, A., Faber, S. M., Filippenko, A. V., Green, R., Grillmair, C., Ho, L. C., Kormendy, J., Lauer, T. R., Magorrian, J., Pinkney, J., and Richstone, D. (2002). The Slope of the Black Hole Mass versus Velocity Dispersion Correlation. *The Astrophysical Journal*, 574:740–753.

Treyer, M., Schiminovich, D., Johnson, B., Seibert, M., Wyder, T., Barlow, T. A., Conrow, T., Forster, K., Friedman, P. G., Martin, D. C., Morrissey, P., Neff, S. G., Small, T., Bianchi, L., Donas, J., Heckman, T. M., Lee, Y.-W., Madore, B. F., Milliard, B., Rich, R. M., Szalay, A. S., Welsh, B. Y., and Yi, S. K. (2007). Extinction-corrected Star Formation Rates Empirically Derived from Ultraviolet-Optical Colors. *The Astrophysical Journal Supp. Series*, 173:256–266.

Ueda, Y., Akiyama, M., Hasinger, G., Miyaji, T., and Watson, M. G. (2014). Toward the Standard Population Synthesis Model of the X-Ray Background: Evolution of X-Ray Luminosity and Absorption Functions of Active Galactic Nuclei Including Compton-thick Populations. *The Astrophysical Journal*, 786:104.

Ueda, Y., Akiyama, M., Ohta, K., and Miyaji, T. (2003). Cosmological Evolution of the Hard X-Ray Active Galactic Nucleus Luminosity Function and the Origin of the Hard X-Ray Background. *The Astrophysical Journal*, 598:886–908.

Vale, A. and Ostriker, J. P. (2004). Linking halo mass to galaxy luminosity. *MNRAS*, 353:189–200.

van der Burg, R. F. J., Hildebrandt, H., and Erben, T. (2010). The UV galaxy luminosity function at z = 3-5 from the CFHT Legacy Survey Deep fields. *Astron. Astrophys.*, 523:A74.

Vattakunnel, S., Tozzi, P., Matteucci, F., Padovani, P., Miller, N., Bonzini, M., Mainieri, V., Paolillo, M., Vincoletto, L., Brandt, W. N., Luo, B., Kellermann, K. I., and Xue, Y. Q. (2012). The radio-X-ray relation as a star formation indicator: results from the Very Large Array-Extended Chandra Deep Field-South. *MNRAS*, 420:2190–2208.

Vazdekis, A. (1999). Evolutionary Stellar Population Synthesis at 2 angstrom Spectral Resolution. *The Astrophysical Journal*, 513:224–241.

Vazdekis, A., Coelho, P., Cassisi, S., Ricciardelli, E., Falcon-Barroso, J., Sanchez-Blazquez, P., Barbera, F. L., Beasley, M. A., and Pietrinferni, A. (2015). Evolutionary stellar population synthesis with MILES - II. Scaled-solar and α-enhanced models. *MNRAS*, 449:1177–1214.

Vega, O., Clemens, M. S., Bressan, A., Granato, G. L., Silva, L., and Panuzzo, P. (2008). Modelling the spectral energy distribution of ULIRGs. II. The energetic environment and the dense interstellar medium. *Astron. Astrophys.*, 484:631–653.

Vernstrom, T., Scott, D., Wall, J. V., Condon, J. J., Cotton, W. D., Fomalont, E. B., Kellermann, K. I., Miller, N., and Perley, R. A. (2014). Deep 3 GHz number counts from a P(D) fluctuation analysis. *MNRAS*, 440:2791–2809.

Vestergaard, M. and Osmer, P. S. (2009). Mass Functions of the Active Black Holes in Distant Quasars from the Large Bright Quasar Survey, the Bright Quasar Survey, and the Color-selected Sample of the SDSS Fall Equatorial Stripe. *The Astrophysical Journal*, 699:800–816.

Vika, M., Driver, S. P., Graham, A. W., and Liske, J. (2009). The Millennium Galaxy Catalogue: the M_{bh}-$L_{spheroid}$ derived supermassive black hole mass function. *MNRAS*, 400:1451–1460.

Vogelsberger, M., Genel, S., Springel, V., Torrey, P., Sijacki, D., Xu, D., Snyder, G., Nelson, D., and Hernquist, L. (2014). Introducing the Illustris Project: simulating the coevolution of dark and visible matter in the Universe. *MNRAS*, 444:1518–1547.

Volonteri, M., Silk, J., and Dubus, G. (2015). The Case for Supercritical Accretion onto Massive Black Holes at High Redshift. *The Astrophysical Journal*, 804:148.

Walcher, J., Groves, B., Budavári, T., and Dale, D. (2011). Fitting the integrated spectral energy distributions of galaxies. *Ap&SS*, 331:1–52.

Walter, F., Riechers, D., Cox, P., Neri, R., Carilli, C., Bertoldi, F., Weiss, A., and Maiolino, R. (2009). A kiloparsec-scale hyper-starburst in a quasar host less than 1gigayear after the Big Bang. *Nature*, 457:699–701.

Walterbos, R. A. M. and Greenawalt, B. (1996). Far-Infrared Radiation from Dust Heated by the Interstellar Radiation Field in Spiral Galaxies. *The Astrophysical Journal*, 460:696.

Wang, B. and Heckman, T. M. (1996). Internal Absorption and the Luminosity of Disk Galaxies. *The Astrophysical Journal*, 457:645.

Wang, J., Navarro, J. F., Frenk, C. S., White, S. D. M., Springel, V., Jenkins, A., Helmi, A., Ludlow, A., and Vogelsberger, M. (2011). Assembly history and structure of galactic cold dark matter haloes. *MNRAS*, 413:1373–1382.

Wang, J.-M., Du, P., Valls-Gabaud, D., Hu, C., and Netzer, H. (2013a). Super-Eddington Accreting Massive Black Holes as Long-Lived Cosmological Standards. *Physical Review Letters*, 110(8):081301.

Wang, R., Carilli, C. L., Wagg, J., Bertoldi, F., Walter, F., Menten, K. M., Omont, A., Cox, P., Strauss, M. A., Fan, X., Jiang, L., and Schneider, D. P. (2008). Thermal Emission from Warm Dust in the Most Distant Quasars. *The Astrophysical Journal*, 687:848–858.

Wang, R., Wagg, J., Carilli, C. L., Walter, F., Lentati, L., Fan, X., Riechers, D. A., Bertoldi, F., Narayanan, D., Strauss, M. A., Cox, P., Omont, A., Menten, K. M., Knudsen, K. K., Neri, R., and Jiang, L. (2013b). Star Formation and Gas Kinematics of Quasar Host Galaxies at z $\sim$ 6: New Insights from ALMA. *The Astrophysical Journal*, 773:44.

Wang, S. X., Brandt, W. N., Luo, B., Smail, I., Alexander, D. M., Danielson, A. L. R., Hodge, J. A., Karim, A., Lehmer, B. D., Simpson, J. M., Swinbank, A. M., Walter, F., Wardlow, J. L., Xue, Y. Q., Chapman, S. C., Coppin, K. E. K., Dannerbauer, H., De Breuck, C., Menten, K. M., and van der Werf, P. (2013c). An ALMA Survey of Submillimeter Galaxies in the Extended Chandra Deep Field-South: The AGN Fraction and X-Ray Properties of Submillimeter Galaxies. *The Astrophysical Journal*, 778:179.

Wardlow, J. L., Cooray, A., De Bernardis, F., Amblard, A., Arumugam, V., Aussel, H., Baker, A. J., Béthermin, M., Blundell, R., Bock, J., Boselli, A., Bridge, C., Buat, V., Burgarella, D., Bussmann, R. S., Cabrera-Lavers, A., Calanog, J., Carpenter, J. M., Casey, C. M., Castro-Rodríguez, N., Cava, A., Chanial, P., Chapin, E., Chapman, S. C., Clements, D. L., Conley, A., Cox, P., Dowell, C. D., Dye, S., Eales, S., Farrah, D., Ferrero, P., Franceschini, A., Frayer, D. T., Frazer, C., Fu, H., Gavazzi, R., Glenn, J., González Solares, E. A., Griffin, M., Gurwell, M. A., Harris, A. I., Hatziminaoglou, E., Hopwood, R., Hyde, A., Ibar, E., Ivison, R. J., Kim, S., Lagache, G., Levenson, L., Marchetti, L., Marsden, G., Martinez-Navajas, P., Negrello, M., Neri, R., Nguyen, H. T., O'Halloran, B., Oliver, S. J., Omont, A., Page, M. J., Panuzzo, P., Papageorgiou, A., Pearson, C. P., Pérez-Fournon, I., Pohlen, M., Riechers, D., Rigopoulou, D., Roseboom, I. G., Rowan-Robinson, M., Schulz, B., Scott, D., Scoville, N., Seymour, N., Shupe, D. L., Smith, A. J., Streblyanska, A., Strom, A., Symeonidis, M., Trichas, M., Vaccari, M., Vieira, J. D., Viero, M., Wang, L., Xu, C. K., Yan, L., and Zemcov, M. (2013). HerMES: Candidate Gravitationally Lensed Galaxies and Lensing Statistics at Submillimeter Wavelengths. *The Astrophysical Journal*, 762:59.

Watarai, K.-y., Fukue, J., Takeuchi, M., and Mineshige, S. (2000). Galactic Black-Hole Candidates Shining at the Eddington Luminosity. *Publ. Astron. Soc. Japan*, 52:133.

Watson, D., Christensen, L., Knudsen, K. K., Richard, J., Gallazzi, A., and Michalowski, M. J. (2015). A dusty, normal galaxy in the epoch of reionization. *Nature*, 519:327–330.

Weiß, A., De Breuck, C., Marrone, D. P., Vieira, J. D., Aguirre, J. E., Aird, K. A., Aravena, M., Ashby, M. L. N., Bayliss, M., Benson, B. A., Béthermin, M., Biggs, A. D., Bleem, L. E., Bock, J. J., Bothwell, M., Bradford, C. M., Brodwin, M., Carlstrom, J. E., Chang, C. L., Chapman, S. C., Crawford, T. M., Crites, A. T., de Haan, T., Dobbs, M. A., Downes, T. P., Fassnacht, C. D., George, E. M., Gladders, M. D., Gonzalez, A. H., Greve, T. R., Halverson, N. W., Hezaveh, Y. D., High, F. W., Holder, G. P., Holzapfel, W. L., Hoover, S., Hrubes, J. D., Husband, K., Keisler, R., Lee, A. T., Leitch, E. M., Lueker, M., Luong-Van, D., Malkan, M., McIntyre, V., McMahon, J. J., Mehl, J., Menten, K. M., Meyer, S. S., Murphy, E. J., Padin, S., Plagge, T., Reichardt, C. L., Rest, A., Rosenman, M., Ruel, J., Ruhl, J. E., Schaffer, K. K., Shirokoff, E., Spilker, J. S., Stalder, B., Staniszewski, Z., Stark, A. A., Story, K., Vanderlinde, K., Welikala, N., and Williamson, R. (2013). ALMA Redshifts of Millimeter-selected Galaxies from the SPT Survey: The Redshift Distribution of Dusty Star-forming Galaxies. *The Astrophysical Journal*, 767:88.

Weiß, A., Kovács, A., Coppin, K., Greve, T. R., Walter, F., Smail, I., Dunlop, J. S., Knudsen, K. K., Alexander, D. M., Bertoldi, F., Brandt, W. N., Chapman, S. C., Cox, P., Dannerbauer, H., De Breuck, C., Gawiser, E., Ivison, R. J., Lutz, D., Menten, K. M., Koekemoer, A. M., Kreysa, E., Kurczynski, P., Rix, H.-W., Schinnerer, E., and van der Werf, P. P. (2009). The Large Apex Bolometer Camera Survey of the Extended Chandra Deep Field South. *The Astrophysical Journal*, 707:1201–1216.

Whitaker, K. E., Franx, M., Leja, J., van Dokkum, P. G., Henry, A., Skelton, R. E., Fumagalli, M., Momcheva, I. G., Brammer, G. B., Labbé, I., Nelson, E. J., and Rigby, J. R. (2014). Constraining the Low-mass Slope of the Star Formation Sequence at $0.5 < z < 2.5$. *The Astrophysical Journal*, 795:104.

White, M., Martini, P., and Cohn, J. D. (2008). Constraints on the correlation between QSO luminosity and host halo mass from high-redshift quasar clustering. *MNRAS*, 390:1179–1184.

Willott, C. J., Albert, L., Arzoumanian, D., Bergeron, J., Crampton, D., Delorme, P., Hutchings, J. B., Omont, A., Reylé, C., and Schade, D. (2010). Eddington-limited Accretion and the Black Hole Mass Function at Redshift 6. *Astronomic. J.*, 140:546–560.

Willott, C. J., Bergeron, J., and Omont, A. (2015). Star Formation Rate and Dynamical Mass of 10^8 Solar Mass Black Hole Host Galaxies At Redshift 6. *The Astrophysical Journal*, 801:123.

Windhorst, R. A., Mather, J., Clampin, M., Doyon, R., Flanagan, K., Franx, M., Gardner, J., Greenhouse, M., Hammel, H., Huchings, J., Jakobsen, P., Lilly, S., McCaughrean, M., Mountain, M., Rieke, G., Sonneborn, G., Stiavelli, M., and Wright,

G. (2009). Galaxies Across Cosmic Time with JWST. In *astro2010: The Astronomy and Astrophysics Decadal Survey*, volume 2010 of *Astronomy*.

Worthey, G. (1994). Comprehensive stellar population models and the disentanglement of age and metallicity effects. *The Astrophysical Journal Supp. Series*, 95:107–149.

Wright, E. L., Eisenhardt, P. R. M., Mainzer, A. K., Ressler, M. E., Cutri, R. M., Jarrett, T., Kirkpatrick, J. D., Padgett, D., McMillan, R. S., Skrutskie, M., Stanford, S. A., Cohen, M., Walker, R. G., Mather, J. C., Leisawitz, D., Gautier, III, T. N., McLean, I., Benford, D., Lonsdale, C. J., Blain, A., Mendez, B., Irace, W. R., Duval, V., Liu, F., Royer, D., Heinrichsen, I., Howard, J., Shannon, M., Kendall, M., Walsh, A. L., Larsen, M., Cardon, J. G., Schick, S., Schwalm, M., Abid, M., Fabinsky, B., Naes, L., and Tsai, C.-W. (2010). The Wide-field Infrared Survey Explorer (WISE): Mission Description and Initial On-orbit Performance. *Astronomic. J.*, 140:1868–1881.

Wu, S., Lu, Y., Zhang, F., and Lu, Y. (2013). Radiative efficiency of disc accretion in individual SDSS QSOs. *MNRAS*, 436:3271–3285.

Wyder, T. K., Treyer, M. A., Milliard, B., Schiminovich, D., Arnouts, S., Budavári, T., Barlow, T. A., Bianchi, L., Byun, Y.-I., Donas, J., Forster, K., Friedman, P. G., Heckman, T. M., Jelinsky, P. N., Lee, Y.-W., Madore, B. F., Malina, R. F., Martin, D. C., Morrissey, P., Neff, S. G., Rich, R. M., Siegmund, O. H. W., Small, T., Szalay, A. S., and Welsh, B. Y. (2005). The Ultraviolet Galaxy Luminosity Function in the Local Universe from GALEX Data. *The Astrophysical Journal Letters*, 619:L15–L18.

Xu, L., Rieke, G. H., Egami, E., Haines, C. P., Pereira, M. J., and Smith, G. P. (2015). The Relation between Luminous AGNs and Star Formation in Their Host Galaxies. *The Astrophysical Journal*, 808:159.

Xue, Y. Q., Brandt, W. N., Luo, B., Rafferty, D. A., Alexander, D. M., Bauer, F. E., Lehmer, B. D., Schneider, D. P., and Silverman, J. D. (2010). Color-Magnitude Relations of Active and Non-active Galaxies in the Chandra Deep Fields: High-redshift Constraints and Stellar-mass Selection Effects. *The Astrophysical Journal*, 720:368–391.

Yu, Q. and Lu, Y. (2004). Constraints on QSO Models from a Relation between the QSO Luminosity Function and the Local Black Hole Mass Function. *The Astrophysical Journal*, 602:603–624.

Yun, M. S., Reddy, N. A., and Condon, J. J. (2001). Radio Properties of Infrared-selected Galaxies in the IRAS 2 Jy Sample. *The Astrophysical Journal*, 554:803–822.

Zhao, D. H., Mo, H. J., Jing, Y. P., and Börner, G. (2003). The growth and structure of dark matter haloes. *MNRAS*, 339:12–24.

Zitrin, A., Labbé, I., Belli, S., Bouwens, R., Ellis, R. S., Roberts-Borsani, G., Stark, D. P., Oesch, P. A., and Smit, R. (2015). Lymanα Emission from a Luminous z = 8.68 Galaxy: Implications for Galaxies as Tracers of Cosmic Reionization. *The Astrophysical Journal Letters*, 810:L12.